A review of Ga_2O_3 materials, processing, and devices

S. J. Pearton, Jiancheng Yang, Patrick H. Cary, F. Ren, Jihyun Kim, Marko J. Tadjer, and Michael A. Mastro

Citation: Applied Physics Reviews **5**, 011301 (2018);
View online: https://doi.org/10.1063/1.5006941
View Table of Contents: http://aip.scitation.org/toc/are/5/1
Published by the American Institute of Physics

Articles you may be interested in

Gallium oxide (Ga_2O_3) metal-semiconductor field-effect transistors on single-crystal β-Ga_2O_3 (010) substrates
Applied Physics Letters **100**, 013504 (2012); 10.1063/1.3674287

High breakdown electric field in β-Ga_2O_3/graphene vertical barristor heterostructure
Applied Physics Letters **112**, 032101 (2018); 10.1063/1.5002138

Highly conductive homoepitaxial Si-doped Ga_2O_3 films on (010) β-Ga_2O_3 by pulsed laser deposition
Applied Physics Letters **111**, 012103 (2017); 10.1063/1.4991363

Radiation hardness of β-Ga_2O_3 metal-oxide-semiconductor field-effect transistors against gamma-ray irradiation
Applied Physics Letters **112**, 023503 (2018); 10.1063/1.5017810

Crystal Structure of β-Ga_2O_3
The Journal of Chemical Physics **33**, 676 (1960); 10.1063/1.1731237

Enhancement-mode Ga_2O_3 wrap-gate fin field-effect transistors on native (100) β-Ga_2O_3 substrate with high breakdown voltage
Applied Physics Letters **109**, 213501 (2016); 10.1063/1.4967931

APPLIED PHYSICS REVIEWS

A review of Ga_2O_3 materials, processing, and devices

S. J. Pearton,[1,a)] Jiancheng Yang,[2] Patrick H. Cary IV,[2] F. Ren,[2] Jihyun Kim,[3,a)]
Marko J. Tadjer,[4] and Michael A. Mastro[4]
[1]*Department of Materials Science and Engineering, University of Florida, Gainesville, Florida 32611, USA*
[2]*Department of Chemical Engineering, University of Florida, Gainesville, Florida 32611, USA*
[3]*Department of Chemical and Biological Engineering, Korea University, Seoul 02841, South Korea*
[4]*US Naval Research Laboratory, Washington, DC 20375, USA*

(Received 28 September 2017; accepted 30 October 2017; published online 11 January 2018)

Gallium oxide (Ga_2O_3) is emerging as a viable candidate for certain classes of power electronics, solar blind UV photodetectors, solar cells, and sensors with capabilities beyond existing technologies due to its large bandgap. It is usually reported that there are five different polymorphs of Ga_2O_3, namely, the monoclinic (β-Ga_2O_3), rhombohedral (α), defective spinel (γ), cubic (δ), or orthorhombic (ε) structures. Of these, the β-polymorph is the stable form under normal conditions and has been the most widely studied and utilized. Since melt growth techniques can be used to grow bulk crystals of β-GaO_3, the cost of producing larger area, uniform substrates is potentially lower compared to the vapor growth techniques used to manufacture bulk crystals of GaN and SiC. The performance of technologically important high voltage rectifiers and enhancement-mode Metal-Oxide Field Effect Transistors benefit from the larger critical electric field of β-Ga_2O_3 relative to either SiC or GaN. However, the absence of clear demonstrations of p-type doping in Ga_2O_3, which may be a fundamental issue resulting from the band structure, makes it very difficult to simultaneously achieve low turn-on voltages and ultra-high breakdown. The purpose of this review is to summarize recent advances in the growth, processing, and device performance of the most widely studied polymorph, β-Ga_2O_3. The role of defects and impurities on the transport and optical properties of bulk, epitaxial, and nanostructures material, the difficulty in p-type doping, and the development of processing techniques like etching, contact formation, dielectrics for gate formation, and passivation are discussed. Areas where continued development is needed to fully exploit the properties of Ga_2O_3 are identified. *Published by AIP Publishing.*
https://doi.org/10.1063/1.5006941

TABLE OF CONTENTS

INTRODUCTION 1
BASIC PROPERTIES AND APPLICATIONS OF Ga_2O_3 2
BULK GROWTH TECHNOLOGY OF Ga_2O_3 6
PROGRESS IN METAL ORGANIC CHEMICAL VAPOR DEPOSITION (MOCVD) GROWTH OF Ga_2O_3 7
HALIDE VAPOR PHASE EPITAXY (HVPE) 9
PULSED LASER DEPOSITION (PLD) 9
MIST-CVD 10
MBE OF Ga_2O_3 10
ATOMIC LAYER EPITAXY (ALE) AND ATOMIC LAYER DEPOSITION (ALD) Ga_2O_3 11
Ga_2O_3 NANOSTRUCTURES 12
PROPERTIES AND PROCESSING OF β-Ga_2O_3 13
DOPING AND DEFECTS IN Ga_2O_3 16
OXIDE p-n JUNCTION HETEROSTRUCTURES 19
THEORY OF DEFECTS IN Ga_2O_3 19
LOW AND HIGH FIELD TRANSPORT IN Ga_2O_3 20
BAND STRUCTURE 21
EPR OF Ga_2O_3 22
HYDROGEN IN Ga_2O_3 23
OHMIC CONTACTS TO Ga_2O_3 24
SCHOTTKY CONTACTS TO Ga_2O_3 26
WET ETCHING OF Ga_2O_3 28
DRY ETCHING OF Ga_2O_3 30
BAND ALIGNMENTS OF DIELECTRICS ON (−201) Ga_2O_3 32
RADIATION DAMAGE IN Ga_2O_3 34
THIN FILM SOLAR-BLIND UV DETECTORS 35
POWER RECTIFIERS 37
POWER MOSFETs AND MESFETs 40
Ga_2O_3-BASED GAS SENSORS 42
SUMMARY AND CONCLUSIONS 44

a)Authors to whom correspondence should be addressed: spear@mse.ufl.edu and hyunhyun7@korea.ac.kr

INTRODUCTION

Gallium oxide (Ga_2O_3) has a long history, and the phase equilibria of the Al_2O_3-Ga_2O_3-H_2O system was first reported in 1952,[1] in which the polymorphs (i.e., different forms or crystal structures) of Ga_2O_3 and their regions of stability were also identified. There are five commonly identified polymorphs of Ga_2O_3, labeled as α, β, γ, δ, and ε.[2–10] These are known as corundum (α), monoclinic (β), defective spinel (γ), and orthorhombic (ε), with the δ phase commonly accepted as being a form of the orthorhombic phase.[1,2,7,11] Among these different phases of Ga_2O_3, the orthorhombic β-gallia structure (β-phase or β-Ga_2O_3) is the most stable crystal structure and has attracted most of the recent attention. The different polymorphs can be either insulators or conductors, depending on the growth conditions.[7] The resulting crystals are layered material, similar to the behavior of GaSe and GaTe. Table I summarizes the lattice parameters, crystal structure, and some of the bulk properties of the polymorphs of Ga_2O_3. The original studies indicated that the other polymorphs of Ga_2O_3 convert to the stable β-form with heat treatment.[1]

In this review, we will primarily focus on the monoclinic structured β-Ga_2O_3 polymorph, which is attracting interest for power electronic devices, as well as solar-blind UV photodetectors, photocatalysts, gas sensors, solar cells, phosphors, and transparent conducting films for electrodes on a variety of optoelectronic devices.[2,3,12–20] Ga_2O_3 is optically transparent to ~250 nm and is electrically conducting, making it useful as a window on some types of optical devices. In terms of device applications, thin films of polycrystalline β-Ga_2O_3 containing O vacancies have long been known as sensors for a variety of gases including H_2, CH_4, CO, and O_2 which change the electrical conductivity upon adsorption.[21–25] In addition, the conduction electron spins in this material produces a magnetic memory effect that is stable to above room temperature (RT).[26,27]

The review will cover basic properties of Ga_2O_3, the role of defects and impurities, the status of doping studies, as well as developments in device fabrication processes such as etching and contacting, gate dielectrics, and passivation films. The current status of power electronic devices, solar-blind UV photodetectors, and gas sensors will also be covered.

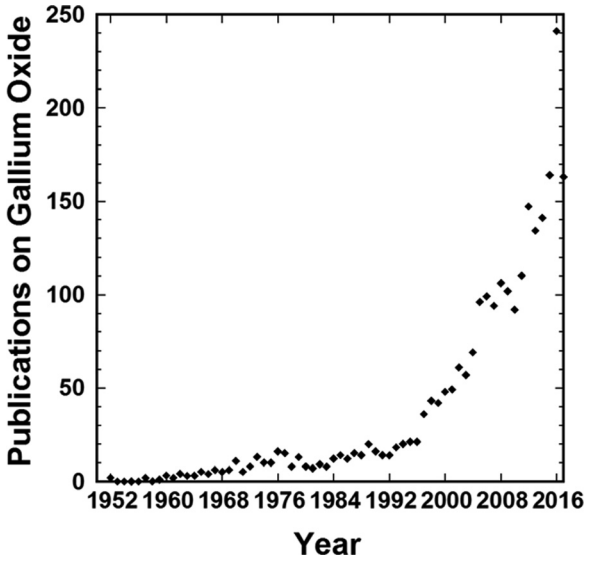

FIG. 1. Number of publications on gallium oxide since 1952. A total of 2492 papers which had either "Ga_2O_3" or "Gallium Oxide" in the title have been published in the last 65 years (Data: Thomson Reuters).

BASIC PROPERTIES AND APPLICATIONS OF Ga_2O_3

The number of publications on Ga_2O_3 has accelerated in recent years, as is evident from Fig. 1, due to the interest in electronic and photonic devices with capabilities beyond existing technologies. There has been a healthy balance of experimental and theoretical investigations of the properties of the Ga_2O_3 system.[5,6,8–11,28,29] The monoclinic phase of β-Ga_2O_3 is the stable one under normal conditions of temperature and pressure, and can be converted into other phases at higher pressures or temperatures.[28,29] For example, it undergoes a transition to the hexagonal α-Ga_2O_3 phase at a pressure of 4.4 GPa at 1000 °C.[30] This high pressure phase can remain as a metastable

TABLE I. Summary of the properties of Ga_2O_3 polymorphs.

Polymorph	Lattice parameters (Å)	Refractive index, n	Optical dielectric constant	Volume expansion at 1200 K	Bulk modulus (300 K, GPa)	Comment	References
α	a, b = 4.98–5.04, c = 13.4–13.6	1.74–1.95	3.03–3.80	0.035	~185	Corundum, rhombohedral structure, space group $R\bar{3}c$, bandgap larger than all other polymorphs (~5.2 eV)	Yoshioka *et al.*,[4] Stepanov *et al.*,[2] and He *et al.*[5]
β	A = 12.12–12.34, b = 3.03–3.04, c = 5.80–5.87	1.68–1.89	2.82–3.57	0.024	~150	Monoclinic structure, space group C2/m	Kohn *et al.*,[10] Stepanov *et al.*,[2] and He *et al.*[6]
γ	A = 8.24–8.30					Defective spinel, cubic structure, space group $Fd\bar{3}m$	Stepanov *et al.*[2]
δ	A = 9.4–10.0			0.04	160	Possibly bixbyite. Suggested to be a nanocrystalline form of ε-Ga_2O_3	Roy *et al.*[1], Playford *et al.*[8]
ε	A = 5.06–5.12, b = 8.69–8.79, c = 9.3–9.4	1.6		0.028	160	Orthorhombic structure, space group $Pna2_1$	Yoshioka *et al.*[4] and Kroll *et al.*[7]

phase if quenched to room temperature.[5,6] The β phase is the only stable phase up to 1800 °C, while the rhombohedral corundum α phase is metastable but can exist under ambient conditions. The β-phase can be transformed into the α-phase under hydrostatic pressure at higher temperatures.

Due to the relative difficulty in isolating the different phases in pure crystalline form,[31–34] much of what we know about the properties has come from theory, especially density functional theory (DFT). For example, Yoshioka *et al.*[4] calculated the lattice parameters, space groups, and volume expansivity normalized to room temperature for the different polymorphs. The results of these calculations are shown in Fig. 2(a). The β-phase has the lowest volume expansion and this increases in the order β, ε, α, and δ. The expansivity of the α-phase is in good agreement with the reported experimental data.[35] The calculated bulk moduli for the different phases are shown in Fig. 2(b)[4] and these increase in the order β, ε, δ, and α below 400 K.

He *et al.*[6] reported the structural parameters, band structure, and Debye temperature of β-Ga_2O_3, also calculated from density functional theory. The band structure showed the conduction band minimum (CBM) is at the zone center, with a fairly flat valence band, as shown in Fig. 3.[6,7] The electron effective mass was calculated as $0.34m_0$ (where m_0 is the free electron mass) for β-Ga_2O_3 and 0.28 for the high pressure hexagonal α-phase. The relative flatness of the valence band for β-Ga_2O_3 in momentum space would indicate a large effective mass for holes. In fact, it is possible that the holes are not free to move but form localized polarons where the hole is localized at a lattice distortion.[3,36,37] The top of the valence and the bottom of the conduction band are made up of the anionic (O 2p states with contributions from Ga 3d and 4s orbitals) and cationic states (Ga 4s states), respectively.[3,6,32,38–43] Since the valence-band states are derived mainly from the O 2p orbitals and are characterized by small dispersion, the holes have large effective masses, and the valence band has a high density of states. Holes tend to form localized small polarons, i.e., localized holes trapped by local lattice distortions. It is common for density functional calculations to produce a slight underestimation of the band gap. There is little difference in energy between the direct and indirect gaps for β-Ga_2O_3, with the direct bandgap being 4.69 eV compared to 4.66 eV for indirect value. The calculations are in good agreement with aborption[44] and angle-resolved photoemission spectroscopy measurements.[45–47]

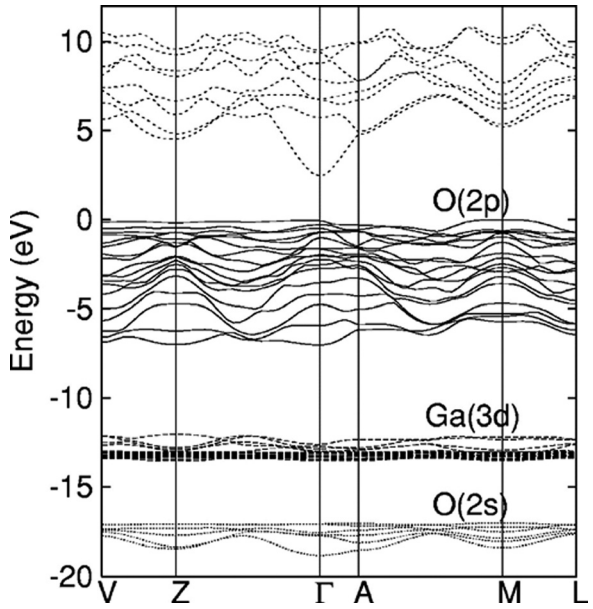

FIG. 3. Band structure of β-Ga_2O_3. The Fermi energy is aligned to zero. The kk points are $\Gamma = (000)$, $A = (0012)$, $Z = (12120)$, $M = (121212)$, $L = (01212)$, and $V = (0120)$. Reprinted with permission from Appl. Phys. Lett. **88**, 261904 (2006). Copyright 2006 American Institute of Physics.[6]

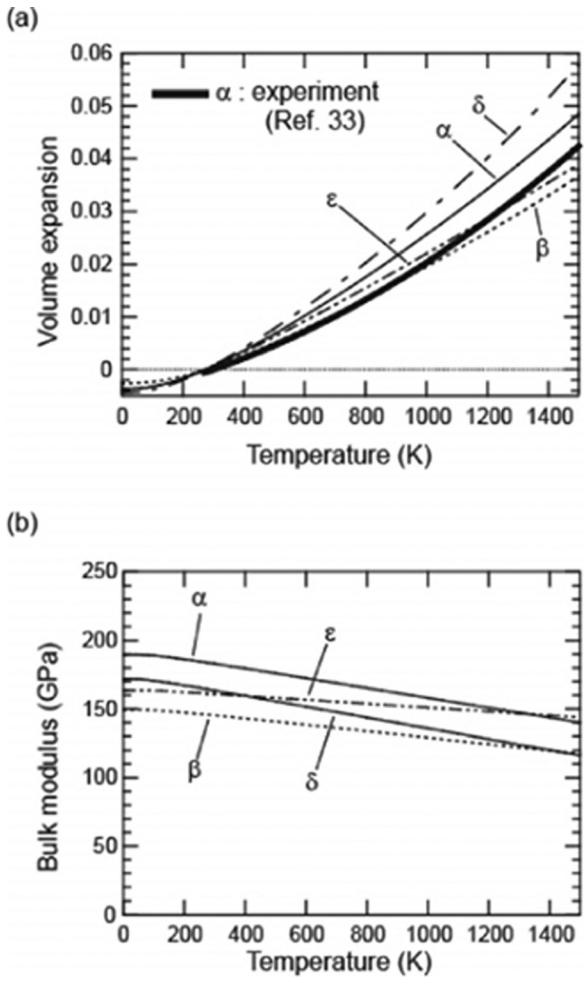

FIG. 2. Temperature dependence of volume expansivity (a) and bulk modulus (b) for α-, β-, δ-, and ε-Ga_2O_3. Reprinted with permission from Yoshioka *et al.*, J. Phys.: Condens. Matter **19**, 346211 (2007). Copyright 2007 IOP.[4]

The room temperature photoluminescence (PL) spectra from Ga_2O_3 are typically dominated by a broad set of transitions centered near 399 nm which have previously been ascribed to oxygen-vacancy related transitions.[48,49] Dong *et al.*[49] reported four bands in this region, with the one at 380 nm in the UV region suggested to be caused by transition levels between the oxygen vacancy and unintended N impurities. They also reported peaks centered at 416 nm, 442 nm (both in the violet region), and 464 nm (blue region), with all three emission peaks suggested to originate from the electron-hole recombination formed by oxygen vacancies, or to the recombination of Ga-O vacancy pair.[50–53] The formation energy of the oxygen vacancies of β-Ga_2O_3 has been

investigated in the past years, and the results can vary with different functional and approximation methods.[50–53] There are three types of O sites in β-Ga_2O_3.[49] As a result, three types of neutral oxygen vacancies exist, denoted as V_{OI}, V_{OII} (both are 3-fold coordinated), and V_{OIII} (4-fold coordinated), respectively, as discussed in the work of Dong *et al.*[49] They predict from density functional calculations that oxygen vacancies can induce absorption peaks at 3.80 eV, 3.52 eV, and 3.37 eV for V_{OI}, V_{OII}, and V_{OIII}, respectively. Historically, Ga_2O_3 has shown three different groups of emission bands, in the UV (3.2–3.6 eV), blue (2.8–3.0 eV), and green (2.4 eV) regions, but it is fair to suggest that the specific origins of the transitions are not finalized.[2,3] Most photoluminescence studies do not show intrinsic emission in the deep UV (~265–278 nm) but only emission in the ultraviolet A (UVA) to visible range (~350–600 nm).[20] An exception is the report of luminescence at ~265 nm and ~278 nm in nanowires (NWs), which correspond to the experimentally reported absorption edges.[20] Several mechanisms have been invoked to explain the UVA/visible luminescence of β-Ga_2O_3, including the influence of native defects and self-trapped holes (polarons).

The unit cell of the stable phase, β-Ga_2O_3, contains two crystallographically different Ga atoms in the asymmetric unit, one with tetrahedral and the other with octahedral coordination geometry.[54–65] The unit cell is composed of two types of gallium ions (Ga_I and Ga_{II}) and three types of oxygen ions (O_I, O_{II}, and O_{III}). This leads to an anisotropy of physical, optical, and electrical,[54,57,60,66–68] predicted both theoretically and observed experimentally.[66–68] For example, the thermal conductivity in Ga_2O_3 shows a strong anisotropy, with the [010] direction showing a thermal conductivity 2.5 times higher than that in the [100] direction,[66–68] although both theory and experiment suggest there is little anisotropy in electron effective mass.[2,3,68] The highest thermal conductivity was ~29 W/m K in the [010] direction. The thermal conductivity of Sn- and Fe-doped samples was lower than undoped samples due to the enhanced phonon-impurity scattering contribution, which reduces the thermal conductivity.

The O_I and O_{III} ions lie in the (010) plane and the O_{II} ions align along the b-axis. The formation free energies have the tendency $\beta < \varepsilon < \alpha < \delta < \gamma$ at low temperatures. There are a number of orientations of β-Ga_2O_3 in common use, including the $(\bar{2}01)$, (010), and (001) planes. Figure 4(a) shows a schematic of the unit cell of β-Ga_2O_3, while Fig. 4(b) shows two of the most commonly used crystal planes for device applications, namely, the (010) and $(\bar{2}01)$. The $(\bar{2}01)$ and (010) surfaces differ significantly in terms of their dangling bond densities of oxygen, and this might be expected to have an effect on processes like wet etching or metal contact formation.

The α-phase has the same corundum crystal structure as Al_2O_3 or sapphire, leading to the possibility of high quality epitaxial layers of Ga_2O_3 on sapphire substrates. At higher temperatures, the difference in free energy between the β-phase and the ε-phase becomes smaller and the other polymorphs find their region of stability. Yan-Mei *et al.*[68] found that the phase transition from the monoclinic β-Ga_2O_3 to the trigonal α-Ga_2O_3 occurs at around 19.2 GPa under cold

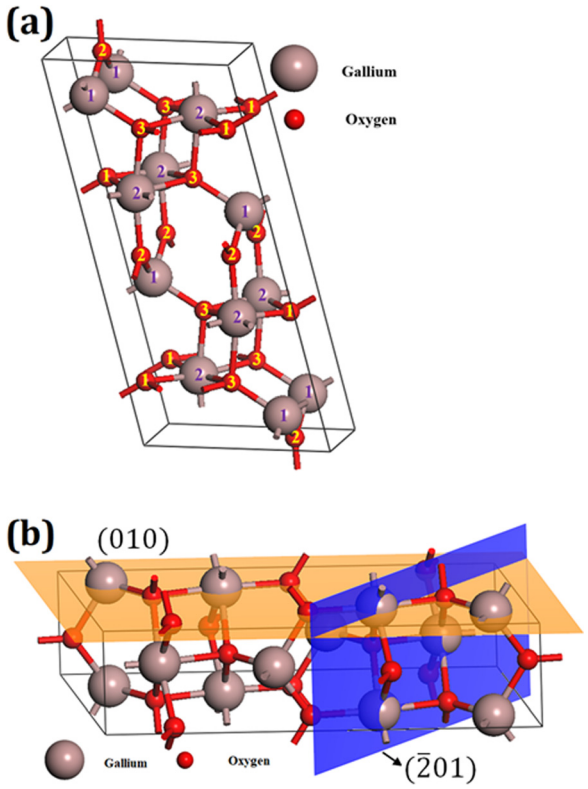

FIG. 4. (a) β-Ga_2O_3 crystal structure and (b) (010) and $(\bar{2}01)$ surfaces.

compression. They heated powdered samples to 2000 K at 30 GPa, and found that α-Ga_2O_3 is the most stable structure at the high pressure.[69] Furthermore, the structural transition from β-Ga_2O_3 to α-Ga_2O_3 was found to be irreversible.[69]

Hexagonal ε-Ga_2O_3 is the second-most stable phase of Ga_2O_3.[54,56,57,61,64] The bandgap of ε-Ga_2O_3 is also approximately 4.9 eV, and this phase is compatible with the common hexagonal wide bandgap semiconductors GaN and SiC.[64,65] It is also predicted that ε-Ga_2O_3 has a large spontaneous polarization and therefore could produce high-density two dimensional (2D) electron gases (2DEG) used for conducting channels in heterostructure field effect transistors. Experimental results using dynamic hysteresis measurements do indeed show the presence of ferroelectricity of ε-Ga_2O_3,[51] as well as pyroelectric properties and large polarization as calculated by the Berry-phase approach.[62]

It is worth commenting on the practical aspects that enable potential technological benefits. In material grown by the edge-defined film-fed growth method,[70,71] the (010) oriented crystals can be cut to produce $(\bar{2}01)$ planes in the specific crystallographic direction. This produces wafers of usable size of a material with a large bandgap of approximately 4.9 eV and associated large estimated critical electric field (E_C) strength of 8 MV/cm.[69,72–84] A useful tool for visualizing the different crystal structures of the polymorphs is from Momma and Izumi.[85] The fairly recent advances in bulk crystal growth are one of the drivers of the interest in Ga_2O_3 for its potential in electronic power switches.[86,87] The suitability of different semiconductors for this and related applications is assessed by the calculating various

figures-of-merit (FOM). Power switch metrics such as Baliga's figure of merit (BFOM) estimating dc conduction losses and Huang's material figure of merit (HMFOM) incorporating dynamic switching losses are functions of either bandgap to the third power or bandgap to first order, respectively.[84–86] Several FOM are listed in Table II. The large bandgap of Ga_2O_3 allows high temperature operation, and the large critical field allows high voltage operation (relative to maximum breakdown). This has been discussed in detail recently by Jessen *et al.*[87] Many of the figures-of-merit involve this reverse breakdown field strength, which scales as a power of the bandgap, typically a power in the range of 2–2.5.[87] The Johnson figure of merit (JFOM) represents the power-frequency product for RF amplification. The large electron saturation velocity ($v_{sat} = 2 \times 10^7$ cm/s) produces a high current density, I_{max} ($I_{max} \approx qn_s v_{sat}$, where $q = 1.6 \times 10^{-19}$ C, n_s = sheet charge density, v_s = electron saturation velocity), and potentially high operating frequency as $f_t = v_{sat}/L_{eff}$. To take several specific cases, the BFOM for Ga_2O_3 is a factor of 4 times larger than for GaN, while the HMFOM for Ga_2O_3 is comparable to GaN.

In addition to its high voltage capability, Ga_2O_3 is attractive for its potential for low power loss during high frequency switching frequency in the GHz regime.[87] Of course, new technologies requiring extensive materials growth development lose out in a comparison of manufacturability and expense, as embodied by Huang's chip area manufacturing FOM (HCAFOM), but even here, the still high cost of GaN and SiC substrates mean that Ga_2O_3 is not uncompetitive. A clear disadvantage from Table II for Ga_2O_3 is the poor thermal conductivity that is embodied in Huang's high temperature figure of merit (HTFOM).[87]

The high-power/high-voltage market is currently primarily dominated by Si lightly-doped metal-oxide semiconductor (LDMOS) and SiC Schottky rectifiers. Ga_2O_3 is a candidate to address the ultra-high power market (>1 kW). The speed with which the cost of Ga_2O_3 substrate decreases will determine whether Ga_2O_3 devices can compete with SiC Schottky and Si-LDMOS in the medium to high power market.

The main market segments for high-power, high-frequency transistors are defense and military applications (radar, jamming, counter-measures, and guided weapons), wireless infrastructure (3G, 3G+, WiMAX/LTE (long term evolution) base stations, and backhaul), and broadcast and communication satellites (SatCom).[14] The relatively low thermal conductivity, λ, of Ga_2O_3 creates self-heating effects that must be mitigated in order to utilize Ga_2O_3 in high-frequency devices.[14]

The bulk and surface properties of the different polymorphs have been the focus of a significant amount of work.[88–91] Bermudez[88] used *ab-initio* theory to examine the structure of the (100), (010), (001), and $(10\bar{1})$ faces of β-Ga_2O_3. The $(10\bar{1})$ surface, which exhibits a high energy when ideally terminated, was found to exhibit changes in bonding during relaxation leading to a lowering of the surface energy. β-Ga_2O_3 was found to cleave easily on the (100) plane, consistent with experimental observations.[89,90] No intrinsic surface states near the valence band minimum were shown,[88] although extrinsic states have been observed by electron energy loss spectroscopy.[91]

Other properties of interest that have been reported include the exciton binding energy band gap of the α-Ga_2O_3 polymorph, which is a metastable phase at ambient conditions. The exciton binding energy was determined as 110 meV, with direct band gaps of 5.61 and 6.44 eV.[92] The direct gap of 5.61 eV is in good agreement with recent theory.[93] The large exciton binding energy is consistent with the presence of a large amount of electron-phonon-coupling in this polar material.[94] This data provide a complement to that for β-Ga_2O_3, where the temperature dependence of the exciton resonance[95] as well as the complete dielectric function[96] has been measured. Similar to the work on α-Ga_2O_3, the assumption of strong lattice polarization on the β-Ga_2O_3 band structure produced a band gap in good agreement with experiment.[97] The low frequency permittivity of β-Ga_2O_3 was determined to be $\varepsilon_r = 10.2 + 0.3$, and this dielectric constant was unchanging over the range 77–297 K, and was also independent of frequency over the range 5–500 kHz.[98]

Furthmuller and Bechstedt reported that the four polymorphs α-, β-, δ-, and ε-Ga_2O_3 exhibit a correlation between

TABLE II. Properties of β-Ga_2O_3 relative to other more commonly used semiconductors. We also show some of the common figures-of-merit used to judge the suitability or potential of these materials for various high temperature, high voltage or power switching applications.

Materials parameters	Si	GaAs	4H-SiC	GaN	Diamond	β-Ga_2O_3	Comments
Bandgap, E_g (eV)	1.1	1.43	3.25	3.4	5.5	4.85	Bandgap of Ga_2O_3 reported in range 4.6–4.9 eV
Dielectric constant, ε	11.8	12.9	9.7	9	5.5	10	
Breakdown field, E_C (MV/cm)	0.3	0.4	2.5	3.3	10	8	Experimental values for Ga_2O_3 have reached ~0.5 times the theoretical maximum
Electron mobility, μ (cm^2/Vs)	1480	8400	1000	1250	2000	300	
Saturation velocity, v_s (10^7 cm/s)	1	1.2	2	2.5	1	1.8-2	1.8 ⟨0 0 1⟩ and ⟨0 1 0⟩, 2.0 ⟨0 1 0⟩
Thermal conductivity λ (W/cm K)	1.5	0.5	4.9	2.3	20	0.1–0.3	0.13 ⟨1 0 0⟩, 0.23 ⟨0 1 0⟩
Figures of merit relative to Si							
Johnson = $E_c^2 \cdot V_s^2/4\pi^2$	1	1.8	278	1089	1110	2844	Power-frequency capability
Baliga = $\varepsilon \cdot \mu \cdot E_c^3$	1	14.7	317	846	24 660	3214	Specific on-resistance in (vertical) drift region
Combined = $\lambda \cdot \varepsilon \cdot \mu \cdot V_s \cdot E_c^2$	1	3.7	248.6	353.8	9331	37	Combined power/frequency/voltage
Baliga high frequency = $\mu \cdot E_c^2$	1	10.1	46.3	100.8	1501	142.2	Measure of switching losses
Keyes = $\lambda \cdot [(c \cdot V_s)/(4\pi \cdot \varepsilon)]^{1/2}$	1	0.3	3.6	1.8	41.5	0.2	Thermal capability for power density/speed
Huang HCAFOM, $\varepsilon \mu^{0.5} E_C^2$	1	5	48	85	619	279	Huang chip area manufacturing FOM

atomic density and energetic stability.[99] They calculated the tensor of elastic constants, lattice parameters, atomic coordinates, electron effective mass (0.268 m_0 for the β-polymorph), and static dielectric constants (3.55 for β-Ga_2O_3 and 3.80 for α-Ga_2O_3), which are in good agreement with experimental values of 3.4–3.8.[100–112]

There is also interest in Ga_2O_3 as a potential surface passivation on Si,[113] as a gate dielectric material[114] and as a thin tunneling layer to improve open-circuit potential in dye-sensitized solar cells.[115] This same kind of tunneling oxide can be employed in non-volatile, floating-gate memory will become thinner.[116] To prevent leakage of stored charge back to the substrate and therefore a loss of stored bits, new approaches are needed,[116–120] such as ferroelectric random access memory,[116] magnetic random access memory, phase change random access memory, and resistance random access memory (RRAM).[116] RRAM has advantages of simple structure, low energy consumption, and higher operating speed.[121–123] Studies on the bipolar switching behavior of Pt/GaOx/TiN show that it originates from conduction associated with oxygen vacancies.[116]

Finally, Ga_2O_3 has attracted attention as a phosphor host material for emissive display thin-film electroluminescent (TFEL) displays.[20] TFEL devices with emitting layers of Ga_2O_3:Mn, Ga_2O_3:Cr, or Ga_2O_3:Eu have shown stable operation and high brightness.[20,124,125]

BULK GROWTH TECHNOLOGY OF Ga_2O_3

As we stated previously, the progress in growing large diameter bulk crystals of β-Ga_2O_3 has been one of the driving forces in pushing interest in the use of this materials for power electronics and solar-blind photodetectors. In particular, the melt-growth methods developed for Ga_2O_3 are likely to be produce crystals at lower cost than the sublimation techniques commonly used for the growth of SiC substrates. This could be a factor in helping to reduce manufacturing costs for Ga_2O_3 based power electronics. Note that since the β-polymorph is the most thermally stable, all melt-grown crystals are in this form. This monoclinic structure gives rise to anisotropic electrical, optical, and thermal properties.

β-Ga_2O_3 crystals have been grown by all the common techniques, including the Czochralski method (CZ),[59,126–129] floating-zone (FZ),[9,66,130–133] edge-defined film fed (EFG),[69,134] or Bridgman (horizontal or vertical, HB and VB)[135–138] growth methods. The bulk crystals can obviously be used for rectifiers, but more importantly, provide a template for growth of epitaxial films of controlled thickness and doping for active channel and contact layers to allow achievement of targeted device parameters such as breakdown voltage, on-state resistance, and reverse recovery time.[139–147] EFG is one of the leading candidates of the established melt growth method in terms of bulk size and quality for high-volume production of large-size single-crystal β-Ga_2O_3 wafers. This method is currently used for mass production of sapphire wafers[69,134] and is the method used by the current commercial suppliers of bulk Ga_2O_3 crystals.[16] The charge material in EFG is typically high-purity (5N is typical) Ga_2O_3 powder which is inductively melted in an Ir crucible under N_2/O_2. The sources for achieving n-type doping with either Sn or Si donors are SnO_2 or SiO_2, respectively.[69,134] Ga_2O_3 single-crystal bulk plates are pulled from a seed crystal in contact with the molten Ga_2O_3 at a typical growth rate of 15 mm h^{-1}. The major unintentional impurities in EFG bulk crystals are Si and Ir,[69,134] which come from the initial Ga_2O_3 source material and the crucible, respectively. This background n-type conductivity can be compensated to produce semi-insulating crystals by addition of deep acceptors such as Mg and Fe. The electrical activity of Ir in Ga_2O_3 is undetermined at this point, but it is likely to have a low solubility.[18]

The CZ approach is also very attractive because of its proven capability in growing large diameter, high quality single crystals. In fact, 2 in. diameter, cylindrical Ga_2O_3 single crystals grown by CZ have been recently reported,[59,127] while EFG has also demonstrated large diameters (4 in.) of commercialized crystals.[69] Figure 5 shows state-of-the-art bulk β-Ga_2O_3 crystals of 2 or 5 cm in diameter grown at either low [(a) and (b)] and high [(c) and (d)] oxygen concentration in Ir crucibles.[59] Control of the melt thermodynamics is critical in avoiding decomposition of the oxide and increasing crystal size in CZ.[127] It is important to note that when trying to achieve highly n-type crystals using Sn doping in CZ, there are growth instabilities that rapidly produce spiral formation and it was necessary to use either Bridgman or gradient freeze approaches to obtain high quality, conducting crystals.[59]

Hoshikawa *et al.*[144] published one of the most detailed studies of growth of β-Ga_2O_3 by vertical Bridgman (VB). Pt–Rh alloy crucibles were used to contain the melt, which was carried out in ambient air and single crystals were grown without seeding. The growth direction was perpendicular to the (100) faceted plane produced in this approach[136] and single crystals 25 mm in diameter were obtained. Examples of the excellent crystals grown by VB in either a full-diameter crucible or in a conical crucible with a thin seed well are shown in Fig. 6. The crystal shown in Fig. 6(a) was grown in a full diameter crucible and that shown in Fig. 6(b) was grown in a conical crucible with a thin seed well.[136] This approach led to facile release of the crystals without destructive adhesion to the crucible.

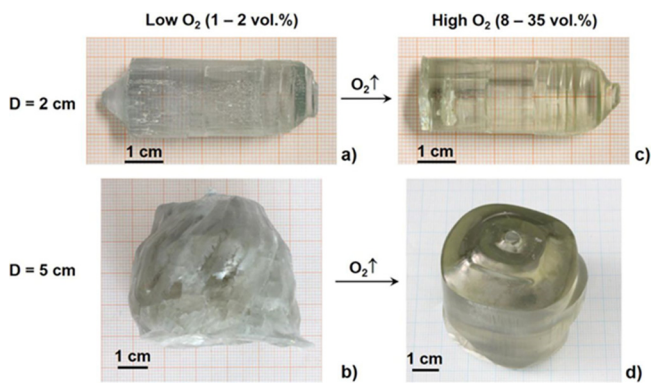

FIG. 5. Bulk β-Ga_2O_3 crystals of 2 [(a) and (c)] and 5 cm [(b) and (d)] in diameter grown at low [(a) and (b)] and high [(c) and (d)] oxygen concentration. Reprinted with permission from Galazka *et al.*, ECS J. Solid State Sci. Technol. **6**, Q3007 (2017). Copyright 2017 The Electrochemical Society.[59]

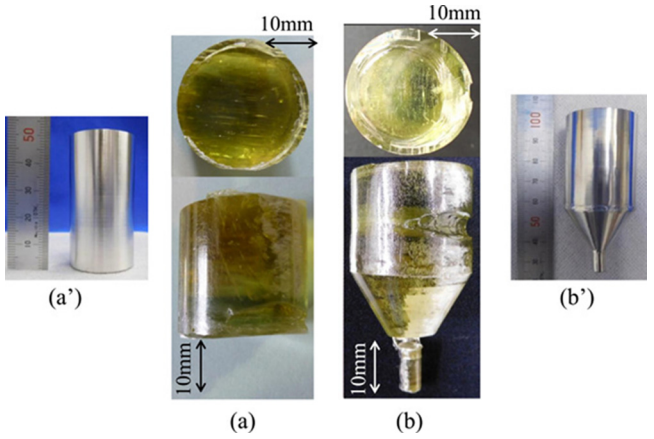

FIG. 6. β-Ga_2O_3 crystals grown by the Vertical Bridgman method in either (a) a full-diameter crucible (a′), and (b) or in a conical crucible (b′). Reprinted with permission from Hoshikawa *et al.*, J. Cryst. Growth **447**, 36 (2016). Copyright 2016 Elsevier.[144]

Zhang *et al.*[138] reported Sn-doped β-Ga_2O_3 single crystals grown by FZ. Compressed powders of β-Ga_2O_3 (5 N) and SnO_2 (5 N) were used as source materials and crystals grown at 1500 °C for 10 h in air. Post-growth annealing was used to control the conductivity of the crystals and this could be varied from semiconducting to insulating.

The defect density in currently available EFG and CZ crystals is of order $10^3\,cm^{-3}$, and in EFG, it is possible to achieve an undetectably low density of twin boundaries.[69] Nakai *et al.*[148] investigated defects in EFG grown (010) β-Ga_2O_3 single crystals by X-ray topography, selective etching, and transmission electron microscopy. Both screw dislocations with Burgers vector parallel to [010] and nanopipes were found. The dislocations produced etch pits of approximately 2 μm dimension after selective etching in potassium hydroxide (KOH) and these had a density in the range 10^6–$10^7\,cm^{-2}$. The nanopipes were hollow pipes of 0.1 μm diameter and approximately 15 μm length, elongated along [010].[148] These led to etch pits approximately 10 μm in dimension and density $\sim 10^2\,cm^{-2}$. Studies of this type that reveal the origin of the defects have aided in optimizing the current state-of-the-art in which much lower defect densities are obtained.[69]

PROGRESS IN METAL ORGANIC CHEMICAL VAPOR DEPOSITION (MOCVD) GROWTH OF Ga_2O_3

As we discussed earlier, bulk growth provides the wafers needed for subsequent epitaxy and can also be used to make bulk devices such as vertical rectifiers. However, it is critically important to develop high quality epitaxial growth processes to enable more complex devices to be realized.[149–177] The two dominant epitaxial growth methods used in GaAs and GaN-based technologies have been Metal Organic Chemical Vapor Deposition (MOCVD) and Molecular Beam Epitaxy (MBE). These provide high quality layers with practical growth rates and excellent control of purity, uniformity, and composition. In these early stages of Ga_2O_3 electronic device development, the fabrication of transistors such as metal-semiconductor field effect transistors (MESFETs) and metal-oxide-semiconductor field effect transistors (MOSFETs) has previously been demonstrated using MBE, MOCVD, and the variant called Mist chemical vapor deposition (Mist-CVD). This is a nonvacuum, solution-processed approach that offers a highly scalable, low-cost route for oxide epitaxy at low growth temperatures. One major challenge to date for all these approaches is to overcome the generally slow growth rates.

Alema *et al.*[149] reported high rate growth of epitaxial β-Ga_2O_3 thin films on c-plane sapphire substrates using a close coupled showerhead MOCVD reactor. This uses a small separation of the substrate-to-showerhead gas entry of only approximately 1 cm. They examined use of a few different Ga precursors, namely, Ga $(DPM)_3$ (DPM = dipivaloylmethanate), triethylgallium (TEGa), and trimethylgallium (TMGa), with separate injection of molecular oxygen used for the oxygen source. The $Ga(DPM)_3$ was able to be sublimated at 155 °C while the TEGa and TMGa sources were kept at or slightly below room temperature and Ar was used as a carrier gas.[149] The sapphire substrates were rotated at 170 rpm to enhance deposition uniformity. Figure 7 shows transmittance (a) and growth rates (b), with up to 10 μm/h achieved using TMGa at a substrate temperature of 900 °C. The bandgap was ~4.9 eV. The fast growth rates and excellent quality of the films indicates this approach can overcome the previously reported low growth rates in MOCVD.[149]

Gogova *et al.*[150] grew Si-doped β-Ga_2O_3 on both Al_2O_3 (0001) and β-Ga_2O_3 (100) substrates by MOCVD. The layers had similar dislocation density to those of the melt grown substrates. The structural properties were not degraded by Si-doping up to $10^{18}\,cm^{-3}$, and in fact, the density of twins and stacking faults were up to an order of magnitude lower in doped layers than in undoped films.[150]

Baldini *et al.*[157,158] grew homoepitaxial layers on (100) β-Ga_2O_3 substrates by MOCVD and investigated the role of In as a surfactant, which influences the growth dynamics of the Ga_2O_3 layers. It was found that In was essential in achieving the best layer quality. By using the In as a surfactant, the density of stacking faults and twins was significantly reduced and step-flow growth mode was achieved.[158] The presence of extended defects is also found to influence the effectiveness of n-type doping in homoepitaxial layers grown by MOCVD.[157]

Zhou *et al.*[170] examined the growth regimes in which β- and ε-Ga_2O_3 were stable when grown on c-plane sapphire by MOCVD. The phase composition was a function of both growth temperature and VI/III ratio, with some conditions leading to a mixture of β- and ε-Ga_2O_3. The structural quality of ε-Ga_2O_3 was superior to that of β-Ga_2O_3 under similar growth conditions.[170] With decreasing growth temperature, the MOCVD layers went from pure β-Ga_2O_3 to a mixture of the β- and ε-Ga_2O_3 polymorphs and finally to microcrystalline structures at the lowest temperatures investigated.[170] Figure 8(a) shows a cross-sectional TEM image for a thicker sample (391 nm) grown at 505 °C. The film contains two pillar-like inclusions. An HRTEM image of inclusion A is shown in Fig. 8(b). The lattice planes correspond to pure ε-Ga_2O_3(0001). The selected area electron diffraction (SAED) patterns of island A and the sapphire substrate are shown in

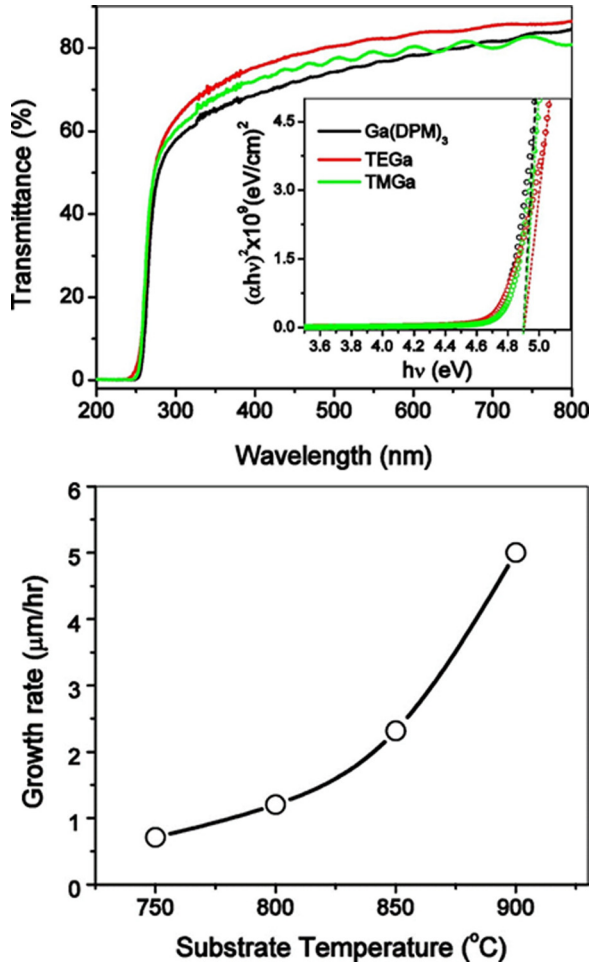

FIG. 7. (Top) UV–Visible transmission spectra for β-Ga_2O_3 thin films grown on (0 0 0 1) sapphire substrates by MOCVD. The black, red, and green traces are representative of films grown using $Ga(DPM)_3$, TEGa, and TMGa, respectively. The inset shows the plot of $(\alpha h\nu)^2$ versus $h\nu$ used to obtain the bandgap. (Bottom) Growth rate as a function of substrate temperature for films grown with $Ga(DPM)_3$ precursor using MOCVD. Reprinted with permission from Alema *et al.*, J. Cryst. Growth **475**, 77 (2017). Copyright 2017 Elsevier.[149]

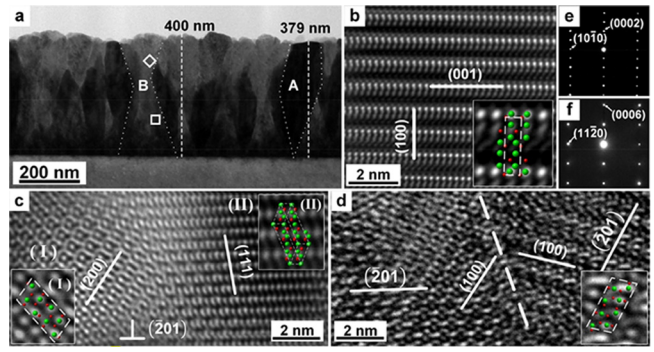

FIG. 8. Cross-sectional TEM analysis for 391-nm-thick Ga_2O_3 sample with electron beam parallel to Al_2O_3 substrate: (a) TEM micrograph with two distinct islands marked as A and B; (b) HRTEM micrograph of island A; (c) HRTEM micrograph of island B ("□" area). Two rotated domains of β-Ga_2O_3 with-orientation present either (I) 010 or (II) nearly 132 parallel to Al_2O_3; (d) HRTEM micrograph of disordered β-Ga_2O_3 in island B ("◇" area); (e) SAED pattern of island A; (f) SAED pattern of sapphire substrate. The insets in (b)–(d) present magnified HRTEM images with the ball-and-stick models of β- and ε-Ga_2O_3 overlaid on the respective projections (the green and red balls represent Ga and O atoms, respectively. Reprinted with permission from Zhou *et al.* Appl Surf. Sci. **420**, 802 (2017). Copyright 2017 Elsevier.[170]

Figs. 8(e) and 8(f), respectively, and inclusion B was shown to be composed of several small β-Ga_2O_3 grains. The metastable ε-Ga_2O_3 tends to stabilize at lower growth temperature, but there was a limited temperature range for the formation of ε-Ga_2O_3.[170]

Kim and Kim[175] investigated effects of annealing on MOVCD films grown at 750–1050 °C. Postdeposition annealing of amorphous Ga_2O_3 showed the onset of crystallization of the β-Ga_2O_3 phase and the photoluminescence spectra of as-deposited Ga_2O_3 went from a dominant blue–green and ultraviolet emission, to a longer wavelength UV band and a new green band after annealing. In addition to the temperature cycling of epitaxial layers, surface cleaning of substrates prior to epi growth is a key step in promoting uniformity and high yield.[176] The surface carbon contamination on Ga_2O_3 substrates was measured as a function of annealing temperature up to 800 °C under UHV conditions. The concentration of adventitious carbon could be reduced by ~approximately 70% by annealing at 800 °C. Annealing also produced defects that led to increased surface bandbending.[176] In concert with this, there is a recent work that investigated the role of ambient on the growth modes of Ga_2O_3 during sputtering, but this also has relevance to the initial stages of MOCVD growth.[174] Films were deposited by RF magnetron sputtering on a- or c-plane sapphire or Si (100) substrates either in an O_2 or H_2O vapor ambient. The orientation of the deposited films was a strong function of ambient and growth temperature.[174] For example, when deposited under O_2 gas flow on c-plane sapphire at 300 °C, $(\bar{2}01)$-oriented β-Ga_2O_3 films were obtained.[174] By sharp contrast, deposition on a-plane sapphire at 600 °C led to (110)-oriented α-Ga_2O_3. The use of Si substrates led to deposition of randomly oriented polycrystalline β-Ga_2O_3.[174] It is clear that the activation barrier of nucleation for the β-polymorph is reduced in the presence of hexagonally packed oxygen atoms on c-plane sapphire. Pseudomorphic growth of α-Ga_2O_3 occurred at higher temperatures since it has the same corundum structure as the sapphire. The presence of water vapor in the ambient promoted nucleation of (311)-oriented γ-Ga_2O_3 on c-plane sapphire.[174] Pseudomorphic growth of α-Ga_2O_3 occured on a-plane sapphire at 800 °C and above, but with the incorporation of small γ-Ga_2O_3 crystallites and both phases were stable at these temperatures. The crystalline phases of Ga_2O_3 films deposited on sapphire and Si(100) substrates using O_2 or H_2O ambient are summarized in Fig. 9 (top).[174] Solid-phase epitaxy proceeds from the interface with the substrate, which provides a templating effect. The stable polymorph that grows is determined by the choice of the substrate and oxygen source gases. The differences in the chemical potential between α-Ga_2O_3, β-Ga_2O_3, and γ-Ga_2O_3 are responsible for the dependence on the surface structure of the substrate.

The bottom of Fig. 9 summarizes the synthesis and interconversion of the different polymorphs of Ga_2O_3 from Playford *et al.*[8] They also discovered a gallium oxyhydroxide, which upon thermal treatment produces the transient,

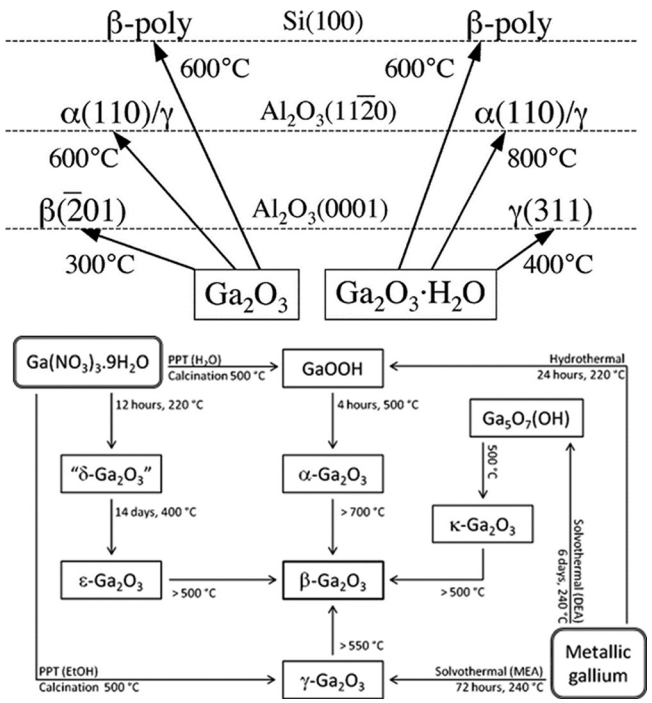

FIG. 9. (Top) Dependence of crystalline phases of Ga_2O_3 deposited on sapphire (0001), sapphire (11$\bar{2}$0), or Si (100) substrates with O_2 (Ga_2O_3) or H_2O gas. Reprinted with permission from H. Akazawa, Vacuum **123**, 8 (2016). Copyright 2016 Elsevier.[174] (Bottom) Summary of the synthesis and interconversion of the polymorphs of Ga_2O_3 (PPT = precipitate, DEA = diethanolamine and MEA = monoethanolamine). Reprinted with permission from Playford *et al.*, Chem.-A Eur. J. **19**, 2803 (2013). Copyright 2013 Wiley.[8]

polymorph κ-Ga_2O_3.[8] The γ-Ga_2O_3 defect spinel has local disorder with similar octahedral site structure to α- and β-Ga_2O_3.[8] Thermal decomposition of gallium nitrate leads to the formation of ε-Ga_2O_3, which has a hexagonal close-packed array of oxide ions with partial filling of octahedral and tetrahedral sites.[8] Thermal treatment always leads to the formation of the thermodynamically stable β-Ga_2O_3 phase. The δ-Ga_2O_3 was found to be a nanocrystalline form of ε-Ga_2O_3, while the κ-Ga_2O_3 is a transient phase.[8]

HALIDE VAPOR PHASE EPITAXY (HVPE)

Halide vapor phase epitaxy (HVPE) is a relatively inexpensive approach that achieves extremely high deposition rates, but usually with a rough surface morphology that is unsuitable for device processing unless some type of planarization by polishing is employed.[177–182] HVPE has been used to produce β-Ga_2O_3 thin films at growth rates up to 250 μm/h on sapphire substrates,[178–180] but with rough surfaces containing a high density of defects and pits, even when grown on bulk Ga_2O_3. It is possible to use chemical mechanical polishing to achieve flat morphologies, but this usually requires removing as much as 10 μm of material, which is not economic. The experience from growing GaN by HVPE shows that there are a number of challenges with this method. These can include the uncontrolled etching of substrates by the HCl or Cl_2 that are used for the formation of GaCl vapor, the high growth temperature, uniformity issues, lack of control of doping, especially for lightly doped layers and difficulty in growing ternary alloys. These same disadvantages pertain to the use of HVPE for growth of Ga_2O_3.

Murakami *et al.*[180] demonstrated that use of GaCl and O_2 precursors in HVPE of Ga_2O_3 produces successful growth on (001) β-Ga_2O_3 substrates. They were able to achieve very smooth surface morphology with the presence of (100) macrosteps for a growth temperature of 1000 °C and a growth rate of approximately 5 μm/h. This slower growth rate was a key to controlling morphology. Figure 10 shows impurity depth profiles measured by Secondary Ion Mass Spectrometry (SIMS) for homoepitaxial β-Ga_2O_3 grown at 1000 °C on a Sn-doped β-Ga_2O_3 substrate. The C and H impurity concentrations were below the background detection limits of this particular SIMS system, but that is too high to conclude their accurate concentrations. Similarly, the Sn and Si levels in the HVPE layer appear to be low and Cl was detected at a level of approximately 10^{16} cm^{-3}. The net carrier concentration (N_D–N_A) measured in the HVPE layer was approximately 10^{13} cm^{-3}, demonstrating that this technique is certainly capable of growing thick, high purity layers with acceptable morphology for diodes and rectifiers.

Nomura *et al.*[181] also showed from a thermodynamic analysis that use of GaCl and O_2 as precursors is appropriate for the growth of β-Ga_2O_3 by HVPE. The concentration of H_2 as a carrier gas was a strong factor in the growth kinetics and with GaCl and O_2 precursors, the growth is thermodynamically controlled.

PULSED LASER DEPOSITION (PLD)

Pulsed laser deposition (PLD) is a versatile deposition technique that is valuable in doping and heterostructure studies because of its relatively low deposition temperature.[183–195] However, the main drawbacks for thick device structures are the low deposition rate and lower material

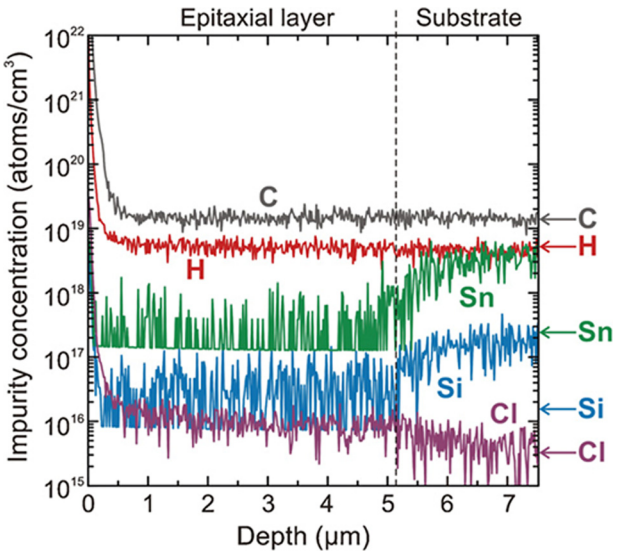

FIG. 10. SIMS depth profiles of an HVPE layer grown at 1000 °C. Arrows represent the background concentrations of the elements. Reprinted with permission from Murakami *et al.* Appl. Phys. Express **8**, 015503 (2015). Copyright 2015 The Japan Society of Physics.[180]

quality compared to the variants of CVD and MBE methods. PLD has often been used to create doped layers of Ga_2O_3 as n-type transparent conducting layers. The normal dopants used have been Sn and Si, and the layers have primarily been deposited on sapphire substrates and with conductivities in the range 1 to 10 S cm^{-1}. The high end of this range is insufficient for application as contact layers. Films of Sn-doped Ga_2O_3 on silica and sapphire with conductivity of approximately 1 S cm^{-1} have been deposited at 500 °C–550 °C for heteroepitaxial Sn-doped Ga_2O_3.[183–189] For a lower growth temperatures of 380 °C, Sn doping of Ga_2O_3 on sapphire, typically leads to poorer conductivities. For Si-doped Ga_2O_3 on sapphire, Zhang[189] achieved a doping level of 9.1×10^{19} cm^{-3} with a maximum conductivity of 2 S cm^{-1} and Müller[190] was able to control conductivity by adjusting the oxygen partial pressure during deposition. Varying the Si content in Ga_2O_3 targets allowed control of carrier density from 10^{15} to 10^{20} cm^{-3}.[191]

The growth of Si-doped Ga_2O_3 by PLD on semi-insulating (010) β-Ga_2O_3 and (0001) sapphire was used to investigate the effect of substrate on crystal quality.[192] The films deposited on β-Ga_2O_3 were single crystal, while those deposited under the same conditions on Al_2O_3 were single phase, polycrystalline β-Ga_2O_3.[192] The conductivity was improved by two orders of magnitude for films on homoepitaxial substrates relative to those of sapphire, with a value of 732 S cm^{-1} (mobility of 27 cm^2 V^{-1} s^{-1} and carrier concentration 1.74×10^{20} cm^{-3}) for the former. This approach might be useful in making low resistance Ohmic contact layer in β-Ga_2O_3 devices, but realistically, the devices need to be grown by one technique and the PLD probably has limited utility.

It has also been found that the presence of a large oxygen deficiency in PLD-grown Ga_2O_3 can lead to a nanocomposite system that has an insulator to metal transition.[193] This mixed system was comprised of crystalline β-Ga_2O_3 and an amorphous gallium sub-oxide, $Ga_2O_{2.4-\alpha}$. Nagarajan *et al.*[193] also found that, as expected, the oxygen partial pressure and deposition temperature were key parameters in determining the properties of the deposited films. For a deposition temperature of 400 °C and low oxygen partial pressure, the film was found to be comprised of Ga metallic clusters embedded in a stoichiometric Ga_2O_3 matrix. This occurs due to a phase separation of oxygen deficient metastable Ga_2O_x ($x = 2.3$) into the stable phases (Ga and Ga_2O_3).[194]

Finally, PLD has been used to study the effects of Er doping in Ga_2O_3 films on sapphire.[195] Chen *et al.*[195] was able to observe the green luminescence line at 550 nm, which was temperature-insensitive up to at least 180 °C. While the intensity of the green emission is quenched with increasing temperature, it was less severe than comparable Er-doped GaN, consistent with the wider bandgap for Ga_2O_3.

MIST-CVD

The Mist CVD method has been successfully applied to grow of α-, β-, and γ-polymorphs of Ga_2O_3.[196–208] It is a low-cost approach that employs chemicals such as gallium (III) acetylacetonate in water as the Ga source, and tin (II) chloride as the source of Sn-doping. Ultrasonic energy is applied to the Ga-containing aqueous solution to create a mist, which is carried to the heated substrate in the reactor using N_2 carrier gas, with growth temperatures in the range of 500–630 °C,[196–200] i.e., the solution is atomized via ultrasonication at a frequency of 2.4 MHz. The diameter of the mist droplets is approximately 3 μm. The mist of the CVD precursors is evaporated and chemically reacts in a heated quartz tube containing the substrate. To take advantage of the fact that α-Ga_2O_3 has the same corundum crystal structure as sapphire, the company Flosfia has developed stress-free epitaxy of Ga_2O_3 on sapphire.[209] The optimized growth process is now able to produce dislocation-free epilayers on 4 in. diameter sapphire substrates, in an effort to minimize production costs. They have also developed a proprietary lift-off process to transfer the α-Ga_2O_3 layers from the sapphire substrate to a high thermal conductivity metal support, alleviating the thermal management issues that are still issues with SiC and GaN power devices and require the use of diamond-based heat management approaches in some cases.[209]

Oshima *et al.*[206] deposited undoped defective-spinel-type γ-phase and corrundum-type α-phase on (100) $MgAl_2O_4$ and (0001) sapphire substrates, respectively, using Mist-CVD. These metastable phases were possible at low growth temperatures, while at higher temperatures, they were transformed to the stable β-Ga_2O_3 polymorph. For the pure γ-phase films, the refractive index was determined to be 2.1 in the visible region, the direct gap was 5 eV, and the indirect gap was 4.4 eV.[206] It was also noted that the growth kinetics of Mist CVD were similar to those of that of conventional CVD[206] and similar trends have been noted with sol–gel derived phase pure α-Ga_2O_3 nanocrystalline thin films.[210] In that case, at low process temperatures, a mixed phase of α-GaO (OH) and α-Ga_2O_3 was found, and above this range, a mixed phase of α-Ga_2O_3 and β-Ga_2O_3 was detected. The pure β-phase was observed at higher annealing temperatures.[210] They determined an optical band gap of α-Ga_2O_3 of 4.98 eV from transmittance measurements.[210]

Mist CVD has been used in numerous device demonstrations, including rectifiers and MESFETs. Dang *et al.*[199] developed a AgO_x Schottky contact process on Mist CVD grown films, where Sn-doped Ga_2O_3 MESFETs and Schottky diodes and MESFETs showed high rectification and ON–OFF ratios and promising breakdown voltages.[199] The Sn-doping was able to achieve a maximum carrier concentration of 7×10^{18} cm^{-3} and a mobility of 0.23 cm^2 V^{-1} s^{-1}.

Nishinaka *et al.*[205,207] used Mist CVD to grow a-, m-, and r-plane α-Ga_2O_3 layers grown on a-, m-, and r-plane sapphire using α-Fe_2O_3 buffer layers. The direct bandgap of the α-Ga_2O_3 films were found to be in the range of 5.15–5.2 eV from transmittance and reflectance measurements.[205,207]

MBE OF Ga_2O_3

From a power device viewpoint, where thick layers are typically needed to achieve high breakdown voltages, the main drawbacks of MBE are a relatively low growth rate and high production cost per wafer. However, MBE is capable of

growing very high quality Ga_2O_3.[211–216] It is a scalable, uniform approach that is well-established in other materials systems. A typical approach is to grow β-Ga_2O_3 on c-plane sapphire substrates using an O_2 plasma source and a standard effusion cell for gallium. The Ga_2O_3 is grown at a substrate temperature typically around 700 °C, with the growth rate under these conditions of around of 50 nm h^{-1},[217] but this can be increased to approximately 700 nm h^{-1}.[214]

Sasaki *et al.*[213] pointed out that typical vertical geometry power β-Ga_2O_3 devices require thick layers (usually well in excess of 2 μm), with low background doping ($<10^{16}$ cm^{-3}). The initial studies typically grew homoepitaxial Ga_2O_3 on (100) β-Ga_2O_3 substrates. Excellent morphology and control of doping was maintained at much higher growth rates by changing from the (100) plane to the (010) plane.[213] The cleavage planes of β-Ga_2O_3 have a high decomposition rate under MBE conditions so epitaxial growth on the cleavage planes yields a low growth rate. By investigating the growth rate on different growth planes, it was noted that the rates were significantly higher (more than an order of magnitude) on the (010) non-cleavage plane. The same group[211] investigated the growth temperature dependence of Sn-doped homoepitaxial films and found optimum growth temperatures in the range 540–570 °C. At higher temperatures, there was an issue with Sn segregation.[211]

Okumura *et al.*[214] showed that for β-Ga_2O_3 (010) homoepitaxial growth under Ga-rich conditions and for growth temperatures >650 °C, the growth rate was independent of the Ga/O ratio (>1). They achieved a growth rate of approximately 130 nm $h^{-1}$with rms surface roughness of approximately ~1 nm under slightly Ga-rich conditions.[214] It is also noted that use of ozone as the oxygen source in MBE produces higher growth rates than O_2 plasma MBE (also called plasma-assisted or PAMBE). However, the latter has better control of doping since it operates at lower pressures.[211–214] Okumura *et al.*[214] employed a PAMBE system with a low background pressure of approximately 10^{-5} Torr and were able to grow high quality β-Ga_2O_3 with good morphologies and decent growth rates, as shown in the (020) ω–2θ scan diffraction spectrum of Fig. 11(a). They were able to observe 7th order satellite thickness fringes. The growth rate of the β-Ga_2O_3 (010) films was found to be a strong function of the O_2 flux at a growth temperature of 700 °C under slightly Ga-rich conditions, as shown in Fig. 11(b).[214]

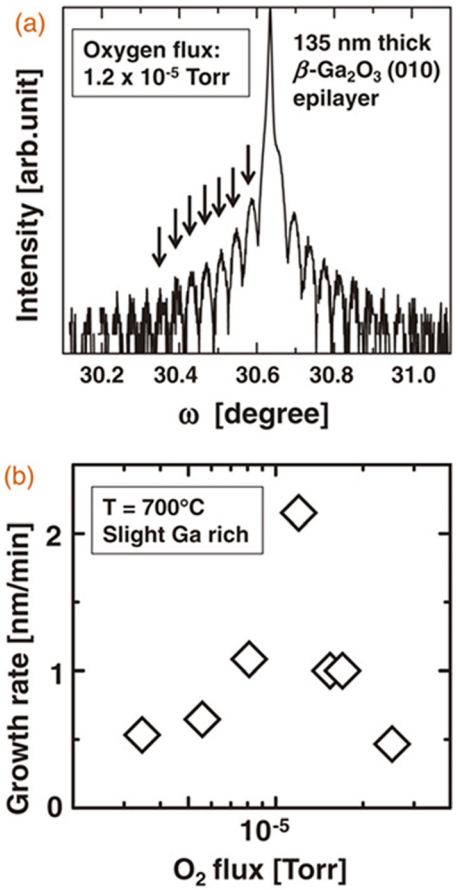

FIG. 11. (a) (020) ω–2θ scan diffraction peak of 135-nm-thick β-Ga_2O_3(010) film grown under slightly Ga-rich condition with an oxygen flux of 1.2×10^{-5} Torr beam equivalent pressure (BEP). (b) Relation of the growth rate of β-Ga_2O_3(010) at 700 °C under slightly Ga-rich conditions to the oxygen flux (BEP). Reprinted with permission from Okumura *et al.*, Appl. Phys. Express **7**, 095501 (2014). Copyright 2014 The Japan Society of Physics.[214]

ATOMIC LAYER EPITAXY (ALE) AND ATOMIC LAYER DEPOSITION (ALD) Ga_2O_3

Atomic Layer Epitaxy (ALE) and Atomic Layer Deposition (ALD) refer to a growth method based on sequential, self-limiting surface reactions. This approach has been used for numerous growth studies of Ga_2O_3.[217–226] When epitaxy occurs (typically at higher temperatures) on a homoepitaxial substrate, ALE is the correct description, while ALD refers to the more general case of deposition. ALD features excellent thickness control and conformal coverage on substrates and is widely used in the microelectronics industry for depositing dielectrics and other thin, exacting layers. It is applicable to a wide variety of materials including oxides, nitrides, and various types of metals.

In terms of ALD of Ga_2O_3, one of the key issues is the choice of the Ga precursor.[217] Most commonly available gallium precursors used in ALD require a temperature >300 °C for deposition. The list of these precursors (with their respective required temperature) includes gallium tris-hexafluoro acetyl acetonate (470 °C), gallium alkoxide (300 °C), gallium trichloride (450 °C), trimethyl gallium (500 °C), and triethyl gallium (470 °C).[217] These temperatures are not an issue for Ga_2O_3 intended for power electronics structures or for insulators or passivation layers in microelectronics. By sharp contrast, the high process temperature is limiting for flexible and transparent electronics.

Choi *et al.*[217] reported on the properties of ALD Ga_2O_3 using gallium tri-isopropoxide [$Ga(OiPr)_3$, GTIP] as a Ga precursor at 150–250 °C and H_2O as the oxygen source. These films were obviously amorphous, but exhibited smooth surface, low carbon background, and high transparency (>90%). The films also had high breakdown fields (7.56 MV/cm at 250 °C) and low leakage current (1.92×10^{-11} A at 1 MV/cm). The growth rate was 0.25 nm/cycle at 250 °C. The Ga_2O_3 films show outstanding transmittance (over 90%) with an optical bandgap energy level of 5.4 eV.

Altuntas *et al.*[226] deposited Ga_2O_3 dielectric thin films (7.5 nm thick) on p-type silicon wafer using plasma enhanced atomic layer deposition (PEALD). After the deposition, annealing was performed up 800 °C to obtain the β-phase. These β-Ga_2O_3 thin films deposited by PEALD technique at low temperatures showed promise as oxide layer for MOS devices.

Ga_2O_3 NANOSTRUCTURES

The various forms of low dimensional, crystalline Ga_2O_3 that includes nanowires (NWs), nanobelts (NBs), and nanosheets (NSHs) are the subject of an extensive literature.[227–303] This is due to both the interest in the fundamental properties of the material at reduced dimensions and the possible application to devices, including nanowire-based field effect transistors (NW-FETs), gas sensors, solar blind photodetectors, and switches. It is well-established that devices such as gas sensors fabricated on nanostructures can have advantages in sensitivity and response time due to the high surface to volume ratio. Of course, the reproducibility of the structures, making high quality contacts with high yield and the reliability are all issues, as well as the need to incorporate dopants to control their electrical and optical properties (including both doping during growth and post growth doping by ion implantation or diffusion).

There have been a large number of approaches used to grow Ga_2O_3 nanostructures, with the most common being the vapor–liquid–solid (VLS) or vapor–solid (VS) process.[228] In this process, metal catalysts or metal alloys are used which form supersaturated alloy droplets by dissolving the vapor component.[249,261,284] Supersaturation in alloy droplets induces the precipitation of a solid phase for nanowire growth. Other methods employed for Ga_2O_3 have included physical evaporation,[252] thermal annealing of compacted gallium nitride powder,[259] solution processing,[265] arc discharge,[253] laser ablation,[254] carbothermal reduction,[255] chemical vapor deposition (CVD),[256,264,266,267,278] metal–organic CVD (MOCVD),[264,268] microwave plasma reaction,[238] and vapor phase epitaxy (VPE).[267] Kumar *et al.*[278] reported a comparative study of Ga_2O_3 nanowires grown on different substrates by CVD.

The most common approach to growing β-Ga_2O_3 NWs has been to use Au as a catalyst.[228] This always has the risk of some level of incorporation of the catalyst into the β-Ga_2O_3. The electrical activity of Au in Ga_2O_3 is not clear, but it likely to be a recombination center. Johnson *et al.*[275] reported the use of Fe as the catalyst, an approach that is commonly used for the growth of carbon nanotubes.

Lithium is of potential interest as a dopant in Ga_2O nanostructures order to modify its conductivity for electrical energy storage applications.[279] Lopez *et al.*[279] reported the results of a study of *in situ* doping with Li on the morphology and optical properties of large Ga_2O_3 nanostructures grown by VLS.[279] Figure 12(a) shows SEM images of Li-doped Ga_2O_3 microwires on the substrate, where images (b)–(d) show the typical pyramidal surface morphology. These Li-doped structures have quite different structure from the undoped case, as shown in Fig. 12(e). Raman spectra

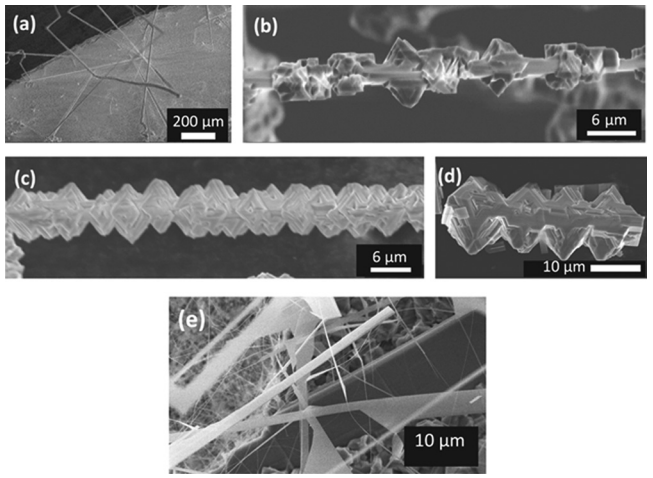

FIG. 12. SEM images of Li doped Ga_2O_3 microwires. (a) General view of the microwires grown on the substrate surface (b)–(d) details of several structures with lateral pyramids. (e) Representative image from a sample grown in the same conditions, but with no presence of Li_2CO_3. Reprinted with permission from López *et al.*, Semicond. Sci. Technol. **31**, 115003 (2016). Copyright 2016 IOP.[279]

revealed the presence of a peak at 270 cm^{-1} only in the Li-doped samples.[279] This was accompanied by a sharp luminescence peak at 717 nm, as shown in the cathodoluminescence (CL) emission from a Li-doped structures (solid line) and an undoped sample (dashed line) of Fig. 13(a). Figure 13(b) shows an expanded view of the Li-related transition/via Ga_2O_3 interband excitation and by defect band excitation.[279]

Hosein *et al.*[283] synthesized high aspect ratio β-Ga_2O_3 nanowires with facetted morphology by VLS. The long axis of the nanowires was in the direction parallel to the crystal b axis ([0 1 0]). The nanowires showed strong blue luminescence under UV laser excitation, ascribed to native defects.[283] Figure 14(a) shows a TEM image of aβ-Ga_2O_3 nanowire, along with the selected area diffraction pattern (SAED) pattern. The streaking in the diffraction pattern was ascribed to the presence of line defects, such as stacking faults and micro-twins.[283] This was not present in all areas and the SAED from the defect-free regions and lattice imaging [Figs. 14(b) and 14(c)] showed the growth direction was

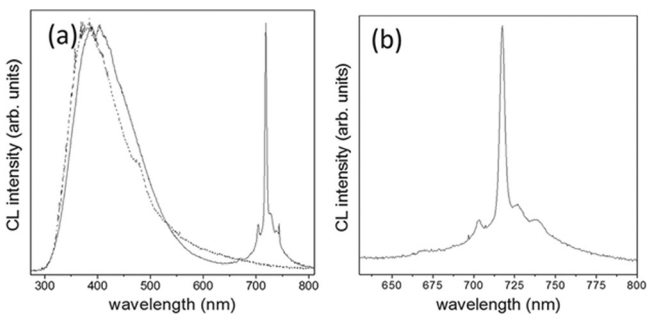

FIG. 13. (a) Room temperature CL emission from Ga_2O_3:Li microstructures (solid line) and a reference undoped sample (dashed line). (b) Details of the red luminescence band observed in Ga_2O_3:Li microstructures. Reprinted with permission from López *et al.*[279] Semicond. Sci. Technol. **31**, 115003 (2016). Copyright 2016 IOP.[279]

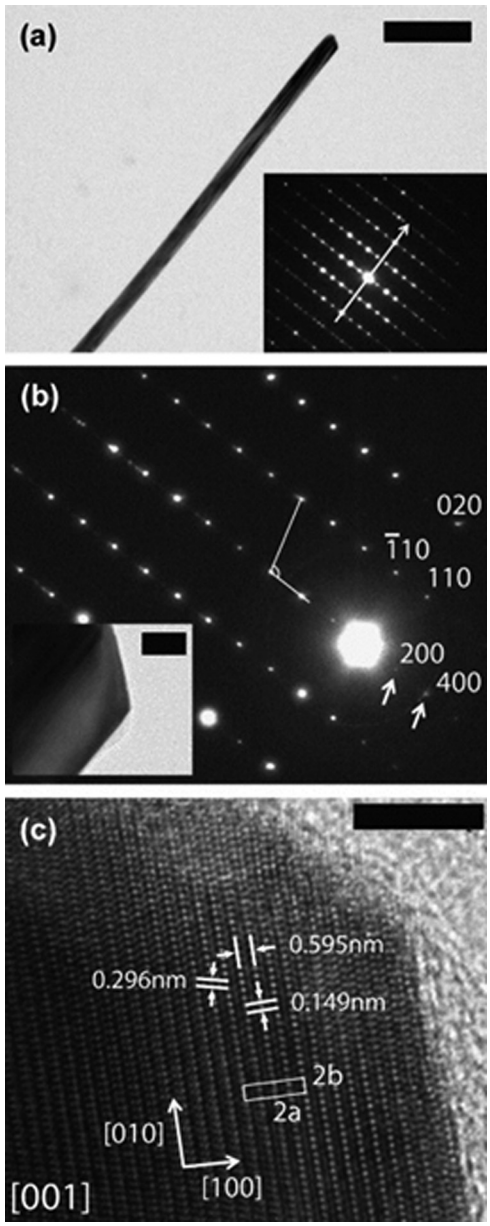

FIG. 14. TEM analysis of faceted nanostructures. (a) Low magnification TEM image of a representative nanowire. Inset shows the corresponding SAED pattern. The arrow indicates the growth direction, which corresponds to [0 1 0]. Scale bar, 0.5 μm. (b) SAED along the [0 0 1] zone axis, on the corner formed by the side wall and the tip. The reciprocal lattice has a unit cell angle $\beta = 104.3°$. Interplanar spacings determined from the diffraction spots match the corresponding labelled directions. Inset shows the nanowire region analyzed. Scale bar, 20 nm. (c) Lattice-resolved TEM image of the corner of the nanowire. Lattice spacing measurements parallel and perpendicular to the growth direction indicate [0 1 0] and [1 0 0] crystalline directions, respectively, in agreement with the SAED. The unit cell face parallel to the lattice plane is indicated, with a = 12.01 Å and b = 2.98 Å, magnified by a factor of 2 for clarity. Scale bar, 5 nm. Reprinted with permission from Hosein *et al.*, J. Cryst. Growth **396**, 24 (2016). Copyright 2016 Elsevier.[283]

along the [0 1 0] direction and the lattice spacing perpendicular to the growth direction corresponded to {1 0 0} planes.

Kumar *et al.*[249] used Fe catalyst to synthesize single crystal β-Ga_2O_3 nanowires with diameters of 30–80 nm and lengths up to tens of micrometers by VLS using CVD. The Raman peak positions from the β-Ga_2O_3 nanowire had a red frequency shift of 0.3–1.4 cm^{-1} for all three active frequency modes compared to an undoped bulk Ga_2O_3 single crystal grown by CZ, while the CL spectra both had a strong broad UV–blue emission band and a weak red emission band. The bandgap of this nanowire was measured to be 4.94 eV. There was little difference in the structural, morphological, and optical properties of Fe-catalyzed β-Ga_2O_3 nanowires compared to those of Au-catalyzed wires grown under similar conditions.[249] Figure 15 shows TEM images of the β-Ga_2O_3 nanowire with the expanded area showing the atomic structure of β-Ga_2O_3 in the $[1\bar{1}2]$ orientation.

Ga_2O_3 can also be used for photocatalytic decomposition of acids in water.[301] Ga_2O_3 nanostructures have been used to efficiently remove trace perfluorooctanoic acid (PFOA) in the secondary effluent of sewage. The decomposition of targeted trace pollutants such as PFOA is generally inhibited by coexisting high-level natural organic matters and bicarbonate, and because of its ubiquity, there is a strong effort focused on its remediation by decomposition.[301]

While many of the VLS and other solid- and gas phase synthesis methods require sophisticated equipment, it is also possible to use simpler solution-based methods to synthesize Ga_2O_3 nanostructures.[302] Metastable γ-Ga_2O_3 nanorods (and cubic In_2O) nanoparticles produced by solution processing using ethylene glycolate precursors are crystalline with narrow size distribution and exhibit intense blue light emission.[302]

PROPERTIES AND PROCESSING OF β-Ga_2O_3

In this section, we focus more specifically on the properties of the β-polymorph,[303–310] since that is the focus of most of the recent interest in power electronics and solar-blind UV detectors. To summarize, a β-Ga_2O_3 single crystal has a thermodynamically stable monoclinic structure (*b*-axis unique) belonging to the space group *C*2/*m*. The crystal structure of β-Ga_2O_3 has two crystallographically nonequivalent Ga positions (tetrahedrally and octahedrally coordinated) and two cleavage planes [(100) and (001)]. β-Ga_2O_3 has two different Ga sites, denoted as Ga(1) and Ga(2), and three different O sites, denoted as O(1), O(2), and O(3). As a

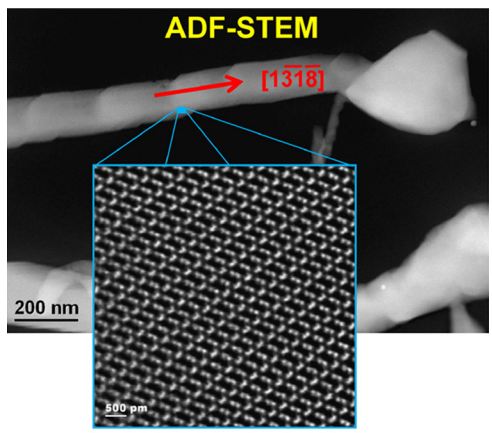

FIG. 15. Annular dark-field scanning transmission electron microscope (ADF-STEM) image of the β-Ga_2O_3 nanowire with a zoomed in area framed on the nanowire, which illustrates the atomic structure of β-Ga_2O_3 in (1–12) orientation. Reprinted with permission from Kumar *et al.*, J. Phys. D: Appl. Phys. **47**, 435101 (2014). Copyright 2014 IOP.[249]

result of this, β-Ga_2O_3 has an anisotropy for the optical and electrical properties.[34,304] There are also orientation-dependent etching and contact effects that are relevant for device fabrication. Ueda *et al.*[13] concluded that the electrical anisotropy is caused by the anisotropic effective mass, and the optical anisotropy is caused by the selection rule of the band-to-band transition.[305] The Ueda *et al.*[57] data showed Hall mobility measured along the b and c axes of high quality FZ crystals to be 46 and 2.6 $cm^2\ V^{-1}s^{-1}$, respectively, corresponding to electron masses of 0.44 m_o and 1.24 m_o, respectively. This shows a higher curvature of the bottom of the conduction band along the b-axis in β-Ga_2O_3.[57] A number of groups have suggested that the CBM belongs to $\Gamma 1+$, and the valence band maximum (VBM) and the second valence band belong to $\Gamma 1-$ and $\Gamma 2-$, respectively.[305]

It is worth pointing out that the bandgap reported for β-Ga_2O_3 is somewhat dependent on the technique used to measure it. For example, Fig. 16 shows the bandgap derived from Reflection electron energy loss spectroscopy (REELS). The bandgap was determined from the onset of the energy loss spectrum. The bandgap of Ga_2O_3 is a function of the polytype and it is common in the literature to quote a value of ~4.8 eV for β-Ga_2O_3, but we and others have noted that optical transmittance and REELS data show a consistent value of 4.6 eV.[69,71] However, note that the REELS spectrum exhibits a tail commonly ascribed to defects and this can affect how the bandgap is derived from the intersection of the slopes. Experimentally reported variations in determination of the gap may also result from the anisotropy of the crystal structure, which causes a dependence of the absorption on the polarization of the incident light.

Rafique *et al.*[311] recently used photoluminescence excitation (PLE) and absorbance spectra to measure the temperature and doping dependence of bandgap of Si-doped layers grown by low pressure CVD in sapphire substrates. The bandgap decreased with temperature and increased with electron concentration up to ~2.5×10^{18} cm^{-3}. Beyond that density, the Burstein-Moss shift was swamped by the onset of the Mott transition to metallic-like conduction.[311] As we discussed earlier, theoretical predictions suggest that β-Ga_2O_3 has an indirect gap which is only 30–40 meV smaller than the direct band gap.[6,51] The Varshni parameters were $\alpha = 4.45 \times 10^{-3}$ eV/K and $\beta = 2000$ K in the relation $Eg(T) = E_g(0) - \alpha T_2/(\beta+T)$.[311] The absorption data and bandgap as a function of n-type carrier concentration are shown in Fig. 17.

Through extended Hückel method calculations together with measurements of the Electron Paramagnetic Resonance (EPR) and electron nuclear double resonance, Binet *et al.*[306] concluded that the electrical anisotropy observed in β-Ga_2O_3 originates from the anisotropy of the conduction electrons. These electrons exhibit an anisotropic distribution along the octahedral chains of the monoclinic structure. Based on semiempirical quantum-chemical calculations, Hajnal *et al.*[307] also concluded that the optical and the electrical anisotropies are attributed to the anisotropy of the electronic structure of the lattice. Hajnal *et al.*[307] also carried out calculations on neutral and doubly charged vacancies and were able to explain the temperature dependence of the electrical conductivity in terms of the donor levels.[307] Yamaguchi[34] and Litimein *et al.*[304] produced some of the earliest comprehensive studies of the electronic structure of β-Ga_2O_3 using the first principles full-potential linearized augmented plane wave method. It was found that β-Ga_2O_3 has an indirect band gap with a conduction band minimum (CBM) at the Γ

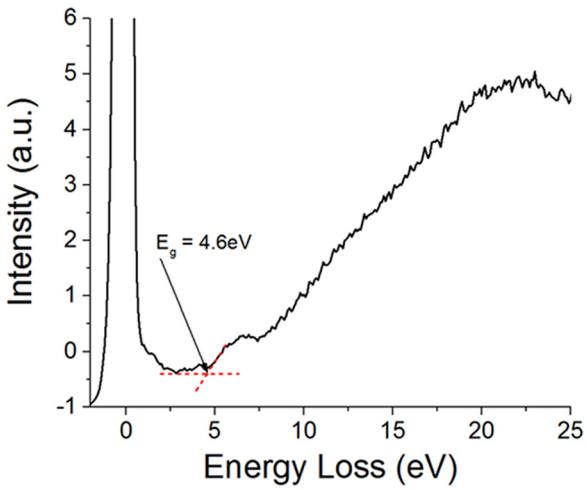

FIG. 16. Typical REELS spectrum from bulk β-Ga_2O_3. Reprinted with permission from Appl. Phys. Rev. **4**, 021301 (2017). Copyright 2017 American Institute of Physics.[560]

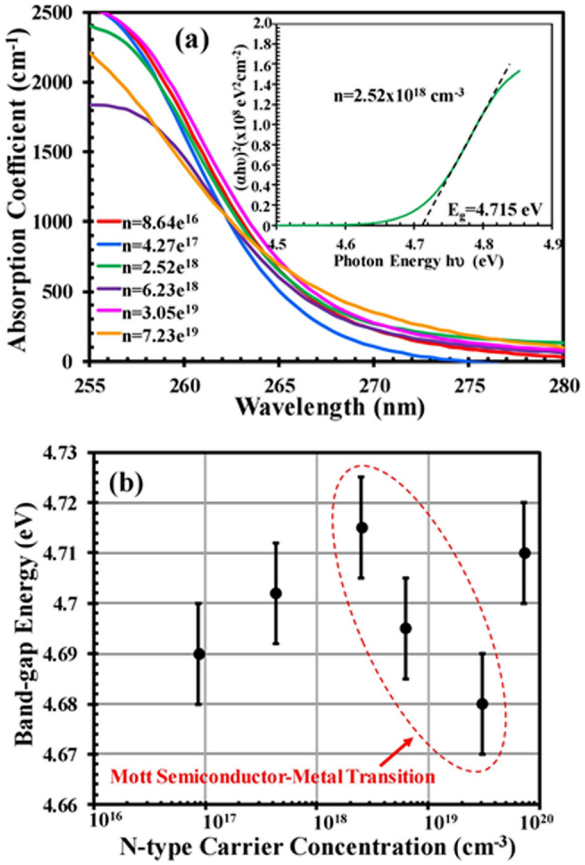

FIG. 17. Carrier concentration dependence of bandgap for β-Ga_2O_3 grown on sapphire by CVD. Reprinted with permission from Rafique *et al.*, Opt. Mater. Express **7**, 3561 (2017). Copyright 2017 Optical Society of America.[311]

point and a valence band maximum on the E line. The anisotropic optical properties were explained by the selection rule of the band-to-band transitions. On the other hand, the shape of the CBM was found to be almost isotropic, and, therefore, the observed electronic anisotropy in the *n*-type semiconducting state should not be attributed to the properties of a perfect lattice but to vacancies.[34,304,308,309] The anisotropic optical properties were explained by the selection rule of the band-to-band transitions.[304] For the monoclinic phase, it was shown that the component with *y*-direction was more pronounced than those along the *x* and *z*.[304]

The surfaces of β-Ga_2O_3 are also of strong interest from a practical viewpoint since their stability will determine how passivation schemes need to be incorporated. One of the biggest drawbacks of ZnO, another electronic oxide that attracted interest for blue light emitters and transparent electronics,[312–319] was the sensitivity of its surface to oxygen and water vapor.[313–318] Similarly, $InGaZnO_4$, (IGZO) an amorphous transparent conducting oxide of interest for transparent thin film transistors (TFTs), has a strong surface sensitivity to water vapor.[312,316–319] The adsorption of oxygen and water vapor from ambient atmosphere on the exposed channel layer create changes in the conductivity of the near-surface on both these materials and an instability of the channel conductivity during device operation of light-emitting diodes (LEDs) and thin film transistors (TFTs). Under vacuum and hydrogen ambient, the threshold voltages of IGZO TFTs showed a negative shift and the drain current increased in the typical transfer curves.[316–319] The trend was in the opposite direction under oxygen-containing ambients.[316–319] The change in the TFT positive threshold voltage shift under the gate-bias stress was larger in hydrogen than in vacuum, or even in oxygen, suggesting that hydrogen plays an important role in the instability of a-IGZO TFTs under gate-bias stresses.

Thus, it is of interest to understand the fundamental properties of the surfaces of Ga_2O_3. Bermudez[88] reported on the physical and electronic structure of the (100), (010), (001), and (10$\bar{1}$) faces of β-Ga_2O_3 using *ab initio* theory. All surfaces exhibited a decrease in surface energy upon relaxation, and the local bonding at the surface is analyzed by comparing nearest-neighbor bond lengths and overlap populations with those in the bulk. The (10$\bar{1}$) surface, which exhibits a high energy when ideally terminated, undergoes large displacements and changes in bonding during relaxation leading to a substantial lowering of the surface energy.

Klinedinst and Stevenson[308] measured the Gibbs energy of formation of β-Ga_2O_3 to be -252 kCal mol^{-1} over the temperature range of 873–1273 K. Onuma *et al.*[309] measured lattice vibration modes from the complete set of polarized Raman spectra from bulk (010) Mg-doped, (100) Si-doped, and (001) unintentionally-doped β-Ga_2O_3. The Ag and Bg Raman optically active modes corresponding to the direction of the electric field vector for the incident light, and that for the back scattered light, respectively, were perfectly separated in the spectra according to the polarization selection rules. As shown in Fig. 18, this was the first experimental observation of the complete set of polarized Raman spectra

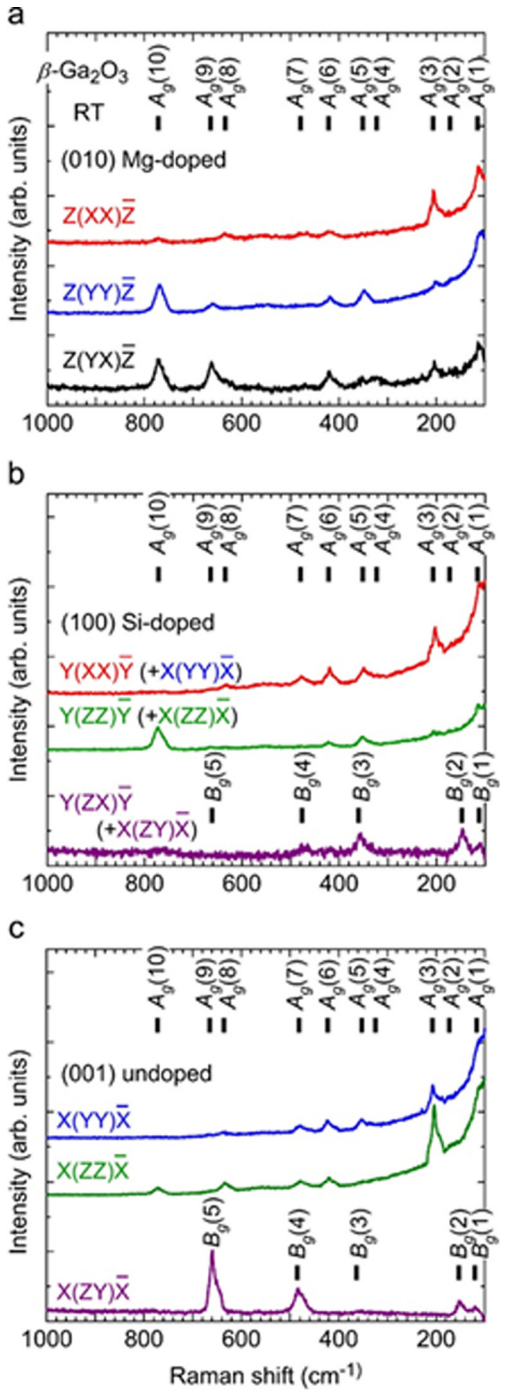

FIG. 18. Polarized Raman spectra of (a) (010) Mg-doped, (b) (100) Si-doped, and (c) (001) undoped β-Ga_2O_3 substrates at room temperature (RT). Reprinted with permission from Onuma *et al.*, J. Cryst. Growth **401**, 330 (2014). Copyright 2014 Elsevier.[309]

of β-Ga_2O_3 and was made possible by the high quality of the crystals produced in this study by EFG and FZ methods.[309]

Defect-related luminescent centers in bulk, FZ, Ga_2O_3 crystals doped with 1 at. % In, Tl, Sn, Pb, Sb, and Bi (ns2) ions were examined by PL and scintillation decay analysis.[310] The Sn-doped samples showed the highest scintillation light yield. Peak emission was observed around 2.8 eV in photoluminescence (PL) under the excitation energy of 4.68 eV and around 3.0 eV in scintillation under X-ray irradiation. Both the PL and scintillation decay times could be

well-fit by assuming the presence of three exponential decay functions with time constants ranging from tens of nanoseconds to several microseconds. The slow component was ascribed to nsnp-ns2 transitions while the fastest and intermediate components were ascribed to defect-related transitions.[310]

The mechanical properties of β-Ga_2O_3 under deformation during indentation have recently been studied.[320] This is relevant due to the current need for polishing of thick HVPE layers on bulk substrates to provide acceptable surface morphology, but also for the grinding and polishing of the initial bulk wafers cut from boules. Wu *et al.*[320] examined the deformation patterns of β-Ga_2O_3 under different loading conditions using TEM. They measured the load and displacement curves from indentation under loads ranging from 0.2 to 10 mN and found that as the load was increased, there was firstly, formation of stacking faults along the (200) lattice planes and twinning structures with the $(2\bar{0}1)$ plane as the twin boundary, then formation of dislocations on (101) lattice planes and, finally at the highest loads, there was bending of the $(2\bar{0}1)$ planes and cracking that propagated along the (200) planes.[319] This behavior is unique to Ga_2O_3 and implies that effective grinding and polishing processes for this material must be developed and not simply transferred from recipes for other materials.[320]

To summarize, a number of parameters, in β-Ga_2O_3 including electron mobility, thermal conductivity, and even bandgap are crystal orientation-dependent, anisotropic, and also a function of the synthesis method. This is expected at this relatively early stage of materials development and much of the spread in reported parameters will be reduced as the material quality becomes more standardized.

DOPING AND DEFECTS IN Ga_2O_3

As with any new wide bandgap materials technology, the control of conductivity through doping and mitigation of trap states is key to realizing device applications.[321] This has been the subject of extensive recent summaries of the challenges and opportunities in the field by Tsao *et al.*[321] and specifically for Ga_2O_3 by Bayraktaroglu.[322] The fact that large area bulk substrates and high quality epitaxial growth processes is available for Ga_2O_3 is a major plus for this material, but the low thermal conductivity must be addressed by active measures to transfer the Ga_2O_3 to more thermally conducting heat-sinks, as has been done with various approaches to incorporating diamond into GaN power device design to facilitate heat removal during high power continuous or pulsed operation.[322–325] It is important to note that this has been to be done in conjunction with a careful analysis of where the thermal bottle-necks occur in the full device structure and that this may require not just a simple heat-sink under the active region, but conformal layers around the gate.[321–325]

Doping in electronic oxides is always complicated by self-compensation, solubility, and defects issues.[326–341] There is also an asymmetry in that one conductivity (usually n-type) is favored over the other.[327–329] An additional consideration is how post-growth annealing when forming contacts or activating dopants affects the conductivity, since this is a function of the ambient employed. In Ga_2O_3, it is often observed that annealing in oxygen reduces the free electron density, while annealing in nitrogen or hydrogen leads to an increase in n-type conductivity.[69,127,329,330] N-type doping of β-Ga_2O_3 in both bulk crystals and epitaxial films has shown to produce controllable carrier concentrations from 10^{16} to $10^{19}\,cm^{-3}$, with an upper limit near $10^{20}\,cm^{-3}$. In MBE, the usual dopants have been Sn and Ge,[334] while Si and Sn are the most common dopants in MOCVD.[2,12,16] Note that there is a good correlation of electrical (from Hall data) and total dopant concentration (from SIMS measurements up to approximately 10^{19} for Sn doping and even higher for Si doping in MOCVD,[72] as shown in Fig. 19).

This choice of dopants for each growth technique appears to be simply a function of availability of those dopants on the particular growth systems used and not due to superiority of one n-type dopant over another. Ion implantation using Si has also been used to enhance the conductivity of n-type layers for Ohmic contact formation.[337,338] The maximum carrier concentration achieved in this case was approximately $5 \times 10^{19}\,cm^{-3}$, although the parameter space for optimized annealing conditions has really not been explored in detail and it is likely even higher carrier concentrations can be achieved. Kang *et al.*[333] have examined the theoretical fundamental limits to mobility in Ga_2O_3. To give some idea of typical electron mobilities achieved for these doping levels, in Sn doped β-Ga_2O_3 grown by MBE, Ahmadi[334] achieved a mobility of $39\,cm^2\,V^{-1}\,s^{-1}$ at a donor concentration of $1 \times 10^{20}\,cm^{-3}$. In Si doped β-Ga_2O_3 grown by MOVPE, Baldini[72,157] achieved a mobility of $50\,cm^2\,V^{-1}\,s^{-1}$ at a donor concentration of $8 \times 10^{19}\,cm^{-3}$.

Understanding the origin of unintentional doping in Ga_2O_3 is necessary in reducing the background conductivity.[338–354] This has implications for devices, where the

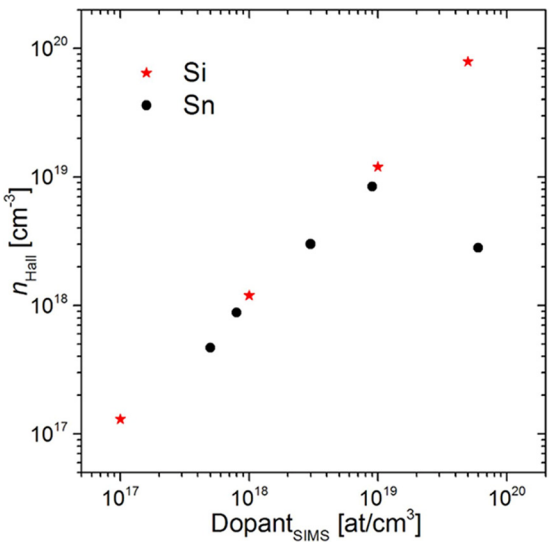

FIG. 19. Hall free carrier concentration versus the dopant (Si and Sn) concentration obtained by SIMS. Reprinted with permission from Baldini *et al.* ECS J. Solid State Sci. Technol. **6**, Q3040 (2017). Copyright 2017 The Electrochemical Society.[72]

breakdown voltage of rectifiers is a strong function of doping level, and obviously, the mobility is degraded by the presence of existing impurities. If they could be minimized, Ma *et al.*[353] showed that polar optical phonon scattering would then be the factor limiting electron mobility for lightly doped samples. Analysis of the main impurities in EFG bulk Ga_2O_3 shows that Si, Fe, and Ir are the main impurities.[69] Varley *et al.*[51] used theory to suggest that oxygen vacancies are deep donors with ionization energies larger than 1 eV and that these cannot explain the unintentional n-type background conductivity. In their work, Si, Ge, Sn, F, and Cl were found to be shallow donors[51] and hydrogen in either interstitial or substitutional sites can act as donors.

By contrast to the case of n-type doping, there is little experimental work on p-type doping of Ga_2O_3 where it was found that Mg doping increases resistivity of the material, but does not lead to p-type conductivity. Theoretically, it has been suggested from the band structure calculations that the holes have large effective mass and tend to form localized polarons rather than mobile free holes in the valence band. This will obviously be an area of active research as novel methods of acceptor incorporation are examined.

Son *et al.*[347] used electron paramagnetic resonance to examine the properties of the background donor in bulk EFG crystals. They found an effective donor ionization energy of 44–49 meV, which was reduced due to banding at higher concentrations. The donor exhibited negative-U behavior, with the negative charge state below the neutral charge state, and the concentration was a strong function of annealing temperature.[347] In their samples, Si was the dominant chemical impurity present.[347] Other studies have reported the ionization level of unintentionally incorporated donors present at a concentration of approximately $10^{16}\,cm^{-3}$ in commercially available (−201) Ga_2O_3 substrates to be 110 meV from temperature dependent Hall effect measurements and 131 meV from admittance spectroscopy.[352] The presence of such relatively deep donors and their ionization percentage at device operating temperatures could have an effect on the on-state resistance and breakdown voltage of rectifiers.[352] The analysis[352] showed that to achieve 10 kV breakdown voltage in Ga_2O_3 Schottky diodes, made on materials containing these deeper unintentional donors, the concentration of these donors must be below $5 \times 10^{14}\,cm^{-3}$.

Korhonen *et al.*[354] investigated the electrical compensation in n-type Ga_2O_3 by Ga vacancies in Ga_2O_3 thin films using positron annihilation spectroscopy, which is a technique for studying vacancy defects in semiconductors. They estimated a V_{Ga} concentration of at least $5 \times 10^{18}\,cm^{-3}$ in their undoped and Si-doped samples.[354] Since theoretical calculations[51] predict that these V_{Ga} should be in a negative charge state for n-type samples, they will compensate the *n*-type doping.[354] Kananen *et al.*[355] used electron paramagnetic resonance (EPR) to demonstrate the presence of both doubly ionized (V_{Ga}^{2-}) and singly ionized (V_{Ga}^{-}) acceptors at room temperature in CZ Ga_2O_3. The singly charged state had the two holes localized on oxygen ions on either side of the V_{Ga} and indicated that both types of vacancies are unlikely to be shallow acceptors.[355]

Nakano[356] used photocapacitance measurements to show there are four dominate traps in state-of-the-art EFG material, with levels at ∼0.8, ∼2.04, ∼2.71, and ∼3.87 eV below the conduction band, plus a deep-level defect with its optical onset at ∼3.71 eV above the valence band Ev.[356] These are shown schematically in Fig. 20.[356] This material also showed strong near band-edge luminescence, an indicator of its high quality and an optical bandgap of ∼4.49 eV.[356]

Wang *et al.*[357] investigated formation energies and transition energies of possible donor-like defects in $GaInO_3$ using hybrid density functional theory. The goal was to understand possible sources of the experimentally observed *n*-type conductivity in this material, which has similar chemistry to Ga_2O_3. They also found that O vacancies are deep donors, while interstitial Ga and In were shallow donors but with much higher formation energies (>2.5 eV), making them less likely to be present.[357] They found that intrinsic defects were not responsible for high levels of *n*-type conductivity. This study found that impurities such as Sn and Ge, as well as other commonly incorporated impurities like H, can act as shallow donors.[357]

The properties of rare earth ions incorporated in *β*-Ga_2O_3 by ion implantation have also been investigated. Peres *et al.*[358] used ion implantation at temperatures of Eu at temperatures up to 1000 °C, using a fixed energy 300 keV Eu^+ beam. Using an elevated implantation temperature in the range of 400–600 °C increased the substitutional Eu fraction present without annealing and the corresponding density of Eu^{3+} ions.[358] The ratio of Eu in the 2+ and 3+ charge states was a strong function of the implantation and subsequent annealing temperature.[358] For Ga_2O_3 damaged by ion implantation, it was found, as expected for a binary lattice with elements of vastly different vapor pressures, that the damage recovery during annealing is complex and a recovery of the crystalline damage was not complete by 1000 °C. Figure 21 shows cathodoluminescence spectra from samples implanted at either (a) 300 °C or (b) 600 °C, which exhibit the sharp Eu^{3+} intra-ionic 4f transition lines in the 600–700 nm region. The broad emission peaked near 400 nm is due to defects and impurities.[359–364]

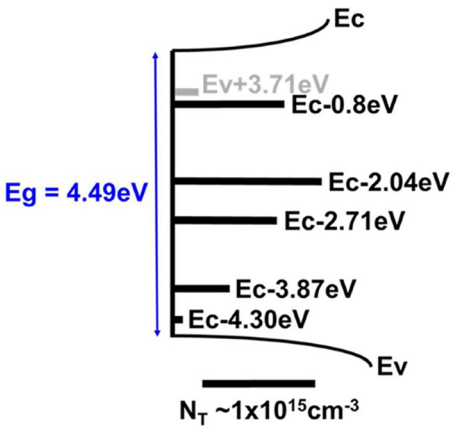

FIG. 20. Schematic of positions in the bandgap of deep level traps in state-of-the-art EFG Ga_2O_3. Reprinted with permission from Y. Nakano, ECS J. Solid State Sci. Technol. **6**, P615 (2017). Copyright 2017 The Electrochemical Society.[356]

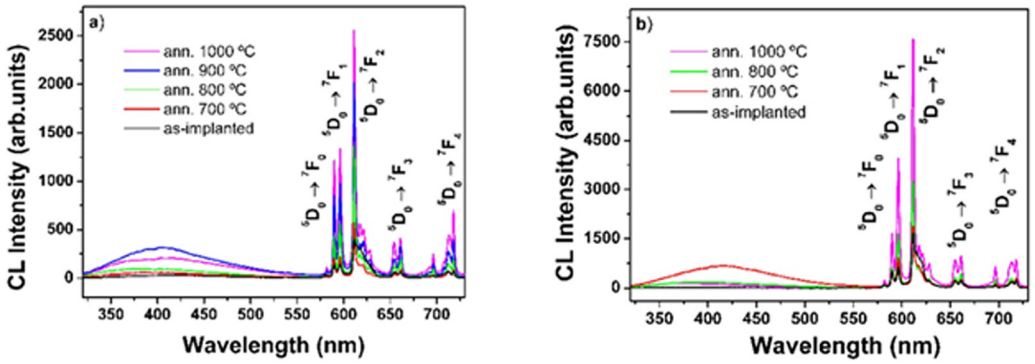

FIG. 21. RT CL spectra of β-Ga_2O_3 samples implanted at 300 °C (a) and at 600 °C (b) annealed at different temperatures. Reprinted with permission from Peres *et al.*, J. Phys. D: Appl. Phys. **50**, 325101 (2017). Copyright 2017 IOP.[358]

Johnson *et al.*[365,366] examined three-dimensional imaging of individual point defects using selective detection angles in annular dark field scanning transmission electron microscopy (STEM). This was related to trying to understand the origin of residual n-type conductivity in Ga_2O_3 and the fact that unlike in some other transparent conducting oxide (TCO), oxygen vacancies may not be the reason because they are deep donors in β-Ga_2O_3. The other suspected causes, such as Si and H, may also complex with native defects such as Ga vacancies. Johnson *et al.*[365,366] reported the imaging of point defects in Ga_2O_3 using electron channeling contrast.[366,367] The channeling contrast method detects the de-channeling of the electron caused by individual point defects, including vacancies and impurity atoms, using multiple narrowly selected detection angles in STEM.[367] The technique can be used to determine the structure and positions of individual point defects, as shown schematically in Fig. 22(a) and in an actual image in Fig. 22(b).[365,366] The left inset shows a simulated image that matches the structure in (a), and the inset at right shows the experimental position averaged convergent beam electron diffraction pattern taken from a unit cell of β-Ga_2O_3.[365,366] The realization of such images requires TEM samples of <10 nm thickness. This is usually achieved by cleaving and mechanical wedge polishing, which limits the orientations that are available.

Thin layers of Ga_2O_3 can also be used as a gate dielectric on GaN for high power metal-oxide-semiconductor devices.[368–381] When GaN is heated at 900 °C, thick films (0.5 μm thick) of β-Ga_2O_3 can be grown in a day on this surface.[374] When non-native oxides are grown on the GaN, they can be contaminated by surface contaminants from this material.[368–372] By directly growing the Ga_2O_3 on GaN, this issue is mitigated and the grown oxide has been shown to be both chemically stable and have a low density of interface states.[374–380] There have been a wide variety of techniques employed to grow or deposit Ga_2O_3 on GaN, including low temperatures approaches such as photoelectrochemical (PEC) oxidation, PLD, excimer laser induced oxidation, microwave plasma oxidation, oxygen plasma oxidation, and saturated water vapor oxidation, in addition to the high temperature thermal oxidation.[368] As expected, the latter produces a significantly lower interface trap density (usually at least an order of magnitude) relative to Ga_2O_3 that is deposited and also compared to other deposited insulator/GaN interfaces.[368] An example of an XRD spectra from GaN

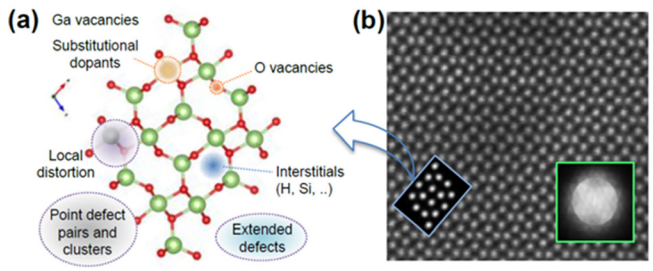

FIG. 22. (a) Potential lattice defects in β-Ga_2O_3. (b) An experimental STEM high angle annular dark field (HAADF) image of β-Ga_2O_3. Inset (left) is the simulated image that matches the structure in (a), and (right) is the experimental position averaged convergent beam electron diffraction pattern taken from a unit cell of β-Ga_2O_3. Reprinted with permission from Johnson *et al.*, Microsc. Microanal. **23**(S1), 1454 (2017). Copyright 2017 Microscopy Society of America.[365]

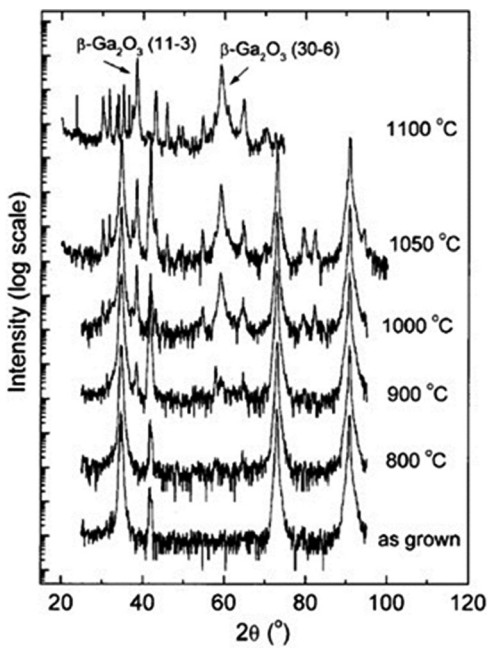

FIG. 23. XRD spectra of GaN epilayers oxidized at 800 °C, 900 °C, 1000 °C, 1050 °C, and 1100 °C for 1 h in dry oxygen ambient. Reprinted with permission from Chen *et al.*, Appl. Phys. A **71**, 191 (2000). Copyright 2000 Springer.[381]

oxidized at oxidized at 800 °C, 900 °C, 1000 °C, 1050 °C, and 1100 °C for 1 h at dry oxygen ambient is shown in Fig. 23.[381] This shows the clear signature of β-Ga_2O_3.[381]

Gallium oxide films have also shown potential as passivation layers on silicon solar cells.[382–387] This is of particular interest for high efficiency solar cells, due to the reduction of the surface recombination of excited carriers. There have been many transparent dielectric films investigated for passivation on solar cells, including SiO_2, silicon nitride (SiN_x), aluminum oxide (Al_2O_3), amorphous silicon, and multilayers of these materials.[382] Ga_2O_3 is known to effectively passivate p and p^+ crystalline Si surfaces, and has been used as an alternative to Al_2O_3 films.[383] Based on its transparency and conductivity, Allen and Cuevas[383] have suggested that Ga_2O_3 might be alternatives to the currently used conductive layers in the photovoltaic devices, such as doped amorphous silicon and tin-doped indium oxide. Xiang *et al.*[382] reported on the characterization of spin-coated Ga_2O_3 films for use as passivation layers on Si. They used gallium nitrate hydrate ($Ga(NO_3)_3 \cdot 9H_2O$) dissolved in deionized water with addition of a surfactant, namely, 1 vol. % of polyethylene glycol monomethyl ether [$HO(CH_2CH_2O)_nC_{12}H_{25}$, $n \cong 25$].[382] The films showed an amorphous-to-crystalline phase transformation above 550 °C.[382] As the temperature was increased from 450 to 850 °C, the interface state density decreased from 4.21×10^{11} to $1.53 \times 10^{11}\,eV^{-1}\,cm^{-2}$. The crystalline β-Ga_2O_3, being monoclinic and thus biaxial, has a triaxial ellipsoidal refractive-index surface.[386]

OXIDE p-n JUNCTION HETEROSTRUCTURES

In the absence of clear demonstrations of p-type doping and the theoretical work that suggests it may not be possible to get free holes in the material, an alternative strategy is to use a natively p-type oxide to produce p-n heterojunctions involving n-type Ga_2O_3. Kokubun *et al.*[387] demonstrated NiO/β-Ga_2O_3 all-oxide p–n heterojunction diodes using p-type NiO epitaxial layers grown on n-type β-Ga_2O_3 substrates.[387] NiO is one of the few wide-bandgap p-type semiconductors, has a bandgap of approximately 3.7 eV, and thus has potential applications in heterojunction devices comprising n-type oxide semiconductors. The diodes exhibited rectifying ratios $>10^8$ at ± 3 V, with a built-in voltage was 1.4 V. The energy band diagram showed this to be a type-II heterojunction, with conduction band offset of 2.2 eV and valence band offset (VBO) of 3.4 eV, respectively.[387]

THEORY OF DEFECTS IN Ga_2O_3

There have been a significant number of theoretical studies of intrinsic defects and p-type dopants in β-Ga_2O_3.[38,45,51,388–392] The electrical properties of all wide band gap semiconductors, and especially oxides, depend critically on the concentration and charge state of defects. As we discussed earlier, β-Ga_2O_3 has intrinsic n-type conductivity because of the presence of unintentional dopants like Si and other donor impurities such as H. The dopants determine whether the current (and, ultimately, the information processed by the device) is carried by electrons or holes. In semiconducting oxides, it is generally possible to achieve one or other of these types, but not both with the carrier concentrations needed for light-emitting devices. Intentional doping with the n-type dopants Si and Sn has allowed demonstration of numerous types of devices and the doping levels are controllable in the range of 10^{15}–$10^{19}\,cm^{-3}$ and higher in some cases when needed for Ohmic contact regions. The development of p-type doping in β-Ga_2O_3 is much less advanced, and there is even a question as to whether p-type conductivity can ever be achieved in Ga_2O_3. The heavy valence band effective mass and a strong Fröhlich interaction favors the formation of polarons with very low conductivity.

Nitrogen has been explored as a dopant for other oxides such as ZnO, but was found theoretically to not lead to acceptor doping.[393,394] The difficulties in achieving p-type doping for ZnO is related to the formation of compensating defects, the presence of donor impurities, the low solubility (typically $<10^{18}\,cm^{-3}$) of the acceptor dopants, and the large ionization energy (170–380 meV) of all of the acceptor candidates. Nitrogen was predicted to have the lowest ionization energy of the possible acceptors. N is a natural choice for an acceptor dopant, since it has about the same ionic radius as that of O, and thus should readily substitute for the latter. While there were reports of successful p-type doping of ZnO with nitrogen,[312–314] the conductivity was often unstable and degraded with time after growth. In addition, the doped ZnO was often found to remain either semi-insulating or n-type due to the sensitivity of the state of the nitrogen on several factors. For example, the N incorporation may be affected by polarity of ZnO and even when N is incorporated in ZnO its efficiency as an acceptor is expected to largely depend on the local surrounding and the presence of other impurities.[393,394] For example, nitrogen substituting for oxygen, N_O, is calculated to be a deep acceptor with an energy level of $E_v + (1.6–1.7)$ eV.[393,394] On the other hand, the acceptor ionization energy is predicted to be significantly reduced if (i) N_O is surrounded by isovalent group II atoms substituting Zn; (ii) N_O is a part of complexes with residual group III contaminants (Al, Ga, In); or (iii) N_O forms the N_O-H-N_O complex.[392,393] In addition, the electrical activity of N can be largely affected by the presence of various intrinsic defects which can act as efficient compensating centers and also facilitate the formation of various N-related complexes, including donor complexes of O_N or Zn_I-N_O.

In Ga_2O_3, N-doped nanowires with a p-type electric conductivity were reported.[395] However, it can be difficult to definitely assign conductivity type unless several different techniques are used to establish it and the lessons from ZnO that N acceptors are strongly compensated by the intrinsic defects, and N atoms cannot be effective acceptors due to their deep levels certainly introduce a note of caution. Dong *et al.*[391] reported first-principles calculations based on density functional theory (DFT) to study the compensation mechanism and interaction of dopants and native defects in N-doped β-Ga_2O_3 with native defects. The introduction of N was found to expand the lattice due to the larger radius of N^{3-}. The band structure calculations found that N dopants act as deep acceptors and cannot be effective p-type dopants.[391] They also found that N formed a variety of complexes with native defects, including oxygen and Ga

vacancies and interstitials.[391] Interstitial Ga and O vacancies were found to be energetically favorable under Ga-rich condition and that the presence of these in N-doped material could compensate any p-type conduction.[388]

Xiao *et al.*[390] carried out first-principles spin-polarized density functional theory calculations to examine the electronic and magnetic properties of N-doped β-Ga_2O_3. They found the spin-polarized state was stable with a magnetic moment of 1.0 μB per nitrogen-dopant. The magnetic moment mainly originated from the p-orbital of the nitrogen and hole-mediated short-range p–p exchange was predicted to cause the predicted ferromagnetism in this material.

Ma *et al.*[389] performed first principles calculations to look at the effect of Al addition to Ga_2O_3 to increase the bandgap. They calculated the effect on absorption (blue-shift) and the energetics of formation of defects in the presence of Al addition. They found that O interstitials were likely to form increasing n-type conductivity.[389] Dong *et al.*[388] examined the stability of O vacancies in β-Ga_2O_3 using the density functional theory. These vacancies were deep donors and lead to deep emission bands in PL spectra.

The work of Varley *et al.*[38] compared the behavior of holes in many wide bandgap oxides and found in Ga_2O_3 that self-trapped holes form with very low mobility of these polarons (approximately 10^{-6} cm^2 V^{-1} s^{-1}), precluding the achievement of p-type conductivity. This certainly highlights the challenges of trying to synthesize p-type β-Ga_2O_3 with practical conductivities and suggests that the experimental efforts should focus on non-equilibrium approaches that minimize other sources of background n-type conductivity and also maximize the solubility of the acceptors, perhaps to form bands.

LOW AND HIGH FIELD TRANSPORT IN Ga_2O_3

Ghosh and Singisetti[396,397] reported calculations of the high-field transport in β-Ga_2O_3 using a combination of *ab-initio* calculations and Monte Carlo simulations. They examined the contribution of electron-phonon interactions on the velocity-field characteristics in this material for electric fields ranging up to 450 kV/cm in different crystal directions. The latter is important because of the known anisotropy of properties in β-Ga_2O_3.[394–398] Figure 24 (top) shows the calculated velocity-field curves in three different Cartesian directions in the crystal.[397] The velocity saturation and negative differential conductivity in β-Ga_2O_3 result from intra-valley short-range scattering, which contrasts to the cases of both GaAs and GaN where these result from inter-valley scattering.[396,397] The calculated average peak velocity at a typically encountered electric field of 200 kV/cm is approximately 2×10^7 cm/s, which is just slightly smaller than in GaN. These same authors reported low field electron mobility calculations in this material from first principles[396] and investigated the interaction between electrons and polar optical phonon modes. At low electric fields strengths, these interactions controlled the electron mobility, which was found to be 115 cm^2 V^{-1} s^{-1}, in good agreement with experiment.[398] Figure 24 (bottom) shows the fit of the calculated mobilities as a function of temperature[396] to experimental data.[398]

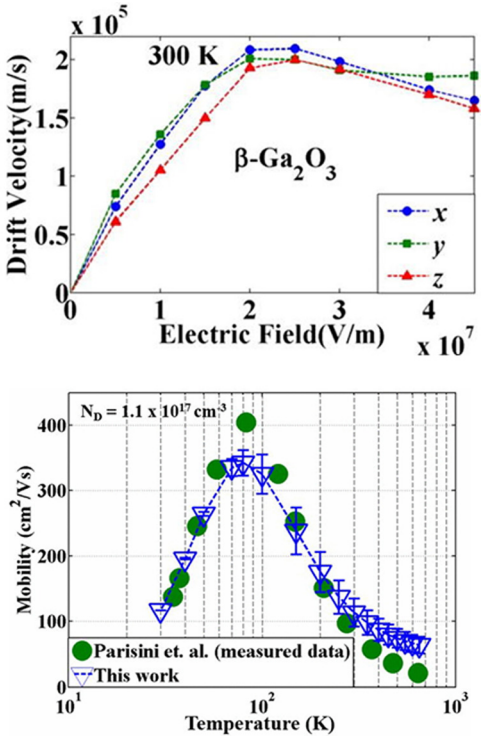

FIG. 24. (Top) Velocity-field characteristic of β-Ga_2O_3 at room temperature in three different directions. (Bottom) Calculated mobility (blue open triangles) for a wide temperature range (30 K–650 K). Experimental data shown as green closed circles. Reprinted with permission from J. Appl. Phys. **122**, 035702 (2017). Copyright 2017 American Institute of Physics.[397]

Parisini and Fornari[398] published a very detailed analysis of the scattering mechanisms in n-type Ga_2O_3 and optical phonons provide the main scattering mechanism, via lattice deformation. They compared their calculated transport properties to their own experimental values as well as those in the literature and found that the high-temperature experimental mobility behavior nearly follows the $T^{-3/2}$ power law, which is the typical temperature dependence for a classical electron gas limited by non-polar acoustic (deformation potential) scattering.[398] Very good agreement with experimental transport data was obtained assuming polar phonons of energy approximately 100 meV, and phonons with energy approximately 30 meV that undergo non-polar interaction with carriers.[398] Ghosh and Singisetti[396,397] also calculated the impact ionization coefficient for avalanche breakdown, α, as being given by $\alpha = a \cdot \exp(-b/E)$, with $a = 2.5 \times 10^6$/cm and $b = 3.96 \times 10^7$ V/cm.[396,397]

The reported anisotropy of electron mobility by some groups as well as some of the optical properties[398–402] has been ascribed to an anisotropy in the conduction band effective mass, but this is not consistent with some calculations that show a nearly isotropic conduction band. Kang *et al.*[403] used first principles calculations to examine whether electron–phonon scattering could show significant anisotropy in the monoclinic lattice. Another important aspect of transport is the dependence of the mobility on the carrier density. Their results indicated that the strong dependence of electron mobility on the electron density, which is more pronounced than in other oxide semiconductors such as

In_2O_3 and ZnO and the anisotropy in mobility (with mobilities differing by approximately 20× depending on the direction) is not intrinsic to β-Ga_2O_3, but is a result of the presence of a high density of extended defects such as twin boundaries. This is easily experimentally testable in state-of-the-art EFG crystals, which are available without significant densities of twins. Kang *et al.*[403] also found that polar longitudinal optical (LO)-mode electron–phonon interactions control mobility at low carrier densities. The phonon spectrum was anisotropic, but did not lead to appreciable anisotropy in mobility.[403]

As reported in Tsao *et al.*,[321] experimental mobilities in n-doped (Si and Sn-doped) β-Ga_2O_3 are typically 100–200 $cm^2\ V^{-1}\ s^{-1}$ at room temperature, 500 $cm^2\ V^{-1}\ s^{-1}$ at 100–200 K in lightly doped bulk material and 5000 $cm^2\ V^{-1}\ s^{-1}$ at 80 K in epitaxial layers. It is generally accepted as discussed above that mobility is limited by optical phonon scattering at high temperature and ionized impurity scattering at low temperature.[399–401] The thermal conductivity for the cases of Sn and Fe-doping has also been determined and compared to the case of undoped β-Ga_2O_3, as shown in Fig. 25.[404] The thermal conductivity in the [001], [100], [010], and [−201] directions were measured from 80 to 495 K. The lowest thermal conductivity at 300 K was along the [100] (10.9 W/m K), while the highest was along the [010] (27 W/m K).[404] The thermal conductivity of the Sn-doped and Fe-doped β-Ga_2O_3 was lower than undoped material due to the enhanced phonon-impurity scattering contribution,[404] while the anisotropy in conductivity results from difference in sound velocities, the anharmonicity in phonon spectrum, and the directional dependence of Debye temperature.[404]

There has been little work to date on transport in β-Ga_2O_3-based alloys and heterostructures, and the properties of 2D electron gases in heterostructures will be of interest for transistor structures.[321,322] Ternary alloys of β-$(Al_xGa_{1-x})_2O_3/Ga_2O_3$ have been reported,[405–408] but the growth is still being optimized. It was established that the phase stability limit of Al_2O_3 in Ga_2O_3 was <18%.[405] Similarly, first-principles calculations[408–410] have indicated that β-$(Ga_{1-x}In_x)_2O_3$ can be stable for low concentrations of In. Clearly, as the materials technologies progress, there will be more studies of transport in both $InGaAlO_x$ epitaxial layers over a range of compositions.

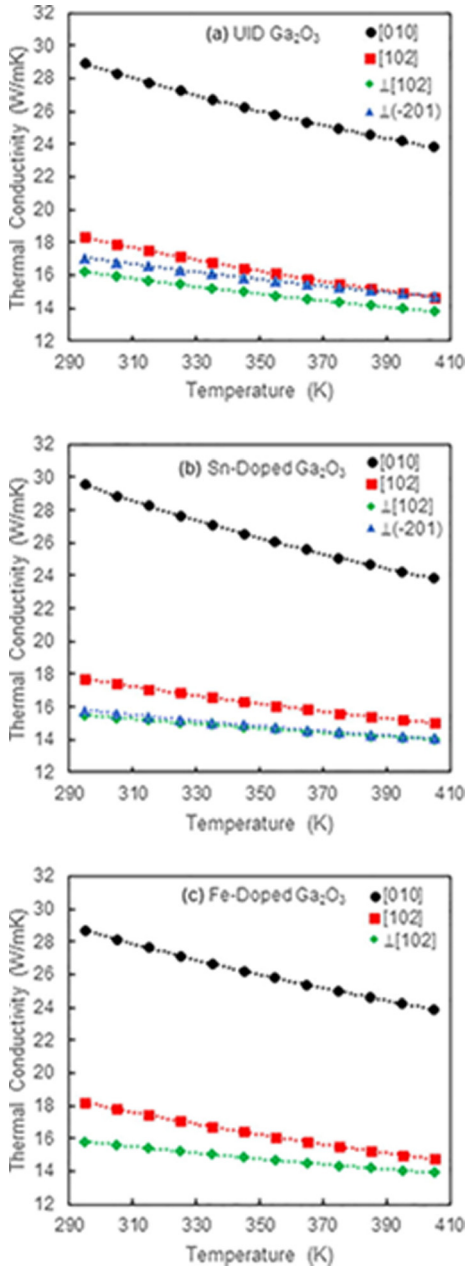

FIG. 25. Temperature dependence of the thermal conductivity for different orientations of undoped (a), Sn-doped (b), and Fe-doped (c) Ga_2O_3. Reprinted with permission from J. Appl. Phys. **121**, 235104 (2017). Copyright 2017 American Institute of Physics.[404]

BAND STRUCTURE

As we discussed earlier, the valence band maximum in β-Ga_2O_3 is mainly composed of weakly interacting oxygen 2p orbital states with contribution of gallium 3d and 4s orbitals,[3] while the conduction band minimum is mainly comprised from the gallium 4s states.[3] Holes in the valence band are localized by lattice distortions to form polarons, while the conduction band is fairly isotropic with an effective mass for electrons of around 0.3 m_o.[3] Mengle *et al.*[411] carried out first principles calculations of the near-edge optical properties of β-Ga_2O_3 explained the broad range of experimentally reported band-gap values (4.4–5.0 eV at room temperature) as resulting from the optical anisotropy of the crystal. They pointed out that linearly polarized light and defined crystal orientations are needed to deduce accurate band-gap values from absorption measurements.[411] It was found that the fundamental band gap is indirect,[411–413] but the minimum direct gap is only 29 meV higher in energy, causing the strong near-edge absorption.[411] They predicted that deep-UV luminescence is possible at sufficiently high excitation powers.[411]

Li *et al.*[414] combined hard X-ray photoelectron spectroscopy (HAXPES) and first-principles band structure calculations to investigate the valence properties and confirmed the main contribution to its formation as being from Ga 4*sp* states.

Onuma *et al.*[412] used polarized reflectance spectra of β-Ga_2O_3 crystals measured as a function of temperature to determine the energies of the absorption edge as 4.48 eV, 4.57 eV, and 4.70 eV, respectively, for an electric field vector

of incidence light parallel to the *c*-axis (*E*//*c*), *a**-axis (*E*//*a**), and *b*-axis (*E*//*b*). The absorption coefficient α for the direct transitions from the upper most valence band to the conduction band minimum at Γ was $10^2\,\mathrm{cm}^{-1} \leq \alpha \leq 10^3\,\mathrm{cm}^{-1}$, but increased rapidly with increasing transition energy ($\alpha > 10^5\,\mathrm{cm}^{-1}$ for $E > 5\,\mathrm{eV}$). They again emphasized that the optical anisotropies were the cause of differences in the reported E_g for β-Ga_2O_3. Exciton energies were 179–268 meV at 5 to 300 K,[412] while the longitudinal optical (LO) phonon energies were in three ranges of 35–48, 70–73, and 88–99 meV. The large exciton changes with temperature result from the exciton-LO-phonon interaction.[412]

Ghose *et al.*[415] used the Cauchy dispersion relation to calculate the bandgap of epitaxial films grown by PA-MBE on sapphire as ~5.02 eV. The refractive index of the films is ~1.89 at 6328 Å.[415] The observed intrinsic broad optical emission of gallate host lattices has been attributed to a self-trapped exciton[416] or a charge transfer-type mechanism.[417] Binet and Gourier[107] pointed out that donors in Ga_2O_3 exhibit impurity band conduction and motionally narrowed electron spin resonance (ESR) signals, but also blue luminescence characterized by strong electron–phonon coupling. They suggested that the blue luminescence would result from the fast recombination of an exciton trapped at an acceptor site after a rate determining tunnel capture of an electron from a donor cluster.[32,107] β-Ga_2O_3 typically exhibits up to three different emissions, UV, blue and green, which are dependent on growth type and purity, except for the UV emission which is ofern attributed to recombination of a self-trapped exciton.[32,107,360,412,417,418] The green emission is related to impurities, while the blue luminescence is generally seen only in conducting samples and may be related to oxygen vacancies.[107] This emission can be selectively excited with less bandgap light at low temperatures. Both UV and blue emissions are broad and have strong Stokes shifts, characteristic of a strong electron–phonon coupling.

Figure 26 (top) shows the emission at room temperature from undoped β-Ga_2O_3 for sub bandgap excitation at 4.67 eV (266 nm). The peaks at 2.85 eV are in the blue range and can be excited in three overlapping bands, indicated by arrows in Fig. 26.[107] The Stokes shift is 1.7 eV. The bottom of Fig. 26 shows the time dependence of the PL after different delays after excitation. For short delays ($t \leq 1$ μs), a fast decaying UV component increases the blue emission. This UV peak disappears for long delays. Harwig *et al.*[418] reported decays with a characteristic time of 120 μs. The kinetics is not exponential, i.e., it is not driven by the transition probability of the recombination center.[107]

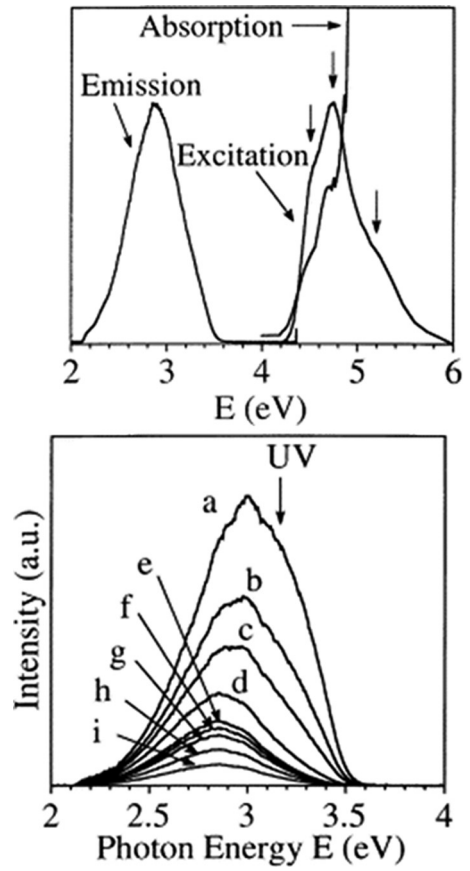

FIG. 26. (Top) Luminescence spectrum of an as-grown undoped single crystal under excitation at 4.67 eV and excitation spectrum of the blue emission, observed at 2.95 eV. Also shown is the absorption spectrum. All the spectra were recorded at room temperature. (Bottom) Time evolution of luminescence spectrum of an as-grown single crystal at room temperature after a laser pulse at 4.67 eV: (a) t = 0.5 μs; (b) t = 0.75 μs; (c) t = 1 μs; (d) t = 2 μs; (e) t = 5 μs; (f) t = 7 μs; (g) t = 10 μs; (h) t = 20 μs; and (i) t = 50 μs. Reprinted with permission from L. Binet and D. Gourier, J. Phys. Chem. Solids **59**, 1241 (1998). Copyright 1998 Elsevier.[107]

EPR OF Ga_2O_3

Electron spin resonance (ESR) and Electron Paramagnetic Resonance (EPR) techniques are powerful tools for exploring the properties of impurities and defects in Ga_2O_3.[354,419,420] Yamaga *et al.*[40] examined valence, occupation site, and symmetry of Si, Zr, Hf, Cr, and Mn dopants in β-Ga_2O_3 using ESR. A single narrow ESR line with an anisotropic *g* value (approximately 1.96) was observed for Si, Zr, or Hf doped β-Ga_2O_3 and ascribed to conduction electrons trapped around oxygen vacancies. Figure 27 shows a single narrow ESR line, measured a t room temperature, with an anisotropic *g* value of approximately 1.96 observed

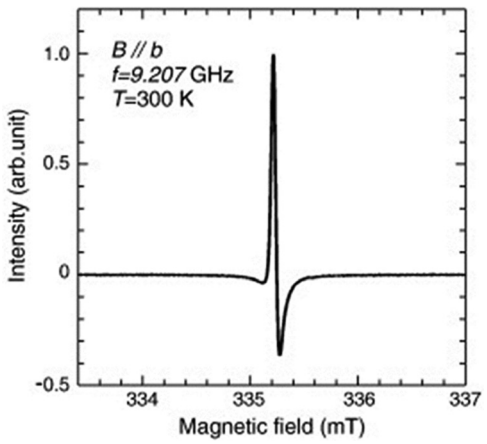

FIG. 27. The ESR spectrum observed for Si^{4+} doped β-Ga_2O_3 at room temperature, with a magnetic field parallel to the *b* axis. Reprinted with permission from Yamaga *et al.*, J. Non-Cryst. Solids **358**, 2548 (2012). Copyright 2012 Elsevier.[420]

in Si doped β-Ga_2O_3 with a magnetic field $\boldsymbol{B}$ parallel to the b axis.[420] The fine structure observed in the ESR spectrum for Mn or Cr doped β-Ga_2O_3 suggested that Mn^{2+} and Cr^{3+} ions substitute for octahedral Ga^{3+} ions in the lattice without charge compensators.[419] The ESR lines were not observed for Si, Zr, or Hf doped β-Ga_2O_3, indicating that Si, Zr, and Hf are non-paramagnetic with a valence of $+4$.[419]

Kananen *et al.*[355,419] used EPR to identify Ga vacancies in Ga_2O_3, as discussed earlier. The V^{2-}_{Ga} exhibited a hyperfine structure due to equal and nearly isotropic interactions with the ^{69,71}Ga nuclei at two Ga sites (the hyperfine parameters are 1.28 and 1.63 mT for the ^{69}Ga and ^{71}Ga nuclei, respectively).[355] This same group used EPR to characterize neutral Mg acceptors (Mg^0_{Ga}) in Mg-doped β-Ga_2O_3.[419] These acceptors were observed after x-ray irradiation at 77 K. This forms neutral acceptors when holes are trapped at singly ionized Mg acceptors (Mg^-_{Ga}), i.e., the hole is localized in a nonbonding p orbital on a threefold-coordinated oxygen ion adjacent to an Mg ion at a sixfold-coordinated Ga site.[419] The Mg^0_{Ga} acceptors converted back to the non-paramagnetic Mg^-_{Ga} charge state above 250 K.[419] They also observed electron traps due to the unintentional impurities Fe^{3+} (3d5) and Cr^{3+} (3d3).[419]

HYDROGEN IN Ga_2O_3

There is a particular interest on the properties of hydrogen in wide bandgap semiconductors, in general,[421–457] and in Ga_2O_3, in particular,[433,443–446,456,457] because of the predictions from density functional theory and total energy calculations that it should be a shallow donor.[51,437,438] The generally observed n-type conductivity, therefore, may at least in part be explained by the presence of residual hydrogen from the growth ambient, rather than to native defects such as Ga interstitials or O vacancies, which are suggested to be deep donors.[51] There is some experimental support to the fact that hydrogen may be a shallow donor in Ga_2O_3 from experiments on its muonium counterpart and from electron paramagnetic resonance of single-crystal samples.[443–445] This would be similar to the case of ZnO, where hydrogen is a shallow donor and contributes significantly to the observed native n-type conductivity in that material in many cases.[422] There is evidence that a number of transparent conducting oxides have commonality of impurity properties.[435,438]

It is well known that atomic hydrogen can passivate virtually all impurities in semiconductors like Si, GaAs, and GaN through the formation of neutral dopant-hydrogen complexes.[421,422,437,438,447] In most semiconductors, hydrogen is a negative-U center, so in the p-type material, hydrogen is a compensating donor, whereas for n-type conductivity, hydrogen is a compensating acceptor, and therefore, in these materials, hydrogen always counteracts the prevailing conductivity.[421,433,435,450] However, different behavior has been found for conducting oxides.[437,438]

In terms of what is known about hydrogen in other electronic oxides, it has been found previously that hydrogen diffuses extremely rapidly in ZnO,[425,431] producing incorporation depths of almost 30 μm for a 0.5 h exposure of bulk, single crystal ZnO to a ^{2}H plasma. The incorporation depths are much larger than in other wide bandgap semiconductors such as GaN, where a similar process leads to incorporation depths of less than 1 μm.[419,420,422,425] Hydrogen was found to be a shallow donor in ZnO and to play a significant role in the background n-type conductivity.[438,441] Similarly, the role played by hydrogen impurities in the conductivity of indium oxide (In_2O_3) was controversial.[440,448] Some studies, based on the effect of oxygen partial pressure in growth or annealing environments,[438,446,447] argued that oxygen vacancies were the cause of the conductivity of In_2O_3. However, both theoretical and experimental work found that hydrogen centers can be important shallow donors in In_2O_3.[422,436,447] Muon-spin-resonance experiments found that implanted muons, whose properties mimic those of hydrogen, form shallow donors in In_2O_3.[443–445] In_2O_3 thin films containing hydrogen show n-type conductivity with high mobility.[438] It was theoretically predicted that interstitial hydrogen (H_i^+) and hydrogen trapped at an oxygen vacancy (H_O^+) were shallow donors, giving rise to n-type conductivity or compensate acceptors in In_2O_3.[436]

The role of hydrogen impurities on the conductivity of In_2O_3 single crystals was studied using IR spectroscopy and theory.[437,438] The annealing of In_2O_3 crystals in an H_2 or D_2 ambients at 500 °C produced a thin conducting layer near the surface with thickness ≈0.06 mm and with a carrier concentration determined by Hall measurements of 1.6×10^{19} cm^{-3}. An OH vibrational line at 3306 cm^{-1} was assigned to the interstitial H shallow-donor center that is responsible for the hydrogen-related conductivity.[438,447] The corresponding Di center had an OD line at 2464 cm^{-1}. The Hi center was stable up to ≈500 °C. Investigations of hydrogen shallow-donor centers in ZnO and SnO_2 found that H_i is only marginally stable at room temperature and H_O is a more thermally stable donor that dominates the n-type conductivity of hydrogenated samples of these materials stored for substantial times at room temperature. The experimental results and complementary theory showed that the conductivity produced by the thermal treatment of In_2O_3 in hydrogen can be explained primarily by a thermally stable H_i center, consistent with theoretical predictions that H_O has a higher formation energy.[438,447]

Interstitial hydrogen (Hi) and hydrogen at an oxygen vacancy (H_O) behave as shallow donors in SnO_2.[437,438] Annealing SnO_2 in a hydrogen-containing ambient gives rise to strong n-type conductivity and produces several hydrogen-containing centers. Bates and Perkins[449] in examining the vibrational properties of OH, OD, and OT centers in TiO_2 found single sharp vibrational lines, while Herklotz *et al.*[450] discovered a more complicated OH (or OD) spectrum with a multiline structure. Herklotz *et al.*[450] proposed that OH and OD centers in TiO_2 are shallow donors with binding energies of 10 meV and that the multiline structure is due to the thermal ionization of the OH or OD center. SnO_2 and TiO_2 both have the rutile structure and have interstitial H centers with similar structures.[437,438] However, interstitial H gives rise to an effective mass theory (EMT) shallow donor in SnO_2 (and In_2O_3) with strong free carrier-absorption and to a small polaron in TiO_2 that leads to a distinctive OD vibrational absorption spectrum.[438] The origin

of the conduction band states is critical in determining the behavior of donor states in these materials, being s- and p-like in SnO_2 (and In_2O_3) and having substantial d-character in TiO_2. These differences cause delocalization of the electrons in effective-mass-like states in SnO_2 and In_2O_3 and to be self-trapped at Ti in TiO_2.[437,438]

We have done some preliminary work on determining the properties of hydrogen in Ga_2O_3. The first set of experiments involved implantation of ^2H ions into bulk Ga_2O_3 and subsequent annealing to measure the thermal stability. As shown in Fig. 28 (top), the deuterium evolves from the sample for annealing up to 650 °C, but the remainder at each temperature decorates the residual ion-induced damage. The fraction of the remaining implanted deuterium is shown at the bottom of the figure and corresponds to a lower activation energy than in materials like GaN. The temperature at which deuterium is retained is also higher when it is implanted compared to introducing it by diffusion from a plasma. This is a result of the deuterium trapping onto residual implant damage in the former case.

OHMIC CONTACTS TO Ga_2O_3

The achievement of acceptable device characteristics for any Ga_2O_3-based structure relies heavily on developing low specific contact resistance Ohmic metallization schemes. Additional contact resistance leads to slower device switching speeds as well as reliability issues due to local contact heating during current flow during device operation. Wide bandgap semiconductors typically have large barrier heights for metals deposited on them.[458–463] To decrease the barrier height and/or width, the insertion of an intermediate semiconductor layer with a smaller band gap and/or a higher doping concentration is one approach to improve carrier transport across the interface.[464–490] In other wide bandgap semiconductors, Ohmic contacts are typically realized by metal-semiconductor structures in which the potential barrier is reduced by heavily doping the semiconductor under the metal, which enhances electron tunneling.[458–463] The doping levels achievable in most wide bandgap semiconductors are usually well below of what can be obtained in Si, and combined with the lower electron affinity of these materials, the Schottky barrier heights of most metals are very high (>2 eV).[321] This leads to the unacceptably high contact resistances. The usual approaches to mitigate these issues in oxides involve surface etching or cleaning to reduce barrier height or increase of the effective carrier concentration of the surface through preferential loss of oxygen. Another approach used in other semiconductors has been to use compositionally graded layers specifically designed to lower the barrier to electron transport.[321,322]

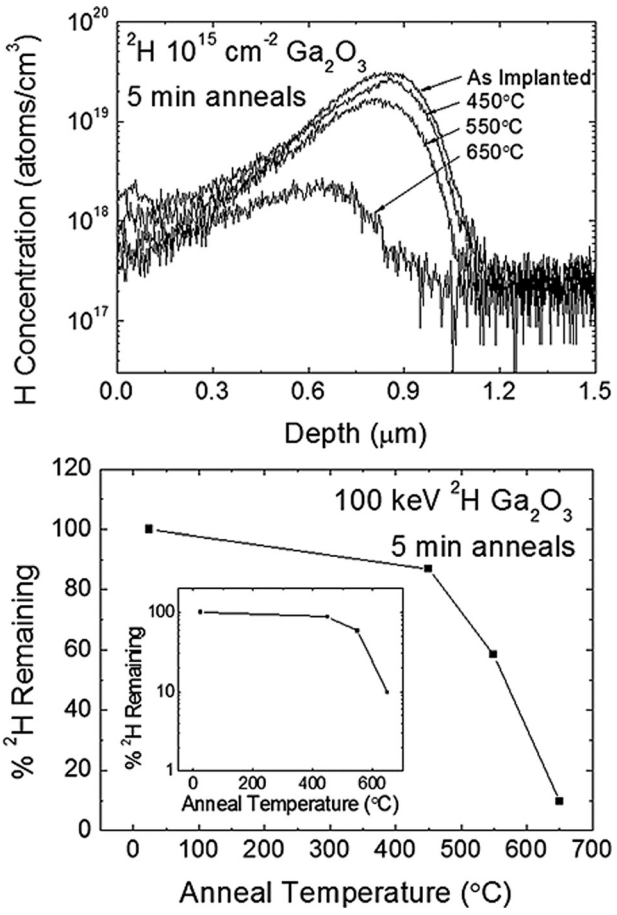

FIG. 28. Profiles of ^2H implanted Ga_2O_3, subsequently annealed at different temperatures to measure the thermal stability (top) and percentage of ^2H remaining as a function of anneal temperature (bottom).

It is desirable to have reliable Ohmic contacts capable of withstanding high temperatures to maximize process flexibility and also the range of device applications. In addition, in devices like rectifiers, their resistance must be negligible compared to the semiconductor drift layer, in order to minimize the device specific on-resistance (R_{on}) and, hence, the power losses of the system. Typically, electronic devices based on wide bandgap semiconductors require specific contact resistance (ρ_c) values in the range of 10^{-5}–10^{-6} Ω cm^2.[321,322]

For an n-type semiconductor, to achieve an Ohmic contact means that the work function of the metal must be close to or smaller than the electron affinity of the semiconductor.[460] The electron affinity of β-Ga_2O_3 is reported to be 4.00 ± 0.05 eV,[481] and thus potential choices if the surface is unpinned include Hf (work function 3.9 eV), Sc and La (both 3.5 eV), and Gd (2.9 eV). It will be interesting to see if these are effective on n-type β-Ga_2O_3, most likely with bilayers of these with Au to reduce the contact sheet resistance. The transport mechanisms in the contacts should then be determined by the temperature-dependent transmission line method (TLM) or circular-TLM (CTLM) measurements.

The contact resistance is an important parameter characterizing the metal/semiconductor interfaces.[460] It is the total resistance of the metal/semiconductor junction (expressed in Ω) and, hence, it depends on the area of the contact. A more useful physical parameter describing the performance of Ohmic contacts is the specific contact resistance ρc, which is independent of the contact geometry, and is typically expressed in Ω cm^2. The relation between the contact resistance and the specific contact resistance in a metal/semiconductor contact can be viewed analogously to that between the resistance and the resistivity in a resistor.

In Ohmic contacts, the specific contact resistance ρ_c depends on the metal/semiconductor Schottky barrier height

Φ_B and on the doping concentration of the semiconductor. For an *n*-type semiconductor, according to the Schottky–Mott theory, the metal/semiconductor Schottky barrier height Φ_B obeys the relation.[458–460]

$$e\Phi_B = e\Phi_m - \chi_s,$$

where Φ_m is the work function of the metal, and χ_s is the electron affinity of the semiconductor.

For an *n*-type semiconductor, depending on the semiconductor doping level N_D, different mechanisms of carrier transport at the interface can occur, owing to the different thickness of the space charge region *W* formed at the metal/semiconductor interface. Consequently, the specific contact resistance ρ_c will have a different dependence on the barrier height Φ_B, on the carrier concentration N_D, and also on the temperature *T*.

A traditional Ohmic contact on semiconductors follows a thermionic field effect (TFE) or field-effect (FE) mechanism depending on the semiconductor effective doping and/or temperature.[458–460] If, for example, there was no significant dependence of the contact resistance on measurement temperature for the samples after annealing, this would indicate that the dominant current transport mechanism is field emission. Thermionic emission has a significant temperature dependence, and thermionic field emission is operative at the doping range of 10^{16}–10^{18} cm^{-3}. In thermionic emission, the specific contact resistance is given by[458–460]

$$\rho_C = \frac{k}{qA^*T}\exp\left(\frac{q\phi_{Bn}}{kT}\right),$$

where k is the Boltzmann's constant, A* the Richardson constant, and T the measurement temperature, may be explained by the tunneling process, which is given by[460]

$$\rho_C \sim \exp\left[\frac{2\sqrt{\varepsilon_S m^*}}{\hbar}\left(\frac{\phi_{Bn}}{\sqrt{N_D}}\right)\right],$$

where q is the electronic charge, ϕ_{Bn} the barrier height, ε_S the semiconductor permittivity, m* the effective mass, $\hbar$ the Planck's constant, and N_D the donor density. In the FE mechanism, the specific contact resistance of Ohmic contacts is strongly dependent on both the Schottky barrier Φ_B and the semiconductor doping N_D level. For fixed values of the barrier height Φ_B and carrier concentration N_D, the temperature determines the carrier transport mechanism through the metal/semiconductor interface. In particular, when the thermal energy *kT* is much lower, tunneling of the carriers by the *FE* mechanism is predominant. At higher temperatures, the carriers can pass through the barrier by the TFE mechanism. Finally, at much higher temperatures, thermionic emission over the barrier becomes relevant for the current transport.

To date, contact schemes involving indium zinc oxide (IZO) interlayers between the metal and the Ga_2O_3, dry etching in BCl_3/Ar to enhance the surface n-type conductivity, followed by Ti/Au,[466] Ti/Al annealed at 500 °C (Refs. 464 and 465) or implantation of Si to increase surface conductivity,[464,480] have been employed to achieve acceptable contact resistance. Table III shows a summary of results from the literature. Specific contact resistances of approximately 8×10^{-6} Ω cm^{-2} were reported for Ti/Au source-drain contacts on n-Ga_2O_3 epitaxial layers in which Si was implanted and annealed at 925 °C, followed by dry etching, metal deposition, and annealing at 470 °C.[467] Other reports with a similar process have achieved 4.6×10^{-6} Ω cm^{-2} for Ti/Au contacts on Si-implanted epitaxial layers.[464]

Oshima *et al.*[470] used the inter-layer approach, but pointed out that the often-used In- and Ti-based electrodes are often utilized as Ohmic contacts, are probably not optimal due to the low melting point of In of 157 °C, while Ti contacts degrade above 600 °C due to oxidation reactions with β-Ga_2O_3. We have found previously in GaN, for example, that there is usually a strong relationship between the electrical performance and interfacial microstructure of Ohmic contacts over different annealing temperatures. The formation of interfacial nitrides, for example, is found to be critical in achieving Schottky-to-Ohmic transition as well as excellent Ohmic contacts. In addition, the interdiffusion, intermixing, and metallurgical reactions within and between the metal layers lead to the formation of second phase consisting of intermetallics, solid solutions, or precipitates. Auger Electron Spectroscopy elemental profiling of the contacts for different anneal temperatures and times will help us to identify any metal reactions with the Ga_2O_3. These phases can be examined in detail with TEM, microprobe, and XPS.

According to all the above considerations, metals with a low Schottky barrier height are recommended to obtain an Ohmic contact with a low specific contact resistance ρ_c. It is worth noting that most of the data reported in the literature (Table III) refer to multilayers in which a capping layer is introduced over a Ti/Al stack (Ti/Al/Ni/Au, Ti/Al/Ti/Au, Ti/Al/Pd/Au, and Ti/Al/Mo/Au). In GaN technology, a typical Ohmic stack consists of a contact layer like Ti or Ta, an overlayer of Al, a barrier layer of a metal such as Ni, Ti, Pt, Pd, Mo, or Ir, and then a cap layer of Au to reduce the sheet resistance of the contact.

The presence of surface states on Ga_2O_3 is crucial to the contact, since high density allows carriers to tunnel through the barrier. This was reported for Au/Ti on Si-implanted β-Ga_2O_3.[491] If there are a few surface states, it should be a Schottky contact.[490] Yao *et al.*[475] also reported recently that the surface states appear to have a more dominant effect on Schottky diode characteristics than the actual choice of the metal. Thus, the orientation of the wafer surface, which defines both the Ga-to-O ratio and the density of dangling bond states, makes a difference. Yao *et al.*[475] investigated the use of Ti, In, Ag, Sn, W, Mo, Sc, Zn, and Zr as electrical contacts to *n*-type β-Ga_2O_3 substrates as a function of annealing temperature up to 800 °C. Some metals displayed Ohmic (Ti and In) or near-Ohmic (Ag, Sn, and Zr) behavior over a particular range of conditions, but the contact morphology was problematic.[475] They concluded that the metal work function is not a dominant factor and the interfacial reactions were key. Baik *et al.*[492] found that Ti (200 Å)/Au (1500 Å) metallization deposited on the two different orientations and annealed at 450 °C showed Ohmic current-voltage (*I-V*) behavior for $(\bar{2}01)$ but rectifying characteristics

TABLE III. Summary of Ohmic contact properties on β-Ga_2O_3.

Metal stack	n-type doping (cm^{-3})	Anneal conditions	ρ_c (Ω cm^2)/method	Comments	Reference
Ti(50 nm)/Au(300 nm)	3×10^{19}	450 °C for contacts (950 °C for implant activation prior to metallization)	4.6×10^{-6}, CTLM	Si implanted to increase doping in contact region	Sasaki *et al.*[469]
Pt(100 nm)/ITO(140 nm)	2×10^{17}	800–1200 °C for Pt/ITO, 450–700 °C for Pt/Ti	Not measured, but Ohmic for anneals above 900 °C	Compared use of ITO interlayers to enhance Ohmic contact formation	Oshima *et al.*[471]
Ti/Al/Au (15/60/50 nm)	2.7×10^{18}	None	Contact resistance of 2.7 Ω mm, TLM	Ar plasma pre-treatment to enhance conductivity under contact	Zhou *et al.*[485]
Ti(20 nm)/Au(230 nm)	$\sim 3 \times 10^{19}$	470 °C, 60 s	Not measured-field-plated MOSFET	Si implant annealed at 950 °C and BCl_3 dry etch to enhance surface conductivity	Wong *et al.*[486]
Ti(20 nm)/Au(230 nm)	7×10^{17}	None	Not measured-MBE grown MESFET	BCl_3/Ar RIE to enhance surface conductivity	Higashiwaki *et al.*[487]
Ti(20 nm)/Au(230 nm)	$\sim 3 \times 10^{19}$	470 °C, 60 s	7.5×10^{-6}	Si implant annealed at 950 °C and BCl_3 dry etch to enhance surface conductivity	Wong *et al.*[473]
Ti/Al	10^{18}	450 °C, 60 s (1100 °C, 5 min for Sn drive-in prior to contact deposition)	2.1×10^{-5}, TLM	Diffusion of Sn from spin-on glass source, as well as BCl_3/Ar RIE	Zeng *et al.*[474]
Ti/Al/Ni/Au	$\sim 10^{19}$	470 °C, 60 s	Contact resistance of 4.7 Ω mm, TLM	e-mode MOSFET	Chabak *et al.*[470]
Ti/Au/ITO (10/20/80 nm)	$\sim 10^{19}$	600 °C	6.3×10^{-5}, TLM	Si implant activated at 950 °C to enhance conductivity	Carey *et al.*[475]
Ti/Au/AZO (10/20/80 nm)	$\sim 10^{19}$	400 °C	2.8×10^{-5}, TLM	Si implant activated at 950 °C to enhance conductivity	Carey *et al.*[477]
Ti, In, Ag, Sn, W,Mo, Sc, Zn and Zr (20 nm), with Au (100 nm) overlayers	5×10^{18}	400–800 °C	Not measured	In and Ti produced linear I-Vs after anneals	Yao *et al.*[476]

for (010). Since the net doping density is the same in both samples, the surface chemistry determines the effective barrier height and hence the dominant carrier transport mechanism.[492]

Carey *et al.*[476,477] also reported the use of IZO or ITO interlayers to improve the contact resistance. Pt/ITO contacts on n-Ga_2O_3 showed superior Ohmic contacts to Pt/Ti and this was attributed to the formation of an interfacial layer with lower bandgap and higher doping concentration than the Ga_2O_3 alone. The band alignment at the heterointerface is also critically important in determining the favorability of the carrier transport.[480,481] Several authors have found that the presence of upward band bending in low conductivity Ga_2O_3 complicates the achievement of Ohmic contacts.[464–469,481,484]

SCHOTTKY CONTACTS TO Ga_2O_3

Schottky rectifiers are attractive applications for β-Ga_2O_3 because of their fast switching speed, which is important for improving the efficiency of the inductive motor controllers and power supplies and also their low turn-on voltages compared to p-n junction rectifiers. Their breakdown voltage is a strong function of bandgap.[493–499] Ga_2O_3 Schottky diodes have numerous advantages over more conventional Si rectifiers, achieving a maximum electric field breakdown strength over 10 times larger and on-state resistance (R_{ON}) approximately four hundred times lower at a given voltage.[500–508] These characteristics make Ga_2O_3 devices attractive for hybrid electric vehicles and power conditioning in large industrial motors.

As we discussed in "Ohmic Contacts to Ga_2O_3" section, the interface-induced gap states, made up of both valence-band and conduction-band states in electronic oxides, often play a determining role in the barrier heights of metal contacts.[505,508–515] Some studies have reported a correlation between Schottky barrier heights of metals on Ga_2O_3 and the electronegativity difference between the oxide and the metal.[501,506,507] The presence of the upward band bending in low conductivity Ga_2O_3 complicates the achievement of Ohmic contacts,[495,505,508–510] and there was a strong dependence of the properties of the barrier height on the energy of incident atoms during deposition.[516,517] The latter implicates surface defects and stoichiometry as being one factor in determining the properties of the contact.

Table IV summarizes the reported values for the Schottky barrier height, ideality factor, and thermal stability of different metals schemes used for rectifying contacts on β-Ga_2O_3. Most groups extract the effective barrier height from the linear portions of the I-V characteristics of Schottky diodes, assuming the ideal thermionic-emission

behavior. However, capacitance-voltage (C-V) and internal photoemission (IPE) measurements are also employed for a complete understanding of the current transport mechanisms.[494–497,518–523] The typical barrier heights are in the range of 1–1.4 eV. Note that different metals yield different barrier heights within a limited range, and so it is of interest to examine possible Fermi-level pinning effects on Ga_2O_3 surfaces.[499] The predicted barrier height for the Ni in the absence of pinning would be the difference in the Ni work function and electron affinity of Ga_2O_3 from the Schottky-Mott relation. This would translate to 1.04–1.35 eV,[501] based on the reported work function of Ni (5.04–5.35 eV) and the electron affinity of Ga_2O_3 (4.00 eV).[508–510] A similar estimate for Pt would yield a value of 1.12–1.53 eV based on the reported work functions of 5.12–5.93 eV. Many of the experimental values are consistent with the Schottky-Mott predicted values for the barrier height. However, the presence of surface states will modify the resultant effective barrier heights and this may explain the fact that the experimental value for some Ni Schottky diode barrier heights is higher than Pt, despite the fact that the Ni work function is lower than Pt.[501] The n_s values reported the range from very near the ideal value of 1 (unity) to approximately 1.5. The reasons for n_s values to be larger than 1

TABLE IV. Table of reported Schottky barrier contacts to β-Ga_2O_3.

Metal	Barrier Height (eV)	Ideality Factor	Process/measurement condition	Comments	References
Ni	1.25	1.01	Evaporation, I-V	Thermionic emission	Oishi *et al.*[499]
Ni	1.05	Not measured	Dc magnetron sputtering, I-V	No photocurrent in forward bias	Armstrong *et al.*[503]
Ni	1.08	1.19	Sputtering, I-V	Piranha clean,BOE,water clean	Jayawardena *et al.*[507]
Ni	1.55	1.04	E-beam deposition, I-V	Similar values obtained with C-V, internal photoemission	Zhang *et al.*[505]
Ni	1.07	1.3	E-beam Pt/Au, I-V	Consistent with Schottky-Mott model	Ahn *et al.*[502]
Ni	0.95	3.38	E-beam Ni/Au, I-V	Epi layer, barrier height increased with temperature	Oh *et al.*[504]
Ni	1.04	1.3	E-beam, I-V and C-V	Much larger barrier height (1.61eV) with C-V	Yao *et al.*[500]
Ni	0.8–1.0	1.8–3.2	Evaporation, I-V	$(Al_xGa_{1-x})_2O_3$ with x up to 0.164. Barrier height increases slightly with Al content	Ahmadi *et al.*[407]
Ni	0.97–1.22	Not measured	Evaporation, I-V and C-V	Cleaved surface, higher barrier measured with C-V	Irmscher *et al.*[496]
Ni	1.54	1.04	E-beam deposition, I-V	Similar values obtained with C-V, internal photoemission	Farzana *et al.*[515]
Pd	1.27	1.05	E-beam deposition, I-V	Similar values obtained with C-V, internal photoemission	Farzana *et al.*[515]
Pt	1.58	1.03	E-beam deposition, I-V	Similar values obtained with C-V, internal photoemission	Farzana *et al.*[515]
Au	1.71	1.09	E-beam deposition, I-V	Interface consistent with inhomogeneous barrier	Farzana *et al.*[515]
Au	1.04	1.01	E-beam deposition, I-V	electron affinity Ga_2O_3 4.00 ± 0.05 eV, work function of Au 5.23 ± 0.05 eV	Mohamed *et al.*[516]
Au	0.98	1.09	E-beam, I-V	Significant degradation above 200 °C	Suzuki *et al.*[517]
Pt	0.71–1.1	1.41–1.61	Thermal evaporation or sputtering, I-V	Long throw sputtering generally better	Muller *et al.*[518]
PtO_x	1.09–1.34	1.52–2.18	Sputtering,I-V	Long throw sputtering generally better	Muller *et al.*[518]
Pt	1.39	1.1	Pt/Ti/Au sputtering, I-V	Barrier height stable to at least 150 °C	He *et al.*[513]
Pt	1.46		Pt/Ti/Au evaporation, I-V	Barrier height may have been enhanced by presence of F at interface	Konishi *et al.*[520]
Pt	1.04	1.28	E-beam Pt/Au, I-V	Consistent with Schottky-Mott model	Ahn *et al.*[502]
Pt	1.35–1.47		Evaporation of Pt/Ti/Au, I-V, C-V		Sasaki *et al.*[498]
Pt	1.01	1.07	E-beam, I-V	Thermionic emission	Tadjer *et al.*[514]
TiN	0.98	1.09	ALD at 350 °C, I-V	Thermionic emission, degrades above 170 °C	Tadjer *et al.*[519]
Cu	1.32	1.03	Sputtering, I-V	Stable up to at least 250 °C	Splith *et al.*[509]
Cu	1.13	1.53	E-beam, I-V and C-V	Optimal cleaning was organic solvent, HCl and H_2O_2 and DI water rinse	Yao *et al.*[500]
W	0.91	1.4	E-beam, I-V and C-V	Higher barrier heights for (010) cf. (−201)	Yao *et al.*[500]
Ir	1.29	1.45	E-beam, I-V and C-V	Not a strong correlation of barrier height with work function	Yao *et al.*[500]
Pt	1.05	1.4	E-beam, I-V and C-V	Larger barrier heights in C-V	Yao *et al.*[500]
Pt	1.09–1.15	∼1	Evaporation of Pt/Ti/Au, I-V and C-V	Richardsons's constant A* of 28–41 $A/cm^2 K^2$	Higashawaki *et al.*[501]

are generation–recombination in the depletion region, thermionic field emission tunneling, and edge leakage, which tend to degrade the electron device performance characteristics.[493,505–510]

Farzana *et al.*[514] carried out a systematic study of Schottky barriers fabricated on (010) β-Ga_2O_3 for Pd, Ni, Pt, and Au Schottky diodes. The diodes exhibited nearly ideal I-V characteristics with the ideality factors from 1.03 to 1.09. Thermionic emission was the dominant mechanism for Ni, Pt, and Pd. The barrier height depended on the metal, ranging from 1.27 V for Pd, 1.54 V for Ni, 1.58 V for Pt, and 1.71 V for Au.[514] While most of the metals showed a good agreement between I-V, C-V, and IPE measurements, for Au a large variation was noted between the methods. This may indicate the presence of a more complex interface for Au/Ga_2O_3. Figure 29 shows the dependence of the barrier height on the metal work function.[499] The lack of a strong correlation indicates that these metal-(010) β-Ga_2O_3 interfaces are not fully pinned. It is also important to note that the literature will always contain a small number of outlier results due to experimental control issues, but the general trend to date is that the barrier heights are not controlled by surface Fermi level pinning, that the deposition method makes a difference through its effect on the energy of the incident species arriving at the surface, the effectiveness of the surface cleaning process, and the orientation of the Ga_2O_3 surface all play a role in determining the effective barrier.[499,501,508–510,518–521]

Muller *et al.*[522] examined both Pt and PtO_x as Schottky contacts, deposited by thermal evaporation, and various sputtering methods. In general, they and others[520–523] have found that oxygen-containing ambients produce better Schottky characteristics on oxides like Ga_2O_3 and that the kinetic energy of the impinging metal species on the oxide surface plays a role in defining the quality of the rectifying contacts. This is an important practical consideration when trying to fabricate rectifiers with reproducible and optimized breakdown voltages.

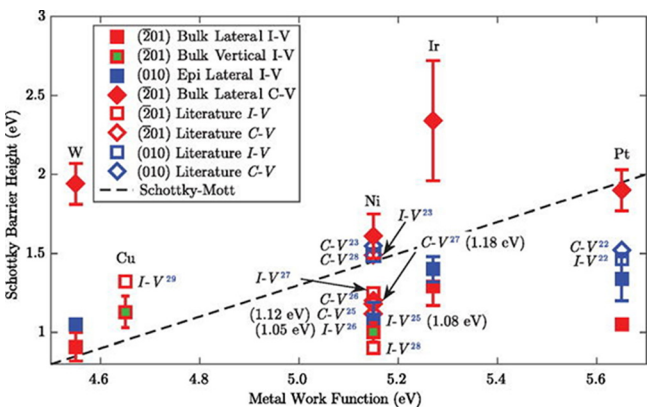

FIG. 29. Schottky barrier heights as a function of metal work function for Schottky diodes on (2̄01) bulk and (010) epitaxial β-Ga_2O_3. Schottky barrier height values on (2̄01) Ga_2O_3. The Schottky–Mott predicted line is calculated based on the Schottky–Mott model. Reprinted with permission from Yao *et al.*, J. Vac. Sci. Technol. B **35**, 03D113 (2017). Copyright, 2017 American Vacuum Society.[500]

WET ETCHING OF Ga_2O_3

There is generally a need to pattern Ga_2O_3 when fabricating devices such as UV solar blind photodetectors, various types of transistors, as well as sensors. The patterning is carried out by etching the semiconductor, using dielectric or photoresist masks to protect the active areas. There are two basic classes of etch processes, those carried out in the liquid phase (known as wet-etching) and those performed in the gas phase (called dry etching, especially when a plasma is used to provide the reactive species for etching). Etch processes may be classified by their rate, selectivity, uniformity, directionality (isotropy or anisotropy), surface quality, and reproducibility. All etching processes involve three basic events: (i) movement of the etching species to the surface to be etched, (ii) chemical reactions to form a compound that is soluble in the surrounding medium, and (iii) movement of the by-products away from the etched region, allowing fresh etchant to reach the surface. Both (i) and (iii) usually are referred to as diffusion, although convection may be present. The slowest of these processes primarily determines the etch rate, which may be diffusion or chemical-reaction limited. While not as chemically resistant as sapphire (Al_2O_3), Ga_2O_3 is still very difficult to wet etch, and there are only a few reports on wet etching of thin films and single crystal substrates.

Wet etching is performed by immersing the wafers in an appropriate solution or by spraying the wafer with the etchant solution. Wet-chemical etching is superior to dry etching in terms of effectiveness, simplicity, low cost, low damage to the wafer, high selectivity and high throughput. However, the main limitations of wet etching include its generally isotropic nature, which results in roughly equal removal of material in all directions, making it incapable of patterning sub-micron features, and the need for disposal of large amounts of corrosive and toxic materials. It is possible to achieve anisotropy with wet etching in specific cases where there is a strong dependence of the etch rate on crystal orientation, such as KOH etching of crystalline silicon. However, the inability to pattern sub-micron features and the need for a high degree of uniformity and reproducibility limit the application of wet etching for most microelectronic devices.

One of the major needs at the moment for Ga_2O_3 is the lack of high quality patterning processes that exist for the more mature semiconductors. As in materials like GaAs and GaN, etching is needed for intra-device isolation or for exposing sub-surface layers for the fabrication of Ohmic contacts. A number of wet etch solutions have been reported to work for Ga_2O_3, including HNO_3/HCl, H_2SO_4, H_3PO_4, and HF.[492,524–537] Wet etching of β-Ga_2O_3 in an HF solution can be attributed to the following reaction:[526]

$$Ga_2O_3 + 6HF \rightarrow 2GaF_3 + 3H_2O.$$

The etch rate in acids and bases strongly depends on the crystal quality. For example, in sputtered Ga_2O_3 films deposited at substrate temperatures from 400 to 1000 °C, the etching rate of gallium oxide grown at 400 °C was about 490 nm/s, while for a 1000 °C film, the etching rate was about 0.196 nm s^{-1}.[536] Table V shows a summary of the wet etch

TABLE V. Summary of wet etch results for β-Ga_2O_3.

Etch solution	Sample description	Etch rate (Å min^{-1})	Comments	Reference
H_3PO_4	Float zone (100) orientation	700 at 150 °C	85 wt. % phosphoric, no etching at 25 °C, activation energy 20.2 kCal mol^{-1}	Oshima *et al.*[528]
H_2SO_4	Float zone (100) orientation	200 at 150 °C	97 wt. % sulphuric, no etching at 25 °C, activation energy 26.3 kCal mol^{-1}	Oshima *et al.*[528]
HF	Undoped, Float zone (100) orientation	10 at 25 °C	47% HF	Ohira and Arai[527]
HF	Undoped, Float zone (001) orientation	5 at 25 °C	Rate approximately half that of (100) orientation	Ohira and Arai[527]
HF	Sputtered, with substrate temp 400–1000 °C	~2.94 × 10^5 at 25 °C (400 °C films) to 120 (1000 °C films)	49% HF	Ou *et al.*[537]
NaOH	Undoped, Float zone (100) orientation	1 at 25 °C	20% NaOH	Ohira and Arai [527]
HNO_3	Undoped, Float zone (100) orientation	14 at 120 °C	60.5% HNO_3	Ohira and Arai[527]
HCl/H_2O	MBE thin films deposited at 100 or 535 °C	~1000 for high temp films, ~8000 for low temp films	1:3 ratio of HCl:H_2O, activation energy 14.1 kCal mol^{-1}	Ren *et al.*[526]
HF	E-Beam deposited thin films grown at 40–350 °C	700–2400 depending on growth temperature	10% HF, etch rate lower for films grown at higher temperatures or annealed postgrowth	Passlack *et al.*[525]
HCl	MIST grown films	300 at 60 °C	32% HCl	Dang *et al.*[538]

rates reported for Ga_2O_3.[524–537] It is worth noting that amorphous Ga_2O_3 is a component of the native oxide on GaAs wafers, and it must be always chemically removed prior to deposition of contacts on that material.

For photoelectrochemical (PEC) etching,[492,528] both $(\bar{2}01)$ and (010) Ga_2O_3 single crystal wafers were immersed in a 5 M potassium hydroxide (KOH) solution for 30 min at a stirring rate of 300 rpm at 80–95 °C with ultraviolet illumination using a 120 W Hg lamp.[528] The photochemical etching rate in KOH solutions of $(\bar{2}01)$ oriented, n-type bulk single crystals grown by the edge-defined film-fed growth method is approximately 3–4 times higher than for the (010) planes.[492] The activation energy for etching was 0.498 eV and 0.424 eV for $(\bar{2}01)$ and (010) orientations, respectively,[492] suggesting that etching is reaction-limited with the same rate-limiting step. This energy is characteristic of that expected for the reaction-limited etching, whose other characteristics include a linear increase in the etch depth with time and an independence of the etch rate on solution agitation. SEM images of the surface morphology of the two types of samples after being etched for 120 min at 95 °C showed triangular shapes formed on the surface of the $(\bar{2}01)$ Ga_2O_3 after KOH PEC etching. By contrast, the (010) surfaces maintained flatness and smoothness after etching at a depth of approximately 10–19 nm. Thus, it is necessary to examine the difference in atomic configurations in detail for both $(\bar{2}01)$ and (010) Ga_2O_3 crystal surfaces.

It is clear that the atomic arrangement for the (010) and $(\bar{2}01)$ planes are different, leading to different atomic configurations and dangling bond densities on a particular crystal orientation. The (010) plane consist of Ga (I) atoms in the tetrahedral site and Ga(II) in the octahedral site, and O atoms in a distorted octahedral arrangement. It is notable that the respective Ga and O atoms have different numbers of dangling bonds depending on the sites of the Ga_2O_3 surface, as follows: 4-fold-coordinated Ga(I) with the number of dangling bonds of 1 and 3, 6-fold-coordinated Ga(II) with 2 and 3 dangling bonds, 3-fold-coordinated O(I) with 1 dangling bond, 3-fold-coordinated O(II) with 1 and 2 dangling bonds, and 4-fold-coordinated O(III) with 1 and 3 dangling bonds. The atomic densities can be calculated for which the parameters were determined from plots of the crystal structure. The number of dangling bonds for Ga or O can then be calculated in a similar fashion, using the number of bonds formed to each atom and the number of atoms per unit cell. For (010) Ga_2O_3, there exist 2 types of surfaces with Ga atomic density of $0.58 \times 10^{15}\,cm^{-2}$ and O of $0.87 \times 10^{15}\,cm^{-2}$. The dangling bond densities of Ga and O atoms on for both (010) surfaces are estimated to be the same: $0.58 \times 10^{15}\,cm^{-2}$ and $0.87 \times 10^{15}\,cm^{-2}$ for Ga and O atoms, respectively. For the two types of $(\bar{2}01)$ surfaces, the Ga and O atomic densities are $0.89 \times 10^{15}\,cm^{-2}$ and $1.34 \times 10^{15}\,cm^{-2}$, respectively. If the surface is terminated with O, the dangling bond densities of O are 1.78 and $2.68 \times 10^{15}\,cm^{-2}$ for type I and II, respectively. Figure 30 (top) shows an SEM image of the etched surface with Miller plane indices, while the bottom of the figure shows the crystal structure of (115), $(\bar{1}1\bar{5})$, and (010) planes of Ga_2O_3. For the etch pits observed after Pec etching, each side of the isosceles triangle with an angle of 70° was found to be (115) and $(\bar{1}1\bar{5})$ planes, and the base is (010) plane. The atomic bond configurations of the cleaved (115) and $(\bar{1}1\bar{5})$ planes demonstrate that the Ga and O atoms coexist on those planes. In the case of Ga-O coexisting surface, OH^- ions may form Ga-O compounds with Ga dangling bonds, but these are not easily soluble due to strong Ga-O bonding in the plane and the repulsive force between Ga-O bonds and OH^- ions. Consequently, wet etching may be impeded on (115), $(\bar{1}1\bar{5})$, and (010) planes in Ga_2O_3, thus resulting in chemically stable surfaces in KOH wet chemicals under UV illumination.

The number of dangling bonds on the surface is believed to control the etching behavior of the different orientations of Ga_2O_3. For example, on an oxygen-terminated surface, the oxygen atoms which exist on the surface after removing the first Ga-layer by OH^- ions have dangling bonds. In KOH-based wet etching, it was suggested that Ga atoms react with OH^- to also form Ga_2O_3, which subsequently dissolved in base solutions. In H_3PO_4-based etching, the Ga_2O_3

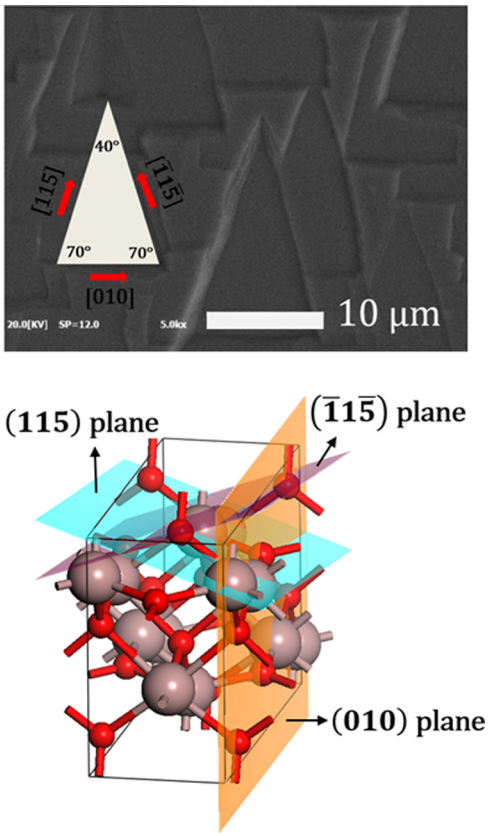

FIG. 30. (a) SEM image of the etched surface with Miller plane indices. (b) The crystal structure of (115), $(\bar{1}1\bar{5})$, and (010) planes of Ga_2O_3.

was suggested to dissolve directly in the acid solution. Clearly, in the case of Ga_2O_3, we can expect that the difference in Ga-to-O ratio and the dangling bond density on different planes will play a strong role in the PEC etching behavior. The $(\bar{2}01)$-oriented Ga_2O_3 crystal etches roughly three to four times faster under PEC conditions in KOH solutions.[492] We speculate that the higher etch rates for the $(\bar{2}01)$ Ga_2O_3 may be due to the higher density of O dangling bonds, which are exposed on the surface.[488] The O dangling bond density for the $(\bar{2}01)$ surface is 2–3 times higher than for the (010) surface. Thus, the (010) surface is more chemically stable than the $(\bar{2}01)$ surface due to low surface energy.[492]

DRY ETCHING OF Ga_2O_3

Dry etching methods are the standard for patterning small feature sizes, such as the one that occur in integrated circuit manufacturing.[538] As discussed in "Wet Etching of Ga_2O_3" section, wet etching is problematic for Ga_2O_3, and thus, dry etch processes are needed. Plasma-driven chemical reactions and/or energetic ion beams are used to remove materials in all the different dry etching techniques.[539–549] Rather than being carried out in beakers or liquid etch baths as is the case for wet etching, a dry etch system is comprised of a stainless steel or aluminum vacuum chamber that can be fitted with endpoint detection tools and vacuum load locks to ensure reproducible conditions. Dry etching includes gas processes where neutral atoms are the etching species, such as the removal of photoresist using oxygen atoms, etching of aluminum in Cl_2 gas (when there is no native oxide to inhibit the etching), or etching of Si using a fluorinated gas such as XeF_2. By far the most important advantage of dry etching over wet etching is that it provides a higher resolution transfer of a pattern by having anisotropic removal rates of the exposed material, i.e., it etches much faster in the vertical direction than in the lateral direction.[538] Dry etching also generally has less chemical waste (although the exhaust gases must be scrubbed). As discussed earlier, for manufacturing of microelectronics, the processing must be automated and have very controlled and reproducible conditions.[538] This is much easier to achieve with dry etching as the patterning technique.

For strongly bonded materials like Ga_2O_3, the so-called high-density plasma etch techniques are preferred. The techniques vary in the plasma source they employ.[538] These different variants include electron cyclotron resonance (ECR) which operates at microwave frequencies (2.45 GHz), and inductively coupled plasma (ICP) and magnetron RIE (MRIE), which operate at rf frequencies (2–13.56 MHz). These techniques are generally flexible enough in terms of the higher ion and reactive neutral densities they produce relative to RIE, that they are favored in most critical etch applications in the industry. The plasma densities are 2–4 orders of magnitude higher than RIE, thus improving the bond breaking efficiency in the semiconductor being etched, while the increased ion density also enhances the desorption of etch products formed on the surface. Additionally, since the ion energy and the ion density can be more effectively decoupled as compared to RIE, the plasma-induced damage is more readily controlled and minimized.

ICP has become the standard high density plasma etching variant platform for patterning semiconductors. ICP plasmas are formed in a vacuum chamber encircled by an inductive coil into which rf power is applied at frequencies of 2–13.56 MHz to couple through a dielectric window. The alternating electric field between the coils induces a strong alternating magnetic field, which acts to trap electrons in the center of the chamber and generates a high-density plasma. Since ion energy and plasma density can be effectively decoupled, uniform ion density and energy distributions are transferred to the sample while keeping ion and electron energies low to minimize the surface damage. Thus, ICP etching can produce low damage while maintaining fast etch rates. Anisotropy is achieved by superimposing of rf bias on the sample.

Studies of dry etching of Ga_2O_3 are still in their infancy and there is much to establish,[539–543] including the appropriate gas chemistries to employ, the etch mechanisms, and the effects of the plasma exposure on the near-surface electrical and optical properties of the Ga_2O_3.[547–549] The high bond strength of β-Ga_2O_3 suggests that ion-assisted etching will be the likely mechanism needed to achieve practical etch rates. We can enhance this using the Ar added to the chlorinated gases. There are a number of things that can occur in this near-surface region, including a change in stoichiometry relative to the bulk, the displacement of lattice atoms by ion bombardment from the plasma, and the presence of etch residues consisting of the reactive species from the plasma

TABLE VI. Summary of dry etch results for β-Ga_2O_3.

Plasma chemistry	Ga_2O_3 samples	Plasma source/frequency	Maximum etch rate (Å min^{-1})	Comments	Reference
SF_6/Ar	Thin film (MOCVD)	ICP/2 MHz	350	Chemical enhancement over pure Ar	Liang *et al.*[541]
Cl_2/BCl_3	Bulk EFG	RIE/13.56 MHz	120	Faster rates for (010) and (−201) relative to (100)	Hogan *et al.*[542]
BCl_3, BCl_3/SF_6, CF_4/O_2	Bulk EFG	ICP/13.56 MHz	450	BCl_3 produced fastest rates	Hogan *et al.*[542]
BCl_3/Ar	Bulk (−201) EFG	ICP/2 MHz	1600	Almost vertical sidewalls	Zhang *et al.*[543]
O_2/Ar, SF_6/Ar, CHF_3/Ar, BCl_3/Cl_2, Cl_2/Ar, BCl_3/Ar	Bulk (−201) EFG	ICP/13.56 MHx	1440	Only BCl_3/Ar showed some selectivity to SiN_X masks. No temperature dependence of etch rate up to 210 °C	Shah and Bhattacharya[540]
SF_6	Bulk EFG	RIE/13.56 MHz	160	Used for thinning of exfoliated quasi-2D flakes	Kwon *et al.*[549]
BCl_3/Ar	Bulk (−201) EFG	ICP/2MHz	800	Damage study-barrier height decreased by 28% and ideality factor increased after etch	Yang *et al.*[548]
Cl_2/Ar, BCl_3Ar	Bulk (−201) EFG	ICP/2 MHz with different frequency chuck biasing (13.56 or 40 MHz)	1300	Surfaces become oxygen-deficient under high power conditions	Yang *et al.*[544]
BCl_3/Ar	Bulk (−201) EFG	ICP/2 MHz, with 13.56 MHz chuck biasing	700	Annealing study-450 °C anneals found to restore barrier height after etching	Yang *et al.*[550]

attached to the dangling surface bonds or lattice atoms. A summary of the reported etch rates and damage characteristics is shown in Table VI. Notable amongst these studies are those of Hogan *et al.*,[541] who measured GaO_3 etch rates in plasmas of Cl_2/BCl_3 under RIE conditions and plasmas of BCl_3, BCl_3/SF_6, and CF_4/O_2 under inductively coupled plasma (ICP) conditions. Compared to the removal rates achieved with other oxides such as ZnO, the etch rates achieved for Ga_2O_3 were lower and the etched surfaces has poorer morphology. Shah and Bhattacharya[539] found that there was basically no temperature dependence of the etch rate in plasmas of BCl_3/Ar or Cl_2/Ar under ICP conditions up to 200 °C. In general, the plasma-induced damage in Ga_2O_3 is of n-type character and thus will increase the conductivity of the etched surface. This can be employed to improve the properties of n-type Ohmic contacts. This same process was used to enhance the Ohmic contact behavior in lightly n-type GaN.[538,544]

Figure 31 (top) shows SEM micrographs of features etched into the bulk Ga_2O_3 using a Cl_2/Ar discharge and a SiO_2 mask, which is still in place on the sample. The etching in this case used a high ICP power (800 W) and a moderate rf power (150 W). There is some sidewall roughness, which is replicated from the initial photoresist used for patterning the SiO_2 mask and the morphology on the etched field is somewhat rough. Figure 31 (bottom) shows similar micrographs, this time using BCl_3/Ar, which leads to a smoother morphology, perhaps because of the ability of the BCl_3 to remove the native oxide effectively. When using Cl_2, the native oxide will be removed in a slower, less uniform manner, leading to variations when the actual etching commences and hence a rougher morphology.

Shah and Bhattarcharya[539] also examined the etching of β-Ga_2O_3 (−201) substrates using ICP-RIE. Fluorine-based plasmas produced low etch rates for Ga_2O_3, as expected since GaF_3 has a low vapor pressure and is not volatile enough to produce fast removal rates. Much higher etch rates

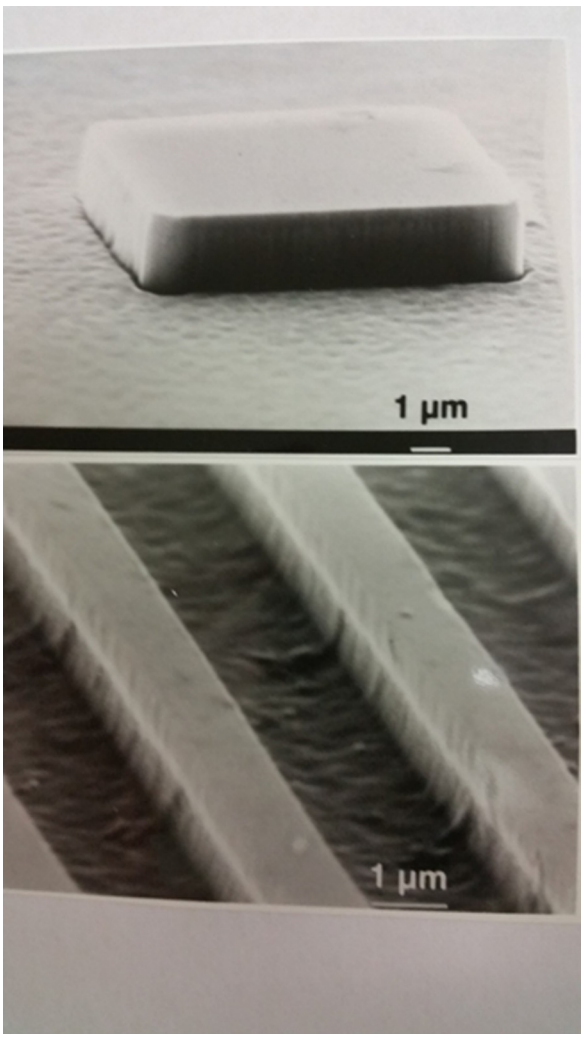

FIG. 31. SEM micrographs of bulk Ga_2O_3 dry etched in an ICP discharge of Cl_2/Ar using a SiO_2 mask, which is still in place. The image at the top shows the anisotropic nature of the etching, while the image at the bottom shows the surface morphology after an etch depth of over 2 μm. The etching in this case used high ICP power (800 W) and moderate rf power (150 W).

were obtained using chlorine-based plasmas.[539] The study looked at the effect of varying the Cl_2/BCl_3 gas content and also the temperature-dependence in the range of 22–205 °C, which is above the sublimation temperature of $GaCl_3$.[539] Despite the chemical similarity between Ga_2O_3 and GaN, the trends for Ga_2O_3 were significantly different from GaN. This was ascribed to the fact that GaN etching in Cl_2/Ar is due to the formation of $GaCl_3$, which has a significant vapor pressure and leads to high removal rates.[539] By contrast, it was suggested that the etching of Ga_2O_3 is limited by the reaction of BCl_2^+ ions from the BCl_3/Ar plasma and then removing oxygen from the Ga_2O_3 substrate to form volatile $B_3Cl_3O_3$ and nonvolatile B_2O_3, with the latter removed by physical sputtering by positive ions incident on the surface.[539] It must be emphasized that these possible reaction products were not directly observed and additional studies are needed to conclusively establish the etch mechanism and products. As seen in Table VI, the BCl_3-based discharges produce higher etch rates than Cl_2-based. A possible explanation is that BCl_3 reacts with the oxygen in the Ga_2O_3, while at the same time, the BCl_2^+ions provide ion-enhanced sputtering. By contrast, in Cl_2-based discharges, the atomic and molecular chlorine species do not have the same ability to remove oxygen.

In terms of electrical effects to the surface as a result of dry etching, Fig. 32 shows the reverse I-V characteristics of diodes fabricated on the etched surfaces using either 40 MHz (top) or 13.56 MHz (bottom) rf chuck biases with different ICP powers and etch times, all with BCl_3/Ar discharges.[549] The reference diodes that were not exposed to the plasma exhibited reverse breakdown voltages of approximately 50 V. In the diodes exposed to the plasma, the reverse breakdown voltage was significantly reduced as a result of both ion-induced damage and non-stoichiometry induced in the surface. The extent of this degradation depended on the self-bias. This controls the incident ion energy and hence the density of point defects created by the impinging ions. The damage induced by plasma exposure could be essentially completely removed by annealing at 450 °C. Photoluminescence (PL) is a non-destructive method for monitoring changes to the near-surface region after plasma processing. If a large concentration of non-radiative centers is introduced by the plasma exposure, this would be expected to decrease the overall PL intensity. We did not observe a significant change in the total intensity from the surface after introduction of the etch damage, as shown in Fig. 33. Based on a comparison of these spectra with the literature, we assign the transitions as due to an O defect donor band to the valence band ($E_{DB} = 3.411$ eV) and to the Ga vacancy band ($E_{D2} = 3.002$ eV to $E_{D3} = 2.39$ eV).

In summary, Ga_2O_3 can be etched at practical rates using chlorine-based plasma chemistries, especially under high ion density conditions such as ICP discharges. Due to the high bond strengths, the rates are lower than for other electronic oxides like ZnO where the same plasma conditions produce etch rates of a factor of two higher than for Ga_2O_3. Schottky barrier height measurements reveal the presence of ion-induced damage that can be effectively removed by annealing at 450 °C. There is a little change in the optical properties of stoichiometry of the etched surface.

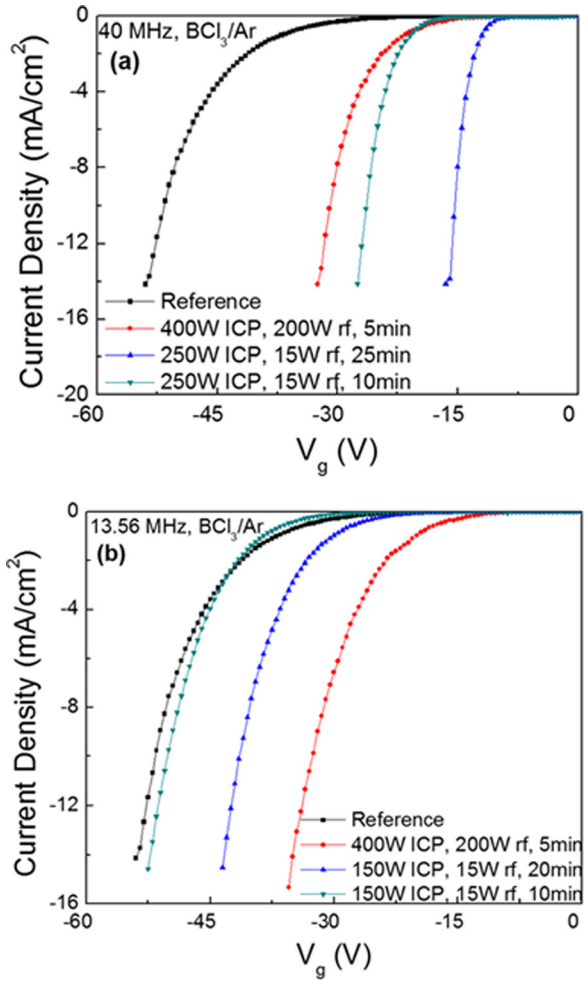

FIG. 32. Reverse I-V characteristics of diodes fabricated on the etched surfaces using either the 40 MHz (top) or 13.56 (bottom) rf chuck biasing conditions with BCl_3/Ar discharges. Reprinted with permission from Yang *et al.*, J. Vac. Sci. Technol. B **35**, 031205 (2017). Copyright 2017 American Vacuum Society.[544]

BAND ALIGNMENTS OF DIELECTRICS ON (−201) Ga_2O_3

There are three main criteria that a gate dielectric must possess to be considered acceptable.[550–552] First, it must be

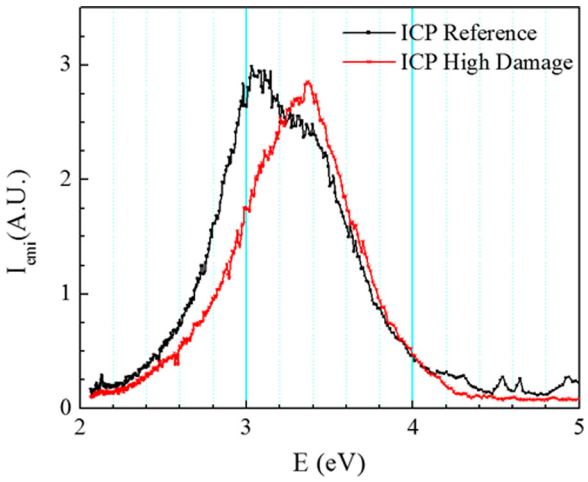

FIG. 33. 10 K PL spectra from reference and plasma damaged Ga_2O_3.

thermodynamically stable with the semiconductor and not react during processing. Second, it must provide a high quality interface with low defect and trap density to ensure high carrier mobility. Finally, it must act as a barrier to both electrons and holes which is among the most important physical parameters for a given heterojunction system. Because these discontinuities can form a barrier for carrier transport across the interface, the knowledge of these quantities is essential for calculating the transport properties of the interface, or the electrostatic potential in a heterojunction device. There are three types of band alignments: type I, type II staggered, and type III broken gap.[550–555]

Numerous experimental methods are used to determine the oxide/semiconductor band alignment. These include external photoemission spectroscopy,[555–558] internal photoemission spectroscopy,[555–557] and x-ray photoelectron spectroscopy (XPS) core-level based method.[553] The method of Kraut *et al.*[553] using x-ray photoemission spectroscopy has been established as a reliable way to determine band offsets at the hetero-junction interface. This method has also been successfully used to provide insights into interfacial properties between different materials.[553,559] It is based on using an appropriate shallow core-level position as a reference. Generally, this approach is based on the assumption that the energy difference between the core-level positions and valence-band maximum (VBM) are both fixed in the bulk.

The basic method, shown in Fig. 34, is to first measure the energy difference between a core level and the VBM for both single layer dielectric and semiconductor of interest.[553,559] One measures the reference core level binding energies in thick films of each material and then measures the binding energy difference between the two reference

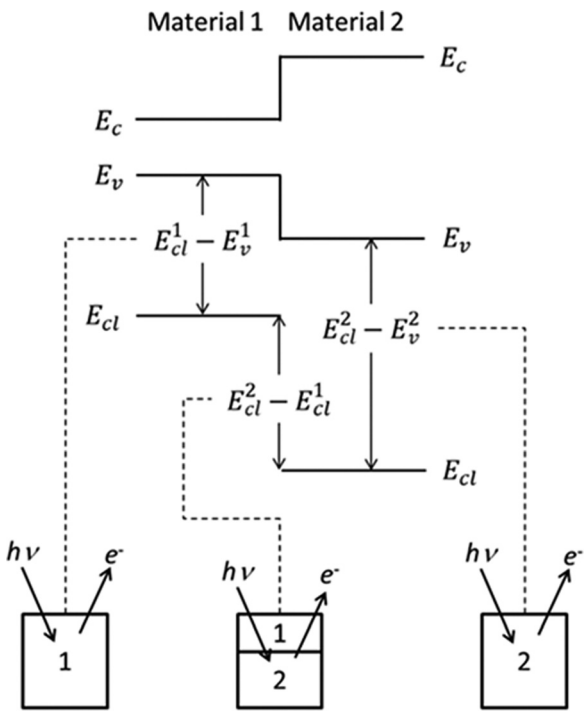

FIG. 34. A schematic energy band diagram illustrating the basic principle of XPS band offset measurements. Reprinted with permission from Appl. Phys. Rev. **4**, 021301 (2017). Copyright 2017 American Institute of Physics.[560]

core levels in the heterojunction. The determination of ΔEv comes by combining those three quantities. Heterojunction samples, consisting of a thin (1–2 nm) layer of dielectric deposited on the semiconductor, are prepared in which the separation between reference core levels in each material is measured. The separation between the reference core levels can be translated directly into a value for the valence band offset (VBO) using the previously measured single layer sample core-level to VBM energies by the following relationship:[553]

$$\Delta E_V = \left(E^1_{core} - E^1_{VBM}\right)_{IGZO} - \left(E^2_{core} - E^2_{VBM}\right)_{Dielectric} - \left(E^{\,1}_{core} - E^2_{core}\right)_{Heterostructure}$$

To determine the conduction band offset, it is necessary to measure the band gap of each material. The samples are measured via UV/Vis or REELS, and the conduction band offset is calculated as follows:

$$\Delta E_C = E_g^{dielectric} - E_g^{IGZO} - \Delta E_V.$$

From these values, it is then possible to construct the flat band diagram and determine if this is a type I, II, or III heterostructure.[555,557]

Table VII contains a list of reported band offsets obtained for different dielectrics deposited by different methods on Ga_2O_3.[560–573] Figure 35 shows a summary of the measured band offsets for different dielectrics on Ga_2O_3.[560–573] This shows that there are a limited number of choices that are appropriate for gate dielectrics on Ga_2O_3, where it is desirable that there be adequate conduction and valence band offsets. These include SiO_2 and Al_2O_3. However, the other films could still be an option as a surface passivation layers on Ga_2O_3 to prevent surface conductivity changes upon exposure to ambient. The sensitivity of Ga_2O_3 to water vapor and hydrogen is not yet firmly established, but many oxides like ZnO and $InGaZnO_4$ do show such sensitivity and require surface passivation to provide device stability in humid ambients. The other thing to note from Fig. 35 is the fact that there is a difference in band offsets reported by different groups for nominally the same types of films. Some of the reasons include metal contamination, interface disorder, dielectric composition, carbon/hydrogen contamination, annealing, stress/strain, and surface termination.[557] The presence of these effects can result in differences in the bandgap of the dielectric and this affects the conduction band offset since the valence band offset is directly measured. However, the latter can also be affected by most of these same issues. For example, sputtered films are more likely to contain metallic contaminants and have interfacial disorder due to the sputter-induced damage and therefore have possible Fermi level pinning effects than a more controlled process such as ALD. Interfacial defects, such as oxygen or metal atom vacancies, may have a pronounced effect on the band offsets. The literature shows that energy band alignment variations of sometimes more than 1 eV depending on interface preparation can be obtained,[557] due to the presence of high defect concentrations in the

TABLE VII. Reported values for band offsets for different materials on Ga_2O_3.

Dielectric material (crystalline nature of Ga_2O_3)	Synthesis method	ΔE_C (eV)	ΔE_V (eV)	Alignment type	Reference
SiO_2 (single crystal)	PECVD	3.1(±0.2)	1.0(±0.2)	I	Konishi *et al.*[567]
SiO_2 (single crystal)	ALD	3.63–3.76	0.3-0.43	I	Jia *et al.*[568]
SiO_2 (single crystal)	ALD	2.9 (±0.7)	1.2 (±0.2)	I	Carey *et al.*[565]
Al_2O_3	ALD	1.5–1.6(±0.2)	0.7(±0.2)	I	Kamimura *et al.*[569]
γAl_2O_3 (single crystal)	PLD	1.9	0.5	I	Hattori *et al.*[570]
Al_2O_3(single crystal)	ALD	2.23(±0.2)	0.07(±0.2)	I	Carey *et al.*[564]
Al_2O_3(single crystal)	PVD	3.16(±0.2)	−0.86(±0.2)	II	Carey *et al.*[559]
$LaAl_2O_3$(single crystal)	PVD	2.01(±0.60)	−0.21 (±0. 02)	II	Carey *et al.*[563]
Si(amorphous)	PLD	−0.2(±0.1)	−3.5(±0.1)	I	Chen *et al.*[571]
GaN(polycrystalline)	oxidation	−0.1(±0.08)	−1.4(±0.08)	I	Wei *et al.*[572]
6H-SiC(amorphous)	PVD	0.89(±0.1)	−2.8(±0.1)	II	Chang *et al.*[573]
ZrO_2 (single crystal)	ALD	1.2	−0.3(±0.04)	II	Wheeler *et al.*[574]
HfO_2(single crystal)	ALD	1.3	−0.5(±0.04)	II	Wheeler *et al.*[574]
$HfSiO_4$ (single crystal)	ALD	2.38 (±0.5)	0.02 (±0.003)	I	Carey *et al.*[565]
AZO (single crystal)	PVD	−0.79(±0.34)	−0.61(±0.023)	I	Carey *et al.*[561]
ITO (single crystal)	PVD	−0.32(±0.34)	−0.78(±0.34)	I	Carey *et al.*[558]
AlN(single crystal)	PLD	1.75(±0.05)	−0.55(±0.05)	II	Sun *et al.*[756]

materials and on a cation effect that will increase the VBM of that material.

RADIATION DAMAGE IN Ga_2O_3

The strong bonding in a wide bandgap semiconductor gives them an intrinsically high radiation resistance.[321,574–593] The fluence of ionizing radiation at which materials and devices such as transistors and light-emitting diodes made from SiC, GaN, and related materials start to show degradation is about two orders of magnitude higher than in their GaAs equivalents.[574–579] This difference is attributed to the stronger bonding of these materials.[574–582] A measure of this bond strength is the energy required to displace an atom from its lattice position or simply the atomic displacement energy, denoted by E_d. This parameter has been measured in several semiconductors and empirically

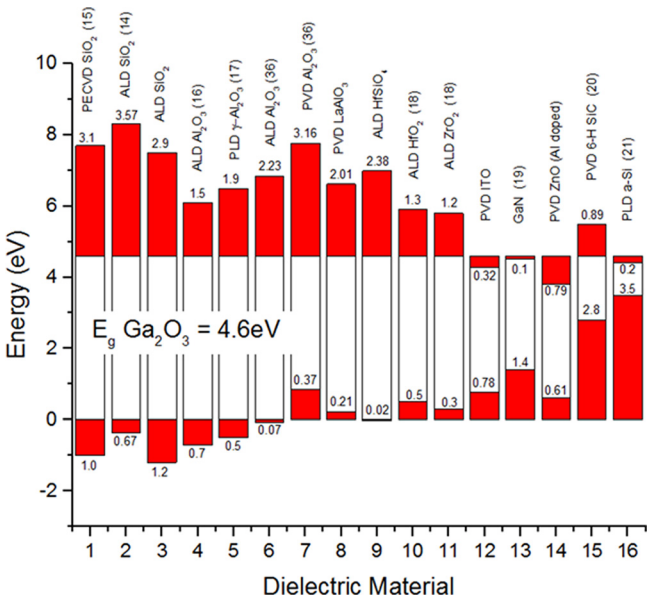

FIG. 35. Summary of reported band offsets for dielectrics on Ga_2O_3.

determined to be inversely proportional to the volume of the unit cell. This generally scales with bandgap, so that these materials have intrinsically higher radiation resistance than Si. Similarly, wide bandgap devices generally employ higher critical fields and smaller active volumes that reduce radiation-induced charge collection. Tsao *et al.*[321] summarized the fact that there are four basic kinds of semiconductor device radiation effects, including total ionizing dose that results in charge accumulation in field oxides in MOS-based devices. This results in the well-known shifts in the threshold voltage, but since most wide-bandgap transistors use Schottky metal gates, this is less of an issue. There are also single event upset effects that result from the transit of energetic ions passing through the semiconductor, creating electron-hole pairs. Again, the device structures employed in wide bandgap semiconductors, involving heterostructures, tend to mitigate this effect. The same applies to the dose-rate radiation effects, which are sensitive to the total volume of a device. The last issue is lattice displacements that typically create traps and recombination sites in the device that degrade the carrier density through trapping and the carrier mobility, with both of these mechanisms scaling with the radiation dose. Si MOSFETs also suffer from single-event burnout when the charge from an energetic ion creates sustained conduction of the parasitic bipolar transistor inherent in Si MOSFETs that leads to thermal degradation and single-event rupture when charge build-up near the gate causes a breakdown in the gate oxide.[321]

Ga_2O_3 has been investigated as a radiation detection material for fast (14 MeV) neutrons,[588] utilizing the $^{16}O(n,\alpha)^{13}C$ reaction. Both diamond and 4H-SiC have previously been used as nuclear detectors under extreme conditions, including temperature up to 700 °C for 4H-SiC and 200 °C for diamond.[588] Pt Schottky diodes of conducting Ga_2O_3 with rear Ti/Au ohmic contacts or insulating samples with Ti/Au ohmic contacts on both sides were examined. The latter could be operated up to 1000 V.[588] Neutrons could be

detected under these conditions.[584] Wong *et al.*[589] examined the gamma-ray irradiation tolerance of Ga_2O_3 MOSFETs to doses of 230 kGy(SiO_2). Hysteresis in the transfer characteristics was negligible after exposure to the highest dose, while degradations in the gate oxide were found to limit the overall radiation resistance.[593] Initial DLTS measurements on neutron-irradiated samples show the introduction of a level near E_C–1.88 eV, whose microstructure is unknown.[515]

Yang *et al.*[589] subjected vertical rectifiers fabricated on epi Ga_2O_3 on bulk β-Ga_2O_3 to 1.5 MeV electron irradiation at fluences from 1.79×10^{15} to 1.43×10^{16} cm^{-2}. The electron irradiation caused a reduction in carrier concentration in the Ga_2O_3, with a carrier removal rate of 4.9 cm^{-1}. Figure 36 (top) shows that the 2kT region of the forward current-voltage characteristics increased due to electron-induced damage, with more than 2 orders of magnitude increase in the on-state resistance at the highest fluence. There was a reduction in the reverse current, which scaled with electron fluence. The on/off ratio at −10 V reverse bias voltage was severely degraded by electron irradiation, decreasing from approximately 10^7 in the reference diodes to approximately 2×10^4 for the 1.43×10^{16} cm^{-2} fluence. The reverse recovery characteristics showed little change even at the highest fluence, with the values in the range of 21–25 ns for all rectifiers. The changes in device characteristics were accompanied by a decrease in electron diffusion length from 325 to 240 μm at 300 K, as shown at the bottom of Fig. 36.

Proton damage in back-gated field-effect transistors (FETs) fabricated on exfoliated quasi-two-dimensional β-Ga_2O_3 nanobelts were studied by exposure to 10-MeV protons.[594] The proton dose and time-dependent characteristics of radiation damaged FETs showed a decrease of 73% in the field-effect mobility and a positive shift of the threshold voltage after proton irradiation at a fluence of 2×10^{15} cm^{-2}, which corresponds to approximately 10^5 times the intensity of a solar proton event. The on/off ratio of the exfoliated β-Ga_2O_3 FETs was maintained even after proton doses of up to 2×10^{15} cm^{-2}. The data are summarized in the drain-source characteristics of Fig. 37, which show the effect of proton dose.[594] The radiation-induced damage in β-Ga_2O_3-based FETs was significantly recovered after rapid thermal annealing at 500 °C.[594] It will be interesting to compare the results from nanobelt transistors with more conventional devices fabricated on bulk or epi Ga_2O_3.

To summarize, the initial data on proton, electron, neutron, and gamma irradiation of photodetectors and transistors show fairly similar radiation resistance to GaN devices under the same conditions.

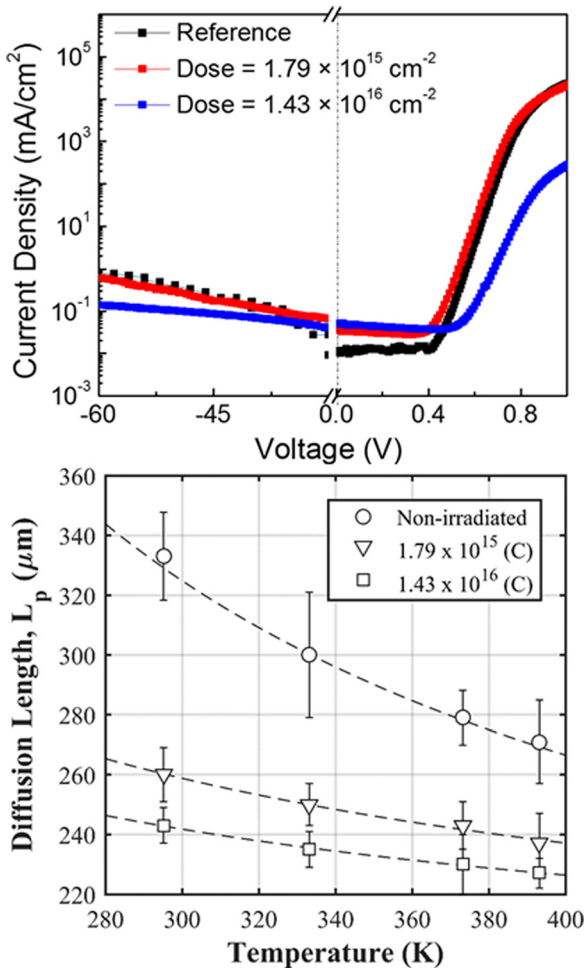

FIG. 36. (a) I-Vs from Ga_2O_3 diodes before and after 1.5 MeV electron irradiation to different doses; (b) diffusion length of electrons as a function of temperature after different electron irradiation doses.

THIN FILM SOLAR-BLIND UV DETECTORS

One of the most promising applications for β-Ga_2O_3 is for deep UV solar blind detectors (cut-off wavelength shorter than 280 nm). These detectors only sense radiation with wavelength shorter than 280 nm while being insensitive to visible and infra-red radiation. Few photons in this wavelength region reach the Earth's surface from the sun due to strong absorption by the stratospheric ozone layer, and thus,

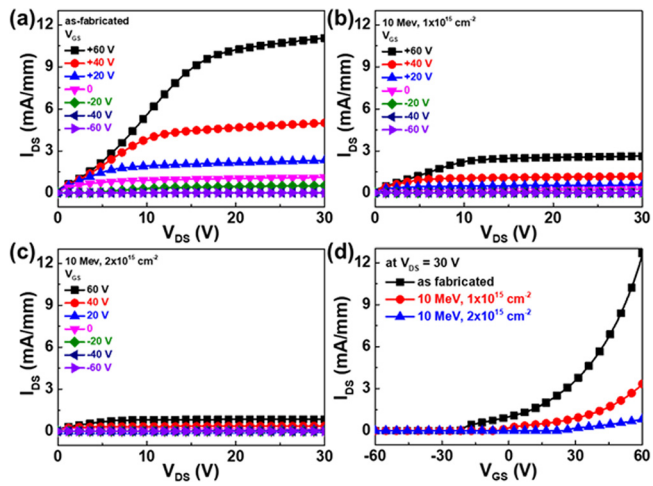

FIG. 37. Output characteristics (I_{DS} vs. V_{DS}) of β-Ga_2O_3 nanobelt FET before and after 10-MeV proton irradiation at different doses: (a) as-fabricated, (b) 1×10^{15} cm^{-2}, and (c) 2×10^{15} cm^{-2}, and (d) transfer characteristics (I_{DS} vs. V_{GS}) of β-Ga_2O_3 nanobelt FET at $V_{DS} = 30$ V before and after 10-MeV proton irradiation at different doses. Reprinted with permission from Yang *et al.*, ACS Appl. Mater. Interfaces **9**, 40471 (2017). Copyright 2017, American Chemical Society.[595]

these devices' photodetectors can respond to a very weak signal even in sunlight or room illumination. These photodetectors have a large number of applications including flame detection, missile guidance systems, underwater communications, photolithography, automatization, intersatellite communication, and biochemical detection.[321,595–629] β-Ga_2O_3 has a cut-off wavelength in the range of 250–280 nm, which leads to detection over the full range of deep ultra-violet (DUV). In addition, the high chemical and thermal stabilities of this material are attractive for applications involving high temperatures or extreme environments. High performance photodetectors based on nanostructure, thin-film, and bulk Ga_2O_3 have been reported. Different device structures, including photoconductors, metal-semiconductor-metal (MSM) or metal-intrinsic-semiconductor-metal photodetectors, avalanche photodiodes, and Schottky barrier photodiodes, have been reported.[623] Among these, MSM structures, which consist of back-to-back Schottky contacts, are simple to fabricate and have low dark currents.

Pratiyush *et al.*[595] reported MBE grown epitaxial β-Ga_2O_3-based solar blind metal-semiconductor-metal (MSM) photodetectors fabricated on (−201) β-Ga_2O_3 films grown using plasma-assisted MBE on c-plane sapphire. MSM geometry devices were fabricated using Ni/Au contacts in an interdigitated geometry. The photodetectors exhibited peak SR > 1.5 A/W at 236–240 nm at a bias of 4 V with a UV to visible rejection ratio > 10^5. The devices had low dark current (< 10 nA at 20 V) with no persistent photoconductivity and a large photo-to-dark current ratio > 10^3. Figure 38 (Ref. 595) illustrates both the steady-state photo, dark I-V characteristics, and time-dependent photo-response at a bias of 20 V after passivation with 20 nm of ALD Al_2O_3. This was an important step in optimizing performance.[595] The photo currents in the steady-state and transient measurements were found to be similar, which are ∼4.6 μA (at 20 V), while the dark current was observed to be in the ∼nA range. Both the photo and the dark current decreased slightly after the passivation of the devices. Yu *et al.* reported similar results using PLD films,[601] showing that the thin film deposition method appears to be less critical for photodetectors than other devices such as rectifiers and transistors, although higher UV to visible rejection ratio is generally obtained with better crystal quality. Hybrid structures, including graphene, Si, BN, ZnO, SiC, Au nanoparticles, SnO_2, and GaN, have also been reported.[602,603,607,623,625] In particular, lower dark current, higher photoresponse, and faster switching time under 254 nm light illumination were obtained by introducing Au nanoparticles.[626] The improved performance has been ascribed to localized surface plasmonic resonance from the nanoparticles.[622] Lu *et al.*[615] showed that higher partial pressures of oxygen (PO_2) in PA-MBE improved the crystal quality, surface morphology, and the chemical performance of the photodetectors, which exhibited the significantly improved photocurrent and responsivity characteristics in comparison with devices grown with lower PO_2 of 0.01 mbar. This was attributed to a reduction in the number of oxygen vacancies.[611] A similar result was found by An *et al.*,[607] and Feng *et al.*[608] reported better performance of thin film photodetectors on bulk Ga_2O_3 relative to sapphire substrates because of a lower defect density.

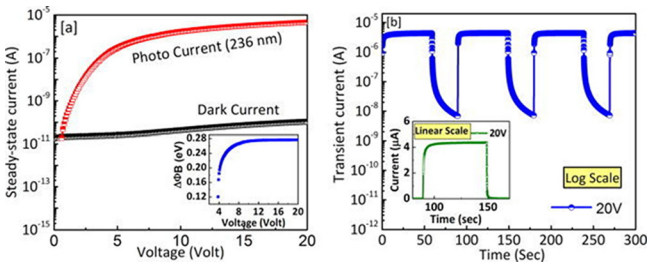

FIG. 38. (a) Steady-state photo and dark I-V characteristics at room temperature after passivation (log scale). (b) Time-dependent photo-response under 236 nm illumination at 20 V (log scale). The inset of (a) shows Schottky barrier lowering variation with the bias voltage. The inset of (b) shows rescaled transient at 20 V (linear scale). Reprinted with permission from Appl. Phys. Lett. **110**, 221107 (2017). Copyright 2017 American Institute of Physics.[596]

The photodetection mode has also been investigated. Qian *et al.*[624] employed a four-terminal photodetector fabricated on β-Ga_2O_3 deposited by PA-MBE. A dark/photo voltage ratio of 15 was achieved, comparable to interdigitated MSM structures. The aperture ratio was >80%, roughly double that of MSM structures. The dark/photo voltage ratio was nearly trebled with use of two Zener diodes.[624]

There has been particular interest in fabricating photodetectors on β-Ga_2O_3 nanobelts exfoliated from bulk substrates because of the high surface-to-volume ratio, low power requirement, and flexibility in transferring to other substrates. Oh *et al.*[620,622] employed β-Ga_2O_3 micro-flakes exfoliated from single crystalline β-Ga_2O_3 using a mechanical exfoliation method by an adhesive tape, similar to mechanical exfoliation of highly oriented pyrolytic graphite to obtain graphene. The exfoliated β-Ga_2O_3 micro-flakes were then transferred onto a Si substrate with a thermally grown 300 nm-thick SiO_2 layer, which was followed by a conventional photolithography process to form a MSM configuration. Figure 39 shows a plot of $(\alpha h\nu)^2$ vs. photon energy, with the inset showing the UV-VIS absorbance of the bulk β-Ga_2O_3 from which the exfoliated flake was taken; (b) Raman spectrum of the exfoliated β-Ga_2O_3 micro-flake; and (c) cross-sectional TEM image of the fabricated β-Ga_2O_3.[622] The dark current was in the pA range, the ratio of photo-to-dark current was > 10^3, responsivity of 1.68 A/W, the 254 nm/365 nm rejection ratio was 1.92×10^3, and no persistent photoconductivity was observed.[622] Oh *et al.*[620] further reported nanobelt photodetectors with responsivities under illumination to 254 nm light of 9.17×10^4 A W^{-1}, 1.67×10^5 A W^{-1}, and 1.8×10^5 A W^{-1} at V_{GS} of 0 V, −15 V, and −30 V, respectively. They suggested that the performance can be further improved by minimizing β-Ga_2O_3 defects through optimizing the fabrication process and increasing the size of the active region to absorb photons, thus reducing the high dark current that is a drawback for such photoconductors.[620] Notably, Oh *et al.*[627] also employed implantation of Si to improve the contact resistance of Ohmic contacts on their thin film photodetector structures grown by MOCVD. Si ions were implanted at 30 keV energy at a dose of 1×10^{15} cm^{-2} and post-implantation annealing to activate the implanted Si atoms was performed under Ar ambient at 900 °C by rapid thermal

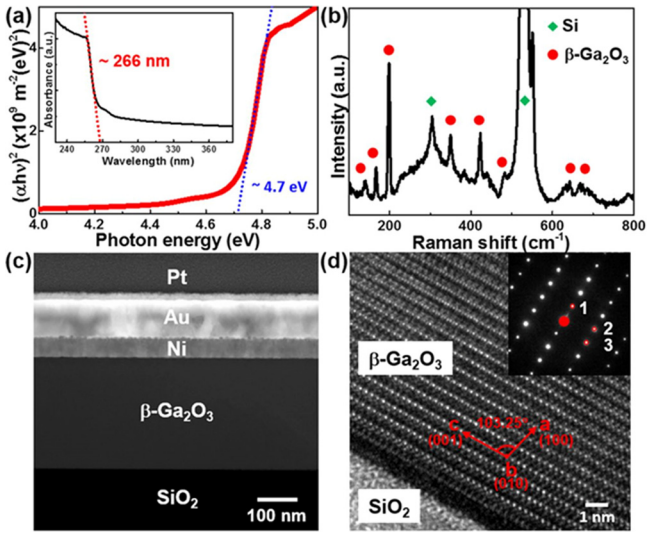

FIG. 39. (a) Plot of $(\alpha h\nu)^2$ vs. photon energy, with the inset showing the UV-VIS absorbance of the bulk β-Ga_2O_3 sample; (b) Raman spectrum of the exfoliated β-Ga_2O_3 micro-flake; (c) cross-sectional TEM image of the fabricated β-Ga_2O_3. Reprinted with permission from Oh *et al*. ECS J. Solid State Sci. Technol. **6**, Q79 (2017). Copyright 2017 The Electrochemical Society.[623]

annealing.[627] The R_S was 164.1 kΩ/□, while the electrical activation efficiency of Si atoms implanted into Ga_2O_3 films was reported to be approximately 75%.[627]

POWER RECTIFIERS

The development of high power electronics capable of operating at elevated temperatures without the need for extensive system cooling requirements is attractive in many industrial and, in particular, military applications. The cost of the electronics components in radar, communication, and guided missile systems is a significant fraction (typically 20%–30%) of the total cost of these systems, leading to the strong support from military agencies in the past to develop GaAs and GaN electronics.[322]

As shown in Table II, the figures of merit for power applications scale with bandgap, and therefore, Ga_2O_3 will have advantages over both SiC and GaN with their smaller bandgaps.[321] Wide bandgap semiconductor power Schottky diodes have numerous advantages over more conventional Si rectifiers, achieving a maximum electric field breakdown strength over 10 times larger and on-state resistance (R_{ON}) more than four hundred times lower at a given voltage.[630–640] These characteristics have made SiC and GaN devices attractive for hybrid electric vehicles and power conditioning in large industrial motors. In particular, Schottky rectifiers are attractive because of their fast switching speed, which is important for improving the efficiency of inductive motor controllers and power supplies. Both GaN and SiC power Schottky diodes have demonstrated shorter turn-on delays than Si devices.[630–640] The advantage of simple Schottky rectifiers over p-n diodes is the shorter switching times due to the absence of minority carriers. This, however, leads to higher Ron values than in p-i-n rectifiers.

Currently, power rectifiers are made from SiC for very large breakdown voltages because of the availability of thick drift layers grown by the established epi methods.[638–640] GaN is preferred for 1 kV range devices because of the lower on-state resistance. Many of the figures-of-merit for device performance in Table II scale with increasing bandgap in a highly non-linear manner, so Ga_2O_3 has the potential for performance far superior to that of SiC and GaN. For a low-frequency unipolar vertical power switch, the Baliga figure of merit (BFOM)[321] is defined as V^2_{BR}/R_{ON}, where V_{BR} is the maximum voltage that the switch can block when it is off, and R_{ON} is the specific on-resistance (the inverse of the conductance per unit area when the switch is on).[321,322] The Johnson FOM relates the high frequency and high voltage capability of a device. The rectifiers should have low on-resistance while having very high blocking voltages in the off state. The critical electric field in semiconductors scales approximately as the square of the bandgap. More precisely, a generally accepted empirical relationship between the breakdown field ε_c and bandgap (E_g) is $\varepsilon_c = (Eg)^n$, where n is between 2 and 2.5. This means that the BFOM scales approximately as the sixth power of bandgap.[321,639,640] Figure 40 shows how the wider bandgap really improves the rectifier performance, with lower on-state resistance at a given reverse voltage.[319] However, this applied to the case of low defect material, where the performance is not limited by defect-assisted breakdown. In the presence of defect such as screw dislocations, nanopipes, or voids, it has been demonstrated that premature breakdown occurs in both GaN and SiC.[627,628] Especially in GaN rectifiers, the reverse breakdown voltage increases dramatically as the contact size is decreased and is also much larger for vertically depleting devices.[627,629] Note that both SiC and GaN rectifiers are at a commercialized stage. Figure 41 shows the current state of the art for commercial SiC and GaN devices,[639] which have reached an impressive level of maturity.

There have been a large number of recent reports on Ga_2O_3-based rectifiers.[641–661] The device structures for the most part have been relatively simple. For example, these rectifiers show performance limited by the presence of defects and by breakdown initiated in the depletion region near the electrode corners.[641,646,647] In SiC and GaN

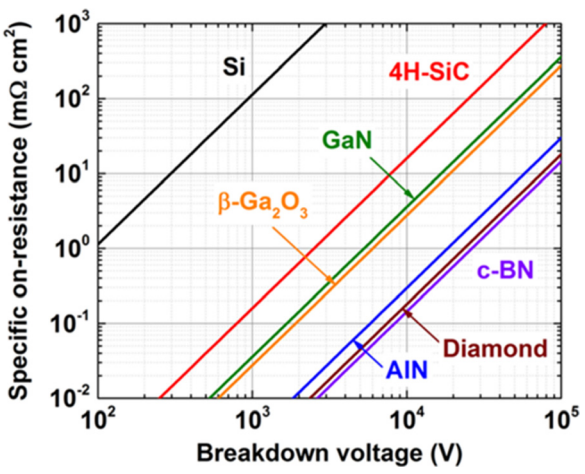

FIG. 40. Comparison of breakdown fields and on-state resistance in candidate materials for high power electronics (Adapted from Higashiwaki *et al*.,[15] Tadjer *et al*.,[54] and Tsao *et al*.[321])

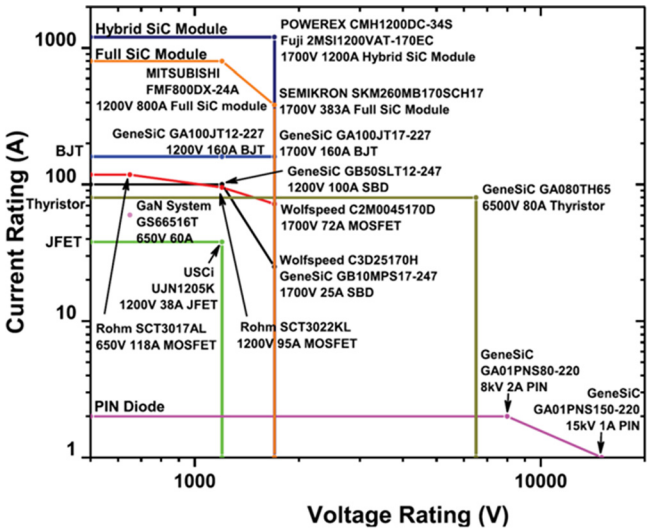

FIG. 41. Performance of commercially available SiC and GaN power diodes. Reprinted with permission from A. Q. Huang, Proc. IEEE **99**, 1 (2017). Copyright 2017 IEEE.[640]

rectifiers, a wide variety of edge termination methods have been employed to smooth out the electric field distribution around the rectifying contact periphery, including mesas, high resistivity layers created by ion implantation, field plates, and guard rings.[631,638–640] In addition, the design of SiC and GaN devices is relatively sophisticated, taking into account effects like incomplete ionization of dopants, temperature dependence of mobility and bandgap, ionization rates due to avalanche multiplication, carrier lifetimes, doping dependence of mobility, and a complete understanding of how edge termination affects reverse breakdown voltage for a given lateral or vertical device geometry.[630,631,636,641] All of these need to be developed for Ga_2O_3.

One thing that is relevant here is the fact that while α-Ga_2O_3 actually has a larger bandgap (~5.16 eV) than β-Ga_2O_3, the few rectifiers demonstrated on this material to date have not shown particularly large breakdown voltages,[322] perhaps at this stage due to the need for continued optimization of material quality.

Compared with lateral diodes grown on insulating substrates, vertical geometry Schottky diodes on conducting substrates can deliver higher power with full back side Ohmic electrodes and have higher current capability since they take advantage of the entire conducting area. Edge termination can also enhance the performance by preventing premature breakdown due to field crowding around the contact periphery. One of the key components of a rectifier is the Schottky contact, which we covered in an earlier section (Schottky Contacts to Ga_2O_3). Schottky contacts to β-Ga_2O_3 have been characterized using a number of metals, including Ni,[478,500,503,504,511,651] Pt,[500,518] Cu,[469] and Au.[136] The transparent Schottky contacts such as poly(3,4-ethylenedioxythiophene) polystyrene sulfonate (PEDOT:PSS) have also been demonstrated for flame detection.[482] To give an example of the control that is possible with different metals on β-Ga_2O_3, Tadjer *et al.*[518] carried out temperature I-V and Schottky barrier height studies on e-beam evaporated Pt/Au bilayers and compared these with novel ALD TiN (65 nm thick) contacts on (−201) β-Ga_2O_3. Both contacts showed thermionic emission, similar barrier heights of about 1 eV and near-unity ideality factor values, independent of temperature. The TiN contact actually had a much lower reverse current at room temperature. Figure 42(a) shows Richardson plots for the two types of contacts. The extracted barrier heights were 1.01 eV for Pt and 0.98 eV for TiN, and this difference was much lower than the ~2.6 eV predicted by the difference in work functions.[518] This may result from image force lowering. Ideality factors as a function of temperature were extracted at low bias in order to eliminate series resistance effects. Both samples had ideality factors close to unity over the whole temperature range investigated, as shown in Fig. 42(b). The only drawback of the TiN was a tendency to oxidize at higher temperatures.

Reverse breakdown voltages of over 1 kV for β-Ga_2O_3 have been reported by several groups,[646–649] either with or without edge termination. A typical device structure is shown in Fig. 43 (top). The highest reverse breakdown voltages have been achieved with similar layer structures, consisting of a thick epitaxial layer grown on a high quality EFG substrate,[646–649] approximately 10 μm thick of lightly Si-doped n-type Ga_2O_3 grown by HVPE on n^+ bulk, (−201) Sn-doped (3.6×10^{18} cm^{-3}) Ga_2O_3 single crystal wafers. The dislocation density from etch pit observation was approximately 10^3 cm^{-2}. The reverse leakage current has been closely correlated to the dislocation density in (0–10) oriented bulk β-Ga_2O_3 which revealed upon a hot H_3PO_4 acid delineation etch for 1 h.[658] Diodes were fabricated by depositing full area back Ohmic contacts of Ti/Au (20 nm/80 nm) by E-beam evaporation, while the Schottky contacts were patterned by lift-off of E-beam deposited Schottky contacts Ni/Au (20 nm/80 nm) on the epitaxial layers.[643,644] Note that this device does not employ edge termination and shows the capability of the Ga_2O_3 to withstand high field strengths. The diameter of these contacts ranged from 20 μm to 0.53 mm. The bottom of Fig. 43 shows the optical images of some of the completed diodes with different diameters.[643,644]

Figure 44 (top) shows the forward and reverse current density-voltage (J-V) characteristic from a 20 μm diameter diode. The V_{BR} was approximately 1600 V for this diode

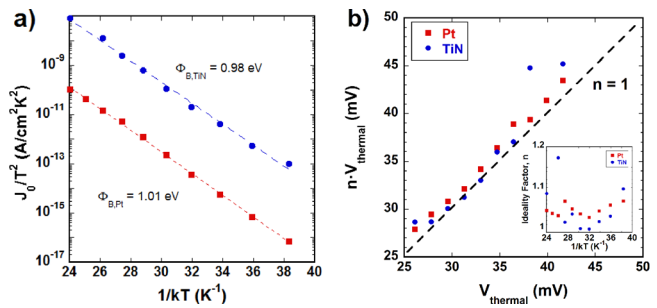

FIG. 42. (a) Richardson plots comparing Pt and TiN contacts to (−201) Ga_2O_3. (b) Ideality factor–thermal voltage (n·Vthermal = n·kT/q) for the two contacts. Reprinted with permission from Tadjer *et al.*, ECS J. Solid State Sci. Technol. **6**, P165 (2017). Copyright 2017 The Electrochemical Society.[519]

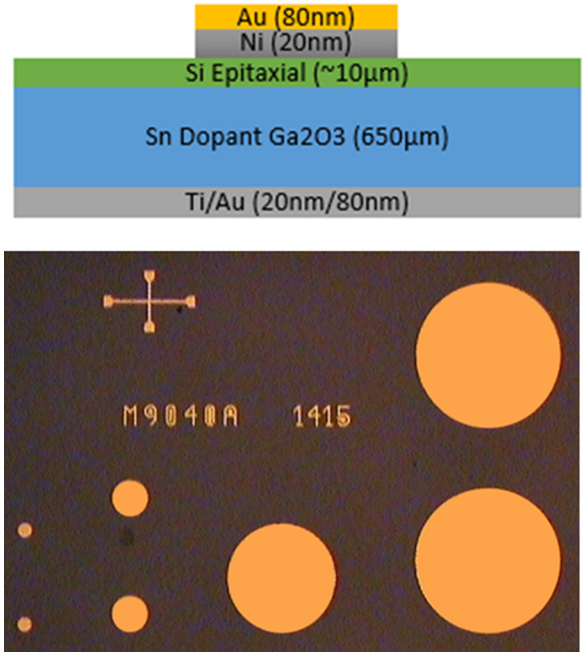

FIG. 43. Schematic of vertical Ni/Au Schottky diode on Ga_2O_3 epi layer on a conducting β-Ga_2O_3 substrate (top) and top-view microscope image of the fabricated β-Ga_2O_3 diodes (bottom). Reprinted with permission from Appl. Phys. Lett. **110**, 192101 (2017). Copyright 2017 American Institute of Physics.[648]

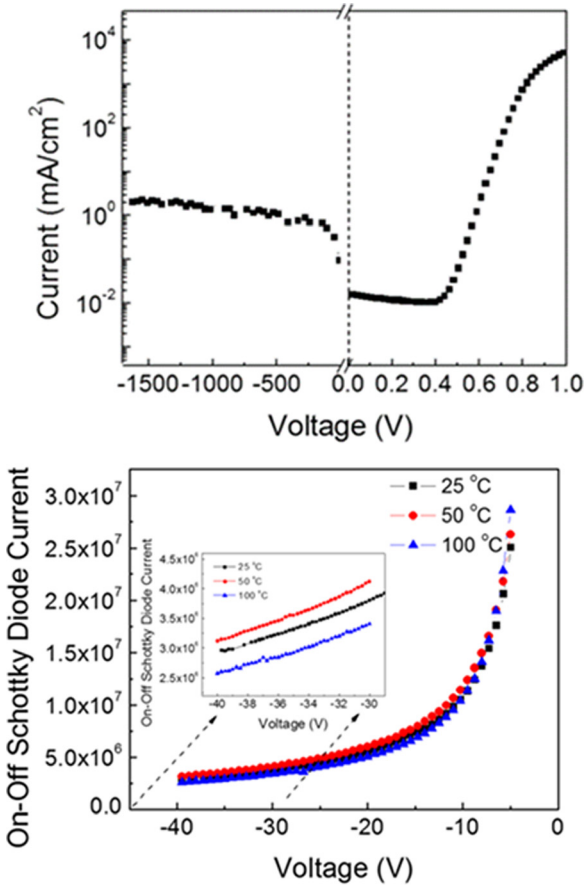

FIG. 44. (Top) Forward and reverse current density-voltage characteristics from a 20 μm diameter diode. (Bottom) Diode on/off ratios for temperatures in the range of 25–100 °C as a function of reverse bias. The forward bias was held constant at 1.3 V. Reprinted with permission from Yang *et al.*, IEEE Electron Device Lett. **38**, 906 (2017). Copyright 2017 IEEE.[649]

with a smaller diameter and 250 V for the largest diameter.[648,649] This trend is typical for newer materials technologies still being optimized in terms of defect density.[656–661] Kasu *et al.*[658] examined the effect of crystal defects revealed by etch pit delineation and found that dislocations are closely related to the reverse leakage current in the rectifier and that not all voids produce leakage current.[658,659] Dislocation defects along the [010] direction were found to act as paths for leakage current, while the Si doping did not affect this dislocation-related leakage current.[658–660] By contrast, in the [102] orientation, three types of etch pits were present, namely, a line-shaped etch pattern originating from a void and extending toward the [010] direction, arrow-shaped pits in the [102] direction, and gourd-shaped pits in the [102] direction. Their average densities were estimated to be 5×10^2, 7×10^4, and 9×10^4 cm^{-2}, respectively, but in this orientation there was no correlation between the leakage current in rectifiers and these crystalline defects.[658–660] Thus, the orientation of the substrate used determines the sensitivity to the defect density.[660,661] Figure 43 (bottom) shows the on-off current ratio measured at a fixed forward voltage of 1.3 V and reverse biases from −5 to −40 V.[647,648] The on-of ratios ranged from 3×10^7 to 2.5×10^6 for this range of biases and showed only a small dependence on temperature in the range of 25–100 °C. This is promising for device operating temperatures in this range, since there would be little change in performance characteristics.

Konishi *et al.*[647] obtained high reverse breakdown voltages in excess of 1 kV for diodes employing an SiO_2 field plate with 300 nm thickness and length 20 μm. This was designed using simulation software to optimize the breakdown voltage.[647] The simulated maximum electric field under the anode edge was 5.1 MV/cm,[647] much larger than the theoretical limits for SiC and GaN and similar to the breakdown field for lateral Ga_2O_3 MOSFETs.[662,663,667] Even higher breakdown voltage should be possible by demonstrating a junction barrier Schottky (JBS) diode architecture, whereas in the reverse bias the drift layer depletes away from the surface by employing a pn junction.[664,665] In the case of Ga_2O_3, pn type heterojunctions have been demonstrated using Li-doped NiO deposited on Ga_2O_3 (Ref. 666) and Ga_2O_3 deposited on 6H-SiC,[386] where the β-Ga_2O_3/6H-SiC anisotype heterojunction appeared to have achieved minority carrier injection.

In summary, there have been a number of 1 kV breakdown voltage rectifiers reported. The maximum current density reported is 3 kA cm^{-2}, with a lowest reported R_{on} of 0.1 mΩ cm^2 and a turn-on voltage of 1.7 V.[322] The growth methods have included HVPE, MBE, and Mist-CVD, and both vertical and horizontal geometries have been demonstrated. It is worth noting again that annealing of EFG-grown materials under oxygen ambients typically leads to a reduction in net carrier concentration of up to an order of magnitude, which can lead to higher reverse breakdown voltages.[69] The usual Schottky contacts are Pt/Au, Au or Pt/Ti/Au, and the Ohmic metallization is usually Ti/Au.[322]

POWER MOSFETs AND MESFETs

Modulation-doping for heterostructures

Tsao *et al.*[321] pointed out that heat removal is going to be a major issue for Ga_2O_3, more so if heterostructure-type devices become necessary since they will contain binary, ternary, and quaternary compounds and interfaces between dissimilar materials. Combined with the poor thermal conductivity of Ga_2O_3, this will lead to a complex set of internal impedances to heat removal. Thus, there is a need to understand the thermal properties of these alloys, in addition to their electrical and structural properties. To this point, there is little known about the solubility limits and carrier confinement at heterostructures with Ga_2O_3.

The first reported heterostructure between a binary and a ternary Ga_2O_3 system was by Kaun *et al.*[406] While the x-ray data demonstrated that an $(Al_xGa_{1-x})_2O_3$/GaO structure was grown, the undoped AlGaO layer and the step-bunching induced surface roughness of the Ga_2O_3 surface prevented the formation of a two-dimensional electron gas (2DEG).[406]

These issues were successfully overcome by Krishnamoorthy *et al.*[668] who reported a modulation-doped two-dimensional electron gas (2DEG) at the β-$(Al_{0.2}Ga_{0.8})_2O_3$/Ga_2O_3 heterojunction by silicon delta doping. This was grown on Fe-doped (010) β-Ga_2O_3 semi-insulating substrates. The device performance was limited by the quality of the Ohmic contacts, with a maximum current normalized to the channel width of 5.5 mA/mm. Figure 45(a) shows the output characteristics and (b) transfer characteristics of AGO/GO MODFET, exhibiting good charge modulation, pinch-off, and a high ON/OFF ratio.[668] The pinch-off voltage was −3 V, on-off ratio of 2.5×10^5, and peak transconductance was 1.75 mS/mm. Oshima *et al.*[669] explored the solubility limits of $(Al_xGa_{1-x})_2O_3$ grown on Ga_2O_3, while Takayoshi *et al.*[670] were able to observe carrier confinement at the interface of similar heterostructures. Several groups have demonstrated β-$(Al_xGa_{1-x})_2O_3$ (Refs. 671–674) and α-$(AlGa)_2O_3$ (Ref. 675) grown by MBE or Mist-CVD.

MOSFETs

The metal-oxide-semiconductor field-effect transistors (MOSFETs) fabricated on Ga_2O_3 to date have predominantly been depletion (d-mode) devices, with a few demonstrations of enhancement (e-mode) operation.[676–691] The channels have been undoped, Si,[682,688] Sn or Ge-doped,[680] and HfO_2,[678] and Al_2O_3 (Ref. 679) and SiO_2 (Refs. 682 and 684) have been the most widely used dielectrics. The first Ga_2O_3 transistors were reported in the 2012–2013 time frame by Higashiwaki *et al.*,[676,677] fabricated on homoepitaxial epitaxial Ga_2O_3 grown by MBE on native substrates. In 2014, a back-gated MOSFET device was fabricated by exfoliating a nm-thick slice of Ga_2O_3 from the (100) face of a Czochralski-grown bulk Ga_2O_3 crystal.[692] In early 2016, Tadjer *et al.* reported a MOSFET fabricated on epitaxial Ga_2O_3 grown by metal organic CVD using a trimethylgallium (TMG) source in O_2 atmosphere.[54] Even though the films were insulating, implantation of Si in the source/drain regions and the good surface roughness obtained by growth on c-plane Al_2O_3 allowed a functional transistor to be fabricated. In addition, Tadjer *et al.*[678] fabricated a (001) β-Ga_2O_3 MOSFET with +2.9 V threshold voltage and HfO_2 as the gate dielectric. Figure 46 shows the I_{DS}-V_{DS} characteristics, (b) I_{DS}-V_{GS} as a function of drain bias (0.1, 1, and 10 V), and (c) off-state I_{DS}-V_{DS} characteristic, showing the soft breakdown regime at around 80 V.[678]

The outstanding devices in the literature to date have generally employed a planar, lateral geometry.[342,343,346,347,677–692] While the report by Tadjer *et al.*[678] was not an enhancement mode device, normally off operation was reported by depleting the channel using a wrap-gate finfet architecture, where e-mode operation and a 600 V breakdown voltage were demonstrated.[679] Furthermore, a prototype lateral MOSFET with a very low-doped channel ($\sim 10^{14}$ cm^{-3}) and gate-overlapped S/D implants was demonstrated in early 2017, which to-date represents the closest demonstration to a textbook enhancement-mode MOSFET in the absence of a pn source/drain junction technology in Ga_2O_3.[683] Si ion implantation has been employed to improve source/drain resistance in some cases.[683] As a group, it is clear that the devices do indeed exhibit high critical field strength and breakdown voltages, but the current densities have been low, typically approximately 10–100 mA/mm or less, and the on-state resistances have been large, especially for e-mode devices. The highest output current density was reported by Zhou *et al.*,[684] by employing an n^+ doped channel exfoliated from a Sn-doped substrate onto an SiO_2/Si substrate. For high voltage and high power ratings, vertical topologies are preferred since chip area utilization is more efficient and device operation is insensitive to surface effects. Two examples of vertical Ga_2O_3-based devices have been reported to date.[689,690] Wong *et al.*[689] adopted a current aperture vertical transistor design (CAVET) with a Mg-implanted current blocking layer. Hu *et al.*,[690] on the other hand, employed a deep-etch process to fabricate ~1 μm thick vertical structures into a low-doped Ga_2O_3 substrate. At this stage, thermal effects have not been a major issue, but if Ga_2O_3 is to realize its promise, this will need significant attention. Given the low thermal conductivity, wafer thinning or backside heat sinks will not be sufficient and the use of thermal shunting on the active device surface will be required for MOSFETs to operate with high-efficiency at higher power.

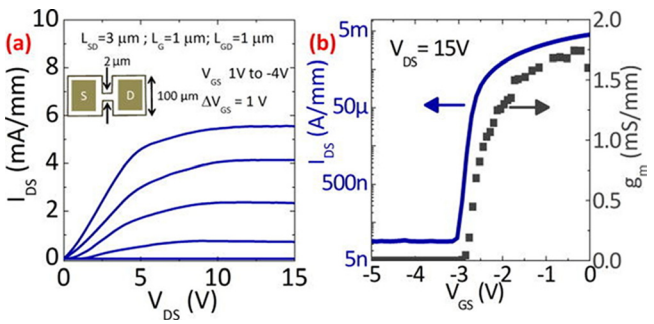

FIG. 45. (a) Output characteristics and (b) transfer characteristics of AlGaO/Ga_2O_3 MODFET showing FET operation with charge modulation, pinch-off, and high on/off ratio. Reprinted with permission from Appl. Phys. Lett. **111**, 023502 (2017). Copyright 2017 American Institute of Physics.[668]

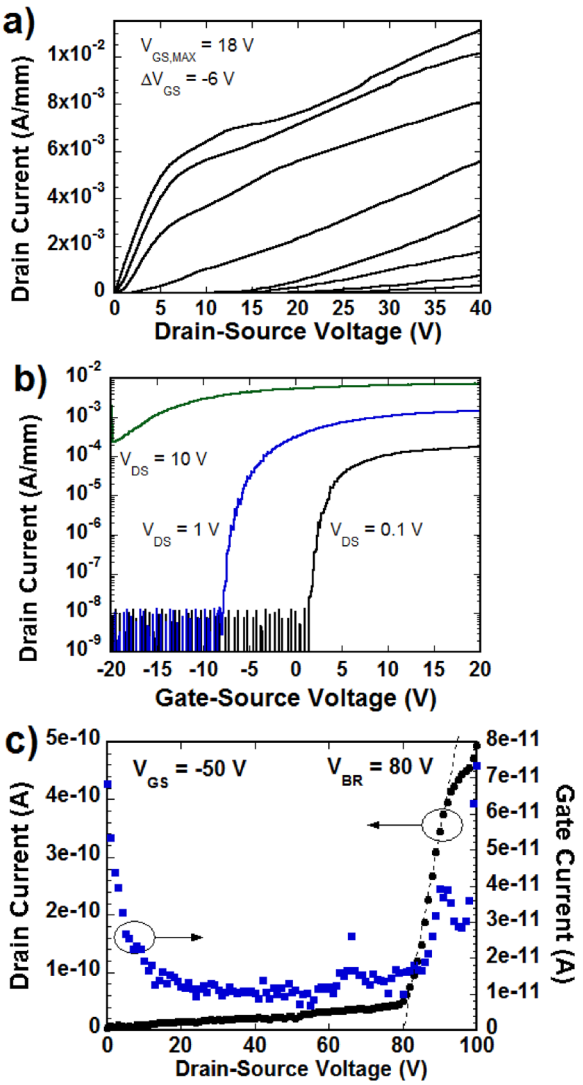

FIG. 46. (a) DC output (I_{DS}-V_{DS}) characteristics, (b) DC input (I_{DS}-V_{GS}) as a function of drain bias (0.1, 1, and 10 V), and (c) off-state I_{DS}-V_{DS} characteristic showing the soft breakdown regime at around 80 V. Reprinted with permission from Tadjer *et al*. ECS J. Solid State Sci. Technol. **5**, P468 (2016). Copyright 2016 The Electrochemical Society.[678]

Moser *et al.*[680] reported MOSFETs on Ge-doped (4×10^{17} cm^{-3}) β-Ga_2O_3 layers grown by MBE on (010) Fe-doped semi-insulating substrates, after the successful demonstration of Ge-doped MOCVD Ga_2O_3 epilayers. The drain current on/off ratios were $>10^8$, and the saturated drain current was >75 mA/mm at $V_G = 0$ V. A MOSFET with a gate-drain spacing of 5.5 μm had a three-terminal breakdown voltage of 479 V.[680] The same group[680] fabricated an enhancement-mode device achieved by gate recess with drain-current >20 mA/mm, on/off ratio $>10^7$, and 200-V breakdown for 3-μm source-drain distance. The Si-doped MBE grown channel was 200 nm thick with approximately 10 nm highly doped epitaxial cap layer to reduce Ohmic contact resistance.[680]

Green *et al.*[687] reported the first rf performance of a Ga_2O_3 MOSFET, based on Si-doped β-Ga_2O_3 (channel doping 10^{18} cm^{-3} and cap doping 10^{19} cm^{-3}) grown by MOCVD on a semi-insulating CZ-grown (100) substrate. The devices achieved a transconductance of 21 mS/mm and extrinsic cutoff frequency (f_T) and maximum oscillation frequency (f_{max}) of 3.3 and 12.9 GHz, respectively. Figure 47 (top) shows the extrinsic small signal RF gain performance at $V_{GS} = -3.5$ V (peak gm) and $V_{DS} = 40$ V. A gain decay of −20 dB/dec is plotted with the dashed line. The bottom of the figure shows the 800 MHz Class-A power sweep of a 2 μm × 50 μm MOSFET.[687]

Zhou *et al.*[684] realized β-Ga_2O_3 on insulator (GOOI) d-mode and e-mode FETs by transferring a β-Ga_2O_3 nanomembrane 50–150 nm thick to a SiO_2/Si substrate, followed by device fabrication. They demonstrated maximum I_D of 600/450 mA/mm for d/e-mode FETs and on/off ratio of 10^{10}. Ar bombardment was used to achieve Ohmic source and drain contacts. E-mode FETs with source-drain separation 0.9 μm had breakdown voltage of 185 V, corresponding to a field strength of 2 MV/cm. Figure 48(a) shows a schematic of a GOOI FET while (b) shows an atomic force microscopy image of the β-Ga_2O_3 surface after cleavage. Figure 48(c) shows the thickness dependence of the I_D-V_{GS} characteristics. The threshold voltage shifts from negative to positive as the membrane thickness is reduced. Figure 48(d) shows the extracted thickness dependent threshold voltage.[684]

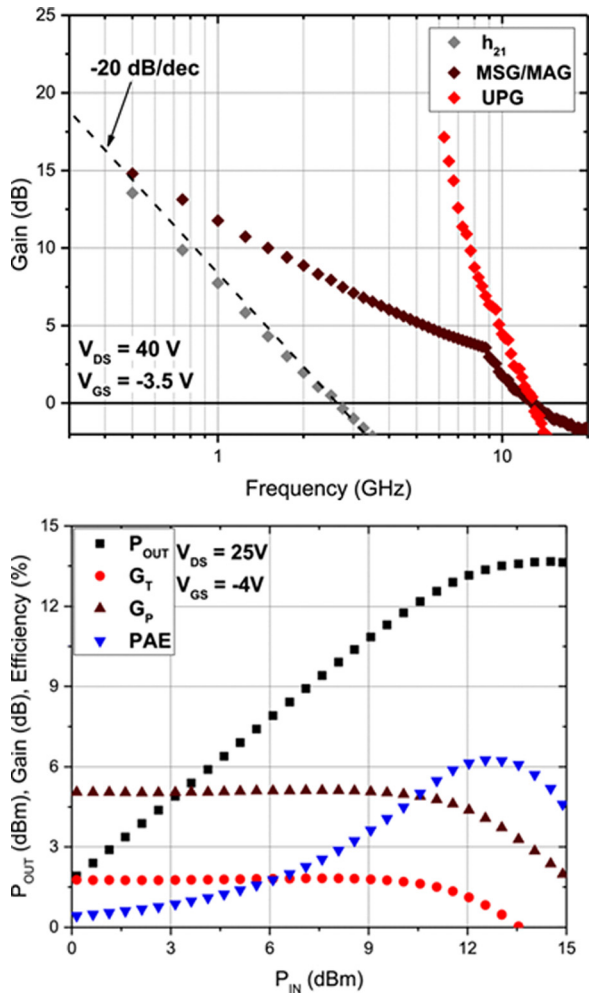

FIG. 47. (Top) Extrinsic small signal RF gain performance recorded at $V_{GS} = -3.5$ V (peak gm) and $V_{DS} = 40$ V. A gain decay of −20 dB/dec is plotted with the dashed line. (Bottom) 800 MHz Class-A power sweep of a 2 × 50 μm gate recessed MOSFET. Reprinted with permission from Green *et al*., IEEE Electron Device Lett. **38**, 790 (2017). Copyright 2017 IEEE.[687]

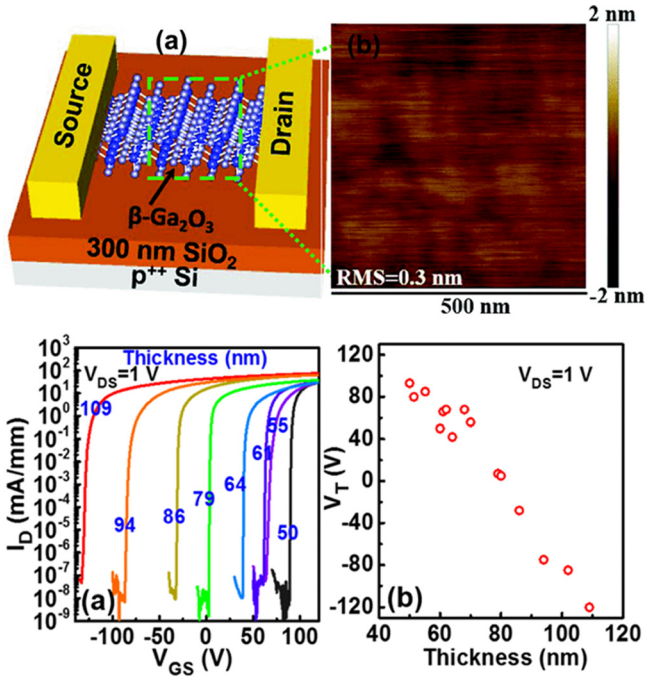

FIG. 48. (a) Schematic view of a GOOI FET with a 300 nm SiO_2 layer on Si substrate and (b) AFM image of β-Ga_2O_3 surface after cleavage. (a) Thickness dependent I_D - V_{GS} plots of various GOOI FETs from d-mode to e-mode. (b) Thickness dependent V_T extracted at $V_{DS} = 1$ V. Reprinted with permission from Zhou *et al.* IEEE Electron Device Lett. **38**, 103 (2017). Copyright 2017 IEEE.[684]

Wong *et al.*[689] demonstrated a vertical Ga_2O_3 MOSFET, in which the source was electrically isolated from the drain by a current blocking layer formed by Mg^+ implantation except at an aperture opening through which the drain current flows. The I_{DS} was modulated through a gated channel above this current blocking layer CBL.

Krishnamoorthy *et al.*[691] reported silicon delta doping in PA-MBE β-Ga_2O_3 to achieve a low sheet resistance of 320 Ω/square (mobility 83 cm^2 $V^{-1}s^{-1}$, sheet charge 2.4×10^{14} cm^{-2}). This delta-doped channel was used in a MESFET with a maximum drain current of 236 mA/mm and transconductance of 26 mS/mm.[690] Dang *et al.*[691] showed that α-phase corundum-structured MESFETs could be realized by Mist-CVD ON low cost sapphire substrates.

Finally, a number of groups have demonstrated air-stable high power and high temperature capable MOSFETs and MESFETs on two dimensional nanobelts or nanomembranes that have been mechanically exfoliated from bulk wafers and transferred to other substrates such as, but not limited to, SiO_2/Si.[692–695] The zero or small band-gap of two dimensional materials like graphene and transition metal dichalcogenides materials has precluded the use of devices fabricated on these materials for high power and high temperature applications. The use of quasi-two dimensional Ga_2O_3 has potential for these applications and a potential large-area, controllable mechanical transfer of Ga_2O_3 thin films onto high thermal conductivity substrates can provide a low-cost thermal solution for this material.[696] Ahn *et al.*[694] reported nanobelt FETs using SiO_2 and Al_2O_3 as the gate oxides for the back and front sides, respectively, which were fabricated on exfoliated two-dimensional (2D) β-Ga_2O_3 nano-belts transferred to a SiO_2/Si substrate. The d-mode transistors exhibited improved channel modulation with both front and back gates operational compared to either front or back-gating alone. The maximum transconductance was approximately 4.4 mS mm^{-1} with front and back-gating, with a maximum drain source current density of 60 mA mm^{-1} at 10 V and on/off ratios of approximately 10^5 at 25 °C. The device characteristics were stable over more than a month for storage in air ambient.

Theoretical studies[697] have suggested that these nano-belts films will not have quantum confinement effects and exhibit the same electronic structure as bulk material because of states that are strongly confined near the surface. However, if the Ga_2O_3 layers are clad in a wider band-gap material such as Al_2O_3, quantum confinement with small effective electron mass of electrons is expected.[697]

In summary, for the epi MOSFETs, the substrate has usually been semi-insulating Fe-or Mg-doped, with the epi grown by MBE or HVPE and doped with Sn or Si.[322] The Ohmic contacts have usually been enhanced using ion implantation or plasma exposure to improve conductivity, with Ti/Au-based Ohmic metallization and gates of Pt/Ti or Ti/Au. The gate dielectric and passivation has usually been ALD Al_2O_3, and both e- and d-mode operations have been reported.[322] The on-off ratios have been in the range of 10^7–10^{10}, with field effect mobilities from 2 to 95.[322] The interface trap densities reported to date range from the 10^{11} cm^{-2} eV^{-1} to values well over an order of magnitude higher. This is an area where further optimization is needed.

Ga_2O_3-BASED GAS SENSORS

Resistive gas sensors based on metal oxide semiconductors have a long history and due to its high melting point (approximately 1800 °C), Ga_2O_3 is one of the most important materials for high temperature gas sensing.[698–737] Gas sensors based on semiconducting, typically polycrystalline, Ga_2O_3 thin films can be used either for sensing oxygen ($T \geqslant 900$ °C) or reducing gases ($T < 900$ °C), depending on the operating temperature.[700–709] Another advantage of Ga_2O_3 is that it has only one stable structural modification, monoclinic, that can be easily obtained by thermal annealing at temperatures between 800 and 900 °C. This structure is then stable in the temperature range up to the melting point.[703–706] A typical application for sensors based on high-temperature-stable semiconducting gallium oxide thin films is monitoring of the composition of exhaust gases from internal combustion engines or furnace installations.[702–705] The resistivity of Ga_2O_3 thin films changes with the concentration of oxygen, leading to the ability to sense oxygen. Table VIII shows a summary of the gas sensor applications, operating temperature range, and detection ranges for Ga_2O_3 gas sensors.[698,699,712,715,724,730,735,737–744]

Fleischer and Meixner[702,703,707–709] were the first to show using polycrystalline thin films sputtered from a ceramic target that Ga_2O_3 is a suitable material for high temperature operating gas sensors. Ogita *et al.*[698,699] used polycrystalline thin films deposited by sputtering from a powder target and fabricated oxygen sensors with interdigitated and

TABLE VIII. Summary of Ga_2O_3 gas sensors and performance.

Sample	Detection gas	Operating temperatures (°C)	Detection range	Comments	Reference
Sputtered, poly	H_2	400–650	0.5%–3% in Ar	Bulk effects due to O_2 exposure present	Fleischer *et al.*[738]
Pt-gated thin films	H_2	400–550	100 ppm	Ga evaporation in O_2 plasma	Nakagomi *et al.*[715]
Poly	H_2	600	1%	Can be used for O_2 sensing at lower temperature	Fleischer *et al.*[745]
Poly	CH_4	Up to 700	15%	Exposure to methane leads to oxygen vacancies	Becker *et al.*[739]
Poly	CO	550–700	4–100 ppm	Excellent stability	Schwebel *et al.*[740]
Pt functionalized nanostructures	CO	100	10–100 ppm	Pt nanoparticles of dimension tens of nm	Kim *et al.*[735]
Sputtered thin films	O_2	600–900	1%	Used CeO_2,Mn_2O_3, La_2O_3 as modifiers to obtain selectivity	Schwebel *et al.*[743]
Sputtered, poly	O_2	300–1000	2–10 Pa	Used Si substrates as template	Ogita *et al.*[698]
Sputtered, poly	O_2	>900	n/a	Examined dependence on sputtering conditions	Ogita *et al.*[699]
Thin films	O_2	>800	n/a	Role of oxygen vacancies	Baban *et al.*[742]
Sol gel thin films	O_2	420–460	100–10 000 ppm	Effect of Ce, Sb, W or Zn doping	Li *et al.*[702]
Multiple nanowires	O_2, CO	100–500	50–500 ppm	Fast response times	Liu *et al.*[737]
Pt/Ga_2O_3/SiC	H_2	310–700	0.1%–1%	Schottky diode	Trinchi *et al.*[724]
Nanocrystallite	NH_3	30	0.5 ppm	Selective in both dry and humid ambients	Pandeeswari *et al.*[730]
SnO_2 doped sputtered films	NH_3	900	30 ppm	Sn doping enhances sensitivity	Frank *et al.*[744]
Nanobelts	NO_2	25	0.5–1000 ppm	30–50 nm width, 10s of microns long	Lin *et al.*[741]
Nanorods	Humidity	25–40	1%–95% RH	Doped with Na or K	Wang *et al.*[746]

mesh electrodes which showed good sensitivity and response times of 14 – 27 s at 1000 °C. Below 700 °C, the sensors were found to exhibit sensitivity to reducing gases such as CO, H_2, and CH_x due to surface reactions while above 900 °C there is a switch to sensitivity to oxygen because of the presence of the oxygen vacancies inside the material.

Lampe *et al.*[710] used Ga_2O_3 sensors in an investigation of both real exhaust gas and mixtures of N_2, O_2, CH_4, CO, NO, and water vapor to produce a synthetic exhaust gas with very precisely defined composition. In the range of 1000–900 °C, the gallium oxide sensors responded to the oxygen partial pressure of the mixtures.[710] With the knowledge of the fuel composition (carbon-hydrogen ratio), they were able to measure the Lambda coefficient (λ) from the relationship between air and gasoline involved in combustion of the mixture.[710] This is a standard parameter that defines the efficiency of the gasoline engine by measuring the percentage of oxygen in the exhaust. Their value was $\lambda = 1.2$–0.85, with a resistance jump of about three decades at the stoichiometric point.[710]

Bartic *et al.*[714] used thin films and FZ single crystals of Ga_2O_3 to investigate the high temperature oxygen sensitivity of these materials. Figure 49 shows the normalized sensitivity in the form of (a) the dynamic response and (b) the recovery of Ga_2O_3 sensors subjected to a change in oxygen content between 0 and 20% in a gas stream at 1000 °C.[714] The grain boundaries in the sputtered films played some role in the results, but the difference in response times between single crystal and poly material was small.[714]

Pt/Ga_2O_3/SiC Schottky diodes were characterized for their hydrogen gas sensitivity as a function of operating temperature and found advantages compared to the pure thin film Ga_2O_3 conductometric sensor.[724] The Ga_2O_3 thin films were prepared by the sol–gel process and deposited onto the transducers by spin-coating. Cycling the ambient from air to 1% H_2 in produced repeatable changes of the forward voltage at fixed forward bias, with a faster response above 500 °C. The decrease in bias voltage for exposure to 1% H_2 was 210 mV.

Koroncentov and Cho[736] recently reviewed the use of metal oxide nanocomposites and complex metal oxides, including SnO_2, ZnO, Ga_2O_3, In_2O_3, WO_3, and the metal oxide modifiers including Fe_2O_3, La_2O_3, Cr_2O_3, Co_3O_4, V_2O_5, NiO, CuO, SiO_2, MoO_3, and CeO_2. The application of nanocomposites and mixed metal oxides in gas sensors greatly improves the sensor performance, and Ga_2O_3 is often used to increase the response of SnO_2 or In_2O_3-based sensors.[736] Figure 50(a) shows the influence of additives to SnO_2 on its sensitivity to N_2O at 500 °C,[726] with Ga_2O_3 being one of the most effective additives. Figure 50(b) shows the N_2O conversion percentage at similar temperatures.[736]

Rahman *et al.*[716] explored the options for use of Ga_2O_3 biosensors. The existing techniques for DNA biosensors include attaching a fluorescent label to a target molecule, but label-free methods are attractive for improving the speed and size, and lowering the sensor cost.[716,747] Field-effect-transistor-based detection is attractive because of its scalability, integration with on-chip wireless, and ease of making arrays. A single-crystal β-Ga_2O_3 electrolyte/oxide diode was investigated for biosensing applications.[716] The surface β-Ga_2O_3 functionalization involved silanization with 3-aminopropyltriethoxysilane (APTES) and modification with *N*-succinimidyl-6-maleimidylhexanoate (EMCS) to immobilize the capture probe DNA (thiol-terminated single-stranded DNA). Upon exposure to bioactive electrolytes, the functionalized β-Ga_2O_3 could be used for detecting complementary DNA sequences from noncomplementary DNA with a nearly twentyfold relative resistivity difference.[716] This showed the feasibility of Ga_2O_3-based integrated bioelectronics.[716]

The development of nanostructured materials for sensor materials is a result of their large active interfacial and surface areas, which can improve the sensor response and

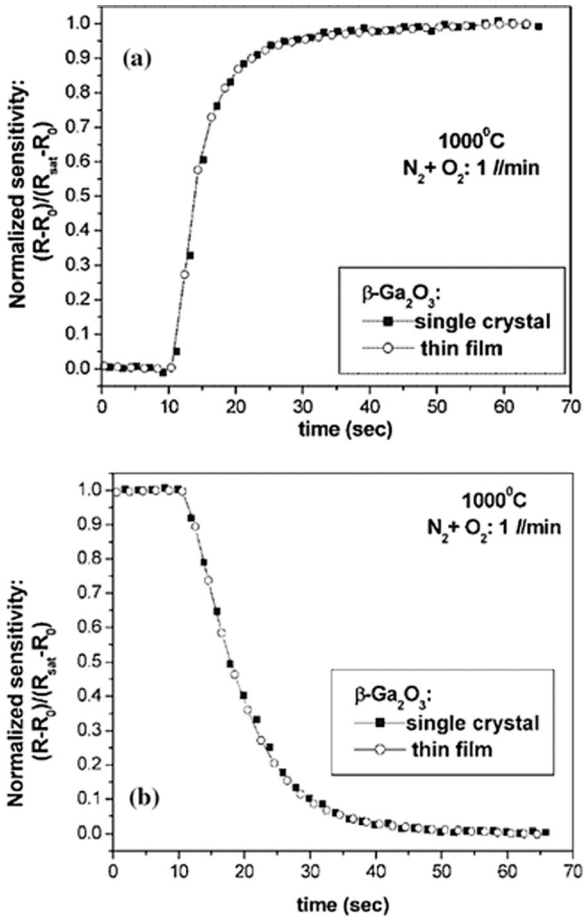

FIG. 49. Dynamic response and (b) recovery of Ga_2O_3 sensors as a function of change in O_2 content from 0% to 20% in a gas stream at 1000 °C. Reprinted with permission from Bartic *et al.*, Jpn. J. Appl. Phys. **45**, 5186 (2006). Copyright 2006 The Japan Society of Physics.[714]

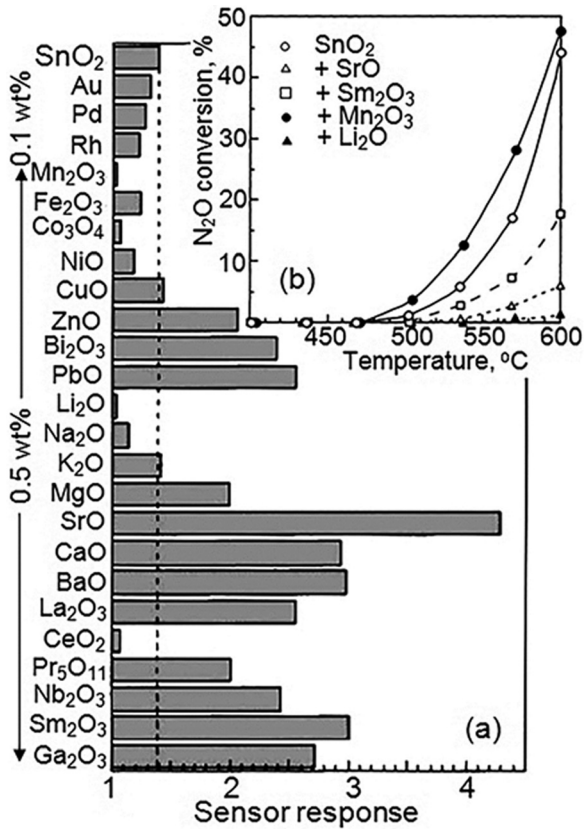

FIG. 50. Influence of additives to SnO_2 on (a) sensitivity to 300 ppm N_2O ($T_{oper} = 500$ °C) and (b) N_2O conversion. Reprinted with permission from G. Korotcenkov and B. K. Cho, Sens. Actuators **244**, 182 (2017). Copyright 2017 Elsevier.[736]

speed. This must be balanced with sensor stability, since high surface area structures are inherently unstable due to their high surface energy. Lin and Wang[734] synthesized β-Ga_2O_3 nano/microbelts under different oxygen pressures by thermal evaporation and measured their oxygen sensing response at 254 nm illumination with different oxygen pressures and they were able to measure rapid changes in conductance due to chemisorption and desorption surface processes.[734]

Pandeeswari *et al.*[730] examined ammonia detection using spray pyrolysis films of Ga_2O_3 at levels near the Occupational Safety and Health Administration (OSHA) maximum recommended exposure level of 25 ppm. Existing techniques are often time consuming and require sophisticated instruments.[730] The resistive sensors detected ammonia concentrations ranging from 0.5 ppm to 50 ppm and suggest that β-Ga_2O_3 thin films can be utilized to sense ammonia at room temperature for environmental monitoring and disease diagnosis through exhaled human breath.[730]

Liu *et al.*[711] reported the gas sensing capabilities of Ga_2O_3 nanowires to O_2 and CO gases. Figure 51 shows the dynamic responses of the nanowire gas sensor to 0.5%, 1%, and 5% O_2 at 300 °C. The resistance increases upon exposure to oxygen ranged from factors of 2–10 times for 0.5%–5% oxygen, respectively. The bottom of Fig. 50 shows the reversible dynamic gas responses to cyclic CO exposures at concentrations of 50–500 ppm at 100 °C. The resistance decreases reversibly upon each CO pulse. Wang *et al.*[746] also showed that Ga_2O_3 nanorods doped with Na or K could be used for relative humidity sensors.

SUMMARY AND CONCLUSIONS

Ga_2O_3 is the least mature of the wide bandgap semiconductors currently being examined for use in high temperature, high power electronics and solar-blind UV detection.[87,321,322] However, its combination of materials properties (with the notable exception of thermal conductivity) and the availability of large, high quality bulk substrates makes it an attractive option and worthy of a significant research focus. The electronic device demonstrations have included kV-class Schottky rectifiers with breakdown voltage >1 kV and e- and d-mode MOSFETs with critical field strengths larger than GaN or SiC values.[87] The theory of band structure, defects, and low and high field transport properties is relatively mature, and strong experimental efforts to confirm these predictions are needed. The absence of solid demonstrations of p-type conductivity and the prediction that holes are self-trapped to form polarons limits the current range of possible devices to unipolar conductivity.

Obviously one of the biggest issues for Ga_2O_3 power electronics is thermal management. The approaches developed for GaN in recent years are relevant here, involving

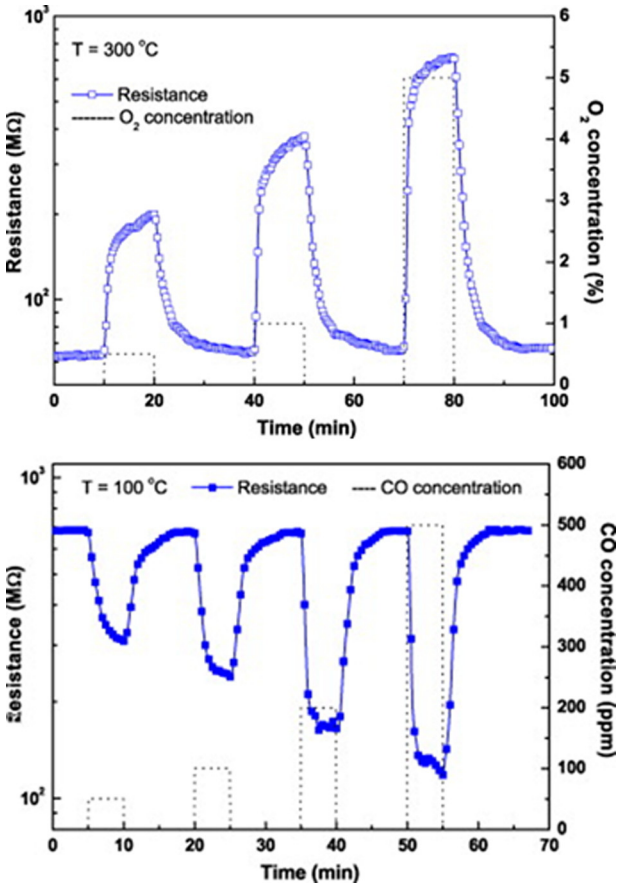

FIG. 51. (Top) Dynamic response of the Ga_2O_3 nanowire sensor to O_2 gas pulse at 300 °C. (Bottom) Dynamic response of the Ga_2O_3 nanowire sensor to O_2 gas pulse at 300 °C. Reprinted with permission from Zhifu Liu *et al.*, Sens. Actuators B **129**, 666 (2008). Copyright 2008 Elsevier.[711]

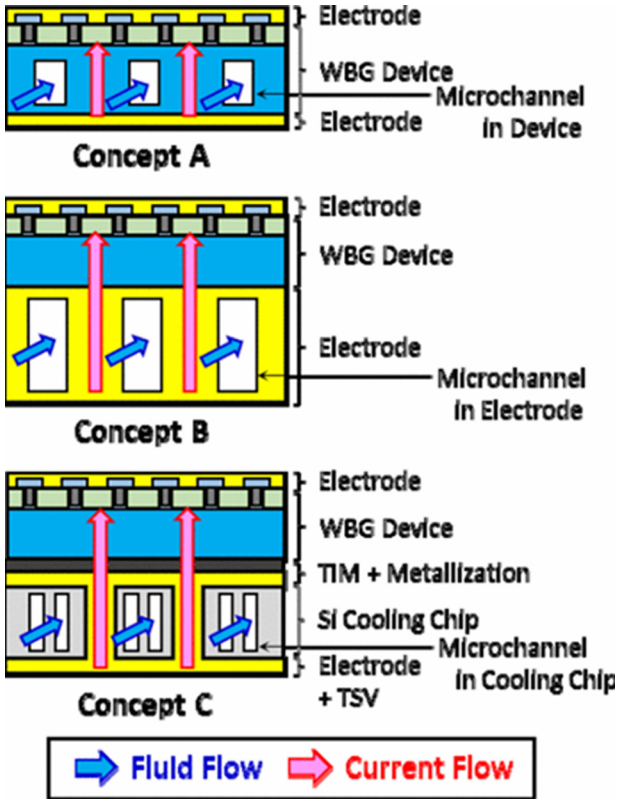

FIG. 52. Schematics of concepts for embedded cooling of vertical current wide bandgap semiconductor devices. Reprinted with permission from Dede *et al.*, in *2017 16th IEEE Intersociety Conference on Thermal and Thermomechanical Phenomena in Electronic Systems (ITherm)* (2017), pp. 508–515. Copyright 2017 IEEE.[748]

embedded cooling.[748–753] It was clear that the near-junction thermal barriers severely limited the capability of GaN power transistors and a variety of approaches including the use of diamond substrates and efficient removal of the dissipated power with convective and evaporative microfluidics have been developed.[748–753] Three of the embedded cooling approaches employed for the reduction of the near-junction thermal resistance are shown schematically in Fig. 52.[748] These are used for large (approximately 1 cm^2) die size vertical current wide bandgap devices. Concept A uses microchannels etched directly into the substrate. Concept B employs a thick metal layer as the back electrode of the vertical device, with this contact containing microchannels for embedded cooling. Concept C is a stacked wafer structure that comprises the device bonded to a Si cooling chip via an intermediate metallization plus thermal interface material layer.[748] For Concept C, through-Si vias are interleaved within the Si cooling chip. This approach allows electrical connection from the bottom electrode of the wide bandgap device and the lowermost electrode in the stack.[748]

The most developed method has been deposition or bonding of diamond to GaN, which enabled significant increases in power handling capability per transistor unit area, while the use of microfluidic cooling enabled heat fluxes of 30 kW/cm^2 at the transistor level and 1 kW/cm^2 at the die-level.[749–753] This translates to an improvement of a factor of 6 in the total RF output power of GaN power amplifiers. Similar embedded cooling approaches are critical to the future success of Ga_2O_3.

There are obviously a large number of areas that need more development and improvements in the understanding of the basic materials science.[14,87,321,322] These include the following:

(i) Identification of the dominant defects in bulk crystals and epitaxial films and the effect on device performance. Experimental clarification of the predictions on the energy levels of native defects such as oxygen vacancies and their role in residual conductivity relative to extrinsic impurities.

(ii) Experimental efforts to obtain p-type conductivity, utilizing non-equilibrium doping methods such as ion implantation/cycled rapid thermal annealing. If polaron formation does preclude p-type conductivity in single films, can charge separation in heterostructures or other novel designs be used to obtain practical hole transport? Evidence of p-type conductivity ascribed to deep Ga vacancies has recently been reported.[757] It is also known that hydrogen has been found to be complexes with the V_{Ga} defect and acts to passivate this important deep acceptor.[758]

(iii) Continued development efforts in epi growth of β-$(Al_xGa_{1-x})_2O_3/Ga_2O_3$ and β-$(In_xGa_{1-x})_2O_3$ heterostructures growth on single crystal Ga_2O_3 substrates

to establish the stability regimes and compositional limits.

(iv) Continued progress in growth of large diameter, high quality EFG, CZ, and FZ crystals.

(v) Novel thermal management approaches for power devices discussed above, including layer lift-off and wafer transfer schemes to exploit the much higher thermal conductivities available with common heat-sink materials like Cu, SiC, or diamond. The design of power devices needs to incorporate accurate thermal modelling.

(vi) Improved Ohmic contacts through optimized surface cleaning, interface tailoring, and increased doping capabilities.

(vii) Surface passivation and encapsulation techniques for ensuring stable device operation.

(viii) Better understanding of carrier removal rates, dominant defects created, and transient dose effects resulting from radiation damage in Ga_2O_3 and related heterostructures.

(ix) Interface state density mitigation processes for dielectrics for MOS devices, as well as how these are affected by process/patterning and contacting conditions.[754] This holds for both conventional wafers and the membranes lifted-off by mechanical exfoliation.[754,755]

(x) Understanding the apparent p-type (hole) conductivity observed at high temperatures, mentioned earlier, tentatively ascribed to deep Ga vacancy acceptors present in the PLD material.[757]

ACKNOWLEDGMENTS

The work at UF is partially supported by HDTRA1-17-1-0011 (Jacob Calkins, monitor). The project or effort depicted is sponsored by the Department of the Defense, Defense Threat Reduction Agency. The content of the information does not necessarily reflect the position or the policy of the federal government, and no official endorsement should be inferred. The work at NRL was partially supported by DTRA Grant No. HDTRA1-17-1-0011 and the Office of Naval Research. The work at Korea University was supported by the Korea Institute of Energy Technology Evaluation and Planning (KETEP) and the Ministry of Trade, Industry and Energy (MOTIE) of Korea (Grant No. 20172010104830) and Space Core Technology Development Program (2017M1A3A3A02015033) through the National Research Foundation of Korea funded by the Ministry of Science, ICT and Future Planning of Korea. The authors thank their many valued colleagues for discussions and input, including Akito Kuramata from Tamura Corporation and Novel Crystal Technology, Leonid Chernyak and Jonathan Lee from University of Central Florida, Soohwan Jang from Dankook University, Kwang Baik from Hongik University, Rohit Khanna from PlasmTherm, and Chip Eddy, Jr., Neeraj Nepal, and Virginia Wheeler from Naval Research Laboratory.

[1]R. Roy, V. G. Hill, and E. F. Osburn, J. Am. Chem. Soc. **74**, 719 (1952).
[2]S. I. Stepanov, V. I. Nikolaev, V. E. Bougrov, and A. E. Romanov, Rev. Adv. Mater. Sci. **44**, 63 (2016); available at http://www.ipme.ru/e-journals/RAMS/no_14416/06_14416_stepanov.pdf.
[3]H. Von Wenckstern, Adv. Electron. Mater. **3**, 1600350 (2017).
[4]S. Yoshioka, H. Hayashi, A. Kuwabara, F. Oba, K. Matsunaga, and I. Tanaka, J. Phys.: Condens. Matter **19**, 346211 (2007).
[5]H. He, R. Orlando, M. A. Blanco, R. Pandey, E. Amzallag, I. Baraille, and M. Rérat, Phys. Rev. B **74**, 195123 (2006).
[6]H. He, M. A. Blanco, and R. Pandey, Appl. Phys. Lett. **88**, 261904 (2006).
[7]P. Kroll, R. Dronskowski, and M. Martin, J. Mater. Chem. **15**, 3296 (2005).
[8]H. Y. Playford, A. C. Hannon, E. R. Barney, and R. I. Walton, Chem.-A Eur. J. **19**, 2803 (2013).
[9]M. Saurat and A. Revcolevschi, Rev. Int. Hautes. Refract. **8**, 291 (1971).
[10]J. Kohn, G. Katz, and J. D. Broder, Am. Mineral. **42**, 398 (1956).
[11]J. Ahman, G. Svensson, and J. Albertson, Acta. Crystallogr. Sect. C Cryst. Struct. Commun. **52**, 1336 (1996).
[12]M. Higashiwaki, K. Sasaki, H. Murakami, Y. Kumagai, A. Koukitu, A. Kuramata, T. Masui, and S. Yamakosh, Semicond. Sci. Technol. **31**, 034001 (2016).
[13]M. Kim, J.-H. Seo, U. Singisetti, and Z. Ma, J. Mater. Chem. C **5**, 8338–8354 (2017).
[14]M. A. Mastro, A. Kuramata, J. Calkins, J. Kim, F. Ren, and S. J. Pearton, ECS J. Solid State Sci. Technol. **6**, P356 (2017).
[15]M. Higashiwaki, K. Sasaki, A. Kuramata, T. Masui, and S. Yamakoshi, Phys. Status Solidi A **211**, 21 (2014).
[16]M. Higashiwaki, H. Murakami, Y. Kumagai, and A. Kuramata, Jpn. J. Appl. Phys. **55**, 1202A1 (2016).
[17]S. Fujita, Jpn. J. Appl. Phys. **54**, 030101 (2015).
[18]M. Higashiwaki, A. Kuramata, H. Murakami, and Y. Kumagai, J. Phys. D: Appl. Phys. **50**, 333002 (2017).
[19]S. Jin, X. Wang, X. Wang, M. Ju, S. Shen, W. Liang, Y. Zhao, Z. Feng, H. Y. Playford, R. I. Walton, and C. Li, J. Phys. Chem. C **119**, 18221 (2015).
[20]See, for example, T. Miyata, T. Nakatani, and T. Minami, J. Lumin. **87–89**, 1183 (2000); Y. Li, T. Tokizono, M. Liao, M. Zhong, Y. Koide, I. Yamada, and J. J. Delaunay, Adv. Funct. Mater. **20**, 3972 (2010).
[21]M. Fleischer, W. Haurierder, and H. Meixner, Thin Solid Films **190**, 93 (1990).
[22]H. J. Lin, H. Gao, and P. X. Gao, Appl. Phys. Lett. **110**, 043101 (2017).
[23]H. J. Lin, J. P. Baltrus, H. Gao, Y. Ding, C. Y. Nam, P. Ohodnicki, and P. X. Gao, ACS Appl. Mater. Interfaces **8**, 8880–8887 (2016).
[24]L. Mazeina, F. K. Perkins, V. M. Bermudez, S. P. Arnold, and S. M. Prokes, Langmuir **26**, 13722–13726 (2010).
[25]M. Ogita, K. Higo, Y. Nakanishi, and Y. Hatanaka, Appl. Surf. Sci. **175**, 721 (2001).
[26]E. Aubay and D. Gourier, Phys. Rev. B **47**, 15023 (1993).
[27]L. Binet and D. Gourier, J. Phys. Chem. **100**, 17630 (1996).
[28]N. D. Cuong, Y. W. Park, and S. G. Yoon, Sens. Actuators, B **140**, 240 (2009).
[29]M. Marezio and J. P. Remeika, J. Chem. Phys. **46**, 1862 (1967).
[30]J. P. Remeika and M. Marezio, J. Am. Chem. Soc. **8**, 87 (1966).
[31]E. A. Albanesi, S. J. Sferco, I. Lefebvre, G. Allan, and G. Hollinger, Phys. Rev. B **46**, 13260 (1992).
[32]L. Binet, D. Gourier, and C. Minot, J. Solid State Chem. **113**, 420 (1994).
[33]Z. Hajnal, J. Miró, G. Kiss, F. Réti, P. Deák, R. C. Herndon, and J. M. Kuperberg, J. Appl. Phys. **86**, 3792 (1999).
[34]K. Yamaguchi, Solid State Commun. **131**, 739 (2004).
[35]L. J. Eckert and R. C. Bradi, J. Am. Ceram. Soc. **56**, 229 (1973).
[36]F. Litmein, D. Rached, R. Khenata, and H. Balache, J. Alloys Compd. **488**, 148 (2009).
[37]H. Peelaers and C. G. Van de Walle, Phys. Status Solidi B **252**, 828 (2015).
[38]J. B. Varley, A. Janotti, C. Franchini, and C. G. Van de Walle, Phys. Rev. B **85**, 081109 (2012).
[39]J. Furthmuller and F. Bechstedt, Phys. Rev. B **93**, 115204 (2016).
[40]Y. Zhang, J. Yan, G. Zhao, and W. Xie, Phys. B: Phys. Condens. Matter **405**, 3899 (2010).
[41]W. Guo, Y. Guo, H. Dong, and X. Zhou, Phys. Chem. Chem. Phys. **17**, 5817 (2015).
[42]H. H. Tippins, Phys. Rev. A **140**, 316 (1965).
[43]M. R. Lorentz, J. F. Woods, and R. J. Gambino, J. Phys. Chem. Solids **28**, 403 (1967).
[44]T. Matsumoto, M. Aoki, A. Kinoshita, and T. Aono, Jpn. J. Appl. Phys. **13**, 1578 (1974).

[45]C. Janowitz, V. Scherer, M. Mohamed, A. Krapf, H. Dwelk, R. Manzke, Z. Galazka, R. Uecker, K. Irmscher, R. Fornari, M. Michling, D. Schmeißer, J. R. Weber, J. B. Varley, and C. G. Van de Walle, New J. Phys. **13**, 085014 (2011).

[46]T. C. Lovejoy, E. N. Yitamben, N. Shamir, J. Morales, E. G. Víllora, K. Shimamura, S. Zheng, F. S. Ohuchi, and M. A. Olmstead, Appl. Phys. Lett. **94**, 081906 (2009).

[47]M. Mohamed, C. Janowitz, I. Unger, R. Manzke, Z. Galazka, R. Uecker, R. Fornari, J. R. Weber, J. B. Varley, and C. G. Van de Walle, Appl. Phys. Lett **97**, 211903 (2010).

[48]C.-H. Ho, C.-Y. Tseng, and L.-C. Tien, Opt. Express **18**, 16360 (2010).

[49]L. Dong, R. Jia, B. Xin, B. Peng, and Y. Zhang, Sci. Rep. **7**, 40160 (2017).

[50]Y. Zhuo, Z. Chen, W. Tu, X. Ma, Y. Pei, and G. Wang, Appl. Surf. Sci. **420**, 802 (2017).

[51]J. B. Varley, J. R. Weber, A. Janotti, and C. G. Van de Walle, Appl. Phys. Lett. **97**, 142106 (2010).

[52]X. Ma, Y. Zhang, L. Dong, and R. Jia, Results Phys. **7**, 1582 (2017).

[53]L. Dong, R. Jia, C. Li, B. Xin, and Y. Zhang, J. Alloys Compd. **712**, 379 (2017).

[54]M. J. Tadjer, M. A. Mastro, N. A. Mahadik, M. Currie, V. D. Wheeler, J. A. Freitas, Jr., J. D. Greenlee, J. K. Hite, K. D. Hobart, C. R. Eddy, Jr., and F. J. Kub, J. Electron. Mater. **45**, 2031 (2016).

[55]K. Irmscher, Z. Galazka, M. Pietsch, R. Uecker, and R. Fornari, J. Appl. Phys. **110**, 063720 (2011).

[56]F. Mezzadri, G. Calestani, F. Boschi, D. Delmonte, M. Bosi, and R. Fornari, Inorg. Chem. **55**, 12079 (2016).

[57]O. Ueda, N. Ikenaga, K. Koshi, K. Iizuka, A. Kuramata, K. Hanada, T. Moribayashi, S. Yamakoshi, and M. Kasu, Jpn. J. Appl. Phys. **55**, 1202BD (2016).

[58]S. Fujita, M. Oda, K. Kaneko, and T. Hitora, Jpn. J. Appl. Phys. **55**, 1202A3 (2016).

[59]Z. Galazka, R. Uecker, D. Klimm, K. Irmscher, M. Naumann, M. Pietsch, A. Kwasniewski, R. Bertram, S. Ganschow, and M. Bickermann, ECS J. Solid State Sci. Technol. **6**, Q3007 (2017).

[60]H. Y. Playford, A. C. Hannon, M. G. Tucker, D. M. Dawson, S. E. Ashbrook, R. J. Kastiban, J. Sloan, and R. I. Walton, J. Phys. Chem. C **118**, 16188 (2014).

[61]M. B. Maccioni and V. Fiorentini, Appl. Phys. Exp. **9**, 041102 (2016).

[62]D. Munima, B. Sahariah, and C. Y. Kadolkar, J. Phys.: Condens. Matter **19**, 156215 (2007).

[63]Y. Oshima, E. G. Villora, Y. Matsushita, S. Yamamoto, and K. Shimamura, J. Appl. Phys. **118**, 085301 (2015).

[64]X. Xia, Y. Chen, Q. Feng, H. Liang, P. Tao, M. Xu, and G. Du, Appl. Phys. Lett. **108**, 202103 (2016).

[65]M. Slomski, N. Blumenschein, P. P. Paskov, J. F. Muth, and T. Paskova, J. Appl. Phys. **121**, 235104 (2017).

[66]N. Ueda, H. Hosono, R. Waseda, and H. Kawazoe, Appl. Phys. Lett. **71**, 933 (1997).

[67]M. Schubert, R. Korlacki, S. Knight, T. Hofmann, S. Schöche, V. Darakchieva, E. Janzén, B. Monemar, D. Gogova, Q.-T. Thieu, R. Togashi, H. Murakami, Y. Kumagai, K. Goto, A. Kuramata, S. Yamakoshi, and M. Higashiwaki, Phys. Rev. B **93**, 125209 (2016).

[68]M. Yan-Mei, C. Hai-Yong, Y. Kai-Feng, L. Min, C. Qi-Liang, L. Jing, and Z. Guang-Tian, Chin. Phys. Lett. **25**, 1603 (2008).

[69]A. Kuramata, K. Koshi, S. Watanabe, Y. Yamaoka, T. Masui, and S. Yamakoshi, Jpn. J. Appl. Phys. Part 1 **55**, 1202A2 (2016).

[70]H. Aida, K. Nishiguchi, H. Takeda, N. Aota, K. Sunakawa, and Y. Yaguchi, Jpn. J. Appl. Phys. **47**(11R), 8506 (2008).

[71]T. Onuma, S. Saito, K. Sasaki, T. Masui, T. Yamaguchi, T. Honda, and M. Higashiwaki, Jpn. J. Appl. Phys. **54**, 112601 (2015).

[72]M. Baldini, M. Albrecht, A. Fiedler, K. Irmscher, R. Schewski, and G. Wagner, ECS J. Solid State Sci. Technol. **6**, Q3040 (2017).

[73]R. Schewski, G. Wagner, M. Baldini, D. Gogova, Z. Galazka, T. Schulz, T. Remmele, T. Markurt, H. von Wenckstern, M. Grundmann, O. Bierwagen, P. Vogt, and M. Albrecht, Appl. Phys. Express **8**, 011101 (2015).

[74]M. Choi and J. Son, Curr. Appl. Phys. **17**, 713 (2017).

[75]Z. Guo, A. Verma, X. Wu, F. Sun, A. Hickman, T. Masui, A. Kuramata, M. Higashiwaki, D. Jena, and T. Luo, Appl. Phys. Lett. **106**, 111909 (2015).

[76]S. Ohira and N. Arai, Phys. Status Solidi C **5**, 3116 (2008).

[77]T. Oshima, T. Okuno, N. Arai, Y. Kobayashi, and S. Fujita, Jpn. J. Appl. Phys. **48**, 040208 (2009).

[78]W. Mi, C. Luan, Z. Li, C. Zhao, X. Feng, and J. Ma, Opt. Mater. **35**, 2624 (2013).

[79]L. Liu, M. K. Li, D. Q. Yu, J. Zhang, H. Zhang, C. Qian, and Z. Yang, Appl. Phys. A **98**, 831 (2010).

[80]M. J. Tadjer, N. A. Mahadik, V. D. Wheeler, E. R. Glaser, L. Ruppalt, A. D. Koehler, K. D. Hobart, C. R. Eddy, Jr., and F. J. Kub, ECS J. Solid State Sci. Technol. **5**, 468 (2016).

[81]E. G. Villora, S. Arjoca, K. Shimamura, D. Inomata, and K. Aoki, "Light-Emitting Diodes: Materials, Devices, and Applications for Solid State Lighting XX," Proc. SPIE **9768**, 976805 (2016).

[82]H. Xie, L. Chen, Y. Liu, and K. Huang, Solid State Commun. **141**, 12 (2007).

[83]T. Tsuchiya, T. Matsuura, K. Shinoda, T. Nakajima, J. Akimoto, and Y. Idemoto, Jpn. J. Appl. Phys. **53**, 05FB14 (2014).

[84]K. Sasaki, Q. Tu Thieu, D. Wakimoto, Y. Koishikawa, A. Kuramata, and S. Yamakoshi, Appl. Phys. Express **10**, 124201 (2017).

[85]K. Momma and F. Izumi, J. Appl. Crystallogr. **41**, 653 (2008).

[86]H. Wang, "Investigation of power semiconductor devices for high frequency high density power converters," Ph.D. thesis (Virgina Tech, 2007).

[87]G. Jessen, K. Chabak, A. Green, J. McCandless, S. Tetlak, K. Leedy, R. Fitch, S. Mou, E. Heller, S. Badescu, A. Crespo, and N. Moser, "Toward realization of Ga_2O_3 for power electronics applications," in 75th IEEE Device Research Conference (DRC), 2017.

[88]V. M. Bermudez, Chem. Phys. **323**, 193 (2006).

[89]Y. Tomm, P. Reiche, D. Klimm, and T. Fukuda, J. Cryst. Growth **220**, 510 (2000).

[90]E. G. Víllora, Y. Murakami, T. Sugawara, T. Atou, M. Kikuchi, D. Shindo, and T. Fukuda, Mater. Res. Bull. **37**, 769 (2002).

[91]G. Schmitz, P. Gassmann, and R. Franchy, J. Appl. Phys. **83**, 2533 (1998).

[92]A. Segura, L. Artús, R. Cuscó, R. Goldhahn, and M. Feneberg, Phys. Rev. Mater. **1**, 024604 (2017).

[93]A. D. Becke, J. Chem. Phys. **98**, 5648 (1993).

[94]H. Fröhlich, H. Pelzer, and S. Zienau, Philos. Mag. **41**, 221 (1950).

[95]T. Onuma, S. Saito, K. Sasaki, K. Goto, T. Masui, T. Yamaguchi, T. Honda, A. Kuramata, and M. Higashiwaki, Appl. Phys. Lett. **108**, 101904 (2016).

[96]C. Sturm, J. Furthmüller, F. Bechstedt, R. Schmidt-Grund, and M. Grundmann, Appl. Phys. Lett. Mater. **3**, 106106 (2015).

[97]A. Ratnaparkhe and W. R. L. Lambrecht, Appl. Phys. Lett. **110**, 132103 (2017).

[98]B. Hoeneisen, C. A. Mead, and M. A. Nicolet, Solid-State Electron. **14**, 1057 (1971).

[99]H. Yusa, T. Tsuchiya, N. Sata, and Y. Ohishi, Phys. Rev. B **77**, 064107 (2008).

[100]M. Passlack, E. F. Schubert, W. S. Hobson, M. Hong, N. Moriya, S. N. G. Chu, K. Konstadinidis, J. P. Mannaerts, M. L. Schnoes, and G. J. Zydzik, J. Appl. Phys. **77**, 686 (1995).

[101]M. Rebien, W. Henrion, M. Hong, J. P. Mannaerts, and M. Fleischer, Appl. Phys. Lett. **81**, 250 (2002).

[102]I. Bhaumik, R. Bhatt, S. Ganesamoorthy, A. Saxena, A. K. Karnal, P. K. Gupta, A. K. Sinha, and S. K. Deb, Appl. Opt. **50**, 6006 (2011).

[103]*CRC Handbook of Chemistry and Physics*, 70th ed., edited by R. C. Weast (CRC, 1989), p. B-92.

[104]T. C. Lovejoy, E. N. Yitamben, N. Shamir, J. Morales, E. G. Villora, K. Shimamura, S. Zheng, F. S. Ohuchi, and M. A. Olmstead, Appl. Phys. Lett. **94**, 081906 (2009).

[105]H. Peelaers, D. Steiauf, J. B. Varley, A. Janotti, and C. G. Van de Walle, Phys. Rev. B **92**(8), 085206 (2015).

[106]T. J. Coutts, D. L. Young, and X. Li, MRS Bull. **25**, 58 (2000).

[107]L. Binet and D. Gourier, J. Phys. Chem. Solids **59**, 1241 (1998).

[108]K. W. Chang and J. J. Wu, Adv. Mater. **16**, 545 (2004).

[109]Z. Hajnal, P. Deák, Th. Köhler, R. Kaschner, and Th. Frauenheim, Solid State Commun. **108**, 93 (1998).

[110]T. Zacherle, P. C. Schmidt, and M. Martin, Phys. Rev. B **87**, 235206 (2013).

[111]S. Nakagomi, S. Kubo, and Y. Kokubun, J. Cryst. Growth **445**, 73 (2016).

[112]X. Cailleaux, M. del Carmen Marco de Lucas, O. Merdrignac-Conanec, F. Tessier, K. Nagasaka, and S. Kikkawa, J. Phys. D: Appl. Phys. **42**, 045408 (2009).

[113]Y. Xiang, C. Zhou, and W. Wang, J. Alloys Compd. **699**, 1192 (2017).

[114]A. Kaya, H. Mao, J. Gao, R. V. Chopdekar, Y. Takamura, S. Chowdhury, and M. Saif Islam, IEEE Trans. Electron Devices **64**, 2047 (2017).

[115]A. K. Chandiran, N. Tetreault, R. Humphry-Baker, F. Kessler, E. Baranoff, C. Yi, M. K. Nazeeruddin, and M. Grätzel, Nano Lett. **12**, 3941 (2012).
[116]J.-B. Yang, T.-C. Chang, J.-J. Huang, S.-C. Chen, and M.-J. Tsai, Thin Solid Films **529**, 200 (2013).
[117]T. C. Chang, F. Y. Jian, S. C. Chen, and Y. T. Tsai, Mater. Today **14**, 608 (2011).
[118]L. P. Ma, J. Liu, and Y. Yang, Appl. Phys. Lett. **80**, 2997 (2002).
[119]Y. E. Syu, T. C. Chang, T. M. Tsai, Y. C. Hung, K. C. Chang, M. J. Tsai, M. J. Kao, and S. M. Sze, IEEE Electron Device Lett. **32**, 545 (2011).
[120]L. W. Feng, Y. F. Chang, C. Y. Chang, T. C. Chang, S. Y. Wang, P. W. Chiang, C. C. Lin, S. C. Chen, and S. C. Chen, Thin Solid Films **519**, 1536 (2010).
[121]H. Shima, F. Takano, H. Muramatsu, H. Akinaga, I. H. Inoue, and H. Takagi, Appl. Phys. Lett. **92**, 043510 (2008).
[122]K. M. Kim, B. J. Choi, and C. S. Hwang, Appl. Phys. Lett. **90**, 242906 (2007).
[123]K. Jung, J. Choi, Y. Kim, H. Lm, S. Seo, R. Jung, D. C. Kim, J. S. Kim, B. H. Park, and J. P. Hong, J. Appl. Phys. **103**, 034504 (2008).
[124]T. Minami, H. Yamada, Y. Kubota, and T. Miyata, Jpn. J. Appl. Phys. **36**, L1191 (1997).
[125]T. Xiao, A. H. Kitai, G. Liu, A. Nakua, and J. Barbier, Appl. Phys. Lett. **72**, 3356 (1998).
[126]V. I. Vasyltsiv, Ya. I. Rym, and Ya. M. Zakharo, Phys. Stat. Sol. B **195**, 653 (1996).
[127]Z. Galazka, K. Irmscher, R. Uecker, R. Bertram, M. Pietsch, A. Kwasniewski, M. Naumann, T. Schulz, R. Schewski, D. Klimm, and M. Bickermann, J. Cryst. Growth **404**, 184 (2014).
[128]Z. Galazka, R. Uecker, K. Irmscher, M. Albrecht, D. Klimm, M. Pietsch, M. Brützam, R. Bertram, S. Ganschow, and R. Fornari, Cryst. Res. Technol. **45**, 1229 (2010).
[129]K. Irmscher, Z. Galazka, M. Pietsch, R. Uecker, and R. Fornari, J. Appl. Phys. **110**, 063720 (2011).
[130]E. G. Víllora, Y. Morioka, T. Atou, T. Sugawara, M. Kikuchi, and T. Fukuda, Phys. Status Solidi **A193**, 187 (2002).
[131]J. Zhang, B. Li, C. Xia, G. Pei, Q. Deng, Z. Yang, W. Xu, H. Shi, F. Wu, Y. Wu, and J. Xu, J. Phys. Chem. Solids **67**, 2448 (2006).
[132]N. Suzuki, S. Ohira, M. Tanaka, T. Sugawara, K. Nakajima, and T. Shishido, Phys. Status Solidi C **4**, 2310 (2007).
[133]S. Ohira, N. Suzuki, N. Arai, M. Tanaka, T. Sugawara, K. Nakajima, and T. Shishido, Thin Solid Films **516**, 5763 (2008).
[134]V. I. Vasyltsiv, Y. I. Rym, and Y. M. Zakharko, Phys. Status Solidi B **195**, 653 (1996).
[135]V. I. Nikolaev, V. Maslov, S. I. Stepanov, A. I. Pechnikov, and A. E. Romanov, J. Cryst. Growth **457**, 132 (2017).
[136]M. Mohamed, K. Irmscher, C. Janowitz, Z. Galazka, R. Manzke, and R. Fornari, Appl. Phys. Lett. **101**, 132106 (2012).
[137]K. Suzuki, T. Okamoto, and M. Takata, Ceram. Int. **30**, 1679 (2004).
[138]J. Zhang, C. Xia, Q. Deng, W. Xu, H. Shi, F. Wu, and J. Xu, J. Phys. Chem. Solids **67**, 1656 (2006).
[139]L. G. Bloor, C. J. Carmall, and D. Pugh, Coord. Chem. Rev. **255**, 1293 (2011).
[140]E. G. Villora, K. Shimamura, Y. Yoshikawa, K. Aoki, and N. Ichinose, J. Cryst. Growth **270**, 420 (2004).
[141]E. G. Villora, K. Shimamura, Y. Yoshikawa, T. Ujiie, and K. Aoki, Appl. Phys. Lett. **92**, 202120 (2008).
[142]E. G. Villora, K. Shimamura, T. Ujiie, and K. Aoki, Appl. Phys. Lett. **92**, 202118 (2008).
[143]M. Bäumer, D. Cappus, H. Kuhlenbeck, G. Brodde, and H. Neddermeyer, Surf. Sci. **253**, 116 (1991).
[144]K. Hoshikawa, E. Ohba, T. Kobayashi, J. Yanagisawa, C. Miyagava, and Y. Nakamura, J. Cryst. Growth **447**, 36 (2016).
[145]D. Klimm, S. Ganschow, D. Schulz, R. Bertram, R. Uecker, P. Reiche, and R. Fornari, J. Cryst. Growth **311**, 534 (2009).
[146]K. Hanada, T. Moribayashi, K. Koshi, K. Sasaki, A. Kuramata, O. Ueda, and M. Kasu, Jpn. J. Appl. Phys. **55**, 1202BG (2016).
[147]F. Zhang, K. Saito, T. Tanaka, M. Nishio, and Q. Guo, Solid State Commun. **186**, 28 (2014).
[148]K. Nakai, T. Nagai, K. Noami, and T. Futagi, Jpn J. Appl. Phys. **54**, 015201 (2015).
[149]F. Alema, B. Hertog, A. Osinsky, P. Mukhopadhyay, M. Toporkov, and W. V. Schoenfeld, J. Cryst. Growth **475**, 77 (2017).
[150]D. Gogova, G. Wagner, M. Baldini, M. Schmidbauer, K. Irmscher, R. Schewski, Z. Galazka, M. Albrecht, and R. Fornari, J. Cryst. Growth **401**, 665 (2014).
[151]S. Rafique, L. Han, M. J. Tadjer, J. A. Freitas, Jr., N. A. Mahadik, and H. Zhao, Appl. Phys. Lett. **108**, 182105 (2016).
[152]G. Wagner, M. Baldini, D. Gogova, M. Schmidbauer, R. Schewski, M. Albrecht, Z. Galazka, D. Klimm, and R. Fornari, Phys. Status Solidi A **211**, 27 (2014).
[153]H. W. Kim and N. H. Kim, Mater. Sci. Eng. B **110**, 34 (2004).
[154]J. Wager, Science **300**(5623), 1245 (2003).
[155]N. M. Sbrockey, T. Salagaj, E. Coleman, G. S. Tompa, Y. Moon, and M. S. Kim, J. Electron. Mater. **44**, 1357 (2015).
[156]R. Schewski, M. Baldini, K. Irmscher, A. Fiedler, T. Markurt, B. Neuschulz, T. Remmele, T. Schulz, G. Wagner, Z. Galazka, and M. Albrecht, J. Appl. Phys. **120**, 225308 (2016).
[157]M. Baldini, M. Albrecht, A. Fiedler, K. Irmscher, D. Klimm, R. Schewski, and G. Wagner, J. Mater. Sci. **51**, 3650 (2016).
[158]M. Baldini, M. Albrecht, D. Gogova, R. Schewski, and G. Wagner, Semicond. Sci. Technol. **30**, 024013 (2015).
[159]L. M. Lin, Y. Luo, P. T. Lai, and K. M. Lau, Thin Solid Films **515**, 2111 (2006).
[160]Y. Chen, H. Liang, X. Xia, R. Shen, Y. Liu, Y. Luo, and G. Du, Appl. Surf. Sci. **325**, 258 (2015).
[161]W. Mi, C. Luan, Z. Li, C. Zhao, and J. Ma, Mater. Lett. **107**, 83 (2013).
[162]Y. Lv, J. Ma, W. Mi, C. Luan, Z. Zhu, and H. Xiao, Vacuum **86**, 1850 (2012).
[163]X. J. Du, Z. Li, C. N. Luan, W. G. Wang, M. X. Wang, X. J. Feng, H. D. Xiao, and J. Ma, J. Mater. Sci. **50**, 3252 (2015).
[164]H. Murakami, K. Nomura, K. Goto, K. Sasaki, K. awara, Q. Tu Thieu, R. Togashi, Y. Kumagai, M. Higashiwaki, A. Kuramata, S. Yamakoshi, B. Monemar, and A. Koukitu, Appl. Phys. Express **8**, 015503 (2015).
[165]V. I. Nikolaev, A. I. Pechnikov, S. I. Stepanov, I. P. Nikitina, A. N. Smirnov, A. V. Chikiryaka, S. S. Sharofidinov, V. E. Bougrov, and A. E. Romanov, Mater. Sci. Semicond. Process **47**, 16 (2016).
[166]L. Kong, J. Ma, C. Luan, and Z. Zhu, J. Solid State Chem. **184**, 1946 (2011).
[167]Y. Oshima, E. G. Víllora, and K. Shimamura, J. Cryst. Growth **410**, 53 (2015).
[168]W. Mi, Z. Li, C. Luan, H. Xiao, and J. Ma, Ceram. Int. **41**, 2572 (2015).
[169]Y. Takiguchi and S. Miyajima, J. Cryst. Growth **468**, 129 (2017).
[170]F. Mezzadri, G. Calestani, F. Boschi, D. Delmonte, M. Bosi, and R. Fornari, Inorg. Chem. **55**, 12079–12084 (2016).
[171]B. Kramm, A. Laufer, D. Reppin, A. Kronenberger, P. Hering, A. Polity, and B. K. Meyer, Appl. Phys. Lett. **100**, 094102 (2012).
[172]F. Boschi, M. Bosi, T. Berzina, E. Buffagni, C. Ferrari, and R. Fornari, J. Cryst. Growth **443**, 25 (2016).
[173]G. Sinha, K. Adhikary, and S. Chauduri, J. Cryst. Growth **276**, 204 (2004).
[174]H. Akazawa, Vacuum **123**, 8 (2016).
[175]H. W. Kim and N. H. Kim, J. Alloy. Compd. **389**, 177 (2005).
[176]A. Navarro-Quezada, Z. Galazka, S. Alamé, D. Skuridina, and N. Esser, Appl. Surf. Sci. **349**, 368 (2015).
[177]Y. Oshima, E. G. Víllora, and K. Shimamura, Appl. Phys. Express **8**, 055501 (2015).
[178]T. Watahiki, Y. Yuda, A. Furukawa, M. Yamamuka, Y. Takiguchi, and S. Miyajima, Appl. Phys. Lett. **111**, 222104 (2017).
[179]S. Jie, L. Tong, L. Jingming, Y. Jun, S. Guiying, B. Yongbiao, D. Zhiyuan, and Z. Youwen, J. Semicond. **37**, 103004 (2016).
[180]H. Murakami, K. Nomura, K. Goto, K. Sasaki, K. Kawara, Q. T. Thieu, R. Togashi, Y. Kumagai, M. Higashiwaki, A. Kuramata, S. Yamakoshi, B. Monemar, and A. Koukitu, Appl. Phys. Express **8**, 015503 (2015).
[181]K. Nomura, K. Goto, R. Togashi, H. Murakami, and A. Koukitu, J. Cryst. Growth **405**, 19 (2014).
[182]M. Orita, H. Ohta, M. Hirano, and H. Hosono, Appl. Phys. Lett. **77**, 4166 (2000).
[183]A. Petitmangin, B. Gallas, C. Hebert, J. Perrière, L. Binet, P. Barboux, and X. Portier, Appl. Surf. Sci. **278**, 153 (2013).
[184]W. Seiler, M. Selmane, K. Abdelouhadi, and J. Perrière, Thin Solid Films **589**, 556 (2015).
[185]S. Penner, M. Stöger-Pollach, F. Klauser, H. Lorenz, B. Klötzer, X. Liu, B. Jenewein, and E. Bertel, Mater. Chem. Phys. **116**, 175 (2009).
[186]K. Matsuzaki, H. Hiramatsu, K. Nomura, H. Yanagi, T. Kamiya, M. Hirano, and H. Hosono, Thin Solid Films **496**, 37 (2006).
[187]M. Orita, H. Hiramatsu, H. Ohta, M. Hirano, and H. Hosono, Thin Solid Films **411**, 134 (2002).

[188]L. M. Garten, A. Zakutayev, J. D. Perkins, B. P. Gorman, P. F. Ndione, and D. S. Ginley, MRS Commun. **6**, 348 (2016).
[189]F. B. Zhang, K. Saito, T. Tanaka, M. Nishio, and Q. X. Guo, J. Mater. Sci.: Mater. Electron. **26**, 9624 (2015).
[190]S. Müller, H. von Wenckstern, D. Splith, F. Schmidt, and M. Grundmann, Phys. Status Solidi A **211**, 34 (2014).
[191]F.-P. Yu, S.-L. Ou, and D.-S. Wuu, Opt. Mater. Exp. **5**, 1240 (2015).
[192]K. D. Leedy, K. D. Chabak, V. Vasilyev, D. C. Look, J. J. Boeckl, J. L. Brown, S. E. Tetlak, A. J. Green, N. A. Moser, A. Crespo, D. B. Thomson, R. C. Fitch, J. P. McCandless, and G. H. Jessen, Appl. Phys. Lett. **111**, 012103 (2017).
[193]L. Nagarajan, R. A. De Souza, D. Samuelis, I. Valov, A. Börger, J. Janek, K. D. Becker, P. C. Schmidt, and M. Martin, Nat. Mater. **7**, 391 (2008).
[194]C. Hebert, A. Petitmangin, J. Perrière, E. Millon, A. Petit, L. Binet, and P. Barboux, Mater. Chem. Phys. **133**, 135 (2012).
[195]Z. Chen, X. Wang, S. Noda, K. Saito, and Q. Guo, Superlattices Microstruct. **90**, 207 (2016).
[196]T. Kawaharamura, Jpn. J. Appl. Phys. **53**, 05FF08 (2014).
[197]S-D. Lee, K. Kaneko, and S. Fujita, Jpn. J. Appl. Phys. **55**, 1202B8 (2016).
[198]T. Kawaharamura, G. T. Dang, and M. Furuta, Jpn. J. Appl. Phys. **51**, 040207 (2012).
[199]G. T. Dang, T. Kawaharamura, M. Furuta, and M. W. Allen, IEEE Electron Device Lett. **36**, 463 (2015).
[200]S. Fujita and K. Kaneko, J. Cryst. Growth **401**, 588 (2014).
[201]K. Akaiwa and S. Fujita, Jpn. J. Appl. Phys. **51**, 070203 (2012).
[202]D. Shinohara and S. Fujita, Jpn. J. Appl. Phys. **47**, 7311 (2008).
[203]K. Kaneko, H. Kawanowa, H. Ito, and S. Fujita, Jpn. J. Appl. Phys. **51**, 020201 (2012).
[204]D. Tahara, H. Nishinaka, S. Morimoto, and M. Yoshimoto, Jpn. J. Appl. Phys. **56**, 078004 (2017).
[205]H. Nishinaka, D. Tahara, S. Morimoto, and M. Yoshimoto, Mater. Lett. **205**, 28 (2017).
[206]T. Oshima, T. Nakazono, A. Mukai, and A. Ohtomo, J. Cryst. Growth **359**, 60 (2012).
[207]H. Nishinaka, D. Tahara, and M. Yoshimoto, Jpn. J. Appl. Phys. **55**, 1202BC (2016).
[208]R. Jinno, T. Uchida, K. Kaneko, and S. Fujita, Appl. Phys. Express **9**, 071101 (2016).
[209]See https://www.ut-ec.co.jp/english/portfolio/flosfia for information on applications of Gallium Oxide rectifiers; See also https://spectrum.ieee.org/semiconductors/materials/gallium-oxide-power-electronics-cool-new-flavor for information on power electronics applications.
[210]K. Sasaki, A. Kuramata, T. Masui, E. G. Villora, K. Shimamura, and S. Yamakoshi, Appl. Phys. Express **5**, 035502 (2012).
[211]K. Sasaki, M. Higashiwaki, A. Kuramata, T. Masui, and S. Yamakoshi, J. Cryst. Growth **392**, 30 (2014).
[212]T. Oshima, T. Okuno, and S. Fujita, Jpn. J. Appl. Phys. **46**, 7217 (2007).
[213]K. Sasaki, M. Higashiwaki, A. Kuramata, T. Masui, and S. Yamakoshi, J. Cryst. Growth **378**, 591 (2013).
[214]H. Okumura, M. Kita, K. Sasaki, A. Kuramata, M. Higashiwaki, and J. S. Speck, Appl. Phys. Express **7**, 095501 (2014).
[215]T. Oshima, N. Arai, N. Suzuki, S. Ohira, and S. Fujita, Thin Solid Films **516**, 5768– 5771 (2008).
[216]A. S. Pratiyush, S. Krishnamoorthy, S. Vishnu Solanke, Z. Xia, R. Muralidharan, S. Rajan, and D. N. Nath, Appl. Phys. Lett. **110**, 221107 (2017).
[217]D-w. Choi, K.-B. Chung, and J.-S. Park, Thin Solid Films **546**, 31 (2013).
[218]C. L. Dezelah, IV, J. Niinisto, K. Arstila, L. Niinisto, and C. H. Winter, Chem. Mater. **18**, 471 (2006).
[219]T. Hisatomi, J. Brillet, M. Cornuz, F. LeFormal, N. Tetreault, K. Sivula, and M. Gratzel, Faraday Discuss. **155**, 223 (2012).
[220]G. X. Liu, F. K. Shan, J. J. Park, W. J. Lee, G. H. Lee, I. S. Kim, B. C. Shin, and S. G. Yoon, J. Electroceram. **17**, 145 (2006).
[221]G. A. Battiston, R. Gerbasi, M. Porchia, R. Bertoncello, and F. Caccavale, Thin Solid Films **279**, 115 (1996).
[222]M. Valet and D. M. Hoffman, Chem. Mater. **13**, 2135 (2001).
[223]R. Binions, C. J. Carmalt, I. P. Parkin, K. F. E. Pratt, and G. A. Shaw, Chem. Mater. **16**, 2489 (2004).
[224]M. Valet and D. M. Hoffman, Chem. Mater. **13**, 2135 (2001).
[225]V. Gottschalch, K. Mergenthaler, G. Wagner, J. Bauer, H. Paetzelt, C. Sturm, and U. Teschner, Phys. Status Solidi A **206**, 243 (2009).
[226]H. Altuntas, I. Donmez, C. Ozgit-Akgun, and N. Biyikli, J. Alloys Compd. **593**, 190 (2014).
[227]P. C. Chang, Z. Fan, W. Y. Tseng, A. Rajagopal, and J. G. Lu, Appl. Phys. Lett. **87**, 222102 (2005).
[228]R. S. Wagner and W. C. Ellis, Appl. Phys. Lett. **4**, 89 (1964).
[229]K. K. Cho, G. B. Cho, K. W. Kim, and K. S. Ryu, Phys. Scr. T **2010**, 014079 (2010).
[230]L.-W. Chang, T.-Y. Lu, Y.-L. Chen, J.-W. Yeh, and H. C. Shih, Mater. Lett. **65**, 2281 (2011).
[231]K. H. Choi, K. K. Cho, G. B. Cho, H. J. Ahn, and K. W. Kim, J. Cryst. Growth **311**, 1195 (2009).
[232]B. Fernandes, M. Hegde, P. C. Stanish, Z. L. Mišković, and P. V. Radovanovic, Chem. Phys. Lett. **684**, 135 (2017).
[233]X. Liu, G. Qiu, Y. Zhao, N. Zhang, and R. Yi, J. Alloys Compd. **439**, 275 (2007).
[234]G. Meligrana, W. Lueangchaichaweng, F. Colò, M. Destro, and C. Gerbaldi, Electrochim. Acta **235**, 143 (2017).
[235]L. Feng, Y. Li, X. Su, S. Wang, H. Liu, J. ang, Z. Gong, W. Ding, Y. Zhang, and F. Yun, Appl. Surf. Sci. **389**, 205 (2016).
[236]A. H. A. Makinudin, T. M. Bawazeer, N. Alsenany, M. S. Alsoufi, and A. Supangat, Mater. Lett. **194**, 53 (2017).
[237]E. Auer, A. Lugstein, S. Löffler, Y. J. Hyun, W. Brezna, E. Bertagnolli, and P. Pongratz, Nanotechnology **20**, 434017 (2009).
[238]F. Zhu, Z. X. Yang, W. M. Zhou, and Y. F. Zhang, Solid State Commun. **137**, 177 (2006).
[239]Y. Huang, S. Yue, Z. Wang, Q. Wang, C. Shi, Z. Xu, X. D. Bai, C. Tang, and C. Gu, Phys. Chem. B **110**, 796 (2006).
[240]K. F. Cai, S. Shen, C. Yan, and S. Bateman, Curr. Appl. Phys. **8**, 363 (2008).
[241]S. P. Arnold, S. M. Prokes, F. K. Perkins, and M. E. Zaghloul, Appl. Phys. Lett. **95**, 103102 (2009).
[242]L. Mazeina, F. K. Perkins, V. M. Bermudez, S. P. Arnold, and S. M. Prokes, Langmuir **26**, 13722 (2010).
[243]E. Nogales, B. Méndez, and J. Piqueras, Ultramicroscopy **111**, 1037 (2011).
[244]L. Mazeina, Y. N. Picard, S. I. Maximenko, F. K. Perkins, E. R. Glaser, M. E. Twigg, J. A. Freitas, Jr., and S. M. Prokes, Cryst. Growth Des. **9**, 4471 (2009).
[245]L. Li, E. Auer, M. Y. Liao, X. S. Fang, T. Y. Zhai, U. K. Gautam, A. Lugstein, Y. Koide, Y. Bando, and D. Golberg, Nanoscale **3**, 1120 (2011).
[246]Q. T. Thieu, D. Wakimoto, Y. Koishikawa, K. Sasaki, K. Goto, K. Konishi, H. Murakami, A. Kuramata, Y. Kumagai, and S. Yamakoshi, Jpn. J. Appl. Phys. **56**, 110310 (2017).
[247]C. H. Hsieh, L. J. Chou, G. R. Lin, Y. Bando, and D. Golberg, Nano Lett. **8**, 3081 (2008).
[248]E. Filippo, M. Tepore, F. Baldassarre, T. Siciliano, and A. Tepore, Appl. Surf. Sci. **338**, 69 (2015).
[249]S. Kumar, G. Sarau, C. Tessarek, M. Y. Bashouti, A. Hähnel, S. Christiansen, and R. Singh, J. Phys. D: Appl. Phys. **47**, 435101 (2014).
[250]M. Kumar, S. Kumar, N. Chauhan, D. S. Kumar, V. Kumar, and R. Singh, Semicond. Sci. Technol. **32**, 085012 (2017).
[251]Y. Guo, J. Zhang, F. Zhu, Z. X. Yang, and J. Yu, Appl. Surf. Sci. **254**, 5124 (2008).
[252]H. Z. Zhang, Y. C. Kong, Y. Z. Wang, X. Due, Z. G. Bai, J. J. Wang, D. P. Yu, Y. Ding, Q. L. Hang, and S. Q. Feng, Solid State Commun. **109**, 677 (1999).
[253]Y. C. Choi, W. S. Kim, Y. S. Park, S. M. Lee, D. J. Bae, Y. H. Lee, G.-S. Park, W. B. Choi, N. S. Lee, and J. M. Kim, Adv. Mater. **12**, 746 (2000).
[254]J. Q. Hu, Q. Li, X. M. Meng, C. S. Lee, and S. T. Lee, J. Phys. Chem. B **106**, 9536 (2002).
[255]C. H. Liang, G. W. Meng, G. Z. Wang, Y. W. Wang, and L. D. Zhang, Appl. Phys. Lett. **78**, 3202 (2001).
[256]M. C. Johnson, S. Aloni, D. E. McCready, and E. D. Bourret-Courchesne, Cryst. Growth Des. **6**, 1936 (2006).
[257]A. K. Narayana Swamy, E. Shafirovich, and C. V. Ramana, Ceram. Int. **39**, 7223 (2013).
[258]J. Zhang, Z. Liu, C. Lin, and J. Lin, J. Cryst. Growth **280**, 99 (2005).
[259]W.-S. Jung, H. U. Joo, B.-K. Min, K. W. Chang, and J. J. Wu, Physica E **36**, 226 (2007).
[260]N. D. Cuong, Y. W. Park, and S. G. Yoon, Sens. Actuators B **140**, 240 (2009).
[261]J.-Y. Jung, W.-S. Cho, J.-H. Kim, K.-T. Hwang, E. T. Kang, and K.-S. Han, Ceram. Int. **42**, 2582 (2016).

[262]K. W. Chang and J. J. Wu, Phys. Chem. B **108**, 1838 (2004).
[263]M. Baldini, M. Albrecht, A. Fiedler, K. Irmscher, D. Klimm, R. Schewski, and G. Wagner, J. Materials Sci. **51**, 3650–3656 (2016).
[264]G. Martínez-Criado, J. Segura-Ruiz, M. H. Chu, R. Tucoulou, I. Lopez, E. Nogales, B. Mendez, and J. Piqueras, Nano Lett. **14**, 5479 (2014).
[265]Y. Luo, Z. Hou, J. Gao, D. Jin, and X. Zheng, Mater. Sci. Eng: B **140**, 123 (2007).
[266]T. Terasako, Y. Kawasaki, and M. Yagi, Thin Solid Films **620**, 23 (2016).
[267]C. L. Kuo and M. H. Huang, Nanotechnology **19**, 155604 (2008).
[268]Z. R. Dai, Z. W. Pan, and Z. L. Wang, J. Phys. Chem. B **106**, 902 (2002).
[269]Z. W. Pan, Z. R. Dai, and Z. L. Wang, Science **291**, 1947 (2001).
[270]J.-S. Hwang, T.-Y. Liu, S. Chattopadhyay, G.-M. Hsu, A. M. Basilio, H.-W. Chen, Y.-K. Hsu, W.-H. Tu, Y.-G. Lin, K.-H. Chen, C.-C. Li, S.-B. Wang, H.-Y. Chen, and L.-C. Chen, Nanotechnology **24**, 055401 (2013).
[271]G. Sinha, A. Dutta, S. K. Panda, P. G. Chavan, M. A. More, D. S. Joag, and A. Patra, J. Phys. D: Appl. Phys. **42**, 185409 (2009).
[272]C. Li, C. Gu, Z. Liu, J. Mi, and Y. Yang, Chem. Phys. Lett. **411**, 198 (2005).
[273]Z. Li, B. Zhao, P. Liu, and Y. Zhang, Microelectron. Eng. **85**, 1613 (2008).
[274]Z. Zhu, T. L. Chen, Y. Gu, J. Warren, and R. M. Osgood, Chem. Mater. **17**, 4227 (2005).
[275]J. L. Johnson, Y. Choi, and A. Ural, J. Vac. Sci. Technol. B **26**, 1841 (2008).
[276]M. Kumar, V. Kumar, and R. Singh, Nano Res. Lett. **12**, 184 (2017).
[277]S. Kumar and R. Singh, Phys. Status Solidi. Rapid Res. Lett. **7**, 781 (2013).
[278]S. Kumar, C. Tessarek, S. Christiansen, and R. Singh, J. Alloys Compd. **587**, 812 (2014).
[279]M. López, M. Alonso-Orts, E. Nogales, B. Méndez, and J. Piqueras, Semicond. Sci. Technol. **31**, 115003 (2016).
[280]L. Mazeina, Y. N. Picard, and S. M. Prokes, Cryst. Growth Des. **9**, 1164 (2009).
[281]M. Suh, M. Meyyappan, and S. Ju, Nanotechnology **23**, 305203 (2012).
[282]S. Phumying, S. Labauyai, W. Chareonboon, S. Phokha, and S. Maensiri, Jpn. J. Appl. Phys. **54**, 06FJ13 (2015).
[283]I. D. Hosein, M. Hegde, P. D. Jones, V. Chirmanov, and P. V. Radovanovic, J. Cryst. Growth **396**, 24 (2014).
[284]X. Xu, M. Lei, K. Huang, C. Liang, and W. H. Tang, J. Alloys Compd. **623**, 24 (2015).
[285]G. Gundiah, A. Govindaraj, and C. N. R. Rao, Chem. Phys. Lett. **351**, 189 (2002).
[286]J. Jie, C. Wu, Y. Yu, L. Wang, and Z. Hu, Nanotechnology **20**, 075602 (2009).
[287]M. Kumar, G. Sarau, M. Heilmann, S. Christiansen, V. Kumar, and R. Singh, J. Phys. D: Appl. Phys. **50**, 035302 (2017).
[288]E. Nogales, J. A. Garcia, B. Mendez, and J. Piqueras, J. Appl. Phys. **101**, 033517 (2007).
[289]E. Nogales, B. Mendez, J. Piqueras, and J. A. Garcia, Nanotechnology **20**, 115201 (2009).
[290]I. Lopez, E. Nogales, B. Mendez, J. Piqueras, A. Peche, J. Ramírez-Castellanos, and J. M. Gonzalez-Calbet, J. Phys. Chem. C **117**, 3036 (2013).
[291]X.-S. Wang, W.-S. Li, J.-Q. Situ, X.-Y. Ying, H. Chen, Y. Jin, and Y.-Z. Du, RSC Adv. **5**, 12886 (2015).
[292]E. Nogales, J. A. Garcia, B. Mendez, and J. Piqueras, Appl. Phys. Lett. **91**, 133108 (2007).
[293]E. Nogales, P. Hidalgo, K. Lorenz, B. Méndez, J. Piqueras, and E. Alves, Nanotechnology **22**, 285706 (2011).
[294]I. Lopez, E. Nogales, B. Mendez, and J. Piqueras, Appl. Phys. Lett. **100**, 261910 (2012).
[295]C. Ronning, C. Borschel, S. Geburt, and R. Niepelt, Mater. Sci. Eng. R **70**, 30 (2010).
[296]J. B. Goodenough and A. Manthiram, MRS Commun. **4**, 135 (2014).
[297]T. Harwig and F. Kellendonk, J. Solid State Chem. **24**, 255 (1978).
[298]M. A. Blanco, M. B. Sahariah, H. Jiang, A. Costales, and R. Pandey, Phys. Rev. B **72**, 184103 (2005).
[299]G. Sinha, D. Ganguli, and S. Chaudhuri, J. Phys.: Condens. Matter **18**, 11167 (2006).
[300]J. Wang, H. Zhuang, X. Zhang, S. Zhang, and J. Li, Vacuum **85**, 802 (2011).
[301]T. Shao, P. Zhang, L. Jin, and Z. Li, Appl. Catal. B: Environ. **142/143**, 654 (2013).
[302]A. Singhal and I. Lieberwirth, Mater. Lett. **161**, 112 (2015).
[303]S. Kumar and R. Singh, Phys. Status Solidi Rapid Res. Lett. **7**, 781 (2013).
[304]N. Boukhari, B. Abidri, S. Hiadsi, D. Rached, M. Rabah, H. Rached, and A. Abdellaoui, Comput. Mater. Sci. **50**(7), 1965–1972 (2011).
[305]J. E. Medvedeva, Europhys. Lett. **78**, 57004 (2007).
[306]C. Vigreux, L. Binet, D. Gourier, and B. Piriou, J. Solid State Chemistry **157**(1), 94–101 (2001).
[307]Z. Hajnal, Á. Gali, J. Miro, and P. Deak, Phys. Status Solidi A **171**(2), R5–R8 (1999).
[308]K. A. Klinedinst and D. A. Stevenson, J. Chem. Thermodyn. **4**, 565 (1972).
[309]T. Onuma, S. Fujioka, T. Yamaguchi, Y. Itoh, and T. Honda, J. Cryst. Growth **401**, 330 (2014).
[310]Y. Usui, T. Oya, G. Okada, N. Kawaguchi, and T. Yanagida, Mater. Res. Bull. **90**, 266 (2017).
[311]S. Rafique, L. Han, S. Mou, and H. Zhao, Opt. Mater. Express **7**, 3561 (2017).
[312]Y. S. Choi, J. W. Kang, D. K. Hwang, and S. J. Park, IEEE Trans. Electron Devices **57**, 26 (2010).
[313]S. J. Pearton and F. Ren, Int. Mater. Rev. **59**, 61 (2014).
[314]S. J. Pearton and F. Ren, Curr. Opin. Chem. Eng. **3**, 51 (2014).
[315]E. M. C. Fortunato, P. M. C. Barquinha, and R. F. P. Martins, Adv. Mater. **24**, 2945 (2012).
[316]S.-Y. Sung, J. H. Choi, U. B. Han, K. C. Lee, J.-H. Lee, J.-J. Kim, W. Lim, S. J. Pearton, D. P. Norton, and Y.-W. Heo, Appl. Phys. Lett. **96**, 102107 (2010).
[317]Y.-L. Wang, H. S. Kim, D. P. Norton, S. J. Pearton, and F. Ren, Appl. Phys. Lett. **92**, 112101 (2008).
[318]Y. L. Wang, F. Ren, H. S. Kim, S. J. Pearton, and D. P. Norton, Appl. Phys. Lett. **90**, 092116 (2007).
[319]Y. L. Wang, H. S. Kim, D. P. Norton, S. J. Pearton, and F. Ren, Electrochem. Solid-State Lett. **11**, H88-H91 (2008).
[320]Y. Q. Wu, S. Gao, and H. Huang, Mater. Sci. Semicond. Proc. **71**, 321 (2017).
[321]J. Y. Tsao, S. Chowdhury, M. A. Hollis, D. Jena, N. M. Johnson, K. A. Jones, R. J. Kaplar, S. Rajan, C. G. Van de Walle, E. Bellotti, C. L. Chua, R. Collazo, M. E. Coltrin, J. A. Cooper, K. R. Evans, S. Graham, T. A. Grotjohn, E. R. Heller, M. Higashiwaki, M. S. Islam, P. W. Juodawlkis, M. A. Khan, A. D. Koehler, J. H. Leach, U. K. Mishra, R. J. Nemanich, R. C. N. Pilawa-Podgurski, J. B. Shealy, M. J. Tadjer, A. F. Witulski, M. Wraback, and J. A. Simmons, "Adv. Electron. Mater. (published online).
[322]B. Bayraktaroglu, "Assessment of gallium oxide technology," Air Force Research Laboratory Report No. AFRL-RY-WP-TR-2017-0167, 2017.
[323]K. D. Chabak, J. K. Gillespie, V. Miller, A. Crespo, J. Roussos, M. Trejo, D. E. Walker, Jr., G. D. Via, G. H. Jessen, and J. Wasserbauer, IEEE Electron Device Lett. **31**, 99 (2010).
[324]M. J. Tadjer, T. J. Anderson, K. D. Hobart, T. I. Feygelson, J. D. Caldwell, C. R. Eddy, Jr., F. J. Kub, J. E. Butler, B. Pate, and J. Melngailis, IEEE Electron Device Lett. **33**, 23 (2012).
[325]P.-C. Chao, K. Chu, C. Creamer, J. Diaz, T. Yurovchak, M. Shur, R. Kallaher, C. McGray, G. D. Via, and J. D. Blevins, IEEE Trans. Electron Device **62**, 3658 (2015).
[326]M. R. Lorenz, J. F. Woods, and R. J. Gambino, J. Phys. Chem. Solids **28**, 403 (1967).
[327]K. Nakai, T. Nagai, K. Noami, and T. Futagi, Jpn. J. Appl. Phys. **54**, 051103 (2015).
[328]M. Grundmann, F. Klüpfel, R. Karsthof, P. Schlupp, F.-L. Schein, D. Splith, C. Yang, S. Bitter, and H. von Wenckstern, J. Phys. D: Appl. Phys. **49**, 213001 (2016).
[329]K. H. L. Zhang, K. Xi, M. G. Blamire, and R. G. Egdell, J. Phys.: Condens. Matter **28**, 383002 (2016).
[330]T. Oshima, K. Kaminaga, A. Mukai, K. Sasaki, T. Maui, A. Kuramata, S. Yamakoshi, S. Fujita, and A. Ohtomo, Jpn. J. Appl. Phys. **52**, 051101 (2013).
[331]G. A. Battiston, R. Gerbasi, M. Porchia, R. Bertoncello, and F. Caccavale, Thin Solid Films **279**, 115 (1996).
[332]Y. Li, C. Yang, L. Wu, and R. Zhang, Mod. Phys. Lett. B **31**, 1750172 (2017).
[333]Y. Kang, K. Krishnaswamy, H. Peelaers, and C. G. Van de Walle, J. Phys.: Condens. Matter **29**, 234001 (2017).
[334]E. Ahmadi, O. S. Koksaldi, S. W. Kaun, Y. Oshima, D. B. Short, U. K. Mishra, and J. S. Speck, Appl. Phys. Express **10**, 041102 (2017).
[335]X. J. Du, W. Mi, M. Jin *et al.* J. Cryst. Growth **404**, 75–79 (2014).
[336]K. Lorenz, M. Peres, M. Felizardo, J. G. Correia, L. C. Alves, E. Alves, I. López, E. Nogales, B. Méndez, J. Piqueras, M. B. Barbosa, J. P. Araújo,

J. N. Gonçalves, J. Rodrigues, L. Rino, T. Monteiro, E. G. Villora, and K. Shimamura, Proc. SPIE **8987**, 89870M (2014).
[337]K. Sasaki, M. Higishiwaki, A. Kuramata, T. Matsui, and S. Yamakoshi, Appl. Phys. Express **6**, 086502 (2013).
[338]M. Higashiwaki, K. Sasaki, A. Kuramata, T. Masui, and S. Yamakoshi, Appl. Phys. Lett. **100**, 013504 (2012).
[339]K. Takakura, S. Funasaki, I. Tsunoda, H. Ohyama, D. Takeuchi, T. Nakashima, and C. Claeys, Physica B **407**, 2900 (2012).
[340]M. Higashiwaki, K. Sasaki, T. Kamimura, M. H. Wong, D. Krishnamurthy, A. Kuramata, T. Masui, and S. Yamakoshi, Appl. Phys. Lett. **103**, 123511 (2013).
[341]N. A. Moser, J. P. McCandless, A. Crespo, K. D. Leedy, A. J. Green, E. R. Heller, K. D. Chabak, N. Peixoto, and G. H. Jessen, Appl. Phys. Lett. **110**, 143505 (2017).
[342]M. H. Wong, K. Sasaki, A. Kuramata, S. Tamakoshi, and M. Higashiwaki, IEEE Electron Device Lett. **37**, 212 (2016).
[343]G. Sinha, K. Adhikary, and S. Chaudhuri, J. Cryst. Growth **276**, 204 (2005).
[344]E. Korhonen, F. Tuomisto, D. Gogova, G. Wagner, M. Baldini, Z. Galazka, R. Schewski, and M. Albrecht, Appl. Phys. Lett. **106**, 242103 (2015).
[345]K. D. Chabak, N. Moser, A. J. Green, D. E. Walker, Jr., S. E. Tetlak, E. Heller, A. Crespo, R. Fitch, J. P. McCandless, K. Leedy, M. Baldini, G. Wagner, Z. Galazka, X. Li, and G. Jessen, Appl. Phys. Lett. **109**, 213501 (2016).
[346]A. Green, K. Chabak, E. Heller, R. Fitch, M. Baldini, A. Fiedler, K. Irmscher, G. Wagner, Z. Galazka, S. Tetlak, A. Crespo, K. Leedy, and G. Jessen, IEEE Electron Device Lett. **37**, 902 (2016).
[347]N. T. Son, K. Goto, K. Nomura, Q. T. Thieu, R. Togashi, H. Murakami, Y. Kumagai, A. Kuramata, M. Higashiwaki, A. Koukitu, S. Yamakoshi, B. Monemar, and E. Janzén, J. Appl. Phys. **120**, 235703 (2016).
[348]F. B. Zhang, K. Saito, T. Tanaka, M. Nishio, and Q. X. Guo, J. Cryst. Growth **387**, 96 (2014).
[349]S.-D. Lee, Y. Ito, K. Kaneko, and S. Fujita, Jpn. J. Appl. Phys. **54**, 030301 (2015).
[350]K. Akaiwa, K. Kaneko, K. Ichino, and S. Fujita, Jpn. J. Appl. Phys. **55**, 1202BA (2016).
[351]T. Harwig, G. J. Wubs, and G. J. Dirksen, Solid State Commun. **18**, 1223 (1976).
[352]A. T. Neal, S. Mou, R. Lopez, J. V. Li, D. B. Thomson, K. D. Chabak, and G. H. Jessen, http://arxiv.org:443/find/cond-mat/1/au:±Mou_S/0/1/0/all/0/1 for Effects of Incomplete Ionization on Beta - Ga_2O_3 Power Devices: Unintentional Donor with Energy 110 meV.
[353]N. Ma, N. Tanen, A. Verma, Z. Guo, T. Luo, H. G. Xing, and D. Jena, Appl. Phys. Lett. **109**, 212101 (2016).
[354]E. Korhonen, F. Tuomisto, O. Bierwagen, J. S. Speck, and Z. Galazka, Phys. Rev. B **90**, 245307 (2014).
[355]B. E. Kananen, L. E. Halliburton, E. M. Scherrer, K. T. Stevens, G. K. Foundos, K. B. Chang, and N. C. Giles, Appl. Phys. Lett. **111**, 072102 (2017).
[356]Y. Nakano, ECS J. Solid State Sci. Technol. **6**, P615 (2017).
[357]V. Wang, W. Xiao, L.-J. Kang, R.-J. Liu, H. Mizuseki, and Y. Kawazoe, J. Phys. D: Appl. Phys. **48**, 015101 (2015).
[358]M. Peres, K. Lorenz, E. Alves, E. Nogales, B. Méndez, X. Biquard, B. Daudin, E. G. Víllora, and K. Shimamura, J. Phys. D: Appl. Phys. **50**, 325101 (2017).
[359]N. F. Santos, J. Rodrigues, A. J. S. Fernandes, L. C. Alves, E. Alves, F. M. Costa, and T. Monteiro, Appl. Surf. Sci. **258**, 9157 (2012).
[360]T. Onuma, S. Fujioka, T. Yamaguchi, M. Higashiwaki, K. Sasaki, T. Masui, and T. Honda, Appl. Phys. Lett. **103**, 041910 (2013).
[361]T. Harwig, G. J. Wubs, and G. J. Dirksen, Solid State Commun. **18**, 1223 (1976).
[362]Y. J. Park, C. S. Oh, T. H. Yeom, and Y. M. Yu, J. Cryst. Growth **264**, 1 (2004).
[363]H. Zhu, R. Li, W. Luo, and X. Chen, Phys. Chem. Chem. Phys. **13**, 4411 (2011).
[364]K. Nishihagi, Z. Chen, K. Saito, T. Tanaka, and Q. Guo, Mater. Res. Bull. **94**, 170 (2017).
[365]J. M. Johnson, S. Krishnamoorthy, S. Rajan, and J. Hwang, Microsc. Microanal. **23**(S1), 1454 (2017).
[366]J. M. Johnson, S. Im, W. Windl, and J. Hwang, Ultramicroscopy **172**, 17 (2017).
[367]J. Hwang, J. Y. Zhang, A. J. D'Alfonso, L. J. Allen, and S. Stemmer, Phys. Rev. Lett. **111**, 266101 (2013).
[368]H. S. Oon and K. Y. Cheong, Mater. Sci. Semicond. Process **16**, 1217 (2013).
[369]Y.-L. Chiou, L.-H. Huang, and C.-T. Lee, Semicond. Sci. Technol. **25**, 045020 (2010).
[370]C.-T. Lee, H.-W. Chen, and H.-Y. Lee, Appl. Phys. Lett. **82**, 4304 (2003).
[371]C.-T. Lee, H.-Y. Lee, and H.-W. Chen, IEEE Electron Device Lett. **24**, 54 (2003).
[372]S. Pal, R. Mahapatra, S. K. Ray, B. R. Chakraborty, S. M. Shivaprasad, S. K. Lahiri, and D. N. Bose, Thin Solid Films **425**, 20 (2003).
[373]Y. Zhou, C. Ahyi, T. Isaacs-Smith, M. Bozack, C.-C. Tin, J. Williams, M. Park, A.-J. Cheng, J.-H. Park, D.-J. Kim, D. Wang, E. A. Preble, A. Hanser, and K. Evans, Solid-State Electron. **52**, 756 (2008).
[374]S. D. Wolter, B. P. Luther, D. L. Waltemyer, C. Onneby, S. E. Mohney, and R. J. Molnar, Appl. Phys. Lett. **70**, 2156 (1997).
[375]S. D. Wolter, S. E. Mohney, H. Venugopalan, A. E. Wickenden, and D. D. Koleske, J. Electrochem. Soc. **145**, 629 (1998).
[376]H. Kim, S. Park, and H. Hwang, J. Vac. Sci. Technol. B **19**, 579 (2001).
[377]Y. Nakano and T. Jimbo, Appl. Phys. Lett. **82**, 218 (2003).
[378]Y. Nakano, T. Kachi, and T. Jimbo, Appl. Phys. Lett. **82**, 2443 (2003).
[379]R. Korbutowicz, J. Prazmowska, Z. Wagrowski, A. Szyszka, and M. Tlaczala, in *International Conference on Advanced Semiconductor Devices and Microsystems* (2008), pp. 163–166.
[380]J. Brendt, D. Samuelis, T. E. Weirich, and M. Martin, Phys. Chem. Chem. Phys. **11**, 3127 (2009).
[381]P. Chen, R. Zhang, X. F. Xu, Y. G. Zhou, Z. Z. Chen, S. Y. Xie, W. P. Li, and Y. D. Zheng, Appl. Phys. A **71**, 191 (2000).
[382]T. G. Allen and A. Cuevas, Phys. Status Solidi. Rapid Res. Lett. **9**, 220–224 (2015).
[383]T. G. Allen and A. Cuevas, Appl. Phys. Lett. **105**, 031601 (2014).
[384]S. S. Kumar, E. J. Rubio, M. Noor-A-Alam, G. Martinez, S. Manandhar, V. Shutthanandan, S. Thevuthasan, and C. V. Ramana, J. Phys. Chem. C **117**, 4194 (2013).
[385]M. Grätzel, Acc. Chem. Res. **42**, 1788 (2009).
[386]*Beta-Gallium Oxide (β-Ga2O3) Handbook of Optical Constants of Solids*, edited by D. F. Edwards (Elsevier, London, 1997), Vol. III, pp. 753–760.
[387]Y. Kokubun, S. Kubo, and S. Nakagomiet, Appl. Phys, Express **9**, 091101 (2016).
[388]D. Liu, Y. Guo, L. Lin, and J. Robertson, J. Appl. Phys. **114**, 083704 (2013).
[389]F. Zhang, K. Saito, T. Tanaka, M. Nishio, M. Arita, and Q. Guo, Appl. Phys. Lett. **105**, 162107 (2014).
[390]W.-Z. Xiao, L.-L. Wang, L. Xu, Q. Wan, and A.-L. Pan, Solid State Commun. **150**, 852 (2010).
[391]K. Matsunaga, T. Tanaka, T. Yamamoto, and Y. Ikuhara, Phys. Rev. B **68**, 214102 (2003).
[392]Z. Yinnü and Y. Jinliang, J. Semicond. **36**, 082004 (2015).
[393]C. H. Park, S. B. Zhang, and S. H. Wei, Phys. Rev. B. **66**, 073202 (2002).
[394]J. L. Lyons, A. Janotti, and C. G. Van de Walle, Appl. Phys. Lett. **95**, 252105 (2009).
[395]L. Vines, C. Bhoodoo, H. von Wenckstern, and M. Grundmann, J. Physics: Condensed Matter (to be published).
[396]K. Ghosh and U. Singisetti, Appl. Phys. Lett. **109**, 072102 (2016).
[397]K. Ghosh and U. Singisetti, J. Appl. Phys. **122**, 035702 (2017).
[398]A. Parisini and R. Fornari, Semicond. Sci. Technol. **31**, 035023 (2016).
[399]F. Ricci, F. Boschi, A. Baraldi, A. Filippetti, M. Higashiwaki, A. Kuramata, V. Fiorentini, and R. Fornari, J. Phys. Condens. Matter **28**, 224005 (2016).
[400]Z. Guo, A. Verma, X. Wu, F. Sun, A. Hickman, T. Masui, A. Kuramata, M. Higashiwaki, D. Jena, and T. Luo, Appl. Phys. Lett. **106**, 111909 (2015).
[401]T. Omata, N. Ueda, N. Hikuma, K. Ueda, H. Mizoguchi, T. Hashimoto, and H. Kawazoe, Appl. Phys. Lett. **62**, 499 (1993).
[402]H. Peelaers and C. G. Van de Walle, Phys. Rev. B **94**, 195203 (2016).
[403]J. L. Lyons, D. Steiauf, A. Janotti, and C. G. Van de Walle, Phys. Rev. Appl. **2**, 064005 (2014).
[404]Y. S. Lee, D. Chua, R. E. Brandt, S. C. Sia, J. V. Li, J. P. Mailoa, S. W. Lee, R. G. Gordon, and T. Buonassisi, Adv. Mater. **26**, 4704 (2014).
[405]G. Schmitz, P. Gassmann, and R. Franchy, J. Appl. Phys. **83**, 2533 (1998).
[406]S. W. Kaun, F. Wu, and J. S. Speck, J. Vac. Sci. Technol. A **33**, 041508 (2015).
[407]E. Ahmadi, Y. Oshim, F. Wu, and J. S. Speck, Semicond. Sci. Technol. **32**, 035004 (2017).

[408]Y. Oshima, E. Ahmadi, S. C. Badescu, F. Wu, and J. S. Speck, Appl. Phys. Express **9**, 61102 (2016).
[409]H. Peelaers, D. Steiauf, J. B. Varley, A. Janotti, and C. G. Van de Walle, Phys. Rev. B **92**, 085206 (2015).
[410]M. B. Maccioni, F. Ricci, and V. Fiorentini, J. Phys.: Condens. Matter **28**, 224001 (2016).
[411]K. A. Mengle, G. Shi, D. Bayerl, and E. Kioupakisa, Appl. Phys. Lett. **109**, 212104 (2016).
[412]T. Harwig, F. Kellendonk, and S. Slappendel, J. Phys. Chem. Solids **39**, 675 (1978).
[413]C. Sturm, J. Furthmüller, F. Bechstedt, R. Schmidt-Grund, and M. Grundmann, APL Mater. **3**, 106106 (2015).
[414]G.-L. Li, F. Zhang, Y.-T. Cui, H. Oji, J.-Y. Son, and Q. Guo, Appl. Phys. Lett. **107**, 022109 (2015).
[415]S. Ghose, M. S. Rahman, J. S. Rojas-Ramirez, M. Caro, R. Droopad, A. Arias, and N. Nedev, J. Vac. Sci. Technol. B **34**, 02L109 (2016).
[416]M. Yamaga, E. G. Villora, K. Shimamura, N. Ichinose, and M. Honda, Phys. Rev. B **68**, 155207 (2003).
[417]G. J. Dirksen, A. N. J. M. Hoffman, T. P. van de Bout, M. P. G. Laudy, and G. Blasse, J. Mater. Chem. **1**, 1001 (1991).
[418]T. Harwig, F. Kellendonk, and S. Slappendel, J. Phys. Chem. Solids **39**, 675 (1978).
[419]B. E. Kananen, L. E. Halliburton, K. T. Stevens, G. K. Foundos, and N. C. Giles, Appl. Phys. Lett. **110**, 202104 (2017).
[420]M. Yamaga, H. Tsuzuki, S. Takano, E. G. Villora, and K. Shimamura, J. Non-Cryst. Solids **358**, 2458–2461 (2012).
[421]S. J. Pearton, J. W. Corbett, and M. Stavola, *Hydrogen in Crystalline Semiconductors* (Springer, Berlin, 1992).
[422]J. B. Varley, H. Peelaers, A. Janotti, and C. G. van de Walle, J. Phys.: Condens. Matter **23**, 334212 (2011).
[423]S. J. Pearton, C. R. Abernathy, C. B. Vartuli, R. J. Shul, R. G. Wilson, and J. M. Zavada, Electron. Lett. **31**(10), 836–837 (1995).
[424]S. J. Pearton, R. J. Shul, R. G. Wilson, F. Ren, J. Zavada, C. R. Abernathy, C. Vartuli, J. W. Lee, J. R. Mileham, and J. D. MacKenzie, J. Electron. Mater. **25**, 845 (1996).
[425]K. Ip, M. E. Overberg, Y. W. Heo, D. P. Norton, S. J. Pearton, S. O. Kucheyev, C. Jagadish, J. S. Williams, R. G. Wilson, and J. M. Zavada, Appl. Phys. Lett. **81**, 3996 (2002).
[426]S. J. Pearton, S. Bendi, K. S. Jones, V. Krishnamoorthy, R. G. Wilson, F. Ren, R. Karlicek, and R. A. Stall, Appl. Phys. Lett. **69**, 1879 (1996).
[427]M. G. Weinstein, C. Song, M. Stavola, S. J. Pearton, R. G. Wilson, R. J. Shul, K. P. Killeen, and M. J. Ludowise, Appl. Phys. Lett. **72**, 1703 (1998).
[428]S. J. Pearton, C. R. Abernathy, R. G. Wilson, J. M. Zavada, C. Y. Song, M. G. Weinstein, M. Stavola, H. Han, and R. J. Shul, Nucl. Instrum. Methods Phys. Res. **B147**, 171 (1999).
[429]J. Zavada, R. Wilson, F. Ren, S. J. Pearton, and R. F. Davis, Solid State Electron. **41**, 677 (1997).
[430]A. Y. Polyakov, N. B. Smirnov, A. Gorokov, K. Ip, M. E. Overberg, Y. Heo, D. P. Norton, S. J. Pearton, B. Luo, F. Ren, and J. M. Zavada, J. Appl. Phys. **94**, 400 (2003).
[431]K. Ip, M. Overberg, Y. Heo, D. Norton, S. J. Pearton, C. E. Stutz, B. Luo, F. Ren, D. C. Look, and J. M. Zavada, Appl. Phys. Lett. **82**, 385 (2003).
[432]R. G. Wilson, S. J. Pearton, C. R. Abernathy, and J. M. Zavada, J. Vac. Sci. Technol. A **13**, 719 (1995).
[433]A. Janotti and C. G. Van de Walle, Nat. Mater. **6**, 44 (2007).
[434]M. A. Blanco, M. B. Sahariah, H. Jiang, A. Costales, and R. Pandey, Phys. Rev. B **72**, 184103 (2005).
[435]H. Li and J. Robertson, J. Appl. Phys. **115**, 203708 (2014).
[436]W. M. H. Oo, S. Tabatabaei, M. D. McCluskey, J. B. Varley, A. Janotti, and C. G. Van de Walle, Phys. Rev. B **82**, 193201 (2010).
[437]W. Beall Fowler, M. Stavola, and F. Bekisli, AIP Conf. Proc. **1583**, 359 (2014).
[438]M. Stavola, F. Bekisli, W. Yin, K. Smithe, W. Beall Fowler, and L. A. Boatnerless, J. Appl. Phys. **115**, 012001 (2014).
[439]F. Bekisli, M. Stavola, W. B. Fowler, L. Boatner, E. Spahr, and G. Lupke, Phys. Rev. B **84**, 035213 (2011).
[440]F. Bekisli, W. B. Fowler, M. Stavola, L. A. Boatner, E. Spahr, and G. Lüpke, Phys. Rev. B **85**, 205202 (2012).
[441]G. Alvin Shi, M. Saboktakin, M. Stavola, and S. J. Pearton, Appl. Phys. Lett. **85**, 5601 (2004).
[442]M. Stavola, AIP Conf. Proc. **671**, 21 (2003).
[443]P. D. C. King, I. McKenzie, and T. D. Veal, Appl. Phys. Lett. **96**, 062110 (2010).
[444]P. D. C. King and T. D. Veal, J. Phys. Condens. Matter **23**, 334214 (2011).
[445]P. D. C. King, R. L. Lichti, Y. G. Celebi, J. M. Gil, R. C. Vilão, H. V. Alberto, J. P. Durte, D. J. Payne, R. B. Egdell, I. McKenzie, C. F. McConville, S. F. J. Cox, and T. D. Veal, Phys. Rev. B **80**, 081201 (2009).
[446]T. Koida, H. Fujiwara, and M. Kondo, Jpn. J. Appl. Phys. **46**, L685 (2007).
[447]P. Weiser, Y. Qin, W. Yin, M. Stavola, W. Beall Fowler, and L. A. Boatnerless, Appl. Phys. Lett. **109**, 202105 (2016).
[448]W. Yin, K. Smithe, P. Weiser, M. Stavola, W. B. Fowler, L. Boatner, S. J. Pearton, D. C. Hays, and S. G. Koch, Phys. Rev. B **91**, 075208 (2015).
[449]J. B. Bates and R. A. Perkins, Phys. Rev. B **16**, 3713 (1977).
[450]E. Herklotz, E. V. Lavrov, and J. Weber, Phys. Rev. B **83**, 235202 (2011).
[451]S. Yang and L. E. Halliburton, Phys. Rev. B **81**, 035204 (2010).
[452]A. T. Brant, S. Yang, N. C. Giles, and L. E. Halliburton, J. Appl. Phys. **110**, 053714 (2011).
[453]S. Yang, A. T. Brant, N. C. Giles, and L. E. Halliburton, Phys. Rev. B **87**, 125201 (2013).
[454]A. T. Brant, N. C. Giles, and L. E. Halliburton, J. Appl. Phys. **113**, 053712 (2013).
[455]F. Bekisli, W. B. Fowler, and M. Stavola, Phys. Rev. B **86**, 155208 (2012).
[456]S. Ahn, F. Ren, E. Patrick, M. E. Law, S. J. Pearton, and A. Kuramata, Appl. Phys. Lett. **109**, 242108 (2016).
[457]S. Ahn, F. Ren, E. Patrick, M. E. Law, and S. J. Pearton, ECS J. Solid State Sci. Technol. **6**, Q3026 (2017).
[458]G. Greco, F. Iucolano, and F. Roccaforte, Appl. Surf. Sci. **383**, 324 (2016).
[459]S. N. Mohammad, J. Appl. Phys. **95**, 7940 (2004).
[460]D. K. Schroder, *Semiconductor Material and Device Characterization* (John Wiley and Sons, New York, 1998).
[461]T. K. Zywietz, J. Neugebauer, and M. Scheffler, Appl. Phys. Lett. **74**, 1695 (1999).
[462]J. D. Guo, C. I. Lin, M. S. Feng, F. M. Pan, G. C. Chi, and C. T. Lee, Appl. Phys. Lett. **68**, 235 (1996).
[463]J. S. Foresi and T. D. Moustakas, Appl. Phys. Lett. **62**, 2859 (1993).
[464]Y. Oshima, E. Ahmadi, S. Kaun, F. Wu, and J. S. Speck, Semicond. Sci. Technol. **33**, 015013 (2018).
[465]R. Suzuki, S. Nakagomi, and Y. Kokubun, Appl. Phys. Lett. **98**, 131114 (2011).
[466]P. Vogt and O. Bierwagen, Appl. Phys. Lett. **108**, 072101 (2016).
[467]A. Ratnaparkhe and W. R. L. Lambrecht, Appl. Phys. Lett. **110**, 132103 (2017).
[468]K. Sasaki, M. Higashiwaki, A. Kuramata, T. Masui, and S. Yamakoshi, IEEE Electron Device Lett. **34**, 493 (2013).
[469]Y. Sawada, N. Weda, K. Konishi, and Y. Kumagai, "Thermodynamic analysis on molecular beam epitaxy of Ga2O3," The 78th JSAP Autumn Meeting, 7p-C17-9 (2017).
[470]D. Splith, S. Müller, F. Schmidt, H. von Wenckstern, J. J. van Rensburg, W. E. Meyer, and M. Grundmann, Phys. Status Solidi A **211**, 40 (2014).
[471]T. Oshima, R. Wakabayashi, M. Hattori, A. Hashiguchi, N. Kawano, K. Sasaki, T. Masui, A. Kuramata, S. Yamakoshi, K. Yoshimatsu, A. Ohtomo, T. Oishi, and M. Kasu, Jpn. J. Appl. Phys. **55**, 1202B7 (2016).
[472]M. Higashiwaki, S. Sasaki, M. H. Wong, T. Kamimura, D. Krishnamurthy, A. Kuramata, T. Masui, and S. Yamakoshi, in *IEDM Technical Digest* (2013), p. 28.7.1.
[473]M. H. Wong, Y. Nakata, A. Kuramata, S. Yamakoshi, and M. Higashiwaki, Appl. Phys. Express **10**, 041101 (2017).
[474]K. Zeng, J. S. Wallace, C. Heimburger, K. Sasaki, A. Kuramata, T. Matsui, J. A. Gardella, and U. Singisetti, IEEE Electron Device Lett. **38**, 513 (2017).
[475]K. Chabak, A. Green, N. Moser, S. Tetlak, J. McCandless, K. Leedy, R. Fitch, A. Crespo, and G. Jessen, in DRC (2017).
[476]Y. Yao, R. F. Davis, and L. M. Porter, J. Electron. Mater. **46**, 2053 (2017).
[477]P. H. Carey, J. Yang, F. Ren, D. C. Hays, S. J. Pearton, S. Jang, A. Kuramata, and I. I. Kravchenko, J. Vac. Sci. Technol. B **35**, 061201 (2017).
[478]P. H. Carey, J. Yang, F. Ren, D. C. Hays, S. J. Pearton, S. Jang, A. Kuramata, and I. I. Kravchenko, AIP Adv. **7**, 095313 (2017).
[479]T. Oshima, T. Okuno, N. Arai, S. Suzuki, S. Ohira, and S. Fujita, Appl. Phys. Express **1**, 011202 (2008).
[480]A. A. Mostofi, J. R. Yates, Y.-S. Lee, I. Souza, D. Vanderbilt, and N. Marzari, Comput. Phys. Commun. **178**, 685 (2008).

[481]S. Oh, Y. Jung, M. Mastro, J. K. Hite, C. R. Eddy, and J. Kim, Opt. Express **23**, 28300 (2015).
[482]S. Müller, H. von Wenckstern, F. Schmidt, D. Splith, F. L. Schein, H. Frenzel, and M. Grundmann, Appl. Phys. Express **8**, 121102 (2015).
[483]T. Oshima, T. Okuno, N. Arai, N. Suzuki, H. Hino, and S. Fujita, Jpn. J. Appl. Phys. **48**, 011605 (2009).
[484]R. Suzuki, S. Nakagomi, Y. Kokubun, N. Arai, and S. Ohira, Appl. Phys. Lett. **94**, 222102 (2009).
[485]H. Zhou, M. Si, S. Alghamdi, G. Qiu, L. Yang, and P. D. Ye, IEEE Electron Device Lett. **38**, 103 (2017).
[486]M. Si, L. Yang, H. Zhou, and P. D. Ye, ACS Omega. **2**(10), 7136–7140 (2017).
[487]K. Sasaki, "Study of homoepitaxial growth and n-type doping of β-Ga2O3" Ph.D. Thesis, Graduate School of Engineering, Kyoto University (2016).
[488]M. H. Wong, K. Sasaki, A. Kuramata, S. Yamakoshi, and M. Higashiwaki, Jpn. J. Appl. Phys. **55**, 1202B9 (2016).
[489]K. Zeng, K. Sasaki, A. Kuramata, T. Masui, and U. Singisetti, in *74th Annual Device Research Conference (DRC), 2016* (IEEE, 2016).
[490]H. Zhou, S. Alghamdi, M. W. Si, and P. D. Ye, IEEE Electron Device Lett. **37**, 1411 (2016).
[491]D. Y. Guo, Z. P. Wu, Y. H. An, X. C. Guo, X. L. Chu, C. L. Sun, L. H. Li, P. G. Li, and W. H. Tangless, Appl. Phys. Lett. **105**, 023507 (2014).
[492]D. Y. Guo, Z. P. Wu, P. G. Li, Y. H. An, H. Liu, X. C. Guo, H. Yan, G. F. Wang, C. L. Sun, L. H. Li, and W. H. Tang, Opt. Mater. Express **4**, 1067 (2014).
[493]K. H. Baik, S. Jang, F. Ren, and S. J. Pearton, J. Alloys Compd. **731**, 118 (2018).
[494]S. M. Sze and K. K. Ng, *Physics of Semiconductor Devices*, 3rd ed. (John Wiley & Sons, Hoboken, 2007), Chap. 3.
[495]M. H. Hecht, Phys. Rev. B **41**, 7918 (1990).
[496]H. J. Kümmerer and G. Denninger, Magn. Reson. Chem. **43**, S145 (2005).
[497]N. A. Moser, R. C. Fitch, D. E. Walker, A. J. Green, D. Chabak, Kelson, E. Heller, J. P. McCandless, E. Tetlak, E. Stephen, A. Crespo,K. D. Leedy, and G. H. Jessen, presented at U.S. Air Force Review, March 2017, Wright Paatterson AFB, Dayton OH. Available at http://www.dtic.mil/get-tr-doc/pdf?AD=AD1041825
[498]M.-Y. Tsai, O. Bierwagen, M. E. White, and J. S. Speck, J. Vac. Sci. Technol. A: Vacuum, Surfaces, Film. **28**, 354 (2010).
[499]T. Oishi, Y. Koga, K. Harada, and M. Kasu, Appl. Phys. Express **8**, 031101 (2015).
[500]Y. Yao, R. Gangireddy, J. Kim, K. K. Das, R. F. Davis, and L. M. Porter, J. Vac. Sci. Technol. B **35**, 03D113 (2017).
[501]M. Higashiwaki, K. Konishi, K. Sasaki, K. Goto, K. Nomura, Q. T. Thieu, R. Togashi, H. Murakami, Y. Kumagai, B. Monemar, A. Koukitu, A. Kuramata, and S. Yamakoshi, Appl. Phys. Lett. **108**, 133503 (2016).
[502]S. Ahn, F. Ren, L. Yuan, S. J. Pearton, and A. Kuramata, ECS J. Solid State Sci. Technol. **6**, P68 (2017).
[503]A. M. Armstrong, M. H. Crawford, A. Jayawardena, A. Ahyi, and S. Dhar, J. Appl. Phys. **119**, 103102 (2016).
[504]S. Oh, G. Yang, and J. Kim, ECS J. Solid State Sci. Technol. **6**, Q3022 (2017).
[505]Z. Zhang, E. Farzana, A. R. Arehart, and S. A. Ringel, Appl. Phys. Lett. **108**, 052105 (2016).
[506]W. Monch, J. Mater. Sci: Mater. Electron. **27**, 1444 (2016).
[507]T. C. Lovejoy, R. Chen, X. Zheng, E. G. Villora, K. Shimamura, H. Yoshikawa, Y. Yamashita, S. Ueda, K. Kobayashi, S. T. Dunham, F. S. Ohuchi, and M. A. Olmstead, Appl. Phys. Lett. **100**, 181602 (2012).
[508]R. Sharma, E. Patrick, M. E. Law, S. Ahn, F. Ren, S. J. Pearton, and A. Kuramata, ECS J. Solid State Sci. Technol. **6**(12), P794–P797 (2017).
[509]J. Bae, H.-Y. Kim, and J. Kim, ECS J. Solid State Sci. Technol. **6**, Q3045 (2017).
[510]S. Müller, H. Wenckstern, F. Schmidt, D. Splith, F.-L. Schein, H. Frenzel, and M. Grundmann, Appl. Phys. Express **8**, 1211102 (2015).
[511]S. Müller, H. Wenckstern, F. Schmidt, D. Splith, H. Frenzel, and M. Grundmann, Semicond. Sci. Technol. **32**, 065013 (2017).
[512]A. Jayawardena, A. C. Ahyi, and D. Sarit, Semicond. Sci. Technol. **31**, 115002 (2016).
[513]Q. He, W. Mu, H. Dong, S. Long, Z. Jia, H. Lv, Q. Liu, M. Tang, X. Tao, and M. Liu, Appl. Phys. Lett. **110**, 093503 (2017).
[514]D. Zhang, W. Zheng, R. C. Lin, T. T. Li, Z. J. Zhang, and F. Huang, J. Alloys and Compounds **735**, 150–154 (published online).
[515]E. Farzana, Z. Zhang, P. K. Paul, A. R. Arehart, and S. A. Ringel, Appl. Phys. Lett. **110**, 202102 (2017).
[516]M. Alonso, R. Cimino, and K. Horn, Phys. Rev. Lett. **64**, 1947 (1990).
[517]H. Mao, B. Alhalaili, A. Kaya, D. M. Dryden, J. M. Woodall, and M. S. Islam, Proc. SPIE **10381**, 103810B (2017).
[518]H. Nishinaka, D. Tahara, S. Morimoto, and M. Yoshimoto, Mater. Lett. **205**, 28–31 (2017).
[519]M. J. Tadjer, V. D. Wheeler, D. I. Shahin, C. R. Eddy, Jr., and F. J. Kub, ECS J. Solid State Sci. Technol. **6**, P165 (2017).
[520]K. Konishi, K. Goto, H. Murakami, Y. Kumagai, A. Kuramata, S. Yamakosji, and M. Higashiwaki, Appl. Phys. Lett. **110**, 103506 (2017).
[521]M. W. Allen, R. J. Mendelsberg, R. Reeves, and S. M. Durbin, Appl. Phys. Lett. **94**, 103508 (2009).
[522]T. Matsumoto, M. Aoki, A. Kinoshita, and T. Aono, Jap. Appl. Phys. **13**, 1578–1582 (1974).
[523]S. H. Müller, H. von Wenckstern, F. Schmidt, D. Splith, R. Heinhold, M. Allen, and M. Grundmann, J. Appl. Phys. **116**, 194506 (2014).
[524]T. Matsumoto, M. Aoki, A. Kinoshita, and T. Aono, Jpn. J. Appl. Phys. **13**, 1578–1582 (1974).
[525]M. Passlack, M. Hong, J. P. Mannaerts, R. L. Opila, S. N. G. Chu, N. Moriya, F. Ren, and J. R. Kwo, IEEE Trans. Electron Devices **44**, 214–225 (1997).
[526]F. Ren, M. Hong, J. P. Mannaerts, J. R. Lothian, and A. Y. Cho, J. Electrochem. Soc. **144**, L239 (1997).
[527]D. Zhuang and J. H. Edgar, Mater. Sci. Eng. R **48**, 1 (2005).
[528]D. P. Norton, Mat. Sci. Eng R **43**, 139 (2004).
[529]K. H. Baik, H.-Y. Song, S.-M. Hwang, Y. Jung, J. Ahn, and J. Kim, J. Electrochem. Soc. **158**, D196 (2011).
[530]Y. Jung, J. Ahn, K. H. Baik, D. Kim, S. J. Pearton, F. Ren, and J. Kim, J. Electrochem. Soc. **159**, H117 (2012).
[531]S. E. Krasavin, Semiconductors **46**, 598 (2012).
[532]G. Blasse and A. Bril, Solid State Commun **7**, 3 (1969).
[533]B. E. Kananen, N. C. Giles, L. E. Halliburton, G. K. Foundos, K. B. Chang, and K. T. Stevens, J. Appl. Phys. **122**, 215703 (2017).
[534]J. Ahman, G. Svensson, and J. Albertsson, Acta Cryst. C **52**, 1336 (1996).
[535]S. Geller, J. Chem. Phys. **33**, 676 (1960).
[536]S. Schulz, G. Bendt, W. Assenmacher, D. Sager, and G. Bacher, Chemical Vapor Deposition **19**, 347 (2013).
[537]S.-L. Ou, D.-S. Wuu, Y.-C. Fu, S.-P. Liu, and Z.-C. Feng, Mater. Chem. Phys. **133**, 700 (2012).
[538]G. T. Dang, T. Kawaharamura, M. Furuta, and M. W. Allen, IEEE Trans. Electron Devices **62**, 3640 (2015).
[539]*Handbook of Advanced Plasma Processing Techniques*, edited by R. J. Shul and S. J. Pearton (Springer, Berlin, 2000).
[540]A. P. Shah and A. Bhattacharya, J. Vac. Sci. Technol. A. **35**, 041301 (2017).
[541]H. Liang, Y. Chen, X. Xia, C. Zhang, R. Shen, Y. Liu, Y. Luo, and G. Du, Mater. Sci. Semicond. Proc. **39**, 582 (2015).
[542]J. E. Hogan, S. W. Kaun, E. Ahmadi, Y. Oshima, and J. S. Speck, Semicond. Sci. Technol. **31**, 065006 (2016).
[543]L. Zhang, A. Verma, H. Grace Xing, and D. Jena, Jpn. J. Appl. Phys. **56**, 030304 (2017).
[544]J. Yang, S. Ahn, F. Ren, S. J. Pearton, R. Khanna, K. Bevlin, D. Geerpuram, and A. Kuramata, J. Vac. Sci. Technol. **B35**, 031205 (2017).
[545]X. Cao, H. Cho, S. J. Pearton, G. T. Dang, A. P. Zhang, F. Ren, R. J. Shul, L. Zhang, R. Hickman, and J. M. Van Hove, Appl. Phys. Lett. **75**, 232 (1999).
[546]X. A. Cao, S. J. Pearton, G. T. Dang, A. P. Zhang, F. Ren, and J. M. Van Hove, IEEE Trans. Electron Devices **47**, 1320 (2000).
[547]K. Ip, K. Baik, M. E. Overberg, E. S. Lambers, Y. W. Heo, D. P. Norton, S. J. Pearton, F. Ren, and J. M. Zavada, Appl. Phys. Lett. **81**, 3546 (2002).
[548]J. Yang, S. Ahn, F. Ren, R. Khanna, K. Bevlin, D. Geerpuram, S. J. Pearton, and A. Kuramata, Appl. Phys. Lett. **110**, 142101 (2017).
[549]Y. Kwon, G. Lee, S. Oh, J. Kim, S. J. Pearton, and F. Ren, Appl. Phys. Lett. **110**, 131901 (2017).
[550]J. Yang, F. Ren, R. Khanna, K. Bevlin, D. Geerpuram, L.-C. Tung, J. Lin, H. Jiang, J. Lee, E. Flitsiyan, L. Chernyak, S. J. Pearton, and A. Kuramata, J. Vac. Sci. Technol. B **35**, 051201 (2017).
[551]J. Robertson and C. W. Chen, Appl. Phys. Lett. **74**, 1168 (1999).
[552]J. Robertson, J. Vac. Sci. Tech. B **18**, 1785 (2000).
[553]J. Robertson, MRS Bull. **27**, 217 (2002).

[554]E. A. Kraut, R. W. Grant, J. R. Waldrop, and S. P. Kowalczyk, Phys. Rev. Lett. **44**, 1620 (1980).
[555]D. A. Shirley, Phys. Rev. B **5**, 4709 (1972).
[556]R. S. List and W. E. Spicer, J. Vac. Sci. Technol. B **6**, 1228 (2016).
[557]S. Tougaard, Surf. Sci. **216**, 343 (1989).
[558]J. C. H. Spence, Rep. Prog. Phys. **69**, 725 (2006).
[559]R. Carli and C. L. Bianchi, Appl. Surf. Sci. **74**, 99 (1994).
[560]D. C. Hays, B. P. Gila, S. J. Pearton, and F. Ren, Appl. Phys. Rev. **4**, 021301 (2017).
[561]P. H. Carey, F. Ren, D. C. Hays, B. P. Gila, S. J. Pearton, S. Jang, and A. Kuramata, Appl. Surf. Sci. **422**, 179 (2017).
[562]P. H. Carey IV, F. Ren, D. C. Hays, B. P. Gila, S. J. Pearton, S. Jang, and A. Kuramata, Vacuum **141**, 103 (2017).
[563]P. H. Carey, F. Ren, D. C. Hays, B. P. Gila, S. J. Pearton, S. Jang, and A. Kuramata, J. Vac. Sci. Technol. B **35**, 041201 (2017).
[564]P. Carey, F. Ren, D. C. Hays, B. P. Gila, S. J. Pearton, S. Jang, and A. Kuramata, Vacuum **142**, 52 (2017).
[565]P. Carey, F. Ren, D. C. Hays, B. P. Gila, S. J. Pearton, S. Jang, and A. Kuramata, Jpn. J. Appl. Phys. **56**, 071101 (2017).
[566]J. Gao, A. Kaya, R. V. Chopdekar, D. M. Dryden, Y. Takamura, M. Saif Islam, and S. Chowdhury, in Device Research Conference, South Bend, IN, June 2017.
[567]K. Konishi, T. Kamimura, M. H. Wong, K. Sasaki, A. Kuramata, S. Yamakoshi, and M. Higashiwaki, Phys. Status Solidi B **253**, 623 (2016).
[568]Y. Jia, K. Zheng, J. S. Wallace, J. A. Gardella, and U. Singisetti, Appl. Phys. Lett. **106**, 102107 (2015).
[569]T. Kamimura, K. Sasaki, M. H. Wong, D. Krishnamurthy, A. Kuramata, T. Masui, S. Yamakoshi, and M. Higashiwaki, Appl. Phys. Lett. **104**, 192104 (2014).
[570]M. Hattori, T. Oshima, R. Wakabayashi, K. Yoshimatsu, K. Sasaki, T. Masui, A. Kuramata, S. Yamakoshi, K. Horiba, H. Kumigashira, and A. Ohtomo, Jpn. J. Appl. Phys. **55**, 1202B6 (2016).
[571]Z. Chen, K. Hishihagi, X. Wang, K. Saito, T. Tanaka, M. Nishio, M. Arita, and Q. Guo, Appl. Phys. Lett. **109**, 102106 (2016).
[572]W. Wei, Z. Qin, S. Fan, Z. Li, K. Shi, Q. Zhu, and G. Zhang, Nanoscale Res. Lett. **7**, 562 (2012).
[573]S. H. Chang, Z. Z. Chen, W. Huang, X. C. Liu, B. Y. Chen, Z. Z. Li, and E. W. Shi, Chin. Phys. B **20**, 116101 (2011).
[574]V. D. Wheeler, D. I. Shahin, M. J. Tadjer, and C. R. Eddy, Jr., ECS J. Solid State Sci. Technol. **6**, Q3052 (2017).
[575]J. Nord, K. Nordlund, and J. Keinonen, Phys. Rev. B **68**, 184104 (2003).
[576]J. R. Srour and J. W. Palko, IEEE Trans. Nucl. Sci. **53**, 3610 (2006).
[577]S. J. Pearton, Y.-S. Hwang, and F. Ren, J. Mater. **67**, 1601 (2015).
[578]A. P. Karmarkar, B. D. White, D. Buttari, D. M. Fleetwood, R. D. Schrimpf, R. A. Weller, L. J. Brillson, and U. K. Mishra, IEEE Trans. Nucl. Sci. **52**, 2239 (2005).
[579]J. Chen, Y. S. Puzyrev, C. X. Zhang, E. X. Zhang, M. W. McCurdy, D. M. Fleetwood, R. D. Schrimpf, S. T. Pantelides, S. W. Kaun, E. C. H. Kyle, and J. S. Speck, IEEE Trans. Nucl. Sci. **60**(6), 4080 - 4086 (2013).
[580]A. Y. Polyakov, S. J. Pearton, P. Frenzer, F. Ren, L. Liu, and J. Kim, J. Mater. Chem. C **1**, 877 (2013).
[581]S. J. Pearton, R. Deist, F. Ren, L. Liu, A. Y. Polyakov, and J. Kim, J. Vac. Sci. Technol. A **31**, 050801 (2013).
[582]T. J. Anderson, A. D. Koehler, J. D. Greenlee, B. D. Weaver, M. A. Mastro, J. K. Hite, C. R. Eddy, F. J. Kub, and K. D. Hobart, IEEE Electron Dev. Lett. **35**, 826 (2014).
[583]J. D. Greenlee, P. Specht, T. J. Anderson, A. D. Koehler, B. D. Weaver, M. Luysberg, O. D. Dubon, F. J. Kub, T. R. Weatherford, and K. D. Hobart, Appl. Phys. Lett. **107**, 083504 (2015).
[584]K.-H. Cho, Y.-H. Choi, J. Lim, and M.-K. Han, IEEE Trans Electron Devices **56**, 365 (2009).
[585]A. Akturk, J. M. McGarrity, S. Potbhare, and N. Goldsman, IEEE Trans. Nucl. Sci. **59**(6), 3258–3264 (2012).
[586]N. E. Ives, J. Chen, A. F. Witulski, R. D. Schrimpf, D. M. Fleetwood, R. W. Bruce, M. W. McCurdy, E. X. Zhang, and L. W. Massengill, IEEE Trans. Nucl. Sci. **62**, 2417 (2015).
[587]S. J. Pearton, F. Ren, E. Patrick, M. E. Law, and A. Y. Polyakov, ECS J. Solid State Sci. Technol. **5**, Q35 (2016).
[588]E. Patrick, M. Choudhury, F. Ren, S. J. Pearton, and M. Law, ECS J. Solid State Sci. Technol. **4**, Q21 (2015).
[589]D. Szalkai, Z. Galazka, K. Irmscher, P. Tüttő, A. Klix, and D. Gehre, IEEE Trans. Nucl. Sci. **64**, 1574 (2017).
[590]J. Yang, F. Ren, S. J. Pearton, G. Yang, J. Kim, and A. Kuramata, J. Vac. Sci. Technol. B **35**, 031208 (2017).
[591]J. Lee, E. Flitsiyan, L. Chernyak, S. Ahn, F. Ren, L. Yuna, S. J. Pearton, J. Kim, B. Meyler, and J. Salzman, ECS J. Solid State Sci. Technol. **6**, Q3049 (2017).
[592]S. Ahn, Y.-H. Lin, F. Ren, S. Oh, Y. Jung, G. Yang, J. Kim, M. A. Mastro, J. K. Hite, C. R. Eddy, Jr., and S. J. Pearton, J. Vac. Sci. Technol. B **34**, 041213 (2016).
[593]E. Wendler, E. Treiber, J. Baldauf, S. Wolf, and C. Ronnig, Nucl. Instrum. Methods Phys. Res. **B379**, 85–90 (2016).
[594]M. H. W. Akinori, T. Takahiro, M. Takeshi, O. Kohei, S. Akito, K. S. Yamakoshi, and M. Higashiwaki, in Device Research Conference, South Bend, IN, June 2017.
[595]G. Yang, S. Jang, F. Ren, S. J. Pearton, and J. Kim, ACS Appl. Mater. Interfaces **9**, 40471 (2017).
[596]A. S. Pratiyush, S. Krishnamoorthy, S. V. Solanke, Z. Xia, R. Muralidharan, S. Rajan, and D. N. Nathless, Appl. Phys. Lett. **110**, 221107 (2017).
[597]Y. L. Wu, S.-J. Chang, W. Y. Weng, C. H. Liu, T. Y. Tsai, C. L. Hsu, and K. C. Chen, IEEE Sens. J. **13**, 2368 (2013).
[598]V. V. Kuryatkov, B. A. Borisov, S. A. Nikishin, Y. Kudryavtsev, R. Asomoza, V. I. Kuchinskii, G. S. Sokolovskii, D. Y. Song, and M. Holtz, J. Appl. Phys. **100**, 096104 (2006).
[599]R. Wakabayashi, K. Yoshimatsu, M. Hattori, and A. Ohtomo, Appl. Phys. Lett. **111**, 162101 (2017).
[600]R. Zou, Z. Zhang, Q. Liu, J. Hu, L. Sang, M. Liao, and W. Zhang, Small **10**, 1848 (2014).
[601]T.-C. Wei, D.-S. Tsai, P. Ravadgar, J.-J. Ke, M.-L. Tsai, D.-H. Lien, C.-Y. Huang, R.-H. Horng, and J.-H. He, IEEE J. Sel. Top. Quantum Electron. **20**(6), 3802006 (2014).
[602]F.-P. Yu, S.-L. Ou, and D.-S. Wuu, Opt. Mater. Express **5**, 1240 (2015).
[603]M. Ai, D. Guo, Y. Qu, W. Cui, Z. Wu, P. Li, L. Li, and W. Tang, J. Alloys Compd. **692**, 634 (2017).
[604]X. C. Guo, N. H. Hao, D. Y. Guo, Z. P. Wu, Y. H. An, X. L. Chu, L. H. Li, P. G. Li, M. Lei, and W. H. Tang, J. Alloys Compd. **660**, 136 (2016).
[605]S. Nakagomi, T. Momo, S. Takahashi, and Y. Kokubun, Appl. Phys. Lett. **103**, 072105 (2013).
[606]Q. Feng, L. Huang, G. Han, F. Li, X. Li, L. Fang, X. Xing, J. Zhang, W. Mu, Z. Jia, D. Guo, W. Tang, X. Tao, and Y. Hao, IEEE Trans. Electron Device **63**, 3578 (2016).
[607]D. Patil-Chaudhari, M. Ombaba, J. Y. Oh, H. Mao, K. H. Montgomery, A. Lange, S. Mahajan, J. M. Woodall, and M. Saif Islam, IEEE Photonics J. **9**, 1–7 (2017).
[608]Y. H. An, D. Y. Guo, S. Y. Li, Z. P. Wu, and Y. Q. Huang, J. Phys. D: Appl. Phys. **49**, 285111 (2016).
[609]Q. Feng, X. Li, G. Han, L. Huang, F. Li, W. Tang, J. Zhang, and Y. Hao, Opt. Mater. Express **7**, 1240 (2017).
[610]D. Guo, X. Qin, M. Lv, H. Shi, Y. Su, G. Yao, S. Wang, C. Li, P. Li, and W. Tang, Electron. Mater. Lett. **13**, 483–488 (2017).
[611]X. Z. Liu, P. Guo, T. Sheng, L. X. Qian, and Y. R. Li, Opt. Mater. **51**, 203 (2016).
[612]Z. Ji, J. Du, J. Fan, and W. Wang, Opt. Mater. **28**, 415 (2006).
[613]S. Cui, Z. Mei, Y. Zhang, H. Liang, and X. Du, Adv. Opt. Mater. **5**, 1700454 (2017).
[614]F. Alema, B. Hertog, O. Ledyaev, D. Volovik, G. Thoma, R. Miller, A. Osinsky, P. Mukhopadhyay, S. Bakhshi, H. Ali, and W. V. Schoenfeld, Phys. Status Solidi A **214**, 1770127 (2017).
[615]Z. Liu, C. Yue, C. T. Xia, and W. L. Zhang, Chin. Phys. B **25**, 017201 (2016).
[616]L. Huang, Q. Feng, G. Han, F. Li, X. Li, L. Fang, X. Xing, J. Zhang, and Y. Hao, IEEE Photonics J. **9**, 6803708 (2017).
[617]S. Nakagomi, T.-A. Sato, Y. Takahashi, and Y. Kokubun, Sens. Actuators A: Phys. **232**, 208 (2015).
[618]W. E. Mahmoud, Sol. Energy Mater. Sol. Cells **152**, 65 (2016).
[619]W. Y. Weng, T. J. Hsueh, S. J. Chang, G. J. Huang, and H. T. Hsueh, IEEE Sens. J. **11**, 999 (2011).
[620]K. Zeng, K. Sasaki, A. Kuramata, T. Masui, and U. Singisetti, in *74th IEEE Device Research Conference* (Technical Digest, 2016), p. 105.
[621]S. Oh, J. Kim, F. Ren, S. J. Pearton, and J. Kim, J. Mater. Chem. C **4**, 9245 (2016).
[622]S. Ahn, F. Ren, S. Oh, Y. Jung, M. A. Mastro, J. K. Hite, C. R. Eddy, Jr., J. Kim, and S. J. Pearton, J. Vac. Sci. Technol. B **34**, 041207 (2016).

[623]S. Oh, M. A. Mastro, M. J. Tadjer, and J. Kim, ECS J. Solid State Sci. Technol. **6**, Q79 (2017).
[624]J. Kim, M. A. Mastro, M. J. Tadjer, and J. Kim, ACS Appl. Mater. Interfaces **9**, 21322 (2017).
[625]I. López, A. Castaldini, A. Cavallini, E. Nogales, B. Méndez, and J. Piqueras, J. Phys. D: Appl. Phys. **47**, 415101 (2014).
[626]L. X. Qian, X. Z. Liu, T. Sheng, W. L. Zhang, Y. R. Li, and P. T. Lai, AIP Adv. **6**, 045009 (2016).
[627]Y. H. An, D. Y. Guo, Z. M. Li, Z. P. Wu, Y. S. Zhi, W. Cui, X. L. Zhao, P. G. Li, and W. H. Tang, RSC Adv. **6**, 66924 (2016).
[628]B. Janjua, H. Sun, C. Zhao, D. H. Anjum, D. Priante, A. A. Alhamoud, F. Wu, X. Li, A. M. Albadri, A. Y. Alyamani, M. M. El-Desouki, T. K. Ng, and B. S. Ooi, Opt. Express **25**, 1381 (2017).
[629]G. C. Hu, C. X. Shan, N. Zhang, M. M. Jiang, S. P. Wang, and D. Z. Shen, Opt. Express **23**, 13554 (2015).
[630]Z. Cheng, M. Hanke, P. Vogt, O. Bierwagen, and A. Trampertless, Appl. Phys. Lett. **111**, 162104 (2017).
[631]K. H. Baik, Y. Irokawa, F. Ren, S. J. Pearton, S. S. Park, and Y. J. Park, Solid-State Electron **47**, 975 (2003).
[632]K. H. Baik, F. Ren, Y. Irokawa, S. J. Pearton, S. S. Park, and S. K. Lee, "Design and fabrication of GaN high power rectifiers," in *Optoelectronic Devices: III Nitrides* (Elsevier, Berlin, 2005), Chap. 12, pp. 323–350.
[633]X. A. Cao, H. Lu, S. F. LeBoeuf, C. Cowen, S. D. Arthur, and W. Wangless, Appl. Phys. Lett. **87**, 053503 (2005).
[634]K. H. Baik, Y. Irokawa, J. Kim, J. R. LaRoche, F. Ren, S. S. Park, Y. J. Park, and S. J. Pearton, Appl. Phys. Lett. **83**, 3192 (2003).
[635]Y. Zhang, M. Sun, Z. Liu, D. Piedra, J. Hu, X. Gao, and T. Palacios, Appl. Phys. Lett. **110**, 193506 (2017).
[636]Y. Cao, R. Chu, R. Li, M. Chen, R. Chang, and B. Hughes, Appl. Phys. Lett. **108**, 062103 (2016).
[637]Y. Zhang, Z. Liu, M. J. Tadjer, M. Sun, D. Piedra, C. Hatem, T. J. Anderson, L. E. Luna, A. Nath, A. D. Koehler, H. Okumura, J. Hu, X. Zhang, X. Gao, B. N. Feigelson, K. D. Hobart, and T. Palacios, IEEE Electron Device Lett. **38**, 1097 (2017).
[638]T.-T. Kao, J. Kim, Y.-C. Lee, A. F. M. S. Haq, M.-H. Ji, T. Detchprohm, R. D. Dupuis, and S.-C. Shen, IEEE Trans. Electron Devices **62**, 2679 (2015).
[639]A. Barkley, M. Schupbach, B. Agrawal, and S. Allen, in *2017 IEEE Applied Power Electronics Conference and Exposition (APEC)* (2017), pp. 2165–2172.
[640]A. Q. Huang, Proc. IEEE **105**(11), 2019–2047 (2017).
[641]X. She, A. Q. Huang, O. Lucıa, and B. Ozpineci, IEEE Trans. Ind. Electron **64**, 8193 (2017).
[642]H. Sun, C. G. Torres Castanedo, K. Liu, K.-H. Li, W. Guo, R. Lin, X. Liu, J. Li, and X. Li, Appl. Phys. Lett. **111**, 162105 (2017).
[643]J. Kim, M. A. Mastro, M. J. Tadjer, and J. Kim, ACS Appl. Mater. Interfaces **9**(25), 21322–21327 (2017).
[644]D. Hu, Y. Wang, S. Zhuang, X. Dong, Y. Zhang, J. Yin, B. Zhang, Y. Lv, Z. Feng, and G. Du, Ceram. Int. **44**(3) 3122–3127 (published online).
[645]Y. P. Qian, D. Y. Guo, X. L. Chu, H. Z. Shi, W. K. Zhu, K. Wang, X. K. Huang, H. Wang, S. L. Wang, P. G. Li, X. H. Zhang, and W. H. Tang, Mater. Lett. **209**, 558–561 (2017).
[646]M. Pavesi, F. Fabbri, F. Boschi, G. Piacentini, A. Baraldi, M. Bosi, E. Gombia, A. Parisini, and R. Fornari, Mater. Chem. Phys. **205**, 502–507 (published online).
[647]Y. Q. Huang, Y. H. An, Z. P. Wu, D. Y. Guo, Y. S. Zhi, W. Cui, X. L. Zhao, and W. H. Tang, J. Alloys Compd. **717**, 8–13 (2017).
[648]J. Yang, S. Ahn, F. Ren, S. J. Pearton, S. Jang, J. Kim, and A. Kuramata, Appl. Phys. Lett. **110**, 192101 (2017).
[649]J. Yang, S. Ahn, F. Ren, S. Jang, S. J. Pearton, and A. Kuramata, IEEE Electron Device Lett. **38**, 906 (2017).
[650]M. Oda, R. Tokuda, H. Kambara, T. Tanikawa, T. Sasaki, and T. Hitora, Appl. Phys. Express **9**, 021101 (2016).
[651]Q. Liu, D. Guo, K. Chen, Y. Su, S. Wang, P. Li, and W. Tang, J. Alloys Compd. **731**, 1225–1229 (published online).
[652]T. Oishi, K. Harada, Y. Koga, and M. Kasu, Jpn. J. Appl. Phys. **55**, 030305 (2016).
[653]E. Ohba, T. Kobayashi, M. Kado, and K. Hoshikawa, Jpn. J. Appl. Phys. **55**, 1202BF (2016).
[654]K. Sasaki, D. Wakimoto, Q. T. Thieu, Y. Koishikawa, A. Kuramata, M. Higashiwaki, and S. Yamakoshi, in Demonstration of Ga2O3 Trench MOS-Type Schottky Barrier Diodes, Device Research Conference, South Bend, IN, June 2017.
[655]M. Oda, J. Kikawa, A. Takatsuka, R. Tokuda, T. Sasaki, K. Kaneko, S. Fujita, and T. Hitora, in *73rd Annual Device Research Conference (DRC)* (2015), pp 137–138.
[656]K. Hanada, T. Moribayashi, T. Uematsu, S. Masuya, K. Koshi, K. Sasaki, A. Kuramata, O. Ueda, and M. Kasu, Jpn. J. Appl. Phys. **55**, 030303 (2016).
[657]Y. Tomm, J. M. Ko, A. Yoshikawa, and T. Fukuda, Sol. Energy Mater. Sol. Cells **66**, 369 (2001).
[658]M. Kasu, K. Hanada, T. Moribayashi, A. Hashiguchi, T. Oshima, T. Oishi, K. Koshi, K. Sasaki, A. Kuramata, and O. Ueda, Jpn. J. Appl. Phys. **55**, 1202BB (2016).
[659]T. Oshima, A. Hashiguchi, T. Moribayashi, K. Koshi, K. Sasaki, A. Kuramata, O. Ueda, T. Oishi, and M. Kasu, Jpn. J. Appl. Phys. **56**, 086501 (2017).
[660]S. Rafique, L. Han, A. T. Neal, S. Mou, J. Boeckl, and H. Zhao, Physica Status Solidi A (to be published).
[661]M. Kasu, T. Oshima, K. Hanada, T. Moribayashi, A. Hashiguchi, T. Oishi, K. Koshi, K. Sasaki, A. Kuramata, and O. Ueda, Jpn. J. Appl. Phys. **56**, 091101 (2017).
[662]F. J. Bruni, C.-M. Liu, and J. Stone-Sundberg, Acta Phys. Pol. A **124**, 213 (2013).
[663]E. Ohba, T. Kobayashi, M. Kado, and K. Hoshikawa, Jpn. J. Appl. Phys. **55**, 1202BF (2016).
[664]A. D. Koehler, T. J. Anderson, M. J. Tadjer, A. Nath, B. N. Feigelson, D. I. Shahin, K. D. Hobart, and F. J. Kub, ECS J. Solid State Sci. Technol. **6**, Q10 (2017).
[665]M. Kumar, S. Kumar, N. Chauhan, D. Sakthi Kumar, V. Kumar, and R. Singh, Semicond. Sci. Technol. **32**, 085012 (2017).
[666]S. Nakagomi, K. Hiratsuka, Y. Kakuda, and K. Yoshihiro, ECS J. Solid State Sci. Technol. **6**, Q3030 (2017).
[667]R. Schewski, M. Baldini, K. Irmscher, A. Fiedler, T. Markurt, B. Neuschulz, T. Remmele, T. Schulz, G. Wagner, Z. Galazka, and M. Albrecht, J. Appl. Phys. **120**, 225308 (2016).
[668]S. Krishnamoorthy, Z. Xia, C. Joishi, Y. Zhang, J. McGlone, J. Johnson, M. Brenner, A. R. Arehart, J. Hwang, S. Lodha, and S. Rajanless, Appl. Phys. Lett. **111**, 023502 (2017).
[669]X. Zhao, Z. Wu, Y. Zhi, Y. An, W. Cui, L. Li, and W. Tang, J. Phys. D: Appl. Phys. **50**, 085102 (2017).
[670]O. Takayoshi, K. Yuji, K. Naoto, K. Akito, Y. Shigenobu, F. Shizuo, O. Toshiyuk, and K. Makoto, Appl. Phys. Express **10**, 035701 (2017).
[671]F. Zhang, K. Saito, T. Tanaka, M. Nishio, M. Arita, and Q. Guo, Appl. Phys. Lett. **105**, 162107 (2014).
[672]C. Kranert, M. Jenderka, J. Lenzner, M. Lorenz, H. von Wenckstern, R. Schmidt-Grund, and M. Grundmann, J. Appl. Phys. **117**, 125703 (2015).
[673]T. Oshima, T. Okuno, N. Arai, Y. Kobayashi, and S. Fujita, Jpn. J. Appl. Phys. **48**, 070202 (2009).
[674]A Paskaleva, D Spassov, and P Terziyska, J. Phys.: Conf. Series **794**, 012017 (2017).
[675]H. Ito, K. Kaneko, and S. Fujita, Jpn. J. Appl. Phys. **51**, 100207 (2012).
[676]J. B. Varley and A. Schleife, Semicond. Sci. Technol. **30**, 024010 (2015).
[677]G. Kresse and J. Furthmüller, Phys. Rev. B **54**, 11169 (1996).
[678]M. J. Tadjer, N. A. Mahadik, V. D. Wheeler, E. R. Glaser, L. Ruppalt, A. D. Koehler, K. D. Hobart, C. R. Eddy, Jr., and F. J. Kub, ECS J. Solid State Sci. Technol. **5**, 468 (2016).
[679]A. Fiedler, R. Schewski, M. Baldini, Z. Galazka, G. Wagner, M. Albrecht, and K. Irmscher, J. Appl. Phys. **122**, 165701 (2017).
[680]N. Moser, J. McCandless, A. Crespo, K. Leedy, A. Green, A. Neal, S. Mou, E. Ahmadi, J. Speck, K. Chabak, N. Peixoto, and G. Jessen, IEEE Electron Device Lett. **38**, 775 (2017).
[681]Y. Zhu, Q. K. Yu, G. Q. Ding, X. G. Xu, T. R. Wu, Q. Gong, N. Y. Yuan, J. N. Ding, S. M. Wang, X. M. Xie, and M. H. Jiang, Nanoscale Res. Lett. **9**, 48 (2014).
[682]K. Zeng and U. Singisetti, Appl. Phys. Lett. **111**, 122108 (2017).
[683]N. Alfaraj, S. Mitra, F. Wu, I. Ajia, B. Janjua, A. Prabaswara, R. A. Aljefri, H. Sun, T. K. Ng, B. S. Ooi, I. S. Roqan, and X. Li, Appl. Phys. Lett. **110**, 161110 (2017).
[684]Y. H. An, Y. S. Zhi, W. Cui, X. L. Zhao, Z. P. Wu, D. Y. Guo, P. G. Li, and W. H. Tang, J. Nanosci. Nanotechnol. **17**(12), 9091–9094 (2017).
[685]M. Baldini, Z. Galazka, and G. Wagner, "Recent progress in the growth of β-Ga_2O_3 for power electronics applications," Mater. Sci. Semicond. Process. (published online).
[686]T. D. Moustakas and R. Paiella, Rep. Prog. Phys. **80**, 106501 (2017).

[687]A. J. Green, K. D. Chabak, M. Baldini, N. Moser, R. Gilbert, R. C. Fitch, G. Wagner, Z. Galazka, J. Mccandless, A. Crespo, K. Leedy, and G. H. Jessen, IEEE Electron Device Lett. **38**, 790 (2017).

[688]K. Chabak, A. Green, N. Moser, S. Tetlak, J. McCandless, K. Leedy, R. Fitch, A. Crespo, and G. Jessen, "Gate-recessed, laterally-scaled β-Ga_2O_3 MOSFETs with high-voltage enhancement-mode operation," in IEEE Device Research Conference (DRC), South Bend, IN, 2017.

[689]M. H. Wong, K. Goto, A. Kuramata, S. Yamakoshi, H. Murakami, Y. Kumagai, and M. Higashiwaki, "First demonstration of vertical Ga_2O_3 MOSFET: Planar structure with a current aperture," in IEEE Device Research Conference, South Bend IN, 2017.

[690]Z. Hu, K. Nomoto, W. Li, L. J. Zhang, J.-H. Shin, N. Tanen, T. Nakamura, D. Jena, and H. G. Xing, "Vertical fin Ga_2O_3 power field-effect transistors with on/off ratio $> 10^9$," in IEEE Device Research Conference, South Bend IN, 2017.

[691]S. Krishnamoorthy, Z. Xia, S. Bajaj, M. Brenner, and S. Rajan, Appl. Phys. Express **10**, 051102 (2017).

[692]M. Peres, K. Lorenz, E. Alves, E. Nogales, B. Méndez, X. Biquard, B. Daudin, E. G. Víllora, and K. Shimamura, J. Phys. D: Appl. Phys. **50**, 325101 (2017).

[693]W. S. Hwang, A. Verma, H. Peelaers, V. Protasenko, S. Rouvimov, H. (Grace) Xing, A. Seabaugh, W. Haensch, C. Van de Walle, Z. Galazka, M. Albrecht, R. Fornari, and D. Jena, Appl. Phys. Lett. **104**, 203111 (2014).

[694]S. Ahn, F. Ren, J. Kim, S. Oh, J. Kim, M. A. Mastro, and S. J. Pearton, Appl. Phys. Lett. **109**, 062102 (2016).

[695]J. Kim, S. Oh, M. Mastro, and J. Kim, Phys. Chem. Chem. Phys. **18**, 15760 (2016).

[696]J. D. Caldwell, T. J. Anderson, J. C. Culbertson, G. G. Jernigan, K. D. Hobart, F. J. Kub, M. J. Tadjer, J. L. Tedesco, J. K. Hite, M. A. Mastro, R. L. Myers-Ward, C. R. Eddy, P. M. Campbell, and D. K. Gaskill, ACS Nano **4**, 1108 (2010).

[697]H. Peelaers and C. G. Van de Walle, Phys. Rev. B **96**, 081409 (2017).

[698]M. Ogita, K. Higo, Y. Nakanishi, and Y. Hatanaka, Appl. Surf. Sci. **175/176**, 721 (2001).

[699]M. Ogita, N. Saika, Y. Nakanishi, and Y. Hatanaka, Appl. Surf. Sci. **142**, 188 (1999).

[700]C. Baban, Y. Toyoda, and M. Ogita, Thin Solid Films **484**, 369 (2005).

[701]C. Baban, Y. Toyoda, and M. Ogita, Jpn. J. Appl. Phys. **43**, 7213 (2004).

[702]M. Fleisher and H. Meixner, J. Mater. Sci. Lett. **11**, 1728 (1992).

[703]M. Fleischer and H. Meixner, Sens. Actuators B **6**, 257 (1992).

[704]J. Frank, M. Fleischer, and H. Meixner, Sens. Actuators B **34**, 373 (1996).

[705]M. Fleischer, L. Höllbauer, and H. Meixner, Sens. Actuators B **18**, 119 (1994).

[706]F. Reti, M. Fleischer, H. Meixner, and J. Giber, Sens. Actuators B **19**, 573 (1994).

[707]M. Fleischer and H. Meixner, Sens. Actuators B **52**, 179 (1998).

[708]M. Fleischer and H. Meixner, Sens. Actuators B **4**, 437 (1991).

[709]M. Fleischer and H. Meixner, Sens. Actuators B **13**, 259 (1993).

[710]U. Lampe, M. Fleischer, and H. Meixner, Sens. Actuators B **17**, 187 (1994).

[711]Z. Liu, T. Yamazaki, Y. Shen, T. Kikuta, N. Nakatani, and L. Yongxiang, Sens. Actuators B **129**, 666 (2008).

[712]Y. Li, A. Trinchi, W. Wlodarski, K. Galatsis, and K. Kalantar-zadeh, Sens. Actuators B **93**, 431 (2003).

[713]J. Frank, M. Fleischer, H. Meixner, and A. Feltz, Sens. Actuators B **49**, 110 (1998).

[714]M. Bartic, Y. Toyoda, C.-I. Baban, and M. Ogita, Jpn. J. Appl. Phys. **45**, 5186 (2006).

[715]S. Nakagomi, T. Sai, and Y. Kokubun, Sens. Actuators B **187**, 413 (2013).

[716]T. Rahman, T. Masui, and T. Ichiki, Jpn. J. Appl. Phys. **54**, 04DL08 (2015).

[717]D. Gonçalves, D. M. F. Prazeres, V. Chu, and J. P. Conde, Biosens. Bioelectron. **24**, 545 (2008).

[718]K.-H. Lee, J. O. Lee, S. Choi, J. B. Yoon, and G. H. Cho, Biosens. Bioelectron. **31**, 343 (2012).

[719]Y. Maruyama, S. Terao, and K. Sawada, Biosens. Bioelectron. **24**, 3108–3112 (2009).

[720]T. G. Drummond, M. G. Hill, and J. K. Barton, Nat. Biotechnol. **21**, 1192 (2003).

[721]R. Lao, S. Song, H. Wu, L. Wang, Z. Zhang, L. He, and C. Fan, Anal. Chem. **77**, 6475 (2005).

[722]F. Li, X. Han, and S. Liu, Biosens. Bioelectron. **26**, 2619 (2011).

[723]A. K. Cheng, B. Ge, and H. Z. Yu, Anal. Chem. **79**, 5158 (2007).

[724]A. Trinchi, W. Wlodarski, and Y. X. Li, Sens. Actuators B **100**, 94 (2004).

[725]Y. Yang and P. Zhang, Phys. Lett. A **374**, 4169 (2010).

[726]W. Jochum, S. Penner, K. Föttinger, R. Kramer, and B. Klötzer, J. Catal. **256**, 268 (2008).

[727]V. Stambouli, M. Labeau, I. Matko, B. Chenevier, O. Renault, C. Guiducci, P. Chaudoü, H. Roussel, D. Nibkin, and E. Dupuisa, Sens. Actuators B **113**, 1025 (2006).

[728]A. Zebda, V. Stambouli, M. Labeau, C. Guiducci, J.-P. Diard, and B. Le Gorrec, Biosens. Bioelectron. **22**, 178 (2006).

[729]V. Stambouli, A. Zebda, E. Appert, C. Guiducci, M. Labeau, J.-P. Diard, B. Le Gorrec, N. Brack, and P. J. Pigram, Electrochim. Acta **51**, 5206 (2006).

[730]R. Pandeeswari and B. G. Jeyaprakash, Sens. Actuators B **195**, 206 (2014).

[731]J. Zeng and U. J. Krull, Chim. Oggi **21**, 48 (2003).

[732]J. Xu, J. J. Zhu, Q. Huang, and H. Y. Chenal, Electrochem. Commun. **3**, 665 (2001).

[733]I. V. Yang and H. H. Thorp, Anal. Chem. **73**, 5316 (2001).

[734]M. Hai-Lin and F. Duo-Wang, Chin. Phys. Lett. **26**, 117302 (2009).

[735]H. Kim, C. Jin, S. An, and C. Lee, Ceram. Int. **38**, 3563 (2012).

[736]G. Korotcenkov and B. K. Cho, Sens. Actuators B **244**, 182 (2017).

[737]W. Cui, X. L. Zhao, Y. H. An, D. Y. Guo, X. Y. Qing, Z. P. Wu, P. G. Li, L. H. Li, C. Cui, and W. H. Tang, J. Phys. D: Appl. Phys. **50**, 135109 (2017).

[738]M. Fleischer, J. Giber, and H. Meixner, Appl. Phys. A **54**, 560 (1992).

[739]F. Becker, C. Krummel, A. Freiling, M. Fleischer, and C. Kohl, Fresenius J. Anal. Chem. **358**, 187 (1997).

[740]T. Schwebel, M. Fleischer, H. Meixner, and C.-D. Kohl, Sens. Actuators B **49**, 46 (1998).

[741]M. H. Lin, F. D. Wang, and N. X. Shan, Chin. Phys. B **19**, 076102 (2010).

[742]C. Baban, Y. Toyoda, and M. Ogita, J. Optoelectron. Adv. Mater. **7**, 891 (2005); available at https://joam.inoe.ro/index.php.

[743]T. Schwebel, M. Fleischer, and H. Meixner, Sens. Actuators B **65**, 176 (2000).

[744]M. Handwerg, R. Mitdank, Z. Galazka, and S. F. Fischer, Semicond. Sci. Technol. **31**, 125006 (2016).

[745]I. E. Demin and A. G. Kozlov, J. Phys.: Conf. Ser. **858**, 012009 (2017).

[746]D. Wang, Y. Lou, R. Wang, P. Wang, and N. Jiang, Ceram. Int. **41**, 14790 (2015).

[747]B. S. Kang, H. T. Wang, F. Ren, and S. J. Pearton, J. Appl. Phys. **104**, 031101 (2008).

[748]E. M. Dede, F. Zhou, and S. N. Joshi, "Concepts for embedded cooling of vertical current wide band-gap semiconductor devices," in *2017 16th IEEE Intersociety Conference on Thermal and Thermomechanical Phenomena in Electronic Systems (ITherm)* (2017), pp. 508–515.

[749]D. H. Altman, A. Gupta, and M. Tyhach, "Development of a diamond microfluidics-based intra-chip cooling technology for GaN," in *2015 Proceedings of the InterPACK Conference* (2015,), Paper No. IPACK2015-48179, p. V003T04A006.

[750]G. Campbell, H. Eppich, K. Lang, C. Creamer, T. Yurovchak, K. Chu, A. Kassinos, M. Ohadi, A. Shooshtari, and S. Dessiatoun, "Advanced cooling designs for GaN-on-diamond MMICs," *2015 Proceedings of the InterPACK Conference* (2015), *Paper No. IPACK2015–48429*, p. V003T04A007.

[751]A. Bar-Cohen, J. J. Maurer, and A. Sivananthan, MRS Adv. **1**, 181 (2016).

[752]K. Bloschock and A. Bar-Cohen, "Advanced thermal management technologies for defense electronics," Proc. SPIE. **8405**, 840501 (2012).

[753]D. C. Dumka, T. M. Chou, F. Faili, D. Francis, and F. Ejeckam, Electron. Lett. **49**(20), 1298–1299 (2013).

[754]M. Kim, J.-H. Seo, U. Singisetti, and Z. Ma, J. Mater. Chem. C **5**, 8338 (2017).

[755]S. Rafique, L. Han, and H. Zhao, ECS Trans. **80**, 203 (2017).

[756]H. Sun, C. G. Torres Castanedo, K. Liu, K.-H. Li, W. Guo, R. Lin, X. Liu, J. Li, and X. Li, Appl. Phys. Lett. **111**, 162105 (2017).

[757]E. Chikoidze, A. Fellous, A. Perez-Tomas, G. Sauthier, T. Tchelidze, C. Ton-That, T. T. Huynh, M. Phillips, S. Russelle, M. Jennings, B. Berini, F. Jomard, and Y. Dumont, "P-type β-gallium oxide: A new perspective for power and optoelectronic devices," Mater. Today Phys. **3**, 118 (2017).

[758]P. Weiser, M. Stavola, W. Beall Fowler, Y. Qin, and S. J. Pearton, "Structure and properties of OH centers in Ga_2O_3," Appl. Phys. Lett. (submitted).